frontiers | Research Topics

Digital holography: Applications and emerging technologies

Edited by
Peter Wai Ming Tsang, Ting-Chung Poon, Yaping Zhang and Pietro Ferraro

Published in
Frontiers in Photonics

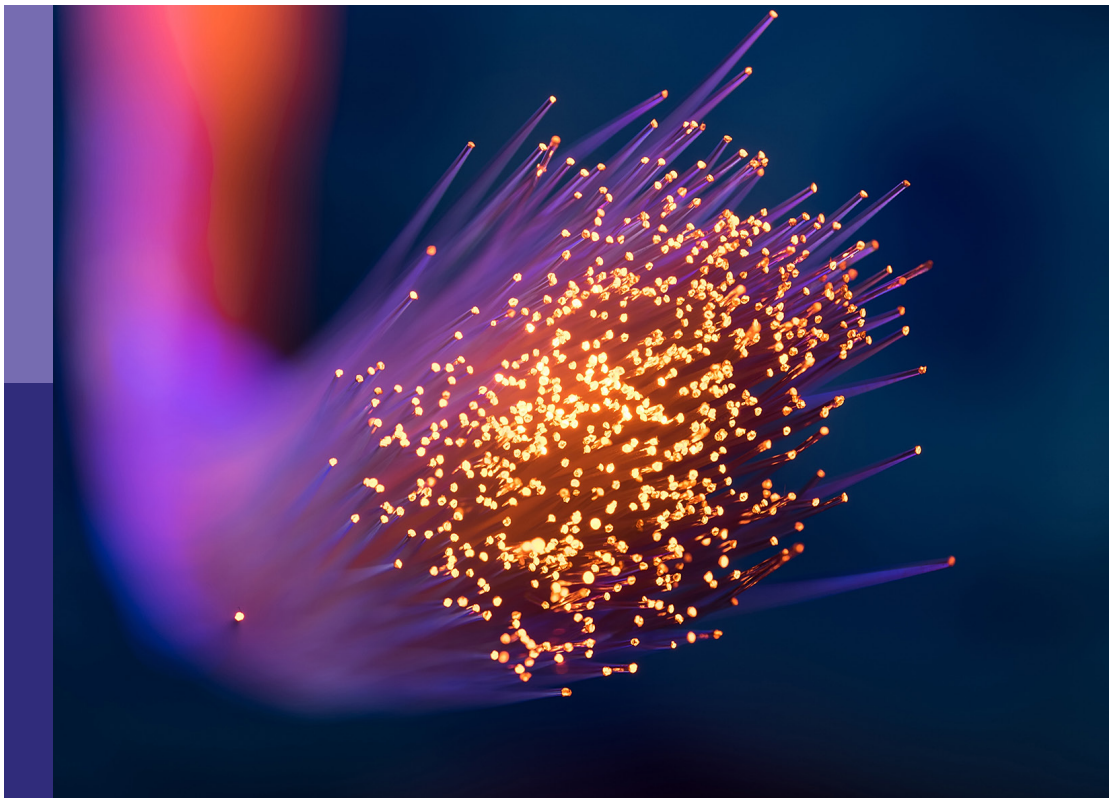

ISSN 1664-8714
ISBN 978-2-83250-921-0
DOI 10.3389/978-2-83250-921-0

About Frontiers

Frontiers is more than just an open access publisher of scholarly articles: it is a pioneering approach to the world of academia, radically improving the way scholarly research is managed. The grand vision of Frontiers is a world where all people have an equal opportunity to seek, share and generate knowledge. Frontiers provides immediate and permanent online open access to all its publications, but this alone is not enough to realize our grand goals.

Frontiers journal series

The Frontiers journal series is a multi-tier and interdisciplinary set of open-access, online journals, promising a paradigm shift from the current review, selection and dissemination processes in academic publishing. All Frontiers journals are driven by researchers for researchers; therefore, they constitute a service to the scholarly community. At the same time, the *Frontiers journal series* operates on a revolutionary invention, the tiered publishing system, initially addressing specific communities of scholars, and gradually climbing up to broader public understanding, thus serving the interests of the lay society, too.

Dedication to quality

Each Frontiers article is a landmark of the highest quality, thanks to genuinely collaborative interactions between authors and review editors, who include some of the world's best academicians. Research must be certified by peers before entering a stream of knowledge that may eventually reach the public - and shape society; therefore, Frontiers only applies the most rigorous and unbiased reviews. Frontiers revolutionizes research publishing by freely delivering the most outstanding research, evaluated with no bias from both the academic and social point of view. By applying the most advanced information technologies, Frontiers is catapulting scholarly publishing into a new generation.

What are Frontiers Research Topics?

Frontiers Research Topics are very popular trademarks of the *Frontiers journals series*: they are collections of at least ten articles, all centered on a particular subject. With their unique mix of varied contributions from Original Research to Review Articles, Frontiers Research Topics unify the most influential researchers, the latest key findings and historical advances in a hot research area.

Find out more on how to host your own Frontiers Research Topic or contribute to one as an author by contacting the Frontiers editorial office: frontiersin.org/about/contact

Digital holography: Applications and emerging technologies

Topic editors

Peter Wai Ming Tsang — City University of Hong Kong, Hong Kong, SAR China
Ting-Chung Poon — Virginia Tech, United States
Yaping Zhang — Kunming University of Science and Technology, China
Pietro Ferraro — National Research Council (CNR), Italy

Citation

Tsang, P. W. M., Poon, T.-C., Zhang, Y., Ferraro, P., eds. (2023). *Digital holography: Applications and emerging technologies*. Lausanne: Frontiers Media SA. doi: 10.3389/978-2-83250-921-0

Table of contents

frontiers | Frontiers in Photonics

TYPE Editorial
PUBLISHED 21 November 2022
DOI 10.3389/fphot.2022.1073297

OPEN ACCESS

EDITED AND REVIEWED BY
Pascal Picart,
Le Mans Université, France

*CORRESPONDENCE
P. W. M. Tsang,
eewmtsan@cityu.edu.hk

SPECIALTY SECTION
This article was submitted to Optical Information Processing and Holography, a section of the journal Frontiers in Photonics

RECEIVED 18 October 2022
ACCEPTED 09 November 2022
PUBLISHED 21 November 2022

CITATION
Tsang PWM, Poon T-C, Zhang Y and Ferraro P (2022), Editorial: Digital holography: Applications and emerging technologies.
Front. Photonics 3:1073297.
doi: 10.3389/fphot.2022.1073297

Editorial: Digital holography: Applications and emerging technologies

P. W. M. Tsang[1]*, Ting-Chung Poon[2], Yaping Zhang[3] and Pietro Ferraro[4]

[1]City University of Hong Kong, Kowloon, Hong Kong SAR, China, [2]Bradley Department of Electrical and Computer Engineering, Virginia Tech, Blacksburg, VA, United States, [3]Yunnan Provincial Key Laboratory of Modern Information Optics, Kunming University of Science and Technology, Kunming, Yunnan, China, [4]National Research Council (CNR), Roma, Italy

KEYWORDS

acoustic field imaging, chemiluminescence tomography, deep neural network, digital holography, fourier ptychographic reconstruction, fringe printer, noise suppression, visual cryptography

Editorial on the Research Topic
Digital holography: Applications and emerging technologies

A lot of researchers in optics have mentioned that holography, pioneered by Gabor in the late 40s could be a major, and possibly the ultimate solution towards three-dimensional (3-D) display. This may not be an overstatement, for as early as 1962, Yuri Denisyuk and his peers have realized optical holograms for recording 3-D images of real-world objects. When lit with a coherent light source, a hologram reconstructs a realistic visual image of the 3-D objects it records. Being different from another effective and widely adopted 3-D technology based on the lenticular lens, observing a hologram does not lead to accommodation-vergence conflict, which could induce visual fatigue or headaches to some people. Despite all its advantages, optical holography does not gain equal acceptance in the consumers market as compared with traditional photography. The discrepancy is mainly due to the need of expensive and delicate optical setups, mounted in a practically vibration-free optical table in a dark room, in capturing a hologram. These kind of stringent requirements basically limit the production of holograms to a laboratory environment that is generally unavailable to consumers at large. Similar to photography, optical holograms records magnitude of light waves encapsulating both amplitude and phase information on photographic films, and the contents cannot be changed afterwards. To produce a hologram with animated content, multiple frames of object images are sequentially recorded onto a multiplexed hologram. In this approach, the optical waves of each object image is mixed with a unique off-axis reference beam, and exposed onto the photographic film. The number of frames is rather limited and only a short video clip can be recorded onto a multiplexed hologram. Insofar, what the holography technology can be provided to the community is perhaps the 3-D holograms that we can purchase from the specialty stores.

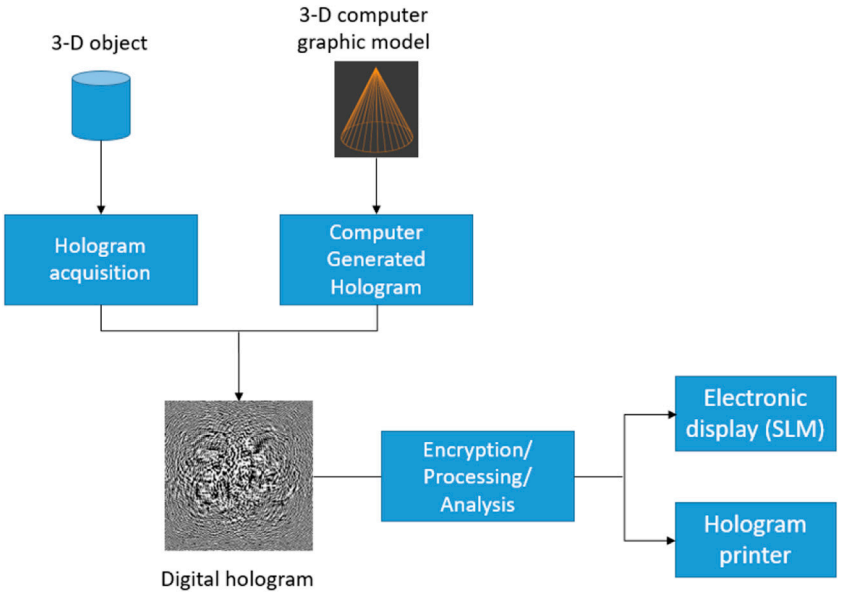

FIGURE 1
Typical infrastructure of digital holography.

However, the rapid advancement of optical, display, and computing technologies have casted light on a promising framework and future for holography, probably extending it to a realm that is comparable, if not exceeding the current digital photography. The new paradigm is realized with the integration of classical optical holography with the digital technology, an amalgamation that is generally referred to as 'digital holography'. For ease of explanation, let's refer to a typical infrastructure of digital holography in Figure 1.

From Figure 1, we observe that digital holography bears similar infrastructure as digital photography. A digital hologram can be captured from a physical object, or numerically generated from a computer graphic model. The digital hologram can be further processed and/or encrypted, and subsequently displayed with a high resolution device, or printed with a hologram printer. However, digital holography can be applied to capture, process, and display 3-D images, which is not possible with digital photography. These processes are more complicated to realize as holographic signals are complex-valued with both magnitude and phase information. Existing cameras and displays are only effective in recording and reconstructing the magnitude component of optical waves, which cannot be directly applied in handling complex-valued signals. Apart from recording and displaying 3-D images, digital holography can also be used in encryption. A digital hologram is comprised of high frequency fringe patterns that do not reveal much clue on the object image it represents. Hence if a digital hologram is encrypted, it is much more difficult to crack the decryption key through trial and error. However, this also makes a digital hologram more difficult to classify, as traditional image analysis techniques (such as contour tracing and corner detection) cannot be applied to extract a meaningful object shape from the hologram fringe patterns. In the past 3 decades, numerous research works have been conducted to develop various components in the digital holography framework. Despite the encouraging progress achieved to date, the art of digital holography keeps on evolving at a rapid pace as it involves sophisticated integration of both existing and emerging technologies. This Research Topic, comprising of 13 papers contributed by renowned scholars and experts in the field, aims to provide readers with a quick overall view on some of the latest and exciting development on digital holography. Hereafter, we shall briefly outline the main emphasis of each paper, so as to provide readers with a summary on the topics that are being covered. For those who have specific interested in selected areas, the succinct descriptions can also facilitate them to identify the relevant paper(s) to focus on.

Shen et al. in their paper, "*High-throughput artifact-free slightly off-axis holographic imaging based on Fourier ptychographic reconstruction*", describe a method for reconstructing the amplitude and phase images from a hologram that is acquired with slightly off-axis digital holographic microscopy. The authors point out that although this hologram capturing method improves the space-bandwidth product, and partially suppressing the background intensities, it

is imposed with a spectral aliasing problem which cannot be discarded with filtering techniques. The phase information is jeopardized as a consequence. To overcome this issue, a non-linear optimization method based on Fourier ptychographic microscopy (FPM), is proposed to recover the object amplitude and phase information from the hologram. Experimental results reveal that the proposed method outweighs conventional off-axis method, as well as the Kramers–Kronig (KK) method in both amplitude and phase reconstruction.

Askari and Park in their paper, "*Augmentation of 3D holographic image graticule with conventional microscopy*", develop a method that projects a graticule image on test subjects. Producing a graticule pattern is often faced with the dilemma that while enlarged (extended) depth-of-field (DOF) is required for lateral measurement, a shallow DOF is needed for longitudinal measurement. The authors overcome this method by generating a hologram at minimum, and maximum angular spectrum range for extended, and shallow DOF, respectively. Experimental results, based on numerical simulation and optical reconstruction, reveal that a hologram generated with the proposed method can produce focused graticule patterns across a depth range of 80 mm. At the same time, it can also generate shallow DOF images that are only focused within a narrow depth range.

Hassad et al. in their paper, "*Multi-view acoustic field imaging with digital color holography*", apply digital holography for acoustic field imaging. Although sound signals can be measured with microphone array, the resolution and fidelity of the measurement are affected by the size and the presence of the sensors. These shortcomings could be avoided with optical imaging. The authors have proposed to use multicolor laser beams to capture three spatially multiplexed off-axis digital holograms of the acoustic field of a volume from three different directions. Experimental results reveal that the amplitude and phase components of the acoustic signal can be reconstructed from the digital holograms. A deviation between the integrated amplitude along the laser direction, and the true amplitude is noted, suggesting good research potential based on the proposed method.

Coherent noise is often a problem in digital holography as it affects the quality of measurement as well as for optical display. Li et al. in their paper, "*Speckle noise suppression algorithm of holographic display based on spatial light modulator (Invited),*" provide an overview on the speckle noise suppression of holographic display.

Past research has demonstrated that coherent noise can be reduced with deep neural network which is trained with a large dataset. The need of the large dataset is overcome in the paper by Tang et al., "*Coherent noise suppression of single-shot digital holographic phase via an untrained self-supervised network*". The authors propose to use a constant random uniform noise, and a single-phase noise as the input and ground truth for training the network.

Zhou et al. in their paper, "*Visual cryptography using binary amplitude-only holograms [Invited],*" investigate visual cryptography (VC). In VC, the useful information can be rendered without the usage of decryption algorithms. However, many VC schemes cannot withstand occlusion attacks. The authors propose the use of holography along with VC to verify their technique that is able to withstand occlusion attacks and noise contamination.

Coherent holographic imaging has a serious drawback as it is extremely susceptible to speckle noise. On the other hand, incoherent holography allows a higher signal-to-noise ratio as compared to its coherent counterpart. Tahara in his paper, "*Review of incoherent digital holography: applications to multidimensional incoherent digital holographic microscopy and palm-sized digital holographic recorder—Holosensor,*" provides a review on the advancement of modern incoherent digital holography.

Pixelated spatial light modulators (SLMs) introduce errors during holographic display. Chen et al. in their paper, "*Compact computational holographic display (invited article),*" use the use of phase shifting holography along with automatic differentiable (AD) optimization to improve the quality of holography reconstruction.

Yamaguchi and Yoshikawa in their paper, "*Development of a fringe printer with 0.35 um pixel pitch*," give a review of the development of a fringe printer that can achieve 0.35um pixel pitch computer-generated holograms and the specification of the printer has been verified experimentally.

Jin and Situ in their paper, "*A survey for 3D flame chemiluminescence tomography: theory, algorithms, and applications (invited),*" give an extensive review on the progress of chemiluminescence tomography (FCT), which is a 3D imaging technique of key physical parameters in the combustion process.

Liu at al. In their paper, "*Compressive interferenceless coded aperture correlation holography with high Imaging quality (Invited),*" use compressive sensing to improve the low signal-to-noise ratio inherent in one of the incoherent digital holographic techniques–interference coded aperture correlation holography (I-COACH). They have been able to suppress the background noise and improved the reconstruction quality of conventional I-COACH without sacrificing the imaging speed.

Zhou et al. in their paper, "*Elimination of quadratic phase aberration in digital holographic microscopy by using transport of intensity*," take advantages of the merits of transport and intensity (TIE) and digital holography (DH) to eliminate quadratic phase aberration introduced by the microscope objective in digital holographic microscopy. A regularization

parameter is employed within the TIE method for phase retrieval.

Deep-leaning has been developing rapidly in recent years. Shimobaba et al. in their paper, "*Deep-learning computational holography: a review (invited)*," provide a comprehensive review on computational holography using deep leaning. The authors believe that the combination of deep leaning and physically-based calculations will lead to ground-breaking computational holography research.

Author contributions

PT: Draft and review the manuscript. T-CP: Draft and review the manuscript. YZ: Review the manuscript and provide advice. PF: Review the manuscript and provide advice.

Funding

National natural science foundation of China (Grant No. 61865007 and 62275113).

Acknowledgments

Once again, we would like to express our deepest thanks to all the authors and co-authors for their valuable contributions to this Research Topics.

Conflict of interest

The authors declare that the research was conducted in the absence of any commercial or financial relationships that could be construed as a potential conflict of interest.

Publisher's note

frontiers in Photonics

ORIGINAL RESEARCH
published: 13 January 2022
doi: 10.3389/fphot.2021.821304

Visual Cryptography Using Binary Amplitude-Only Holograms

*Lina Zhou, Yin Xiao, Zilan Pan, Yonggui Cao and Wen Chen**

Department of Electronic and Information Engineering, The Hong Kong Polytechnic University, Hong Kong SAR, China

Visual cryptography (VC) is developed to be a promising approach to encoding secret information using pixel expansion rules. The useful information can be directly rendered based on human vision without the usage of decryption algorithms. However, many VC schemes cannot withstand occlusion attacks. In this paper, a new VC scheme is proposed using binary amplitude-only holograms (AOHs) generated by a modified Gerchberg-Saxton algorithm (MGSA). During the encryption, a secret image is divided into a group of unrecognizable and mutually-unrelated shares, and then the generated shares are further converted to binary AOHs using the MGSA. During image extraction, binary AOHs are logically superimposed to form a stacked hologram, and then the secret image can be extracted from the stacked hologram. Different from conventional VC schemes, the proposed VC scheme converts a secret image into binary AOHs. Due to the redundancy of the generated binary AOHs, the proposed method is numerically and experimentally verified to be feasible and effective, and possesses high robustness against occlusion attacks.

Keywords: optical security, visual cryptography, binary amplitude-only holograms, modified gerchberg-saxton algorithm, occlusion attacks

OPEN ACCESS

Edited by:
Peter Wai Ming Tsang, City University of Hong Kong, Hong Kong SAR, China

Reviewed by:
Atsushi Shiraki, Chiba University, Japan
Naveen Nishchal, Indian Institute of Technology Patna, India

****Correspondence:***
Wen Chen
owen.chen@polyu.edu.hk

Specialty section:
This article was submitted to Optical Information Processing and Holography, a section of the journal Frontiers in Photonics

Received: *24 November 2021*
Accepted: *16 December 2021*
Published: *13 January 2022*

Citation:
Zhou L, Xiao Y, Pan Z, Cao Y and Chen W (2022) Visual Cryptography Using Binary Amplitude-Only Holograms. Front. Photonics 2:821304. doi: 10.3389/fphot.2021.821304

INTRODUCTION

Information security plays an important role nowadays, and has attracted much current attention (Javidi, 1997; Alfalou and Brosseau, 2009; Chen et al., 2014). One promising approach to realizing information security is optical encryption, which exploits physical properties of light (e.g., amplitude, phase, frequency and polarization) to secure information (Javidi, 1997; Alfalou and Brosseau, 2009; Chen et al., 2014). Owing to the striking properties of optical means, optical encryption opens up a new research perspective for information security in the field of data transmission and data storage. Since double random phase encoding (DRPE) was demonstrated (Refregier and Javidi, 1995), its variations have been continuously developed in different domains, e.g., Fresnel domain and fractional Fourier domain (Situ and Zhang, 2004; Wang et al., 2014). Other optical technology-based encryption schemes have been studied based on DRPE architecture, e.g., diffractive imaging and computer-generated hologram (Johnson and Brasher, 1996; Zhang and Wang, 2008; Chen et al., 2010; Xi et al., 2017). However, many optical encryption schemes use digital decryption algorithms to decode secret information. There is also a high demand of new types of cryptographic schemes, which could enable the authorized users to realize decryption of secret information in a simple way. Since visual cryptography (VC) was developed (Naor and Shamir, 1995), there are many relevant studies for its applications. The VC offers a feasible and straightforward solution for the decryption of secret information based on human vision (Naor and Shamir, 1995; Blundo et al., 2000; Hou, 2003; Wan et al., 2018; Yang et al., 2018; Jiao et al., 2019; Li et al., 2019; Jiao et al., 2020). The first visual cryptographic technique was proposed by Naor and Shamir in 1995, which broke up a secret image

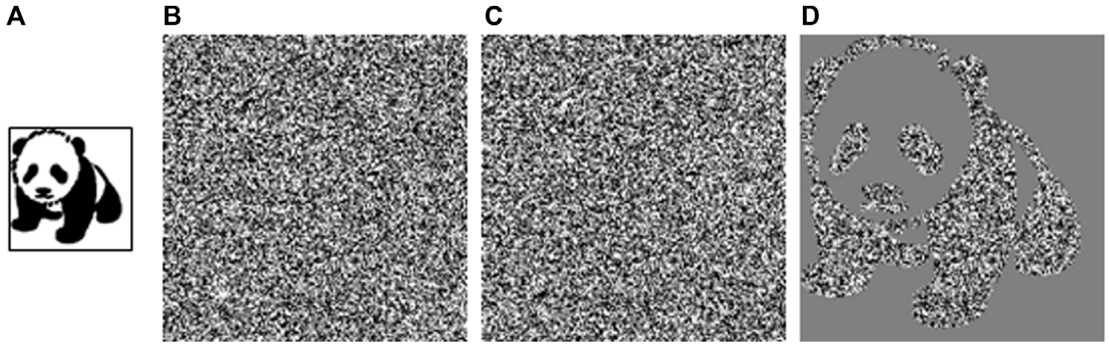

FIGURE 1 | A typical example for conventional VC scheme to encrypt a secret image into two visual key images, and then the secret image can be retrieved by overlapping these two visual key images. **(A)** A secret image. **(B)** and **(C)** Two visual key images generated by using conventional VC scheme. **(D)** A retrieved image obtained by overlapping **(B)** and **(C)**.

into multiple shares (i.e., visual key images) (Naor and Shamir, 1995). Subsequently, the secret image can be directly and visually decrypted by overlapping all the shares. In practice, these visual key images are printed onto separate transparent sheets, and then the secret image can be decoded by overlaying these sheets. It is worth mentioning that no meaningful information about the secret image can be retrieved from any one of the shares. The VC has been rapidly developed, and recent developments of VC are focused on the generation of visual key images. In the developed VC techniques, the generated visual key images can be random binary patterns, natural binary images, grayscale images and color images (Naor and Shamir, 1995; Blundo et al., 2000; Hou, 2003). Moreover, visual key images can be further designed using quick response patterns or phase holograms (Wan et al., 2018; Jiao et al., 2020). The visual key images are printed onto holographic optical elements (HOEs) or metasurface, and then the secret images can be visually decoded when these visual key images are overlapped (Yang et al., 2018; Li et al., 2019). Although VC scheme provides an effective way to realize encryption by using pixel expansion rule and decode the secret information based on human vision, conventional VC techniques could have some disadvantages. It is required that visual key images should be printed onto transparent sheets but not opaque materials (Naor and Shamir, 1995; Blundo et al., 2000; Hou, 2003). There are also some concerns with visual key images printed on HOEs or meta-devices, e.g., fabrication difficulty (Yang et al., 2018; Li et al., 2019). Furthermore, many VC techniques have a risk due to information occlusion, which usually happens in data transmission and data storage. Therefore, the potential of VC schemes has not been fully explored. It is desirable that new VC schemes can be continuously proposed to explore the potentials with enhanced robustness and reduced fabrication difficulty.

In this paper, we propose a new VC scheme using binary amplitude-only holograms (AOHs) with a modified Gerchberg-Saxton algorithm (MGSA). During the encryption, a secret image is expanded into a set of random binary patterns using pixel expansion rule, and then these random binary patterns are transformed into binary AOHs using the designed MGSA. Owing to the redundancy of binary AOHs, a high level of robustness is achieved in the proposed method to withstand occlusion attacks. During image extraction, binary AOHs are logically superimposed to form a stacked hologram, and then the secret image can be extracted from the stacked hologram. Feasibility and effectiveness of the proposed method are fully demonstrated in numerical simulations and optical experiments. It is numerically and experimentally verified that the proposed VC scheme can achieve high robustness to withstand occlusion attacks. It is believed that the proposed method could provide a promising solution for visual cryptography.

PRINCIPLES

Conventional VC Scheme

Conventional VC scheme is developed based on pixel expansion rules to expand each pixel to be a set of sub-pixels (Naor and Shamir, 1995). **Figure 1** shows a typical example of conventional VC scheme. A secret image with 64 × 64 pixels in **Figure 1A** is encrypted into two random binary shares with 256 × 256 pixels (i.e., visual key images) in **Figures 1B,C**. In this case, each pixel is expanded to be four sub-pixels. As can be seen in **Figures 1B,C**, no information about original secret image can be visually obtained from visual key images. If the two shares (i.e., visual key images) are overlapped, the secret image can be visually rendered as shown in **Figure 1D**. However, many conventional VC schemes are proven to be vulnerable to occlusion attacks owing to the dependence on expansion rules of pixels. Furthermore, high fabrication difficulty of the shares could also limit the application of VC schemes. It is desirable that VC schemes can be developed with enhanced robustness and reduced fabrication difficulty.

The Proposed VC Scheme Using Binary AOHs via MGSA

Here, the redundancy of digital holograms is applied to enhance capability of VC scheme to withstand occlusion attacks. To reduce fabrication difficulty, binary AOHs rather than phase-only holograms are integrated into VC scheme to convert visual key images into binary AOHs. **Figure 2** shows a schematic of the

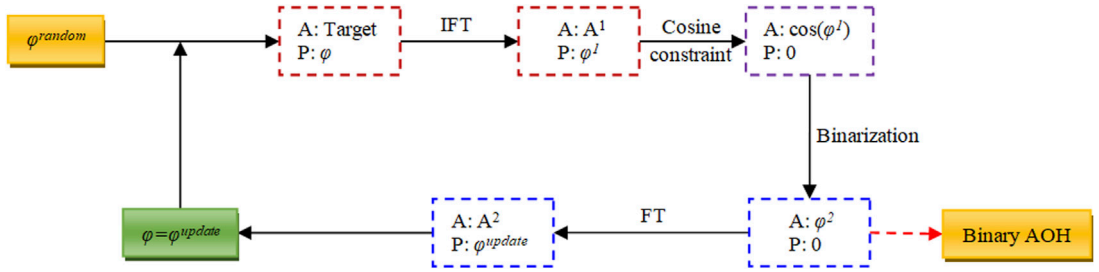

FIGURE 2 | A schematic of the designed MGSA to generate binary AOHs. A: Amplitude; P: phase; IFT: Inverse Fourier transform; FT: Fourier transform.

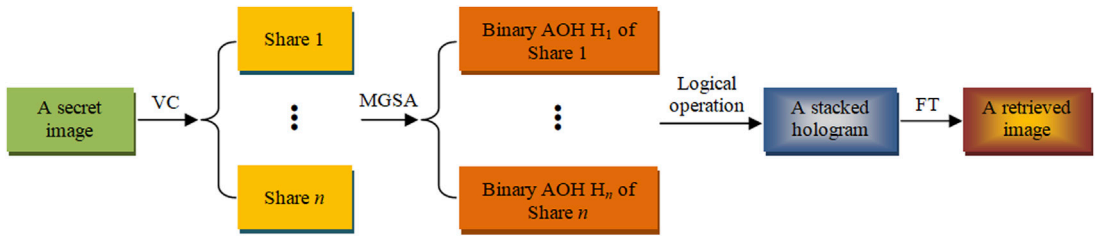

FIGURE 3 | A flow chart for the proposed VC scheme using binary AOHs via MGSA.

proposed MGSA to generate binary AOHs (Xu et al., 2020; Zhou et al., 2021). A target image with a random phase φ^{random} is inverse Fourier transformed, and then the generated phase φ^1 is constrained by a cosine function to form an amplitude-only pattern cos (φ^1). To reduce complexity of amplitude retrieval, amplitude-only pattern cos (φ^1) is binarized to generate a binary AOH φ^2. With the usage of Fourier transform to the binary AOH φ^2, new complex amplitude can be obtained and an updated phase φ^{update} is correspondingly retrieved. Then, the updated phase φ^{update} together with the target image is inverse Fourier transformed in a new iteration. When a preset condition is satisfied, the final binary AOH is used as an optimal binary AOH of the target image. To solve the twin-image problem, the target image can be placed at the upper left corner. Since the redundancy of digital holograms provides high robustness, the generated binary AOHs can be used for secret-image retrieval, e.g., under occlusion attacks (Gerritsen et al., 1968; Kreis, 2005; Schnars and Jüptner, 2005; Hwang et al., 2009; Xu et al., 2017; Xu et al., 2020; Zhou et al., 2021).

Owing to the generation of binary AOHs to withstand occlusion attacks, a new VC scheme is proposed by integrating binary AOHs into VC scheme. **Figure 3** shows a flow chart for the proposed VC scheme using binary AOHs with the MGSA. During the encryption, a secret image is encoded into a set of visual key images (i.e., Share 1, . . . , Share n) using conventional VC scheme. Then, the visual key images are further processed by the designed MGSA, yielding n binary AOHs (i.e., H_1, . . . , H_n). The binary AOHs are used as new shares to be delivered to the authorized users in the proposed VC scheme. During image extraction, a logical operation (e.g., AND, OR, or XOR) is implemented on these new shares (i.e., binary AOHs) to generate a stacked hologram. Finally, an image can be retrieved from the stacked hologram to visually render information of the secret image.

RESULTS AND DISCUSSION

Simulation Results and Discussion

To verify feasibility and effectiveness of the proposed VC scheme, numerical simulation is first conducted. **Figure 4** shows a schematic of the proposed VC scheme. For the sake of brevity, encoding a secret image into only two shares is conducted. In addition, an AND operation is adopted to illustrate the proposed VC scheme. It is worth noting that the generated stacked hologram is still a binary AOH when an AND operation is applied. By using conventional VC algorithm, a secret image with 64 × 64 pixels is encoded into two visual key images (i.e., Share 1 and Share 2 with 256 × 256 pixels). Then, these two shares are converted to binary AOHs (i.e., H_1 and H_2) to further enhance the robustness. Here, size of binary AOHs is 512 × 512 pixels to avoid the overlapping with twin image. To extract the secret image, the two binary AOHs are collected and processed by an AND operation to generate a stacked hologram with 512 × 512 pixels. Finally, an image can be retrieved from the stacked hologram to visually render information of the secret image.

By using the proposed VC scheme, each secret image can be encoded into a pair of binary AOHs, and then the two binary AOHs are delivered to two authorized users. When the pair of binary AOHs is collected and processed by an AND operation, a stacked hologram can be generated. Then, the generated stacked

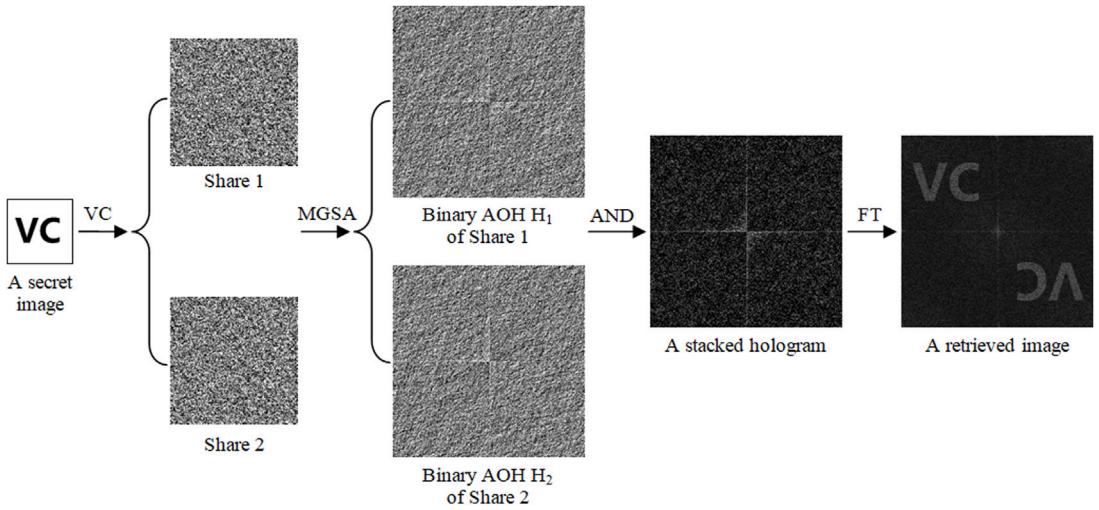

FIGURE 4 | A schematic of the proposed VC scheme using two shares.

hologram can be further used for the retrieval of the secret image. **Figure 5** shows several secret images (64 × 64 pixels) encoded by using the proposed VC scheme into binary AOHs (512 × 512 pixels). As can be seen in **Figures 5A,B,E,F,I,J**, three secret images have been respectively converted to binary AOHs, which do not visually render any information about secret images. To extract the secret images, an AND operation is implemented to each pair of binary AOHs (i.e., **Figures 5A,B**, **Figures 5E,F** and **Figures 5I,J**) to generate the stacked holograms as respectively shown in **Figures 5C,G,K**. Finally, the corresponding images are retrieved from the stacked holograms by using Fourier transform, as shown in **Figures 5D,H,L**. It is illustrated that the retrieved images can clearly render information of the secret images based on human vision. To quantitatively evaluate the retrieved images, peak signal-to-noise ratio (PSNR) is calculated. Since twin images are generated in the retrieved images as shown in **Figures 5D,H,L**, only area of interest (i.e., the top left corner with 256 × 256 pixels) is used. Meanwhile, original secret images are resized from 64 × 64 pixels to 256 × 256 pixels to calculate PSNR. PSNR values of the retrieved images in **Figures 5D,H,L** are 10.30, 14.08 and 14.88 dB, respectively.

The proposed method uses binary AOHs to enhance robustness of VC schemes. When Fourier transform is directly **Figure 6** applied to retrieve the shares from binary AOHs, it is also studied whether secret images can be extracted by overlapping the retrieved shares without the usage of logical operations. For a comparison, original secret images used in **Figure 6** are the same as those used in **Figure 5**. **Figures 6A,B,F,G,K,L** show three pairs of binary AOHs, and the images in **Figures 6C,D,H,I,M,N** are obtained by directly using Fourier transform to the images in **Figures 6A,B,F,G,K,L**, respectively. Then, the image retrieval is conducted by overlapping **Figures 6C,D,H,I,M,N**, respectively. As can be seen in **Figures 6E,J,O**, no information about secret images can be visually rendered in the retrieved images without the usage of logical operations. Therefore, it is compulsory for the proposed VC scheme to use logical operations for secret-image retrieval. It is also demonstrated that the proposed VC scheme is feasible and effective.

Experimental Results and Discussion

Optical experiments are also conducted to demonstrate feasibility and effectiveness of the proposed VC scheme. **Figure 7** shows a schematic experimental setup for extracting secret images from the stacked holograms. He-Ne laser beam (Newport, R-30993) with wavelength of 633.0 nm is expanded and collimated. The collimated optical wave is reflected by a mirror to illuminate an amplitude-only spatial light modulator (SLM, Holoeye LC-R720). The stacked holograms are sequentially embedded into the SLM. Then, the modulated wave propagates through a lens (f = 10.0 cm), and is recorded by a CCD camera with 1,280 × 1,024 pixels and pixel size of 5.30 μm (Thorlabs, DCC3240M). When the pairs of binary AOHs are collected, stacked holograms are generated by applying an AND operation. The secret images are experimentally retrieved from the stacked holograms. **Figures 8A–D** show the stacked holograms generated by using binary AOHs, and **Figures 8E–H** show the corresponding images recorded by CCD camera. Information of the secret images is visually recognized, which is sufficient in optical encryption field. To quantitatively evaluate quality of the retrieved images in optical experiments, visibility is used and calculated by (Kellock et al., 2011; Ghaleh et al., 2018)

$$\text{Visibility} = \frac{< I_s > - < I_b >}{< I_s > + < I_b >} \tag{1}$$

where I_s and I_b respectively denote intensity in the signal part and background part, and average intensity is respectively denoted as $<I_s>$ and $<I_b>$. Visibility of the retrieved images in **Figures 8E–H** is 0.17, 0.16, 0.19 and 0.22, respectively.

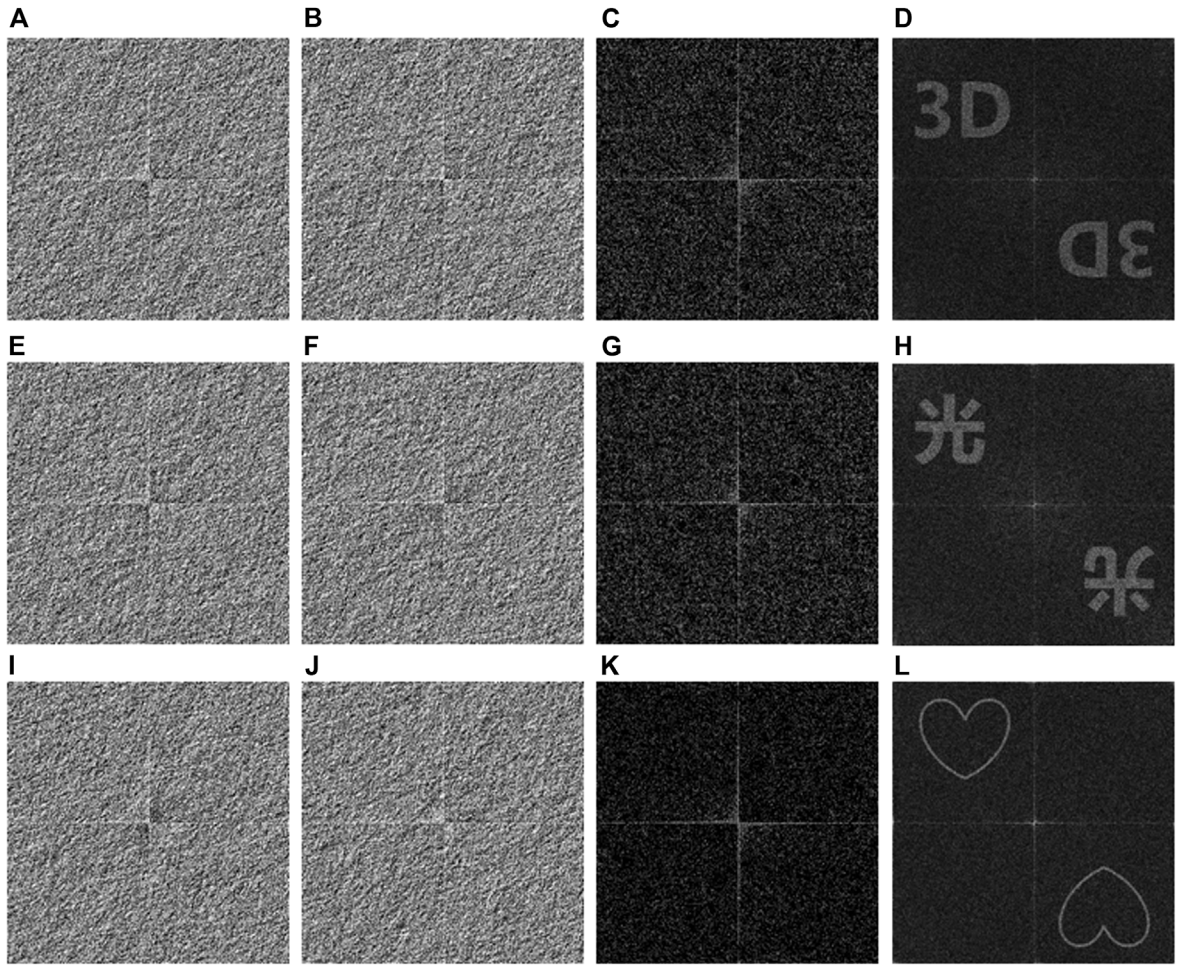

FIGURE 5 | Typical examples of the proposed VC scheme. **(A, E, I)** Binary AOHs H_1. **(B, F, J)** Binary AOHs H_2. **(C, G, K)** Stacked holograms respectively generated by an AND operation between **(A)** and **(B) (E)** and **(F)**, and **(I)** and **(J)**. **(D, H, L)**. The retrieved images obtained by respectively using Fourier transform to **(C, G, K)**.

In optical experiments, Fourier transform of binary AOHs for image retrieval without the usage of logical operations is also investigated. **Figures 9A,B** show two binary AOHs corresponding to a secret image 'EIE'. Then, binary AOHs in **Figures 9A,B** are experimentally Fourier transformed to retrieve the shares as shown in **Figures 9C,D**, respectively. Finally, the retrieved shares are overlapped to extract the secret image, and the retrieved image is shown in **Figure 9E**. As can be seen in **Figure 9E**, the retrieved image cannot visually provide any information about secret image 'EIE'. It is experimentally verified that secret images cannot be retrieved without the usage of logical operations, and Fourier transform of binary AOHs will not result in information leakage.

Since occlusion of binary AOHs could happen during data transmission or data storage, occlusion attacks have also been experimentally conducted to demonstrate robustness of the proposed VC scheme. Here, a secret image 'EIE' is used and tested, and its corresponding binary AOHs are shown in **Figures 9A,B**. **Figures 10A–E** show the stacked holograms generated by occlusion contamination of the first binary AOH H_1 in **Figure 9A**, when the second binary AOH H_2 in **Figure 9B** remains unchanged. When the first binary AOH is respectively occluded with 3.81% (100 × 100 pixels), 15.26% (200 × 200 pixels), 34.33% (300 × 300 pixels), 61.04% (400 × 400 pixels) and 77.25% (450 × 450 pixels), the generated stacked holograms are correspondingly occluded at the top left corner as shown in **Figures 10A–E**. The secret images are experimentally retrieved and shown in **Figures 10F–J**. When occlusion percentage of the first binary AOH is lower than 61.04%, the retrieved images can still be recognized as shown in **Figures 10F–I**. **Figure 11** shows the performance of the proposed VC scheme, when the second binary AOH in **Figure 9B** is occluded from 3.81 to 77.25% and the first binary AOH in **Figure 9A** remains unchanged. In this case, the corresponding stacked holograms are generated and shown in **Figures 11A–E**. It is also demonstrated that information of the secret image can be extracted when occlusion percentage of

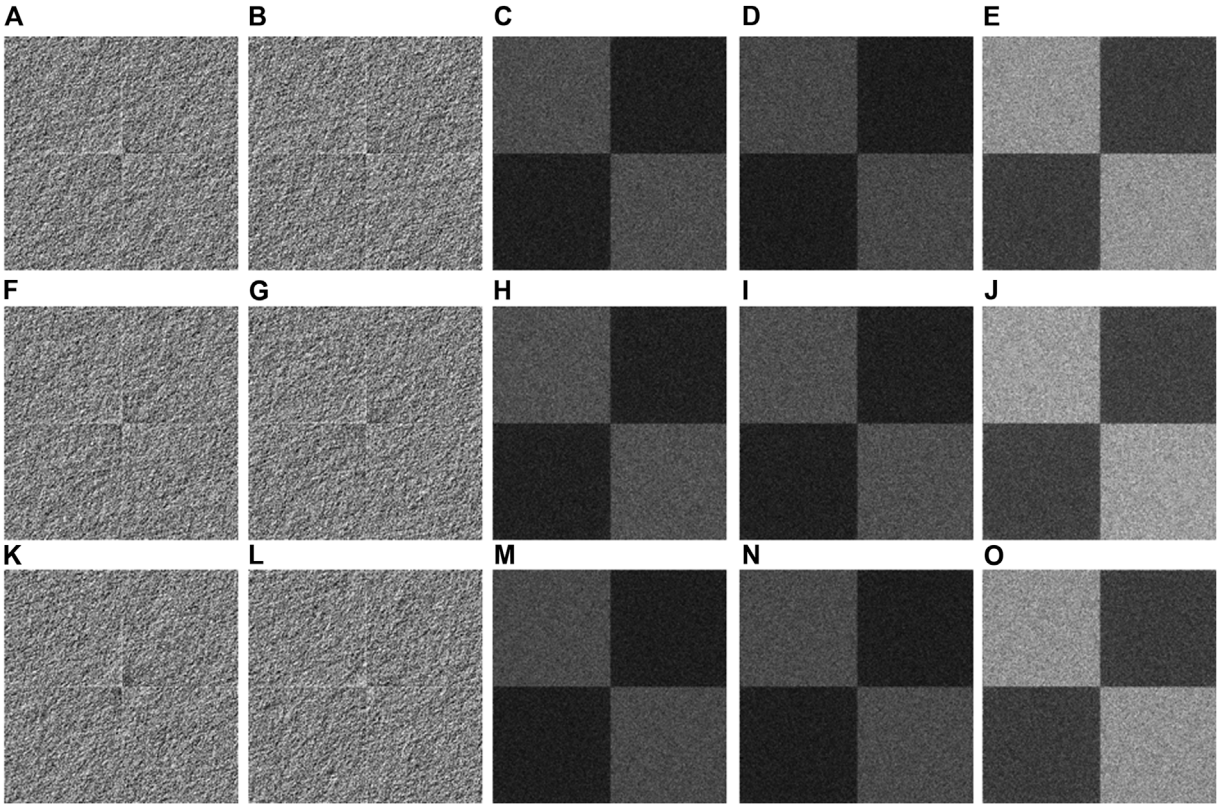

FIGURE 6 | Secret images retrieved without the usage of logical operations. **(A, F, K)** Binary AOHs H_1. **(B, G, L)** Binary AOHs H_2. **(C, H, M)** Share 1 respectively extracted from **(A, F, K)**. **(D, I, N)** Share 2 respectively extracted from **(B, G, L)**. **(E, J, O)** The images obtained by respectively overlapping **(C)** and **(D), (H)** and **(I)**, and **(M)** and **(N)**.

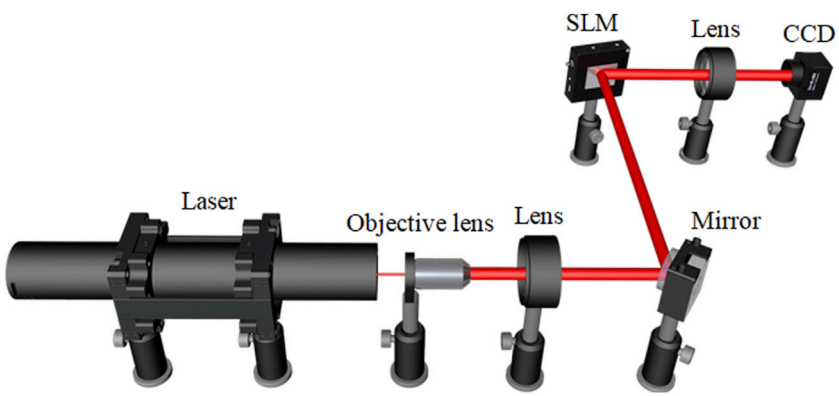

FIGURE 7 | A schematic optical setup for retrieving secret images from the stacked holograms. CCD: charge-coupled device.

the second binary AOH is lower than 61.04%, as shown in **Figures 11F–I**.

Figure 12 shows the effect of occlusion attacks on visibility of the retrieved images in optical experiments. In **Figure 12A**, only the first binary AOH in **Figure 9A** is occluded with the increased percentage from 0.000381 to 95.37%, and the occluded region is from the upper left to the lower right. As can be seen in **Figure 12A**, there is a downward trend of visibility values from 0.21 to 0.06. The same trend is found for the occlusion attack on the second binary AOH, as shown in **Figure 12B**. Although quality of the retrieved images decreases with the increased occlusion percentage, effective information of the

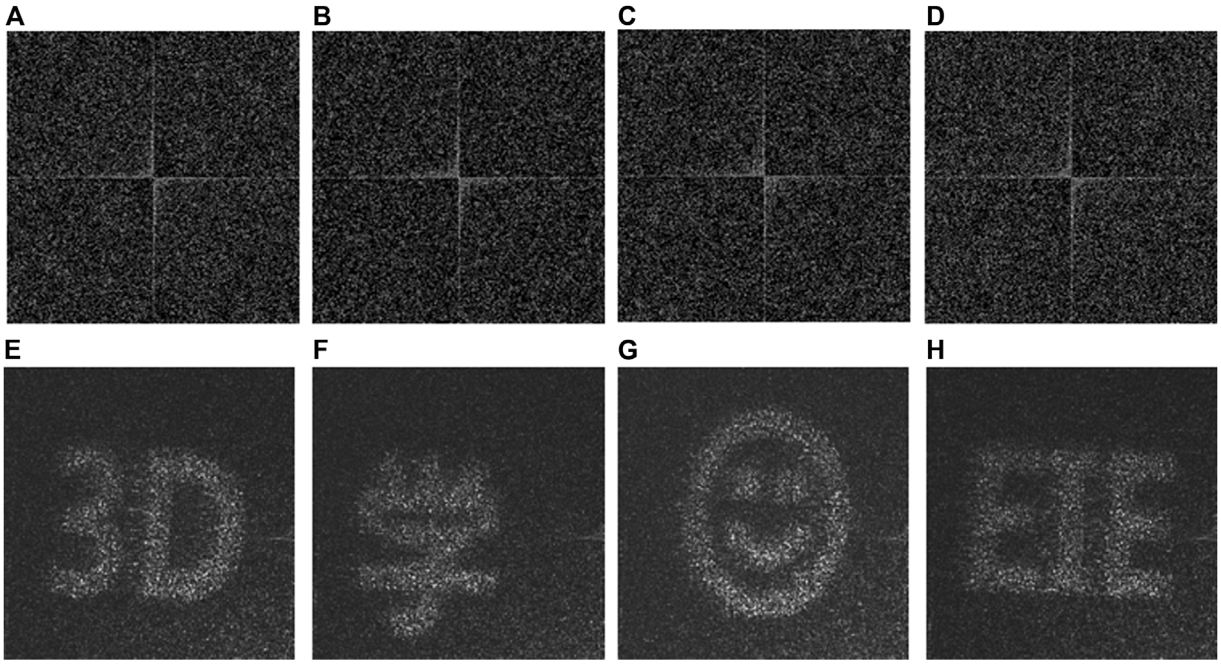

FIGURE 8 | The four images retrieved in optical experiments. **(A-D)** The stacked holograms. **(E-H)** The retrieved images respectively corresponding to **(A-D)**.

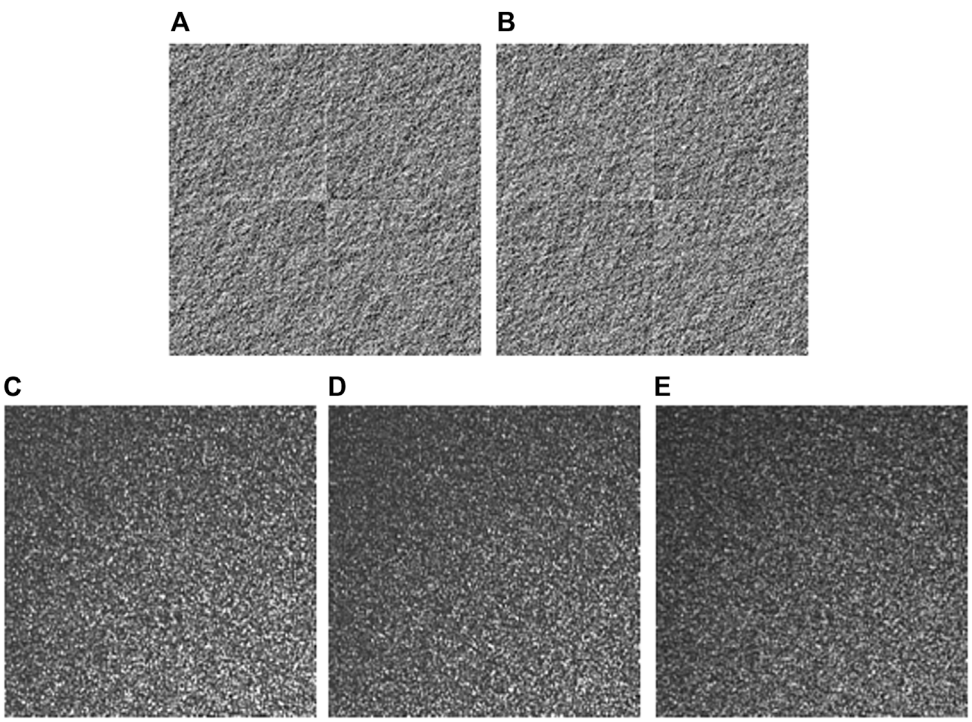

FIGURE 9 | The proposed VC scheme without the usage of logical operations. **(A)** and **(B)** Binary AOHs H_1, and H_2 for a secret image 'EIE'. **(C)** and **(D)** The retrieved shares experimentally obtained respectively using Fourier transform to **(A)** and **(B)**. **(E)** A retrieved image by overlapping **(C)** and **(D)**.

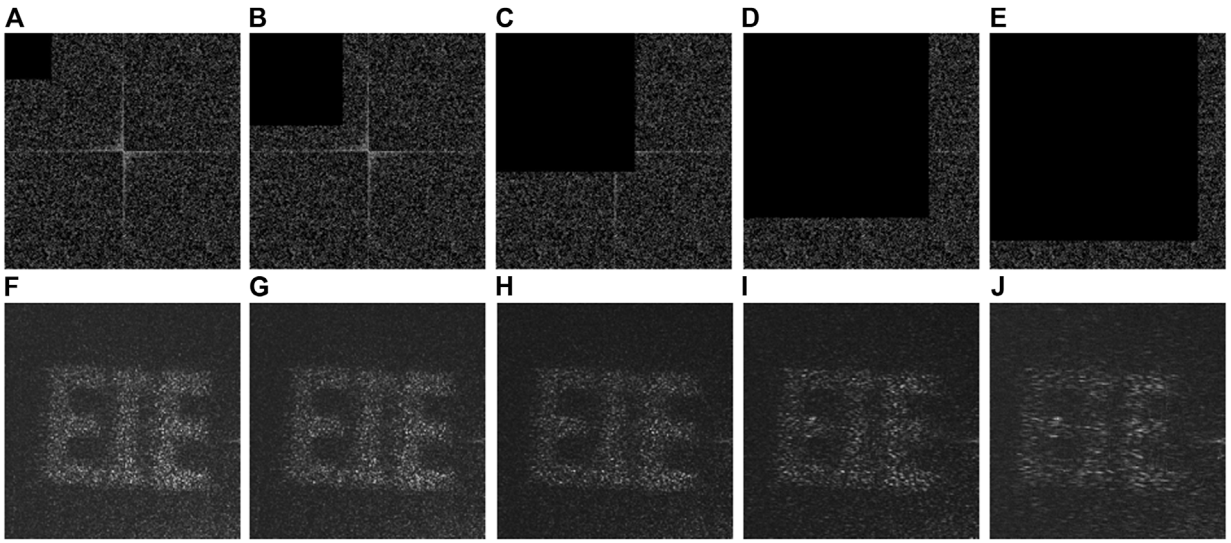

FIGURE 10 | Occlusion contamination on the first binary AOH in **Figure 9A** when the second binary AOH in **Figure 9B** remains unchanged in optical experiments. **(A-E)** The stacked holograms generated when occlusion percentage of 3.81, 15.26, 34.33, 61.04 and 77.25% is respectively used. **(F-J)** The retrieved images experimentally obtained respectively corresponding to **(A-E)**.

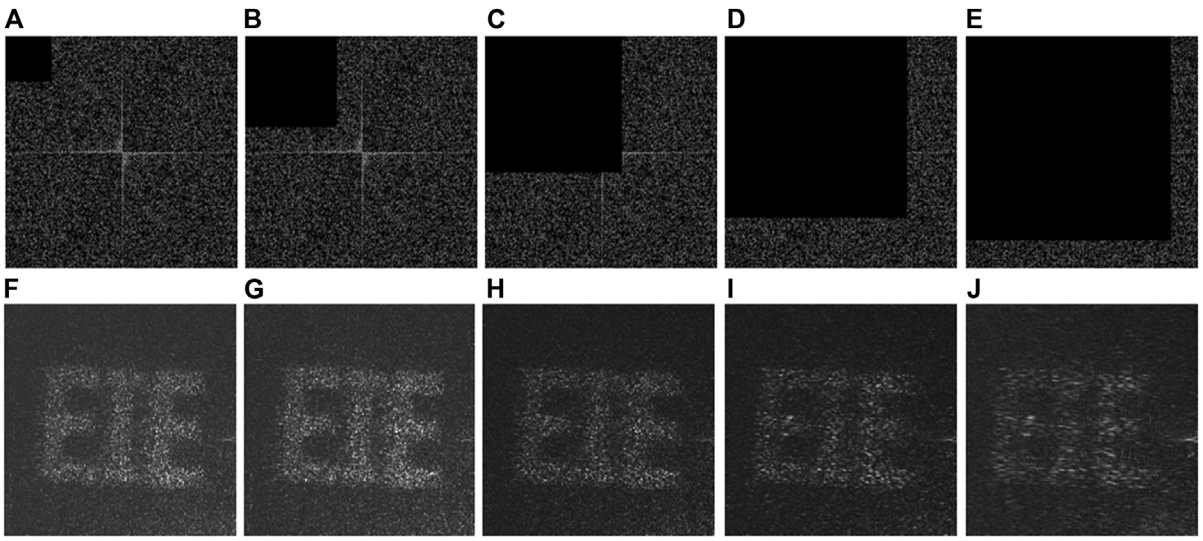

FIGURE 11 | Occlusion contamination on the second binary AOH in **Figure 9B** when the first binary AOH in **Figure 9A** remains unchanged in optical experiments. **(A-E)** The stacked holograms generated when occlusion percentage of 3.81, 15.26, 34.33, 61.04 and 77.25% is respectively used. **(F-J)** The retrieved images experimentally obtained respectively corresponding to **(A-E)**.

secret images can still be visually recognized from the retrieved images, as can be seen in **Figures 10F–J** and **11F–J**. Therefore, it is experimentally verified that the proposed VC scheme possesses high robustness against occlusion attacks.

In practice, both binary AOHs could be occluded at the same time. Optical experiments are further conducted to demonstrate performance of the proposed VC scheme when occlusion attacks on the two binary AOHs happen, and experimental results are shown in **Figures 13A–H**. For instance, the first binary AOH is occluded by 3.81% as shown in **Figure 13A**, and the second binary AOH is occluded by 46.73% (350 × 350 pixels) as shown in **Figure 13B**. By using an AND operation between **Figures 13A,B**, a stacked hologram is obtained and shown in

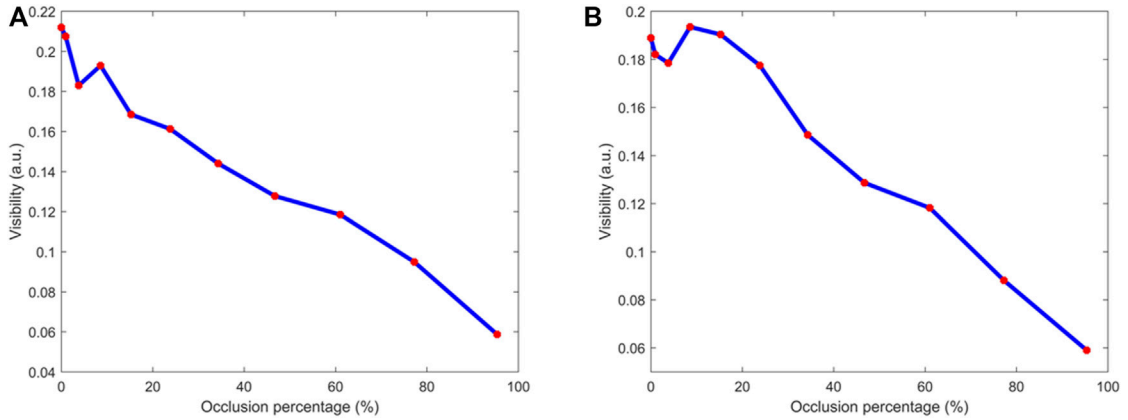

FIGURE 12 | Occlusion attacks. **(A)** A relationship between occlusion percentage and visibility of the retrieved images when only the first binary AOH in **Figure 9A** is occluded. **(B)** A relationship between occlusion percentage and visibility of the retrieved images when only the second binary AOH in **Figure 9B** is occluded.

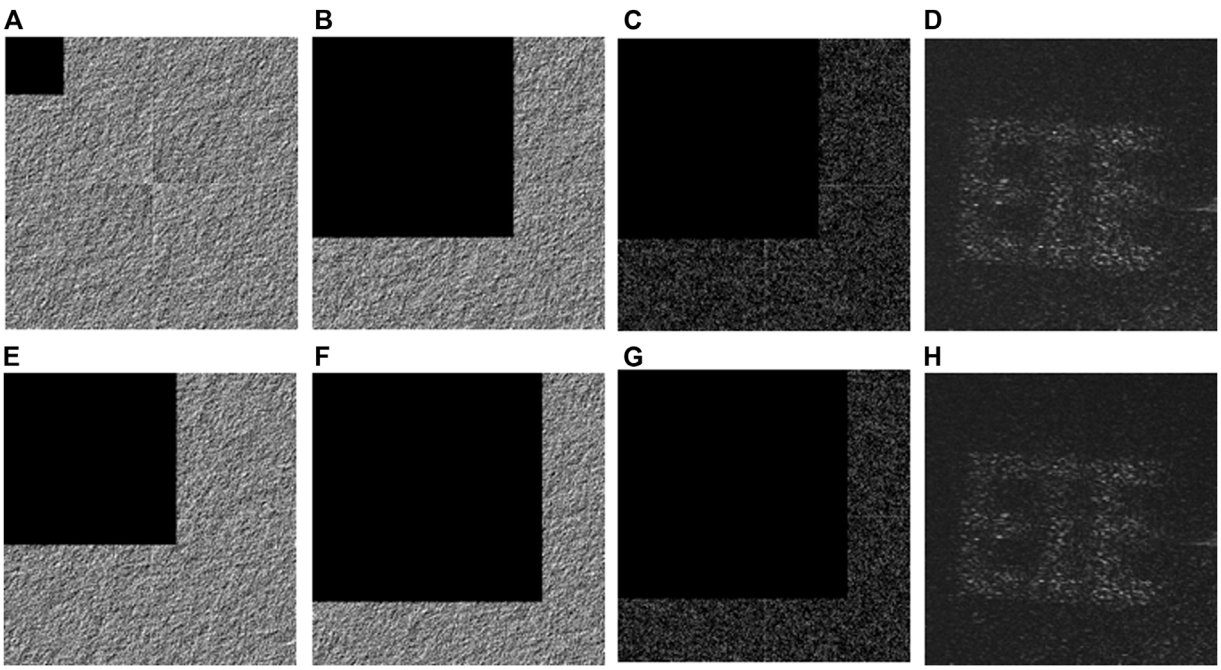

FIGURE 13 | Occlusion attacks on both binary AOHs (i.e., those in **Figures 9A,B**) in optical experiments. **(A)** The first binary AOH occluded by 3.81%. **(B)** The second binary AOH occluded by 46.73% (350 × 350 pixels). **(C)** A stacked hologram generated by using **(A)** and **(B)**. (**D**) A retrieved image experimentally obtained from **(C)**. **(E)** The first binary AOH occluded by 34.33%. **(F)** The second binary AOH occluded by 61.04%. **(G)** A stacked hologram generated by using **(E)** and **(F)**. **(H)** A retrieved image experimentally obtained from **(G)**.

Figure 13C. Therefore, an image can be experimentally retrieved and shown in **Figure 13D** to visually render information of the secret image. When occlusion percentage for the first binary AOH is 34.33% and that for the second binary AOH is 61.04%, a retrieved image still can visually render information of secret image as shown in **Figure 13H**. It is experimentally verified that the proposed VC scheme is robust against occlusion attacks.

CONCLUSION

In this paper, a new VC scheme has been proposed by using binary AOHs with the MGSA. During the encryption, a secret image can be divided into a group of unrecognizable and mutually-unrelated shares by using conventional VC schemes, and then the generated shares are further converted to binary AOHs using the MGSA. During image extraction, binary AOHs are logically

superimposed to form a stacked hologram, and then an image can be directly extracted from the stacked hologram to visually render information of the secret image. Numerical simulations and optical experiments have been conducted to demonstrate validity of the proposed VC scheme. Owing to the usage of binary AOHs, the proposed VC scheme can reduce fabrication difficulty when metasurface devices or other materials are used, and is also able to withstand occlusion attacks and noise contamination.

DATA AVAILABILITY STATEMENT

The original contributions presented in the study are included in the article/supplementary material, further inquiries can be directed to the corresponding author.

AUTHOR CONTRIBUTIONS

LZ conducted data recording and validation, developed methodology, and wrote original draft. YX conducted data validation, and reviewed and edited the writing. ZP reviewed and edited the writing. YC reviewed and edited the writing. WC developed methodology, reviewed and edited the writing, and supervised research project.

FUNDING

This work was supported by Hong Kong Research Grants Council (C5011-19G) and The Hong Kong Polytechnic University (G-R006, 4-R006, 4-ZZLF, 1-W167).

REFERENCES

Alfalou, A., and Brosseau, C. (2009). Optical Image Compression and Encryption Methods. *Adv. Opt. Photon.* 1 (3), 589–636. doi:10.1364/AOP.1.000589

Blundo, C., De Santis, A., and Naor, M. (2000). Visual Cryptography for Grey Level Images. *Inf. Process. Lett.* 75 (6), 255–259. doi:10.1016/S0020-0190(00)00108-3

Chen, W., Chen, X., and Sheppard, C. J. R. (2010). Optical Image Encryption Based on Diffractive Imaging. *Opt. Lett.* 35 (22), 3817–3819. doi:10.1364/OL.35.003817

Chen, W., Javidi, B., and Chen, X. (2014). Advances in Optical Security Systems. *Adv. Opt. Photon.* 6 (2), 120–155. doi:10.1364/AOP.6.000120

Gerritsen, H. J., Hannan, W. J., and Ramberg, E. G. (1968). Elimination of Speckle Noise in Holograms with Redundancy. *Appl. Opt.* 7 (11), 2301–2311. doi:10.1364/AO.7.002301

Ghaleh, S. R., Ahmadi-Kandjani, S., Kheradmand, R., and Olyaeefar, B. (2018). Improved Edge Detection in Computational Ghost Imaging by Introducing Orbital Angular Momentum. *Appl. Opt.* 57 (32), 9609–9614. doi:10.1364/AO.57.009609

Hou, Y.-C. (2003). Visual Cryptography for Color Images. *Pattern Recognition* 36 (7), 1619–1629. doi:10.1016/s0031-3203(02)00258-3

Hwang, H.-E., Chang, H. T., and Lie, W.-N. (2009). Multiple-image Encryption and Multiplexing Using a Modified Gerchberg-Saxton Algorithm and Phase Modulation in Fresnel-Transform Domain. *Opt. Lett.* 34 (24), 3917–3919. doi:10.1364/OL.34.003917

Javidi, B. (1997). Securing Information with Optical Technologies. *Phys. Today* 50 (3), 27–32. doi:10.1063/1.881691

Jiao, S., Feng, J., Gao, Y., Lei, T., and Yuan, X. (2020). Visual Cryptography in Single-Pixel Imaging. *Opt. Express* 28 (5), 7301–7313. doi:10.1364/OE.383240

Jiao, S., Zhou, C., Shi, Y., Zou, W., and Li, X. (2019). Review on Optical Image Hiding and Watermarking Techniques. *Opt. Laser Tech.* 109, 370–380. doi:10.1016/j.optlastec.2018.08.011

Johnson, E. G., and Brasher, J. D. (1996). Phase Encryption of Biometrics in Diffractive Optical Elements. *Opt. Lett.* 21 (16), 1271–1273. doi:10.1364/OL.21.001271

Kellock, H., Setälä, T., Shirai, T., and Friberg, A. T. (2011). Higher-order Ghost Imaging with Partially Polarized Classical Light. *Proc. SPIE* 8171, 81710Q. doi:10.1117/12.896826

Kreis, T. (2005). *Handbook of Holographic Interferometry: Optical and Digital Methods*. Weinheim, Germany: Wiley VCH, 35–219. doi:10.1002/3527604154.ch4

Li, Z., Dong, G., Yang, D., Li, G., Shi, S., Bi, K., et al. (2019). Efficient Dielectric Metasurface Hologram for Visual-Cryptographic Image Hiding. *Opt. Express* 27 (14), 19212–19217. doi:10.1364/OE.27.019212

Naor, M., and Shamir, A. (1995). Visual Cryptography. *Adv. Cryptography–Eurocrypt* 950 (7), 1–12. doi:10.1007/BFb0053419

Refregier, P., and Javidi, B. (1995). Optical Image Encryption Based on Input Plane and Fourier Plane Random Encoding. *Opt. Lett.* 20 (7), 767–769. doi:10.1364/OL.20.000767

Schnars, U., and Jüptner, W. P. O. (2005). *Digital Holography: Digital Hologram Recording, Numerical Reconstruction, and Related Techniques*. Berlin: Springer. doi:10.1007/b138284

Situ, G., and Zhang, J. (2004). Double Random-phase Encoding in the Fresnel Domain. *Opt. Lett.* 29 (14), 1584–1586. doi:10.1364/OL.29.001584

Wan, S., Lu, Y., Yan, X., Wang, Y., and Chang, C. (2018). Visual Secret Sharing Scheme for (K,n) Threshold Based on QR Code with Multiple Decryptions. *J. Real-time Image Proc.* 14 (1), 25–40. doi:10.1007/s11554-017-0678-3

Wang, X., Chen, W., and Chen, X. (2014). Fractional Fourier Domain Optical Image Hiding Using Phase Retrieval Algorithm Based on Iterative Nonlinear Double Random Phase Encoding. *Opt. Express* 22 (19), 22981–22995. doi:10.1364/OE.22.022981

Xi, S., Wang, X., Song, L., Zhu, Z., Zhu, B., Huang, S., et al. (2017). Experimental Study on Optical Image Encryption with Asymmetric Double Random Phase and Computer-Generated Hologram. *Opt. Express* 25 (7), 8212–8222. doi:10.1364/OE.25.008212

Xu, W., Luo, Y., Li, T., Wang, H., and Shi, Y. (2017). Multiple-image Hiding by Using Single-Shot Ptychography in Transform Domain. *IEEE Photon. J.* 9 (3), 1–10. doi:10.1109/JPHOT.2017.2695398

Xu, Z., Huang, L., Li, X., Tang, C., Wei, Q., and Wang, Y. (2020). Quantitatively Correlated Amplitude Holography Based on Photon Sieves. *Adv. Opt. Mater.* 8 (2), 1901169. doi:10.1002/adom.201901169

Yang, N., Gao, Q., and Shi, Y. (2018). Visual-cryptographic Image Hiding with Holographic Optical Elements. *Opt. Express* 26 (24), 31995–32006. doi:10.1364/OE.26.031995

Zhang, Y., and Wang, B. (2008). Optical Image Encryption Based on Interference. *Opt. Lett.* 33 (21), 2443–2445. doi:10.1364/OL.33.002443

Zhou, L., Xiao, Y., Pan, Z., Cao, Y., and Chen, W. (2021). Optical Hiding Based on Single-Input Multiple-Output and Binary Amplitude-Only Holograms via the Modified Gerchberg-Saxton Algorithm. *Opt. Express* 29 (16), 25675–25696. doi:10.1364/OE.428564

Conflict of Interest: The authors declare that the research was conducted in the absence of any commercial or financial relationships that could be construed as a potential conflict of interest.

Publisher's Note: All claims expressed in this article are solely those of the authors and do not necessarily represent those of their affiliated organizations, or those of the publisher, the editors and the reviewers. Any product that may be evaluated in this article, or claim that may be made by its manufacturer, is not guaranteed or endorsed by the publisher.

frontiers in Photonics

REVIEW
published: 19 January 2022
doi: 10.3389/fphot.2021.825610

Speckle Noise Suppression Algorithm of Holographic Display Based on Spatial Light Modulator

Nan-Nan Li[1], Chun Chen[2], Byoungho Lee[2], Di Wang[1] and Qiong-Hua Wang[1]**

[1]School of Instrumentation and Optoelectronic Engineering, Beihang University, Beijing, China, [2]School of Electrical and Computer Engineering, Seoul National University, Seoul, South Korea

Holography has emerged as one of the most attractive three-dimensional display technologies. With the technological development of computer science and coherent light source, the computer-generated holography has been applied in many fields. However, the speckle noise of the holographic reconstructed image seriously affects the viewing experience. In this paper, the cause of speckle noise generation in holographic display is introduced. Then, discussions about the speckle noise suppression methods are provided. The discussions are categorized into iterative and non-iterative approaches. Besides, we also introduce other speckle noise suppression techniques which are proposed from the perspective of light coherence, human visual system and optical system. Finally, the prospects of different types of approaches are summarized.

Keywords: speckle noise, computer-generated holography, holographic display, three-dimensional display, speckle noise suppression method

OPEN ACCESS

Edited by:
Pietro Ferraro,
National Research Council (CNR), Italy

Reviewed by:
Michal Makowski,
Warsaw University of Technology, Poland
Shuming Jiao,
Peng Cheng Laboratory, China
Vittorio Bianco,
National Research Council (CNR), Italy

****Correspondence:***
Di Wang
diwang18@buaa.edu.cn
Qiong-Hua Wang
qionghua@buaa.edu.cn

Specialty section:
This article was submitted to Optical Information Processing and Holography, a section of the journal Frontiers in Photonics

Received: *30 November 2021*
Accepted: *28 December 2021*
Published: *19 January 2022*

Citation:
Li N-N Chen C, Lee B, Wang D and Wang Q-H (2022) Speckle Noise Suppression Algorithm of Holographic Display Based on Spatial Light Modulator. Front. Photon. 2:825610. doi: 10.3389/fphot.2021.825610

INTRODUCTION

Holography was first proposed by D. Gabor in 1948 (Gabor, 1948). It can record and reconstruct the entire wave-front information of the object. In 1965, A.W. Roman successfully made the first computer-generated hologram (CGH) and the theoretical foundation of CGH was established (Brown and Lohmann, 1966). In this period, the researchers mainly focused on the hologram encoding methods, and the main device for producing holograms was a plotter. Then, Lohmann proposed three different forms of circuitous phase-encoded holograms (Brown and Lohmann, 1969). Subsequently, Paris applied the fast Fourier transform (FFT) algorithm to speed up the calculation of the Fourier hologram, which greatly shortened the calculation time (Lohmann and Paris, 1967). After the 1980s, various types of spatial light modulators (SLMs) and new recording materials were developed (Zhan et al., 2020), which created new opportunities for holographic display. Many researchers gradually paid attention to the display effects of the different types of SLMs, and the researchers focused on the various hologram generation algorithms. So, different methods were developed, such as the look-up table method (Lucente, 1993), stereo holography method (Yamaguchi et al., 1992) and integrated holography method (St. Hilaire et al., 1992). Since 2000, liquid crystal on silicon (LCoS) has become a new research hotspot. The LCoS uses electrical signals to control the deflection of liquid crystal molecules for achieving modulation of the incident light phase (Chen et al., 2018). Then, the focus of researches was to improve the calculation speed of holograms by using GPU acceleration and optimizing physical models based on the LCoS (Nishitsuji et al., 2018; Lin et al., 2021). In addition, an increasing number of researchers paid attention to the field of view (FOV) and image quality of the holographic display (Maimone et al., 2017; Shi et al., 2017; Jang et al., 2018; Wang et al., 2020a; Zhao et al., 2020; Wu and Zhang, 2021; Yoo et al., 2021).

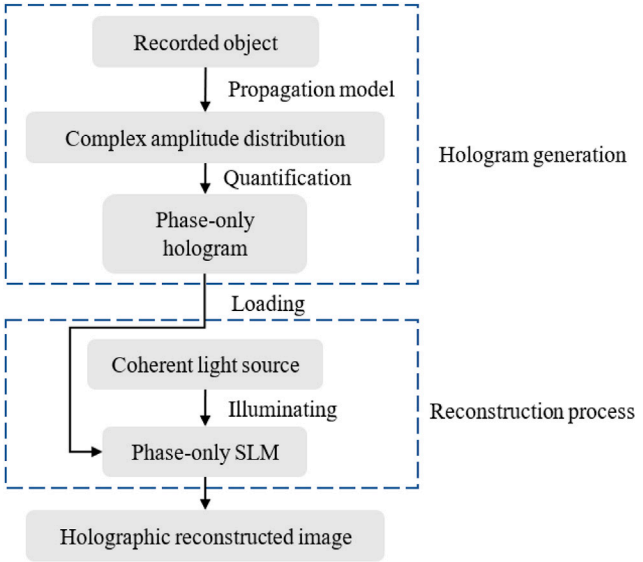

FIGURE 1 | Principle of CGH display based on the phase-only SLM.

Although CGH has many advantages, there still exists many problems needed to be solved in the display field. One of the key issues is the speckle noise because it seriously affects the viewing experience. It is generally considered that the speckle noise in holographic displays is generated from the quantization error and the spatial coherence. In the past 20 years, more and more researchers have focused on the method for speckle noise suppression. Recently, the requirements to improve the quality of reconstructed images become more urgent. There are a large variety of methods for speckle noise reduction.

This paper gives the overview on the speckle noise suppression of holographic display based on spatial light modulator, and the main body is divided into the following sections. Firstly, the reason for speckle noise in CGH is described. Meanwhile, three criteria for quantizing the effect of speckle noise in the holographic reconstruction are provided. Besides, we introduce the speckle noise suppression process by considering various strategies. The described speckle noise reduction methods are mainly categorized into iterative method and non-iterative methods. In addition, other speckle noise suppression techniques are also introduced, which are proposed from the perspective of light coherence, human visual system and optical system. Finally, the prospects of these methods are summarized.

SPECKLE NOISE PROBLEM IN HOLOGRAPHIC DISPLAY

Since the commercial SLMs are either phase-only type or amplitude-only type, the holograms need to be encoded into phase-only or amplitude-only type to fit the type of SLM. Among them, the phase-only SLM has higher diffraction efficiency, so it is currently widely used in the holographic display. The principle of CGH display based on the phase-only SLM is shown in **Figure 1**.

In the hologram generation process, the complex amplitude distribution of the recorded object can be obtained by using the point-based propagation model. Then, the phase-only hologram can be generated by encoding the complex amplitude distribution of the recorded object. The encoding process can also be regarded as a quantization process, which is the sampling and approximation of the complex amplitude distribution. In the reconstruction process, the phase-only SLM is needed to realize the optical reconstruction of the CGH. By loading the phase-only hologram on the phase-only SLM and illuminating it with the coherent light source, the image can be reconstructed.

In general, the speckle noise in holographic display is considered generated from the perspective of software and hardware. The software and hardware refer to the computer generation process of the hologram and the optical reconstruction process, respectively. Speckle noise results from the interference. In encoding process, the approximate sampling is regarded as the quantization error of the holographic reconstruction and it is inevitable. Due to the quantization error, the speckle noise is generated by the uncontrolled coherence effects of the reconstructed image. When the phase in the reconstructed image is a random distribution, the reconstructed image points will disturb each other and produce a randomly changed intensity because of the phase difference. In order to simulate the scattered light on the surface of the recorded object, the random phase is added to the recorded object in hologram algorithms. As shown in **Figure 2**, the recorded object consists of parts with low frequencies and high spatial frequencies. For a recorded object without random phase, only high-frequency and part of low-frequency of the information can be recorded on the CGH, while the edge of the low-frequency cannot be recorded. Although the random phase is a generator to ensure that the recorded object information spread completely over the CGH, it is also the main cause of the speckle noise generation (Shimobaba and Ito, 2015).

Moreover, during the optical holographic reconstruction, coherent light sources and optical devices are also the causes of the speckle noise generation. The reconstructed points exist in the form of Airy disks because of the limited aperture of the optical elements and the diffraction effects, as shown in **Figure 3**. The speckle noise becomes more serious with increasing of the superposition area. The optical reconstruction process is imperfect since the dust, scratches in the lens and aberrations can produce additional speckle noises. Different from the quantization error, this kind of error caused by the hardware is called systematic error.

Finally, to assess the speckle noise suppression effect, three criteria can be used to investigate: the peak signal-to-noise ratio (PSNR), structural similarity (SSIM) index and speckle contrast (SC). Besides, the foveal perception, wirtinger flow method and subjective quality evaluation can also be used for evaluation (Bolek and Makowski, 2019; Chakravarthula et al., 2021). PSNR is the most commonly used objective measurement method for evaluating image quality, which can be defined as follows:

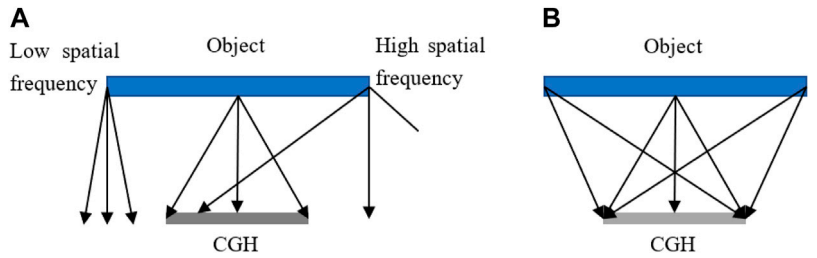

FIGURE 2 | Propagation model for the hologram generation **(A)** without random phase **(B)** with random phase.

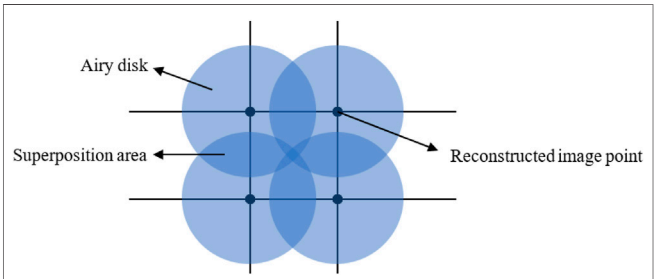

FIGURE 3 | Superposition of the Airy disk in the reconstructed image points.

$$PSNR = 20 \cdot \lg\left(\frac{255}{\sqrt{\frac{1}{mn}\sum_{i=0}^{m-1}\sum_{j=0}^{n-1}\left\|X(i,j) - Y(i,j)\right\|^2}}\right), \quad (1)$$

where X and Y represent the object image and the reconstructed image, respectively, m and n represent the resolutions. The unit of PSNR is 1dB. A higher value of the PSNR usually means the effect of speckle noise suppression is better.

SSIM is also a very important parameter for evaluating the reconstructed image quality. For the holographic reconstructed image x and recorded object y, the SSIM of the two images can be expressed as follows:

$$SSIM(x,y) = \frac{\left(2\mu_x\mu_y + c_1\right)\left(2\sigma_{xy} + c_2\right)}{\left(\mu_x^2 + \mu_y^2 + c_1\right)\left(\sigma_x^2 + \sigma_y^2 + c_2\right)}, \quad (2)$$

where μ_x and μ_y are the average of image x and image y, respectively. σ_x^2 and σ_y^2 are the variance of image x and image y, respectively. σ_{xy} is the covariance between images x and y. $c_1=(k_1L)^2$ and $c_2=(k_2L)^2$ are two constants used to maintain stability and L is the dynamic range of pixel values, where K_1 equals to 0.01 and K_2 equals to 0.02 (Duan et al., 2019).

SC is the simplest parameter to evaluate the speckle noise of the reconstructed image, and it satisfies the following equation:

$$C = \frac{\sigma}{\bar{I}}, \quad (3)$$

where σ and $\bar{I}$ represent the standard deviation of intensity and the average of intensity, respectively. The lower SC indicates the less speckle noise in the reconstructed image.

METHODS OF SPECKLE NOISE SUPPRESSION

There are many kinds of methods for suppressing the speckle noise, and they can be discussed based on the hologram generation process and the reconstruction process. Based on the hologram generation process, the CGH algorithm can be divided into two categories: iterative and non-iterative methods. Based on the reconstruction process, we also introduce other speckle noise suppression techniques which are proposed from the perspective of light coherence, human visual system and optical system.

Iterative Methods

Among the iterative methods that can generate phase-only holograms, the iterative Fourier transform algorithm is a representative method. The characteristic of this type of algorithm is the iterative propagation in two planes by using the Fourier transform (Bu et al., 2021). The most famous and mostly used method is the Gerchberg-Saxton (GS) algorithm (Gerchberg and Saxton, 1972). As shown in **Figure 4**, the amplitude constraint is imposed on the object plane and hologram plane, then the phase is continuously iterated between the hologram plane and object plane. After several iterations, the phase distribution on the hologram plane converges to an optimal value. Therefore, the amplitude information of the object can be encoded into the phase-only hologram. Moreover, it is also possible to use the Fresnel transform instead of the Fourier transform to simulate light field propagation.

Many improved CGH algorithms have been developed based on the GS algorithm. The GS algorithm with weight coefficients (GSWC) has been proposed to improve the convergence rate and suppress the speckle noise (Kuzmenko et al., 2011; Wu et al., 2021a). The GSWC algorithm replaces the original constraint with the weight coefficients multiplied by the amplitude of the recorded object. The quality of the reconstructed image using the GSWC algorithm is improved by 75% compared with the GS algorithm. Moreover, the uniform random phase generator used

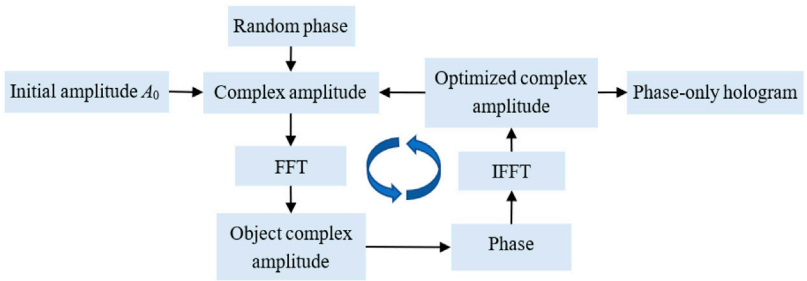

FIGURE 4 | Schematic of the GS algorithm.

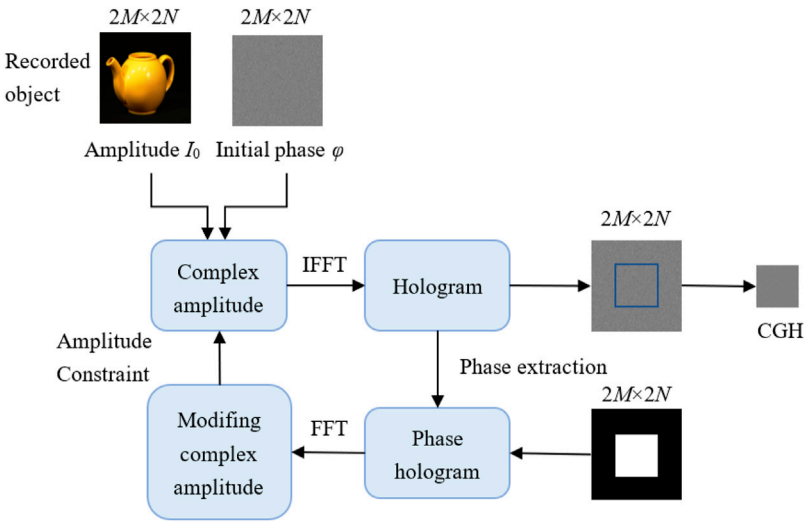

FIGURE 5 | Schematic diagram of bandwidth constraint optimization algorithm.

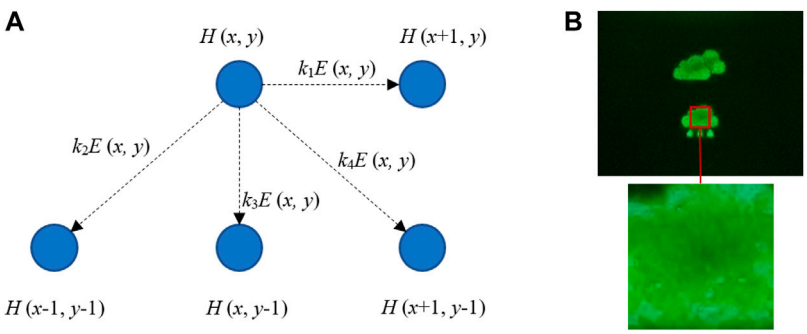

FIGURE 6 | Illustration of the ED method. **(A)** Schematic diagram of the ED method and **(B)** the reconstructed image by using the ED method.

by the GS algorithm is also an important cause of the speckle noise. To optimize the random phase generator, an iterative method with bandwidth constraint strategy has been proposed (Chen et al., 2021a). As shown in **Figure 5**, in order to suppress the speckle noise and provide effectively controls of the reconstructed intensity fluctuations, the iterative method can optimize the phase of the CGH by using the bandwidth constraint strategy of the reconstructed image and quadratic initial phase. The SC of the method with bandwidth constraint strategy is 46% lower than that of the GS method.

Different from the iteration between the object plane and the hologram plane, the error diffusion (ED) method is another type

of iterative algorithm, which iterates between the pixels of the hologram (Barnard et al., 1989). As shown in **Figure 6**, H represents a pixel of the CGH, (x, y) represents the pixel coordinate point, E and k represent the quantization error of the pixel point and the weight coefficient, respectively. Since the ED method diffuses the quantization error to adjacent pixels of the phase-only hologram and homogenizes them, the speckle noise generated by the quantization error can be suppressed. However, the calculation time of the ED method increases proportionally with the resolution of the hologram.

Based on the ED method, some researchers have introduced two enhanced methods which are known as the localized error diffusion and redistribution (LERDR) and bidirectional error diffusion (BERD). In these methods, the conversion of a complex Fresnel hologram to a phase-only hologram can be conducted in a parallel manner (Ysang et al., 2014). Compared with the localized error diffusion (LERD) algorithm, the PSNR of the reconstructed image by using LERDR and BERD algorithm is nearly 10 dB higher on average. Besides, the combination of the ED and the digital lens has been proposed (Chang et al., 2015; Wang et al., 2020b; Jiao et al., 2020; Li et al., 2020). The suppression effect of speckle noise can be improved by more than 60% on average compared with the ED method.

Recently, with the rapid development of the camera and computation, the camera with an algorithm can be used to optimize the phase distribution of the CGH. Camera-in-the-loop (CITL) holographic algorithm has been proposed to reduce the gap between the numerical simulation and optical reconstruction, since the optical system is imperfect. However, the direct current (DC) noise from the SLM cannot be eliminated in CITL on-axis setup. To solve this problem, a holographic display system has been proposed by using a new CITL optimization and two phase-only SLM (Choi et al., 2021a). This display system is inspired by the design of Michelson interferometers, so that called Michelson holography (MH). Compared with the double phase-amplitude coding (DPAC) method, the PSNR of the reconstructed image by using MH method is about 6 dB higher in the optical experiment. Nonetheless, the calculation time of the MH method is too much for the multi-depth recorded object. To solve this problem, a multi-depth holographic display method has been proposed by using stochastic gradient descent (SGD) with complex loss function (Chen et al., 2021b). For the recorded object with 20 depth layers, the calculation time of the proposed method is faster 94.36% than that of the SGD based on amplitude loss method.

Non-Iterative Methods

As non-iterative methods, the multi-random phase method and multiple fractional Fourier transform method have been used for reducing the speckle noise (Jun et al., 1995; Zheng et al., 2009; Wang et al., 2020c). These methods are effective in speckle noise suppression, but they are time-consuming. To reduce the calculation time and suppress the speckle noise at the same time, the random phase-free method has been proposed by multiplying the recorded object with the virtual convergence light (Shimobaba and Ito, 2015; Nagahama et al., 2019). As shown in **Figure 7**, the recorded object multiplies with the virtual convergence light instead of the random phase. The recorded object information is completely diffused in the CGH by using the virtual convergence light. The virtual convergence light also avoids the speckle noise generated by the random phase. It should be noted that the incident angle θ of the convergence light must be smaller than the maximum diffraction angle of the SLM to avoid the aliasing error. Compared with the random phase method, the PSNR of the numerically reconstructed image using the random-phase-free method is nearly 30 dB higher.

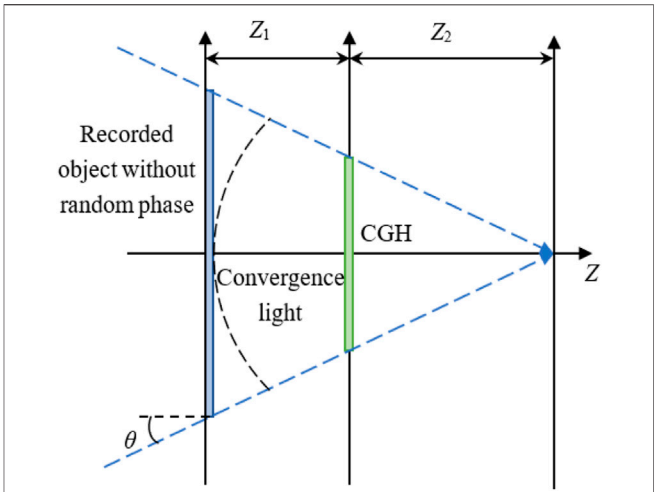

FIGURE 7 | Random phase-free CGH by using the convergence light.

Since the random phase could lead to the excessive diffusion of information and degrades the image quality, the gradient-limited random phase (GL-RP) addition method and the limited-random-phase (L-RP) time average method have been developed to avoid excessive diffusion of the object information (Ma et al., 2017; Zhao et al., 2019). In the numeral simulation of the GL-RP method, the PSNR and SSIM of the reconstructed image increase by 10 and 13%, respectively. The L-RP method finds that the random phase of the recorded object has an appropriate range, which is limited to 1.2π–1.5π. When the limited random phase is applied in the hologram generation process, the speckle noise can be reduced significantly.

The pixel separation method is also one of the most famous methods. The recorded object is separated into different point groups by pixel separation. For each point group, the sub-CGHs with independent initial random phases are generated. Then, the speckle noise is reduced by the time average (Mori et al., 2014; Liu et al., 2019; Masaya and Yuji, 2019). Compared with the non-separation method, the speckle contrast of the reconstructed image by using these methods is reduced by more than 80%. Therefore, a combination of the pixel separation method and the time average can suppress the speckle noise effectively. However, the high-refresh SLM is necessary for these methods since the time average reduces frame rates of the holographic display. The speckle noise can be further suppressed with the increase of the separated interval and the number of the sub-CGHs.

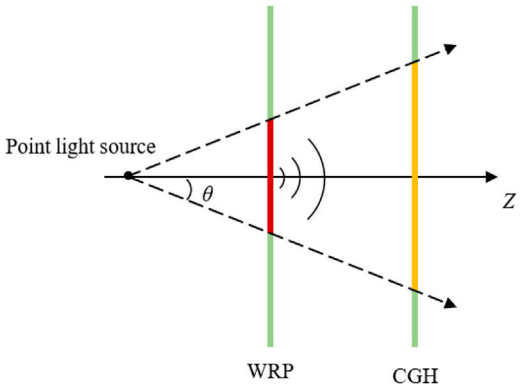

FIGURE 8 | Schematic diagram of the WRP method with a limited diffraction region.

In the generation process, the Fresnel CGH can be binarized in a non-iterative manner through down-sampling the recorded object with a grid lattice prior. Meanwhile, the down-sampling method can suppress the speckle noise as well. However, the results of the down-sampling method have a prominent texture of regularly that is spaced voids in the shaded regions. To solve this problem, an enhanced method based on grid-cross down-sampling (GCD) has been proposed (Cheung et al., 2011; Tsang et al., 2013). The reconstructed images of these methods have proved that the speckle noise can be suppressed effectively. However, a sparse appearance with many empty voids is generated in reconstructed image when using the GCD method. To suppress the speckle noise and the sparse appearance at the same time, a combination of the GCD and a time-division comb filtering (TDCF) approach has been proposed (Liu et al., 2020; Tsang et al., 2020). The PSNR of the reconstructed image by using the LRDS method can reach almost 30 dB. Moreover, the intermediate angular-spectrum method (IASM) has been proposed by avoiding the numerical circular convolution (Chen et al., 2019). Compared with the zero-padding method, the PSNR of the reconstructed image based on the IASM method can be improved by 36%.

On the other hand, the size of the diffraction region affects the quality of the reconstructed image. In order to reduce the speckle noise caused by the useless diffraction region, a wave-front recording plane (WRP) method with a limiting diffraction region has been proposed (Yanagihara et al., 2020). As shown the green area in **Figure 8**, the useless diffraction region can be avoided in CGH generation process. The experimental results demonstrate that the speckle noise can be reduced efficiently by using the WRP method with the limited circular diffraction region. Besides, a method to suppress the speckle noise in the holographic display based on effective utilization of two phase-only SLMs has also been verified availably (Wang et al., 2019). This method combines the pixel separation, the time multiplexing and the limit diffraction region to reduce the speckle noise. Compared with the conventional point-based method, the speckle contrast of the reconstructed image by using this method is reduced by 21.57%, and the calculation time is reduced by 48.53%.

The speckle noise can also be efficiently suppressed by using the complex amplitude encoding method. For the speckle reduction, an efficient coding method by using lossy compression has been verified (Bernardo et al., 2021). Both the effect of the speckle noise caused by the encoding process and the speckle noise caused by the compression in the recorded object have been discussed in this method. In addition, a combination of the time-multiplexing and the hologram optimization approach has been proposed (Hamann et al., 2018). This approach suppresses the speckle noise by an alternating direction method of multipliers optimization. The simulation demonstrates a significant improvement in the PSNR of the reconstructed image under higher rank factorization. Besides, the double-phase hologram (DPH) provides a better approximation to encode complex amplitude fields. Recently, the speckle-less holographic display based on DPH method has been proposed (Mendoza-Yero et al., 2014; Qi et al., 2016). In DPH method, the complex amplitude information is encoded as two-phase values, then the two phase values are combined into the pixel of the phase-only CGH by using two binary complementary chessboard masks. Since the two-phase values can be synthesized into the corresponding complex amplitude values, the quantization error is reduced and the speckle noise is suppressed. Furthermore, these methods can suppress the speckle noise and reduce the calculation time at the same time because of the free of iteration. Compared with the iterative Fourier transform algorithm, the speckle contrast of the reconstructed image by using the DPH method is reduced by more than 60%.

The hologram generation method based on deep learning is also a non-iterative method, which has great potential to realize real-time and speckle-free holographic display (LeCun et al., 2015; Horisaki et al., 2018; Eybposh et al., 2020; Lee et al., 2020a; Curtis et al., 2021; Park and Park, 2020). The convolutional neural network (CNN) has been demonstrated usefully in revealing the deep relationships between the input object and output hologram (Lee et al., 2020a). The learned CNN has the advantages of speckle reduction and fast calculation speed. Recently, a combination of the CNN and a modified double phase approach has been proposed to achieve a high-quality real-time holographic display (Shi et al., 2021). As shown in **Figure 9**, they introduce an anti-aliasing double phase method (AA-DPM) to generate the hologram dataset, which can reduce both high-frequency noise and speckle noise. The CNN is utilized to learn the relationship between the input 3D object and the Fresnel hologram dataset. The loss function in the training period consists of two types of loss functions: one is to measure the error of the predicted hologram, and the other one is to measure the quality of the reconstructed 3D object. Through the training strategy, the CNN can learn the characteristic of the hologram with high precision, so as to eliminate speckle noise effectively (Chakravarthula et al., 2020; Peng et al., 2020; Choi et al., 2021b; Wu et al., 2021b).

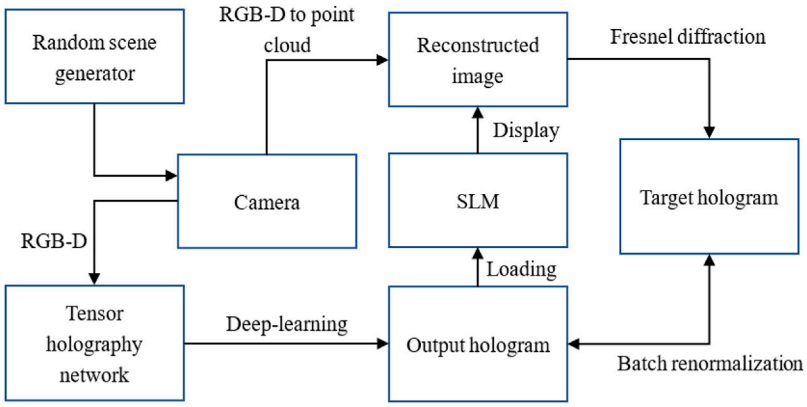

FIGURE 9 | Schematic of the tensor holography.

Methods Based on the Light Coherence and Optical System

During the optical holographic reconstruction, the coherent light source is one of the main causes of speckle noise generation. Therefore, reducing the coherence of the light source is helpful to suppress the speckle noise. To reduce the coherence, a random laser has been demonstrated usefully (Redding et al., 2012). In conventional coherent light sources, the low spatial coherence and the laser-level intensity are mutually exclusive. As a new kind of light source, the random laser is ideal for display because it has both properties.

Furthermore, in conventional holographic display, the reconstructed images suffer from the trade-off between the speckle noise and the resolution. To alleviate the trade-off problem, the theoretical models for quantifying the effect of the low-coherence have been introduced (Lee et al., 2020b). In this theoretical model, an optimal coherence light source with the maximum effect of the speckle suppression can be found. However, although the light source is optimized for considerable speckle noise suppression, the sacrifice of the resolution and the depth of field is inevitable. Then, this method has been demonstrated to alleviate the trade-off. Moreover, by combining the tunable-focus lens and the local illumination module, a speckle reduced holographic display prototype has been built (Lee et al., 2020c). In order to reduce the speckle noise while maintaining resolution, depth of field and frame rate, the tomographic synthesis method has been applied. The experimental results demonstrate that this method can suppress the speckle contrast averagely by 37.8% while keeping the resolution and depth of field unchanged.

Besides, a novel CGH encoding method based on a low-coherence light source has also been proved feasible for speckle noise reduction (Duan et al., 2019). Compared with the angular spectrum method, the PSNR of the reconstructed image by using this novel encoding method is improving by more than 60%. It is meaningful that this novel encoding method can be combined with other algorithms based on the low-coherence light source. The previous methods of suppressing speckle noise do not take the perceptual characteristics of the human visual system (HVS) into account (Chakravarthula et al., 2021). Considering the HVS, a method by incorporating anatomically-informed model of human perception has been proposed to reduce the speckle noise. Some users have been invited to evaluate the reconstructed image by using the proposed method.

Finally, we summarize the prospects of three types of methods. Iterative algorithms based on GS method have good flexibility to suppress the speckle noise. However, the computational speed of these algorithms is limited by the number of iterations, which makes it difficult to implement real-time holographic display. As another iterative method, the ED method requires fewer computational resources and reduces the speckle noise well. However, it is not suitable for the CGH with random phase involved because of the limited complex amplitude information correction ability.

As the non-iterative algorithms, the random-phase-free method, the pixel separation method, the down-sampling method, the double phase method and the deep learning method can suppress the speckle noise and improve the quality of the reconstructed image. Generally, the non-iterative algorithms are suitable for the real-time holographic display because they occupy less computational resources. Among them, deep-learning-based hologram generation methods are the most promising one because of the effectiveness in the speckle noise suppression. However, although the speckle noise suppression method based on the current deep-learning-based algorithms is impressive, the whole display system is still a bit huge and complex to commercialization.

On the other hand, reducing the coherence of the light source and systematic errors are also helpful to suppress the speckle noise. However, the low-coherence light source has drawbacks, which are the serious impact on the sharpness and contrast of the reconstructed image (Memmolo et al., 2014; Montrésor et al., 2019). It is important to find an intermediate point balance value between the coherence and incoherence of the

light source. In practice, the strategy can include one or more of these methods.

CONCLUSION

In this paper, the reason of the speckle noise generation in holographic display is provide by analyzing the hologram generation process and the reconstruction process. Meanwhile, the evaluation criteria for speckle noise in holographic display is introduced. In addition, the speckle noise suppression methods are introduced by considering the hologram generation process and the reconstruction process. Based on the hologram generation process, the discussed methods are divided to the iterative and non-iterative methods. In the reconstruction process, other speckle noise reduction methods are also introduced based on the perspective of light coherence, human visual system and optical system. Finally, we summarize the prospects of each type of method.

AUTHOR CONTRIBUTIONS

Conceptualization: N-NL and DW; writing-original draft preparation, N-NL, CC, DW, BL, and Q-HW.

FUNDING

This work is supported by the National Natural Science Foundation of China under Grant Nos. 62020106010, 62011540406 and the National Research Foundation of Korea (2020K2A9A2A06038623).

ACKNOWLEDGMENTS

We thank Dr. Yi-Wei Zheng, Dr. Zhao-Song Li and Dr. Yi-Long Li for revising the manuscript. We would like to thank Nanofabrication facility in Beihang Nano for technique consultation.

REFERENCES

Barnard, E., Vermeulen, P., and Casasent, D. P. (1989). Optical Correlation CGHs with Modulated Error Diffusion. *Appl. Opt.* 28, 5358–5362. doi:10.1364/ao.28.005358

Bernardo, M. V., Fonseca, E., Pinheiro, A. M. G., Fiadeiro, P. T., and Pereira, M. (2021). Efficient Coding of Experimental Holograms Using Speckle Denoising. *Signal. Processing: Image Commun.* 96, 116306. doi:10.1016/j.image.2021.116306

Bolek, J., and Makowski, M. (2019). Non-invasive Correction of Thermally Induced Wavefront Aberrations of Spatial Light Modulator in Holographic Projection. *Opt. Express* 27 (7), 10193–10207. doi:10.1364/oe.27.010193

Brown, B. R., and Lohmann, A. W. (1966). Complex Spatial Filtering with Binary Masks. *Appl. Opt.* 5, 967–969. doi:10.1364/ao.5.000967

Brown, B. R., and Lohmann, A. W. (1969). Computer-generated Binary Holograms. *IBM J. Res. Dev.* 13, 160–168. doi:10.1147/rd.132.0160

Bu, H.-Z., Jiao, S.-M., and Jiao, S.-m. (2021). Review of Computer-Generated Phase-Only Hologram Optimization Algorithm. *Chin. J. Liq. Cryst. Disp.* 36, 810–826. doi:10.37188/cjlcd.2021-0035

Chakravarthula, P., Tseng, E., Srivastava, T., Fuchs, H., and Heide, F. (2020). Learned Hardware-In-The-Loop Phase Retrieval for Holographic Near-Eye Displays. *ACM Trans. Graph.* 39, 1–18. doi:10.1145/3414685.3417846

Chakravarthula, P., Zhang, Z., Tursun, O., Didyk, P., Sun, Q., and Fuchs, H. (2021). Gaze-contingent Retinal Speckle Suppression for Perceptually-Matched Foveated Holographic Displays. *IEEE Trans. Vis. Comput. Graphics* 27, 4194–4203. doi:10.1109/tvcg.2021.3106433

Chang, C., Xia, J., Yang, L., Lei, W., Yang, Z., and Chen, J. (2015). Speckle-suppressed Phase-Only Holographic Three-Dimensional Display Based on Double-Constraint Gerchberg-Saxton Algorithm. *Appl. Opt.* 54, 6994–7001. doi:10.1364/ao.54.006994

Chen, C., Chang, K., Liu, C., Wang, J., and Wang, Q. (2019). Fast Hologram Generation Using Intermediate Angular-Spectrum Method for High-Quality Compact on-axis Holographic Display. *Opt. Express* 27, 29401–29414. doi:10.1364/oe.27.029401

Chen, C., Lee, B., Li, N.-N., Chae, M., Wang, D., Wang, Q.-H., et al. (2021). Multi-depth Hologram Generation Using Stochastic Gradient Descent Algorithm with Complex Loss Function. *Opt. Express* 29, 15089–15103. doi:10.1364/oe.425077

Chen, H.-M., Yang, J.-P., Yen, H.-T., Hsu, Z.-N., Huang, Y., and Wu, S.-T. (2018). Pursuing High Quality Phase-Only Liquid crystal on Silicon (LCoS) Devices. *Appl. Sci.* 8, 2323–2338. doi:10.3390/app8112323

Chen, L., Tian, S., Zhang, H., Cao, L., and Jin, G. (2021). Phase Hologram Optimization with Bandwidth Constraint Strategy for Speckle-free Optical Reconstruction. *Opt. Express* 29, 11645–11663. doi:10.1364/oe.422115

Cheung, W. K., Tsang, P., Poon, T. C., and Zhou, C. (2011). Enhanced Method for the Generation of Binary Fresnel Holograms Based on Grid-Cross Downsampling. *Chin. Opt. Lett.* 9, 120005–120009. doi:10.3788/col201109.120005

Choi, S., Gopakumar, M., Peng, Y., Kim, J., and Wetzstein, G. (2021). Neural 3D Holography: Learning Accurate Wave Propagation Models for 3D Holographic Virtual and Augmented Reality Displays. *ACM Trans. Graph.* 40, 240. doi:10.1145/3478513.3480542

Choi, S., Kim, J., Peng, Y., and Wetzstein, G. (2021). Optimizing Image Quality for Holographic Near-Eye Displays with Michelson Holography. *Optica* 8, 143–146. doi:10.1364/optica.410622

Curtis, V.-R., Cairam, N.-W., Xu, J., Sata, A. S., and Pégard, C. N. (2021). "Dynamic Computer Generated Holography for Speckle-free, High Fidelity 3D Displays," in Proceedings of the 2021 IEEE Virtual Reality and 3D User Interfaces (VR), Lisboa, Portugal, 27 March-1 April 2021, 1–9.

Duan, X., Liu, J., Li, X., Xue, G., Zhao, T., and Duan, J. (2019). Novel Computer-Generated Hologram Encoding Method Based on Partially Temporal Coherent Light. *Opt. Express* 27, 6851–6862. doi:10.1364/oe.27.006851

Eybposh, M. E., Caira, N. W., Atisa, M., Chakravarthula, P., and Pégard, N. C. (2020). DeepCGH: 3D Computer-Generated Holography Using Deep Learning. *Opt. Express* 28, 26636–26650. doi:10.1364/oe.399624

Gabor, D. (1948). A New Microscopic Principle. *Nature* 161, 777–778. doi:10.1038/161777a0

Gerchberg, R.-W., and Saxton, W.-O. (1972). A Practical Algorithm for the Determination of Phase from Image and Diffraction Plane Pictures. *Optik* 35, 237–246.

Hamann, S., Shi, L., Solgaard, O., and Wetzstein, G. (2018). Time-multiplexed Light Field Synthesis via Factored Wigner Distribution Function. *Opt. Lett.* 43, 599–602. doi:10.1364/ol.43.000599

Horisaki, R., Takagi, R., and Tanida, J. (2018). Deep-learning-generated Holography. *Appl. Opt.* 57, 3859–3863. doi:10.1364/ao.57.003859

Jang, C., Bang, K., Li, G., and Lee, B. (2018). Holographic Near-Eye Display with Expanded Eye-Box. *ACM Trans. Graph.* 37, 195. doi:10.1145/3272127.3275069

Jiao, S., Zhang, D., Zhang, C., Gao, Y., Lei, T., and Yuan, X. (2020). Complex-amplitude Holographic Projection with a Digital Micromirror Device (DMD) and Error Diffusion Algorithm. *IEEE J. Select. Top. Quan. Electron.* 26, 1–8. doi:10.1109/jstqe.2020.2996657

Jun, A., Hirotsuna, M., and Tomio, S. (1995). Speckle-noise Reduction on Kinoform Reconstruction Using a Phase-Only Spatial Light Modulator. *Appl. Opt.* 34, 3165–3171. doi:10.1364/AO.34.003165

Kuzmenko, A., Iezhov, P., and Kim, J.-T. (2011). "Weighting Iterative Fourier Transform Algorithm for Kinoform Implemented with Phase-Only SLM," in *Digital Holography and Three-Dimensional Imaging*. Editors H. Yoshikawa and M. K. Kim (Washington, D.C., United States: Optical Society of America), DTuC37. doi:10.1364/dh.2011.dtuc37

LeCun, Y., Bengio, Y., and Hinton, G. (2015). Deep Learning. *Nature* 521, 436–444. doi:10.1038/nature14539

Lee, J., Jeong, J., Cho, J., Yoo, D., Lee, B., and Lee, B. (2020). Deep Neural Network for Multi-Depth Hologram Generation and its Training Strategy. *Opt. Express* 28, 27137–27154. doi:10.1364/oe.402317

Lee, S., Kim, D., Nam, S.-W., Lee, B., Cho, J., and Lee, B. (2020). Light Source Optimization for Partially Coherent Holographic Displays with Consideration of Speckle Contrast, Resolution, and Depth of Field. *Sci. Rep.* 10, 18832–18844. doi:10.1038/s41598-020-75947-0

Lee, S., Kim, D., Nam, S.-W., and Lee, B. (2020). Speckle Reduced Holographic Displays Using Tomographic Synthesis. *Opt. Lett.* 45, 4686–4689. doi:10.1364/ol.399623

Li, N.-N., Wang, D., Li, Y.-L., and Wang, Q.-H. (2020). Method of Curved Composite Hologram Generation with Suppressed Speckle Noise. *Opt. Express* 28, 34378–34389. doi:10.1364/oe.406265

Lin, S.-F., Gentet, P., Wang, D., Lee, S.-H., Kim, E.-S., and Wang, Q.-H. (2021). Simply Structured Full-Color Holographic Three-Dimensional Display Using Angular-Compensating Holographic Optical Element. *Opt. Lasers Eng.* 138, 106404. doi:10.1016/j.optlaseng.2020.106404

Liu, J.-P., Wu, M.-H., and Tsang, P. W. M. (2020). 3D Display by Binary Computer-Generated Holograms with Localized Random Down-Sampling and Adaptive Intensity Accumulation. *Opt. Express* 28, 24526–24537. doi:10.1364/oe.399011

Liu, S.-J., Wang, D., and Wang, Q.-H. (2019). Speckle Noise Suppression Method in Holographic Display Using Time Multiplexing Technique. *Opt. Commun.* 436, 253–257. doi:10.1016/j.optcom.2018.12.038

Lohmann, A. W., and Paris, D. P. (1967). Binary Fraunhofer Holograms, Generated by Computer. *Appl. Opt.* 6, 1739–1748. doi:10.1364/ao.6.001739

Lucente, M. E. (1993). Interactive Computation of Holograms Using a Look-Up Table. *J. Electron. Imaging* 2, 28–34. doi:10.1117/12.133376

Ma, H., Liu, J., Yang, M., Li, X., Xue, G., and Wang, Y. (2017). Influence of Limited Random-phase of Objects on the Image Quality of 3D Holographic Display. *Opt. Commun.* 385, 153–159. doi:10.1016/j.optcom.2016.10.042

Maimone, A., Georgiou, A., and Kollin, J. S. (2017). Holographic Near-Eye Displays for Virtual and Augmented Reality. *ACM Trans. Graph.* 36, 1–16. doi:10.1145/3072959.3073624

Masaya, M., and Yuji, S. (2019). "Effect of point Pitch on Speckle Noise in Computer-Generated Hologram Using point-based Method," in Proceedings Volume 10944, Practical Holography XXXIII: Displays, Materials, and Applications, San Francisco, California, United States, March 2019, 10944. doi:10.1117/12.2509088

Memmolo, P., Bianco, V., Paturzo, M., Javidi, B., Netti, P. A., and Ferraro, P. (2014). Encoding Multiple Holograms for Speckle-Noise Reduction in Optical Display. *Opt. Express* 22, 25768–25775. doi:10.1364/oe.22.025768

Mendoza-Yero, O., Mínguez-Vega, G., and Lancis, J. (2014). Encoding Complex fields by Using a Phase-Only Optical Element. *Opt. Lett.* 39, 1740–1743. doi:10.1364/ol.39.001740

Montrésor, S., Memmolo, P., Bianco, V., Ferraro, P., and Picart, P. (2019). Comparative Study of Multi-Look Processing for Phase Map De-noising in Digital Fresnel Holographic Interferometry. *J. Opt. Soc. Am. A. Opt. Image Sci. Vis.* 36, A59–A66. doi:10.1364/JOSAA.36.000A59

Mori, Y., Fukuoka, T., and Nomura, T. (2014). Speckle Reduction in Holographic Projection by Random Pixel Separation with Time Multiplexing. *Appl. Opt.* 53, 8182–8188. doi:10.1364/ao.53.008182

Nagahama, Y., Shimobaba, T., Kakue, T., Takaki, Y., and Ito, T. (2019). Image Quality Improvement of Random Phase-free Holograms by Addressing the Cause of Ringing Artifacts. *Appl. Opt.* 58, 2146–2151. doi:10.1364/ao.58.002146

Nishitsuji, T., Yamamoto, Y., Sugie, T., Akamatsu, T., Hirayama, R., Nakayama, H., et al. (2018). Special-purpose Computer HORN-8 for Phase-type Electro-Holography. *Opt. Express* 26, 26722–26733. doi:10.1364/oe.26.026722

Park, D.-Y., and Park, J.-H. (2020). Hologram Conversion for Speckle Free Reconstruction Using Light Field Extraction and Deep Learning. *Opt. Express* 28, 5393–5409. doi:10.1364/oe.384888

Peng, Y., Choi, S., Padmanaban, N., and Wetzstein, G. (2020). Neural Holography with Camera-In-The-Loop Training. *ACM Trans. Graph.* 39, 1–14. doi:10.1145/3414685.3417802

Qi, Y., Chang, C., and Xia, J. (2016). Speckleless Holographic Display by Complex Modulation Based on Double-phase Method. *Opt. Express* 24, 30368–30378. doi:10.1364/oe.24.030368

Redding, B., Choma, M. A., and Cao, H. (2012). Speckle-free Laser Imaging Using Random Laser Illumination. *Nat. Photon* 6, 355–359. doi:10.1038/nphoton.2012.90

Shi, L., Huang, F.-C., Lopes, W., Matusik, W., and Luebke, D. (2017). Near-eye Light Field Holographic Rendering with Spherical Waves for Wide Field of View Interactive 3D Computer Graphics. *ACM Trans. Graph.* 36, 236. doi:10.1145/3130800.3130832

Shi, L., Li, B., Kim, C., Kellnhofer, P., and Matusik, W. (2021). Towards Real-Time Photorealistic 3D Holography with Deep Neural Networks. *Nature* 591, 234–239. doi:10.1038/s41586-020-03152-0

Shimobaba, T., and Ito, T. (2015). Random Phase-free Computer-Generated Hologram. *Opt. Express* 23, 9549–9554. doi:10.1364/oe.23.009549

St. Hilaire, P., Benton, S. A., and Lucente, M. (1992). Synthetic Aperture Holography: a Novel Approach to Three-Dimensional Displays. *J. Opt. Soc. Am. A.* 9, 1969–1977. doi:10.1364/josaa.9.001969

Tsang, P. W. M., Liu, J.-P., Lam, H., and Poon, T.-C. (2020). Enhancing the Quality of Sampled Phase-Only Hologram (SPOH) Based on Time-Division Comb Filtering. *Appl. Sci.* 10, 2732–2746. doi:10.3390/app10082732

Tsang, P. W. M., Poon, T.-C., and Jiao, A. S. M. (2013). Embedding Intensity Image in Grid-Cross Down-Sampling (GCD) Binary Holograms Based on Block Truncation Coding. *Opt. Commun.* 304, 62–70. doi:10.1016/j.optcom.2013.04.019

Wang, D., Li, N.-N., Chang, C.-L., Liu, C., and Wang, Q.-H. (2020). Method of Speckle Noise Suppression for Holographic Zoom Display Based on Layered-Pixel-Scanning Algorithm. *IEEE Access* 8, 102128–102137. doi:10.1109/access.2020.2999476

Wang, D., Li, N.-N., Liu, C., and Wang, Q.-H. (2019). Holographic Display Method to Suppress Speckle Noise Based on Effective Utilization of Two Spatial Light Modulators. *Opt. Express* 27, 11617–11625. doi:10.1364/oe.27.011617

Wang, D., Liu, C., Shen, C., Xing, Y., and Wang, Q.-H. (2020). Holographic Capture and Projection System of Real Object Based on Tunable Zoom Lens. *PhotoniX* 1, 6. doi:10.1186/s43074-020-0004-3

Wang, Z., Lv, G., Feng, Q., Wang, A., and Ming, H. (2020). Enhanced Resolution of Holographic Stereograms by Moving or Diffusing a Virtual Pinhole Array. *Opt. Express* 28, 22755–22766. doi:10.1364/oe.396639

Wu, J., Liu, K., Sui, X., and Cao, L. (2021). High-speed Computer-Generated Holography Using an Autoencoder-Based Deep Neural Network. *Opt. Lett.* 46, 2908–2911. doi:10.1364/ol.425485

Wu, L., and Zhang, Z. (2021). Domain Multiplexed Computer-Generated Holography by Embedded Wavevector Filtering Algorithm. *PhotoniX* 2, 1. doi:10.1186/s43074-020-00023-9

Wu, Y., Wang, J., Chen, C., Liu, C.-J., Jin, F.-M., and Chen, N. (2021). Adaptive Weighted Gerchberg-Saxton Algorithm for Generation of Phase-Only Hologram with Artifacts Suppression. *Opt. Express* 29, 1412–1427. doi:10.1364/oe.413723

Yamaguchi, M., Ohyama, N., and Honda, T. (1992). Holographic Three-Dimensional Printer: New Method. *Appl. Opt.* 31, 217–222. doi:10.1364/ao.31.000217

Yanagihara, H., Shimobaba, T., Kakue, T., and Ito, T. (2020). Image Quality Improvement of Holographic 3-D Images Based on a Wavefront Recording Plane Method with a Limiting Diffraction Region. *Opt. Express* 28, 17853–17867. doi:10.1364/oe.395091

Yoo, D., Jo, Y., Nam, S.-W., Chen, C., and Lee, B. (2021). Optimization of Computer-Generated Holograms Featuring Phase Randomness Control. *Opt. Lett.* 46, 4769–4772. doi:10.1364/ol.437375

Ysang, P.-W.-M., Jiao, A.-S.-M., and Poon, T.-C. (2014). Fast Conversion of Digital Fresnel Hologram to Phase-Only Hologram Based on Localized Error Diffusion and Redistribution. *Opt. Express* 22, 5060–5066.

Zhan, T., Xiong, J., Zou, J., and Wu, S.-T. (2020). Multifocal Displays: Review and prospect. *PhotoniX* 1, 10. doi:10.1186/s43074-020-00010-0

Zhao, R., Huang, L., and Wang, Y. (2020). Recent Advances in Multi-Dimensional Metasurfaces Holographic Technologies. *PhotoniX* 1, 20. doi:10.1186/s43074-020-00020-y

Zhao, T., Liu, J., Duan, J., Li, X., and Wang, Y. (2019). Image Quality Enhancement via Gradient-Limited Random Phase Addition in Holographic Display. *Opt. Commun.* 442, 84–89. doi:10.1016/j.optcom.2019.02.026

Zheng, H., Yu, Y., Wang, T., and Dai, L. (2009). High-quality Three-Dimensional Holographic Display with Use of Multiple Fractional Fourier Transform. *Chin. Opt. Lett.* 7, 1151–1154. doi:10.3788/col20090712.1151

Conflict of Interest: The authors declare that the research was conducted in the absence of any commercial or financial relationships that could be construed as a potential conflict of interest.

frontiers in Photonics

REVIEW
published: 01 February 2022
doi: 10.3389/fphot.2021.829139

Review of Incoherent Digital Holography: Applications to Multidimensional Incoherent Digital Holographic Microscopy and Palm-Sized Digital Holographic Recorder—Holosensor

*Tatsuki Tahara**

Applied Electromagnetic Research Center, Radio Research Institute, National Institute of Information and Communications Technology, Koganei, Japan

We review advancements in incoherent digital holography (IDH) with an image sensor and its applications to multidimensional microscopy and a palm-sized hologram recorder termed "holosensor". There are two types of representative IDH technique: IDH with a structured illumination and a single photodetector termed optical scanning holography and self-interference IDH. The latter IDH is a technique to obtain an incoherent digital hologram by modulating an incoherent light wave between an object and an image sensor. Multidimensional information such as three-dimensional space and wavelengths is simultaneously recorded without changing optical filters by introducing interferometric techniques invented in laser holography. Applications to high-speed color-multiplexed holographic fluorescence microscopy, single-shot incoherent full-color holographic microscopy with white light, and a palm-sized multidimensional incoherent hologram recorder have been developed using multidimensional IDH systems. Schematics and experimental results obtained using IDH techniques, incoherent holographic microscopy systems, and compact IDH systems are introduced.

Keywords: incoherent digital holography, digital holography, digital holographic microscopy, color holography, three-dimensional microscopy, holographic fluorescence microscopy, computational coherent superposition, holosensor

OPEN ACCESS

Edited by:
Peter Wai Ming Tsang, City University of Hong Kong, Hong Kong SAR, China

Reviewed by:
Jung-Ping Liu, Feng Chia University, Taiwan
Myung Kim, University of South Florida, United States

***Correspondence:**
Tatsuki Tahara
tahara@nict.go.jp

Specialty section:
This article was submitted to Optical Information Processing and Holography, a section of the journal Frontiers in Photonics

Received: *05 December 2021*
Accepted: *27 December 2021*
Published: *01 February 2022*

Citation:
Tahara T (2022) Review of Incoherent Digital Holography: Applications to Multidimensional Incoherent Digital Holographic Microscopy and Palm-Sized Digital Holographic Recorder—Holosensor. Front. Photonics 2:829139. doi: 10.3389/fphot.2021.829139

1 INTRODUCTION

Multidimensional imaging is one of the most actively researched themes in both science and industry. Multidimensional information, such as three-dimensional (3D), wavelength, and polarization images, has been applied to observe realistic scenes of remote locations, microscopic and nanoscopic fields of view, and invisible images at infrared wavelength bands. 3D information is important, particularly when a person and a machine perceive and observe 3D structures of samples and scenes. Color and polarization information is useful for accurately identifying and distinguishing objects. Image sensors at various wavelength bands and polarization-imaging cameras have been developed, and multimodal imaging with such sensors has been performed to date. Multiple image

sensors and various optical filters are generally used to record multidimensional information. However, advanced optical techniques have been desired to make it possible to realize a compact multidimensional imaging system.

Incoherent digital holography (IDH) is an optical technique of 3D imaging with a single sensor. 3D information of a light wave is recorded using light interference. A hologram is digitally recorded even for a spatially incoherent light wave. The 3D image of a light wave is reconstructed from the recorded hologram using a computer. Multiple image sensors are not required for 3D imaging. The invention of IDH originated from the proposal of incoherent holography (Lohmann, 1965). Lohmann proposed several optical implementations including self-interference and self-reference holography to obtain a hologram of spatially incoherent light and demonstrated holographic imaging with an implementation (Lohmann and Bryngdahl, 1968). After that, Poon *et al.* invented IDH with a single photodetector termed optical scanning holography (OSH) (Poon and Korpel, 1979; Poon, 1985). OSH is a single-pixel DH technique with a structured illumination. By exploiting point-spread-function (PSF) engineering of illumination light and a temporal heterodyne technique, one can encode 3D information of fluorescence light as time-series intensity values. The 3D information of fluorescence light is recorded by a single photodetector. Holographic fluorescence microscopy was initially invented with OSH in 1997 (Schilling et al., 1997), and IDH imaging was performed for fluorescence light. On the other hand, research on incoherent holography with a 2D recording material has been continued. Sirat and Psaltis proposed and experimentally demonstrated an incoherent holography system equipped with a birefringent material and polarizers to generate interference light, and they termed the technique conoscopic holography (CH) (Sirat and Psaltis, 1985). CH has been implemented with a unique phase-shifting interferometry (PSI) system employing a liquid crystal phase modulator and a rotational amplitude mask (Mugnier and Sirat, 1992; Mugnier et al., 1993; Mugnier, 1995). Such a single-path polarimetric interferometer contributes to the construction of today's compact IDH system. Then, Yoshimori proposed an IDH technique to conduct hyperspectral 3D imaging of natural light based on Fourier spectroscopy (Yoshimori, 2001). After that, Rosen and Brooker proposed an IDH technique that adopts a phase-only spatial light modulator (SLM) both to construct a self-interference IDH system and to conduct PSI, and the technique was termed Fresnel incoherent correlation holography (FINCH) (Rosen and Brooker, 2007). An incoherent digital hologram is obtained without the use of a structured illumination, and incoherent holographic imaging is conducted with several exposures. Application to holographic fluorescence microscopy with an image sensor was demonstrated (Rosen and Brooker, 2008), and then PSF improvement in incoherent imaging by FINCH was achieved (Rosen et al., 2011). As another application of IDH, Kim performed high-quality incoherent holographic imaging, including full-color 3D imaging of an outdoor scene illuminated by sunlight (Kim, 2013; Clark and Kim, 2015). From these research achievements, IDH can be applied to the holographic imaging of various light waves. Progress on IDH comes from exploiting optical devices and state-of-the art holographic techniques that are invented in incoherent and laser holography. An image sensor with a wide dynamic range and low noise enables us to record low-visibility incoherent holograms. The combination of PSI (Bruning et al., 1974; Yamaguchi and Zhang, 1997) with a phase-only SLM or a highly accurate piezo actuator improves image quality because undesired-order diffraction images are removed by digital signal processing based on interferometry. Further advancement of IDH is expected by adopting a laser holography technique to IDH.

Research on laser DH has been continuously conducted, and techniques invented in laser DH have been actively adopted to IDH in the last 5 years: single-shot IDH (Tahara et al., 2017a; Nobukawa et al., 2018; Choi et al., 2019; Tahara et al., 2020a; Liang et al., 2020) with single-shot phase-shifting (SSPS) (Zhu and Ueda, 2003; Awatsuji et al., 2004; Millerd et al., 2004), single-path multiwavelength-multiplexed IDH (Tahara et al., 2019; Tahara et al., 2020b; Hara et al., 2020; Tahara et al., 2021a; Tahara et al., 2021b) based on computational coherent superposition (CCS) (Tahara et al., 2015a; Tahara et al., 2015b; Tahara et al., 2017b; Tahara et al., 2018a), and single-shot multicolor IDH techniques (Tahara et al., 2020c; Tahara et al., 2021). Applications of IDH, such as multidimensional holographic microscopy with incoherent light and the palm-sized hologram recorder "holosensor" (Tahara, 2021; Tahara and Oi, 2021; Tahara et al., 2021; Tahara et al., 2021c), are proposed using the developed IDH techniques. In this review, IDH techniques are explained and applications to multidimensional microscopy and holosensor are introduced.

2 INCOHERENT DIGITAL HOLOGRAPHY

IDH is implemented by PSF engineering of an illumination light wave or an object wave. OSH is for the former and other proposed IDH techniques are for the latter. **Figure 1** illustrates examples of IDH with a structure illumination, which is termed OSH, and IDH with self-interference light. **Figure 1A** is a schematic of OSH. A Gabor zone plate (GZP) pattern illuminates an object. The generation of the GZP pattern means PSF engineering of illumination light in 3D space. The GZP pattern moves along an *X*-*Y* plane. A single-pixel photo detector records time-sequence intensity data and this data contains 3D information of the object. A 3D image without the zeroth-order diffraction wave and the conjugate image is reconstructed using a temporal heterodyne technique. This technique is categorized as single-pixel DH and spatially incoherent DH. A book and comprehensive review articles for OSH have been written by experts to date, and these will help readers understand DH techniques with a single photodetector (Poon, 2007; Ting-Chung Poon et al., 1996; Poon, 2009; Liu et al., 2018). **Figures 1B,C** are schematics of self-interference IDH using rotational and radial shears, respectively. A shear is utilized to generate self-interference in many IDH techniques. Yoshimori and co-workers have proposed and experimentally demonstrated hyperspectral 3D imaging with commonly used light by constructing a Michelson-type IDH system utilizing a

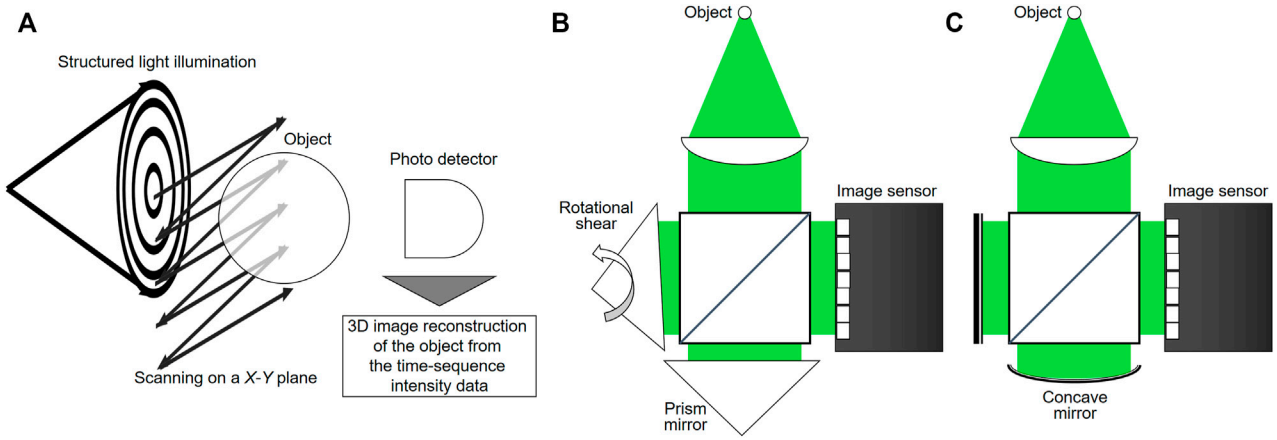

FIGURE 1 | Schematics of **(A)** OSH and self-interference IDH with **(B)** rotational and **(C)** radial shears.

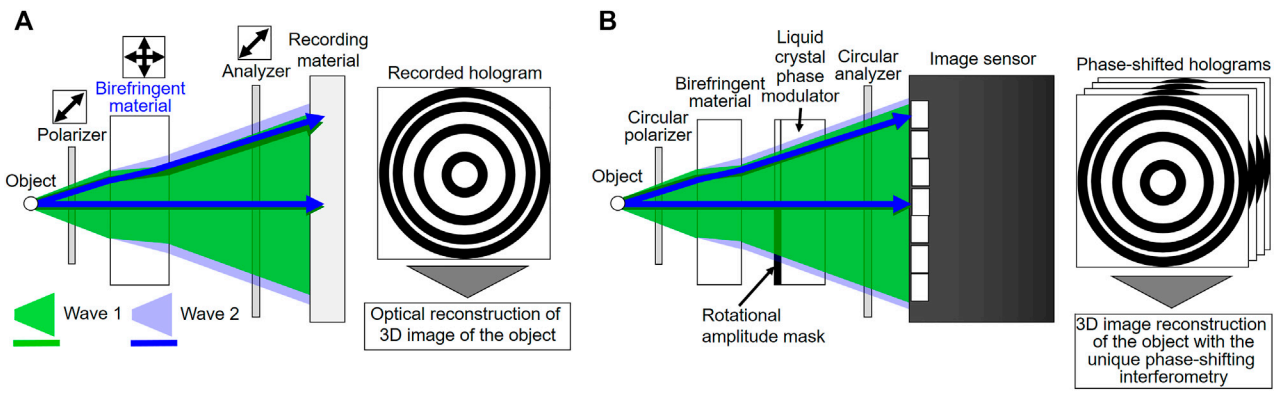

FIGURE 2 | Schematics of conoscopic holography using **(A)** a chemical recording material and **(B)** unique PSI and an image sensor.

rotational shear shown in **Figure 1B** (Yoshimori, 2001; Teeranutranont and Yoshimori, 2013). Kim and co-workers and other researchers have proposed a Michelson-type self-interference IDH system using a concave mirror to generate a radial shear shown in **Figure 1C** (Kim, 2012; Hong and Kim, 2013; Kim, 2013). Kim has demonstrated full-color 3D imaging of an outdoor scene using sunlight and the IDH system. As another way, IDH has also been implemented with Mach-Zehnder-type radial shearing self-interference interferometer by many researchers (Pedrini et al., 2012; Naik et al., 2014). Furthermore, a unique IDH technique exploiting the nature of coherence has been proposed by Takeda *et al.*, which is termed Coherence holography (Takeda et al., 2005; Naik et al., 2009).

A self-interference IDH system using an image sensor described above adopts one of two-arm interferometers and tolerance against external vibration is a serious problem. It is said that an IDH system has been constructed on a wagon table to record phase-shifted incoherent holograms of an outdoor scene. However, motion-picture recording for the scene has not been successfully demonstrated until now. It seems that this is because it is difficult to stably record phase-shifted holograms. Therefore, such IDH systems have been constructed on an anti-vibration table to obtain the reproductivity. On the other hand, a single-path self-interference IDH system is highly stable and enables us to construct an IDH system on a commonly used table. It is notable that such a phase-shifting IDH system using an image sensor was, in my knowledge, initially proposed in 1990s, based on CH (Mugnier and Sirat, 1992; Mugnier et al., 1993; Mugnier, 1995). In this section, we describe CH as an important single-path polarimetric interferometer and then IDH techniques with a single-path interferometer and an image sensor.

2.1 Conoscopic Holography

CH (Sirat and Psaltis, 1985) was proposed for recording 3D information of incoherent light as an incoherent hologram. The main feature of CH is that it enables us to construct a compact single-path incoherent holography system by exploiting the polarization of light. CH is also useful for IDH and we briefly explain the technique. **Figure 2** illustrates the schematic of CH. In the initially proposed system (Sirat and Psaltis, 1985), between an incoherent object-wave point and an image sensor, a polarizer, a birefringent material, and an analyzer are set to generate self-

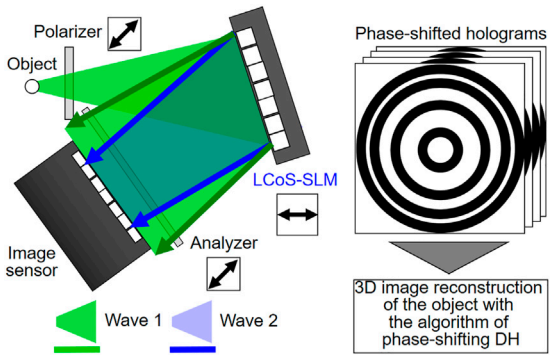

FIGURE 3 | Schematic of Fresnel incoherent correlation holography.

interference light of the object wave as shown in **Figure 2**. A polarizer aligns the polarization direction of the object wave. A birefringent material such as a crystal introduces different wavefront modulations against the orthogonally polarized light waves. In **Figure 2**, a birefringent material has fast and slow axes for vertical and horizontal directions. Two wavefronts of vertically and horizontally polarized object waves are generated from an object wave. Different wavefront curvature radii are introduced to the orthogonal polarizations when using a birefringent lens or a thick birefringent plate. An analyzer aligns the polarization directions of the two waves, and the two waves interfere with each other when the optical-path-length difference is carefully adjusted. A recording material such as a photographic plate and a film records an interference fringe image. Here, a 3D object illuminated by spatially incoherent light is regarded as the summation of spatially incoherent object-wave points in 3D space. Therefore, incoherent superpositions of GZP patterns of multiple object-wave points are formed on the recording material, and the formed image is recorded as an incoherent hologram of the 3D object. A 3D image of the object is optically reconstructed using the recorded incoherent hologram. Undesired-order diffraction images such as zeroth-order diffraction light and the conjugate image are suppressed with optical filtering in CH. A clear interference fringe pattern is formed owing to the proposed single-path polarimetric interferometer. Then, CH has adopted PSI with the designed PSI method to remove undesired-order diffraction waves. **Figure 2B** illustrates its schematic. A liquid crystal phase modulator and a designed amplitude mask attached with a rotational stage are set to conduct the designed PSI. The detailed explanations can be seen in refs. (Mugnier and Sirat, 1992; Mugnier et al., 1993; Mugnier, 1995). It is notable that phase-shifting DH was proposed and implemented for CH and spatially incoherent light before the proposal of famous phase-shifting DH using a laser (Yamaguchi and Zhang, 1997).

2.2 Fresnel Incoherent Correlation Holography

FINCH (Rosen and Brooker, 2007; Rosen et al., 2019) is an IDH technique exploiting a phase-only SLM and digital signal processing based on DH with PSI. Instead of a solid birefringent material, FINCH adopts a diffractive optical element as shown in **Figure 3**. A liquid crystal on silicon SLM (LCoS-SLM) is set to generate two object waves with different wavefront curvature radii. Phase-shifted Fresnel phase lens patterns are displayed on the LCoS-SLM, and phase-shifted incoherent holograms are sequentially recorded by changing the phases of the phase lenses. A compact single-path phase-shifting IDH system has been realized by exploiting the LCoS-SLM as a two-wavefront generator and a phase shifter. Space-division (Rosen and Brooker, 2007) and polarization (Brooker et al., 2011) multiplexing techniques were proposed to generate two waves. PSF improvement in incoherent imaging was clarified after the experimental demonstrations (Rosen et al., 2011). FINCH has clarified that IDH is effective for not only incoherent holographic 3D imaging but also improving the resolution in general incoherent imaging techniques.

2.3 Computational Coherent Superposition Incoherent Digital Holography

DH techniques that are invented in laser holography contribute to the development of IDH. OSH and FINCH have demonstrated incoherent 3D imaging without undesired-order diffraction images by applying digital signal processing based on interferometry. Progress on laser DH techniques is continuing, and PSI selectively extracting wavelength information was invented (Tahara et al., 2015a; Tahara et al., 2015b; Tahara et al., 2017b; Tahara et al., 2018a). Not only 3D information but also wavelengths and polarization directions are simultaneously and selectively extracted with PSI by introducing different phase shifts for different physical information (Tahara et al., 2018a). Therefore, multidimensional information (3D space, phase, wavelengths, and polarization) are multiplexed on the image sensor plane with phase shifts and individually reconstructed by applying the PSI technique. This PSI is termed the computational coherent superposition (CCS) scheme and CCS has been applied to IDH (Tahara et al., 2019; Tahara et al., 2020b; Hara et al., 2020; Tahara et al., 2021a; Tahara et al., 2021b). **Figure 4** shows the schematic of CCS applied to IDH. CCS-IDH is implemented with arbitrary IDH systems that adopt PSI. **Figures 4A,B** are the combinations of CCS with FINCH and CH, respectively. The main difference of CCS from CH and FINCH is the recording of wavelength-multiplexed phase-shifted incoherent holograms. Wavelength information is simultaneously recorded without changing optical filters and obtained with digital signal processing based on CCS. The combination of CCS and FINCH is implemented by introducing an LCoS-SLM whose phase modulation range is sufficiently wide to apply a CCS algorithm (Hara et al., 2020). This is because different phase shifts for different wavelength bands should be introduced in CCS. The LCoS-SLM displays phase-shifted Fresnel phase lens patterns that are required for CCS-FINCH. The high spatial resolution of an LCoS-SLM enables us to generate fine interference fringes and to conduct high-resolution incoherent holographic 3D imaging. However, a

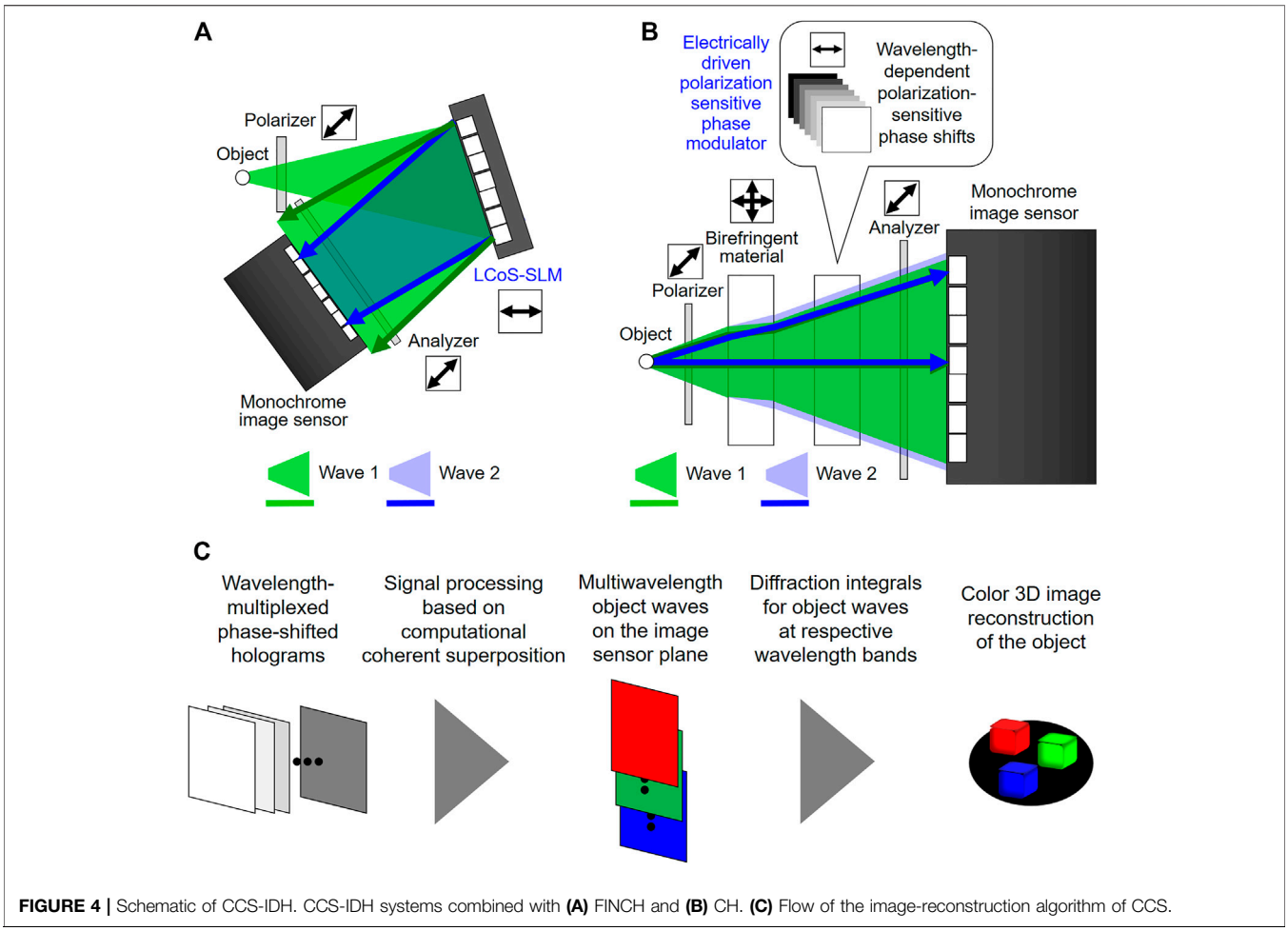

FIGURE 4 | Schematic of CCS-IDH. CCS-IDH systems combined with **(A)** FINCH and **(B)** CH. **(C)** Flow of the image-reconstruction algorithm of CCS.

diffractive optical element has strong selectivity and dependence in wavelength. A Fresnel phase lens works as a lens correctly only for the designed wavelength. Diffraction efficiency is decreased, and undesired-order diffraction waves are generated, as the wavelength of the incident light is different from the designed wavelength. Such a problem causes multiple object-image generations and image-quality degradations. To solve this problem, CCS is combined with CH as another optical implementation as shown in **Figure 4B** (Tahara et al., 2019; Tahara et al., 2020b; Tahara et al., 2021a; Tahara et al., 2021b). The combination of CCS with CH is implemented by inserting an electrically driven polarization-sensitive phase modulator such as a liquid crystal phase retarder or a nonlinear optical element. A liquid crystal generally has wavelength dependence for phase shifts and therefore applicable to phase encoding required for CCS. An SLM is not always required when using the IDH system shown in **Figure 4B**. **Figure 4C** illustrates the flow of the image-reconstruction algorithm of CCS-IDH. From the recorded wavelength-multiplexed phase-shifted incoherent holograms, multiwavelength object waves are selectively extracted using a CCS algorithm. As mathematical expressions, where $A_{ok}(x, y)$ and $\phi_k(x, y)$ are respectively the amplitude and phase distributions at wavelength λ_k, $k = 1, \ldots, N$ is the number of the wavelength bands, α_{kl} is the lth phase shift at a wavelength λ_k, C_k is a coefficient, j is the imaginary unit, and $I_{0th}(x, y)$ is the summation of zeroth-order diffraction waves, the relationship between $I(x, y; \alpha_{1l}, \ldots, \alpha_{kl}, \ldots, \alpha_{Nl})$ and complex amplitude distributions at wavelengths $U_k(x, y) = C_k A_{ok}(x, y)[\cos\phi_k(x, y) + j \sin\phi_k(x, y)]$ is expressed as

$$\boldsymbol{I} = \boldsymbol{P}\boldsymbol{U}, \tag{1}$$

where

$$\boldsymbol{I} = \begin{pmatrix} I_1(x, y) \\ I_2(x, y) \\ I_3(x, y) \\ \cdot \\ \cdot \\ \cdot \\ I_{2N}(x, y) \\ I_{2N+1}(x, y) \end{pmatrix}, \tag{2}$$

$$\boldsymbol{P} = \begin{pmatrix} 1 & 1 & 0 & \cdots & 1 & 0 \\ 1 & \cos\alpha_{11} & \sin\alpha_{11} & \cdots & \cos\alpha_{N1} & \sin\alpha_{N1} \\ 1 & \cos\alpha_{12} & \sin\alpha_{12} & \cdots & \cos\alpha_{N2} & \sin\alpha_{N2} \\ \cdot & \cdot & \cdot & \cdot & \cdot & \cdot \\ \cdot & \cdot & \cdot & \cdot & \cdot & \cdot \\ \cdot & \cdot & \cdot & \cdot & \cdot & \cdot \\ 1 & \cos\alpha_{1(2N-1)} & \sin\alpha_{1(2N-1)} & \cdots & \cos\alpha_{N(2N-1)} & \sin\alpha_{N(2N-1)} \\ 1 & \cos\alpha_{1(2N)} & \sin\alpha_{1(2N)} & \cdots & \cos\alpha_{N(2N)} & \sin\alpha_{N(2N)} \end{pmatrix}, \tag{3}$$

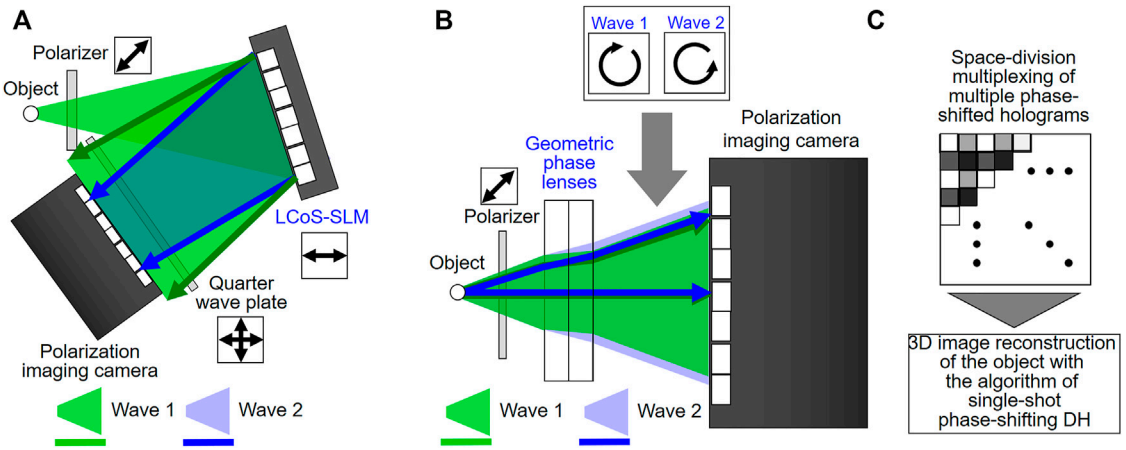

FIGURE 5 | Schematic of SSPS-IDH. SSPS-IDH systems combined with **(A)** FINCH and **(B)** geometric phase lenses. **(C)** Flow of the image-reconstruction algorithm of SSPS.

$$\boldsymbol{U} = \begin{pmatrix} I_{0th}(x,y) \\ C_1 A_{o1}(x,y)\cos\phi_{o1}(x,y) \\ C_1 A_{o1}(x,y)\sin\phi_{o1}(x,y) \\ \cdot \\ \cdot \\ \cdot \\ C_N A_{oN}(x,y)\cos\phi_{oN}(x,y) \\ C_N A_{oN}(x,y)\sin\phi_{oN}(x,y) \end{pmatrix}, \tag{4}$$

Then, complex amplitude distributions at multiple wavelengths are derived by solving

$$\boldsymbol{U} = \boldsymbol{P}^{-1}\boldsymbol{I}, \tag{5}$$

Equation 5 means that object waves at multiple wavelengths are selectively extracted from multiplexed holograms using CCS. Diffraction integrals are calculated for the retrieved multiwavelength object waves, and a multiwavelength 3D image of the object is reconstructed.

It is noted that phase shifts are introduced to respective wavelengths simultaneously. Arbitrary phase shifts can be set to $\alpha_{1l}, \ldots, \alpha_{Nl}$ in **Eq. 3**. When $\boldsymbol{P}$ is a regular matrix, N-wavelength object waves are generally derived from $2N + 1$ wavelength-multiplexed phase-shifted holograms. A small condition number of $\boldsymbol{P}$ should be selected for a CCS algorithm, and phase shifts to set a small condition number should be designed for high-quality imaging. The image quality becomes higher as the condition number becomes smaller. The design of the smallest $\boldsymbol{P}$ using the prepared phase shifter and the measured wavelengths is effective. This is due to the numerical stability of a CCS algorithm and finite signal-to-noise ratio and finite bit depth of the recorded digital images.

2.4 Single-Shot Phase-Shifting Incoherent Digital Holography

Single-shot phase-shifting (SSPS) DH (Zhu and Ueda, 2003; Millerd et al., 2004; Awatsuji et al., 2004) is a technique used in laser holography and has been applied to IDH (Tahara et al., 2017a; Nobukawa et al., 2018; Choi et al., 2019; Liang et al., 2020; Tahara et al., 2020a). Several optical implementations have been presented in IDH to date. **Figure 5** shows examples of optical implementations in SSPS-IDH. SSPS-IDH can be implemented with the combinations of optical systems in SSPS with FINCH (Tahara et al., 2017a; Tahara and Sato, 2019), geometric phase lens (es) (Choi et al., 2019; Liang et al., 2020; Tahara et al., 2020a), and a grating (Nobukawa et al., 2018). SSPS is implemented using the polarization of interference light and a polarization-imaging camera (Millerd et al., 2004). FINCH also utilizes polarization light and can be easily combined with SSPS as shown in **Figure 5A** (Tahara et al., 2017a; Tahara and Sato, 2019). On the other hand, the use of a geometric phase lens for IDH was proposed and then several IDH systems have been presented (Choi et al., 2019; Liang et al., 2020; Choi et al., 2018). A geometric phase lens generates two circularly polarized light waves whose polarization is orthogonal. This feature is suitable for implementing self-interference DH with SSPS and therefore applicable to SSPS-IDH. After that, a thin SSPS-IDH system without a refractive lens was proposed as shown in **Figure 5B** (Tahara et al., 2020a; Tahara and Oi, 2021). In SSPS, multiple phase-shifted holograms are simultaneously recorded by space-division multiplexing as shown in **Figure 5C** (Zhu and Ueda, 2003; Awatsuji et al., 2004; Millerd et al., 2004). A de-mosaicking procedure is conducted in a computer, and then an image-reconstruction algorithm of PSDH is applied with multiple de-mosaicked holograms to reconstruct a holographic 3D image of the object. Note that single-shot incoherent holographic 3D imaging is conducted with a compact single-path IDH system (Tahara and Oi, 2021).

3 APPLICATIONS OF INCOHERENT DIGITAL HOLOGRAPHY

IDH has potential to considerably extend the applicability of DH. Laser light is no longer mandatory when using IDH. Any light

source including self-luminous light and natural light can be recorded as a hologram. Various techniques such as 3D microscopy for self-luminous light (Schilling et al., 1997; Rosen and Brooker, 2008; Jang et al., 2015; Yanagawa et al., 2015; Quan et al., 2017; Liebel et al., 2020a; Liebel et al., 2020b; Kumar et al., 2020; Marar and Kner, 2020; Potcoava et al., 2021), 3D imaging with a single image sensor (Kim, 2013; Clark and Kim, 2015; Jang et al., 2015; Vijayakumar et al., 2016; Vijayakumar and Rosen, 2017; Nobukawa et al., 2018; Choi et al., 2019; Nobukawa et al., 2019; Wu et al., 2020; Tahara et al., 2021d; Wu et al., 2021; Yoneda et al., 2021; Tahara et al., 2022), 3D thermal measurement (Imbe, 2019), and spectroscopic 3D imaging (Yoshimori, 2001; Teeranutranont and Yoshimori, 2013; Naik et al., 2014; Kalenkov et al., 2019) have been proposed to date. Research on applications of IDH is ongoing and a challenging theme. In this section, applications of IDH to multidimensional microscopy and the holosensor are presented.

3.1 Incoherent Digital Holographic Microscopy: Microscopy Application of Incoherent Digital Holography

Incoherent digital holographic microscopy (IDHM) is considered a prospective application of IDH. In the field of microscopy, it is important to record both 3D information and wavelength information simultaneously with weak illumination-light intensity and a compact optical setup. In the fluorescence microscopy application, wavelength information is used as the label for molecule compositions. Measurements with weak illumination-light intensity are required to suppress phototoxicity in cells and to conduct high-speed sensing of molecules. Full-color 3D imaging and restoration as quantitative and digital information are also highly required for Raman scattering microscopy and the widely used optical microscopy with a halogen lamp. Hyperspectral incoherent holography with a two-arm interferometer has been proposed as a conventional spectroscopic and incoherent holographic 3D imaging technique (Yoshimori, 2001; Teeranutranont and Yoshimori, 2013; Naik et al., 2014; Kalenkov et al., 2019). However, tolerance against vibrations is low owing to the use of a two-arm interferometer. However, two arms were required to adopt a temporal heterodyne technique in IDH with the Fourier spectroscopy. To solve this problem is one of the challenging research topics in multiwavelength IDH. In this section we present several ways to solve this problem.

3.1.1 CCS Incoherent Digital Holographic Microscopy

We can realize spectroscopic IDHM with high tolerance against external vibrations, using CCS-IDH. We have constructed a CCS-IDHM system that is shown in **Figure 6** to apply a novel type of spectroscopic IDHM. CCS-IDHM is composed of a CCS-IDH system and an incoherent optical microscope (Tahara et al., 2020b; Tahara et al., 2021a; Tahara et al., 2021b). An optical microscope with incoherent light such as self-luminous light including fluorescence light, Raman scattering light, thermal light generated from a halogen lamp, and light generated from a light-emitting diode (LED) can be combined with a CCS-IDH system. The magnified 3D image of a specimen is irradiated from

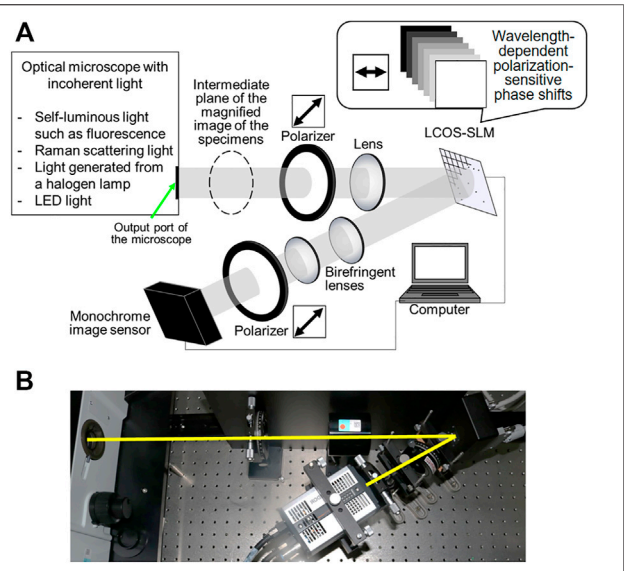

FIGURE 6 | Constructed CCS-IDHM system. **(A)** Schematic of the entire microscopy system. **(B)** Photograph of the constructed CCS-IDH system.

the output port of the microscope, and the magnified 3D image that is focused on the intermediate plane is treated as the 3D specimen in the CCS-IDH system. **Figure 6** also shows the single-path wavelength-multiplexed IDH system constructed as described in **section 2.3**, which provides high tolerance against vibrations in spectroscopic holographic interferometry. A full-color holographic 3D microscope with a halogen lamp and a multiband-pass filter was constructed to first demonstrate CCS-IDHM (Tahara et al., 2020b). Experiments on HE-stained mouse kidney cells were successfully conducted. Then, PSF improvement in full-color incoherent imaging was achieved (Rosen et al., 2021). The CCS-IDH system was also combined with a fluorescence microscope, and color-multiplexed holographic fluorescence microscopy was presented (Tahara et al., 2021a; Tahara et al., 2021b). In the experimental demonstration, fluorescence-stained HeLa cells were prepared. Cell nuclei and cell bodies were stained by different fluorescence markers. As a result, different molecule compositions were labelled by different fluorescence light wavelengths. Detailed conditions for cell staining and the constructed optical setup were described in (Tahara et al., 2021a). **Figure 7** shows the experimental results, which indicate that a monochrome image sensor records wavelength-multiplexed fluorescence holograms, and wavelengths are successfully separated by the CCS. Different molecule compositions are separately obtained by wavelength separations, and focused color fluorescence images of the cells are reconstructed. It is expected that CCS-IDHM is applied to spontaneous Raman imaging and works as multicolor holographic Raman scattering microscopy with a single-path wavelength-multiplexed interferometer.

3.1.2 Full-Color SSPS-IDHM With White Light

Utilization of SSPS-IDH is also effective as another way to realize multiwavelength IDHM with high tolerance against external

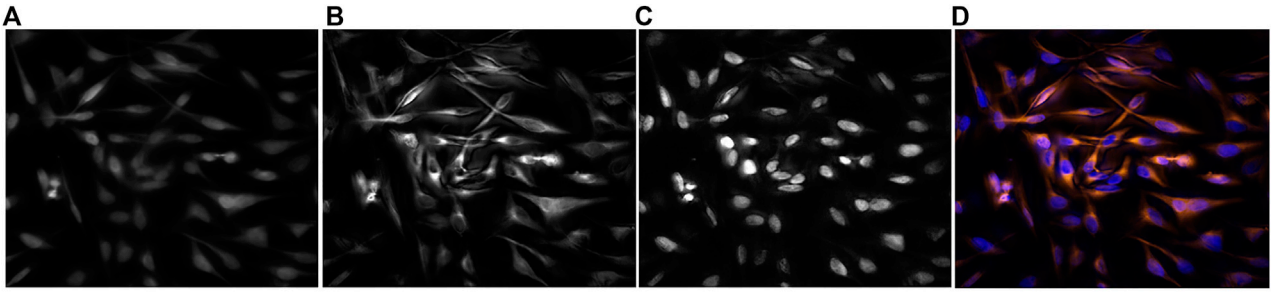

FIGURE 7 | Experimental results for the demonstration of color-multiplexed holographic fluorescence microscopy. **(A)** One of the recorded wavelength-multiplexed holograms obtained by a monochrome image sensor. Reconstructed fluorescence-light images of **(B)** cell bodies and **(C)** cell nuclei. **(D)** Color-merged image of **(B)** and **(C)**.

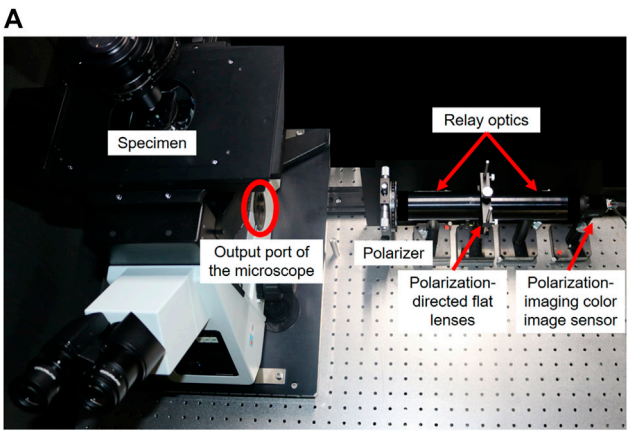

FIGURE 8 | (A) Photograph of the constructed SSPS-IDHM system for single-shot full-color holographic imaging with white light. Adapted with permission from (Tahara et al., 2020a)© IOP Publishing.

vibrations. Currently, one can construct an SSPS-IDH system (Tahara et al., 2017a; Nobukawa et al., 2018; Choi et al., 2019; Liang et al., 2020; Tahara et al., 2020a; Tahara and Sato, 2019). Optical components and a polarization-imaging camera shown in **Figures 5A,B** are commercially available and can be obtained at a low cost. In comparison to CCS-IDHM, higher-temporal resolution is obtained using SSPS-IDHM with a color polarization-imaging camera. Full-color holographic 3D imaging with SSPS-IDHM and a halogen lamp was experimentally demonstrated. **Figure 8A** shows a photograph of one of the constructed SSPS-IDHM systems. The constructed system is composed of an optical microscope with a halogen lamp and an SSPS-IDH system. The SSPS-IDH system treats the magnified 3D image that is focused on the intermediate plane as the 3D specimen. In the constructed SSPS-IDH system, the relay optics is set to collect the light wave of the magnified specimen and to conduct Fourier transform (FT) and inverse FT optically. Polarization-directed flat lenses that are ones of geometric phase lenses are set on the FT plane of relay optics for shift-invariant PSF engineering. A red, green, and blue (RGB) color-filter array of a polarization-imaging color camera selects a wavelength band from the continuous spectral bandwidth of white light generated from a halogen lamp. RGB channels of the color-filter array select the corresponding RGB wavelength bandwidths. The selected bandwidths are within 100 nm. With the color-filter array, not only RGB color information is obtained but also temporal coherency is improved. Detailed experimental conditions are described in (Tahara et al., 2020a). **Figure 9** shows the experimental results, which indicate that both color information and 3D information are reconstructed from the recorded single incoherent hologram. Defocused images on the image sensor plane can be seen at red and green channels, although a focused image was obtained at the blue channel as shown in **Figures 9A–C**. This is attributable to the chromatic aberration of optical elements in the constructed SSPS-IDH system. However, focused images at RGB channels are obtained by the digital refocusing of DH as shown in **Figures 9D–G**. The results indicate that aberration can be compensated with digital signal processing based on holography. Thus, single-shot incoherent color 3D imaging of the specimen is successfully performed. An application to color holographic fluorescence microscopy was also attempted.

3.1.3 The Combination of CCS and SSPS for IDHM

Single-shot wavelength-multiplexed IDH is realized by combining CCS-IDH and SSPS-IDH (Tahara et al., 2020c).

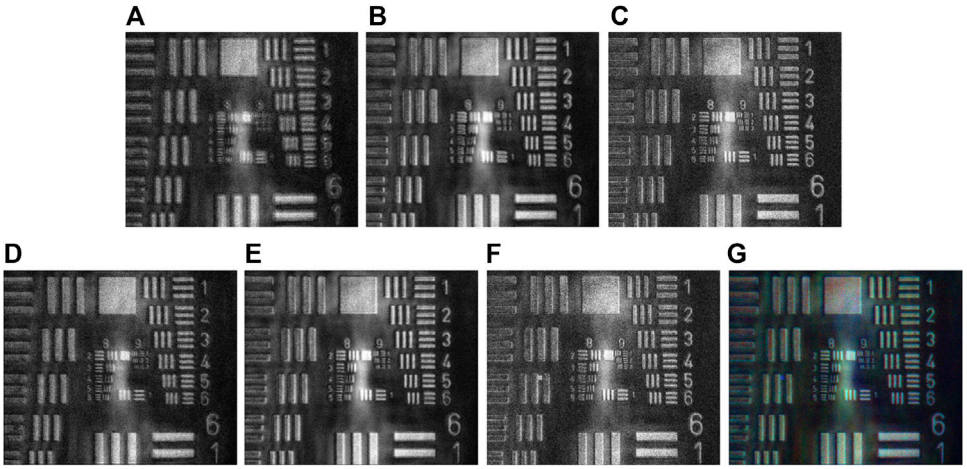

FIGURE 9 | Experimental results of full-color imaging of USAF1951 test target. Images reconstructed on the image sensor plane at **(A)** red, **(B)** green, and **(C)** blue channels. Images numerically focused on the magnified image plane at **(D)** red, **(E)** green, and **(F)** blue channels. **(G)** Color-synthesized image from **(D–F)**. Adapted with permission from (Tahara et al., 2020)© The Optical Society.

Here, we call the combined technique single-shot CCS (SS-CCS) IDH. **Figure 10** shows the schematic of the SS-CCS IDH. Light generated from objects/specimens is converted two light waves by an IDH system using polarization. A monochrome image sensor with a wavelength-dependent polarization-sensitive phase-modulation (WPP) array and a polarizer records two light waves as a wavelength-multiplexed self-interference hologram. In the recorded hologram, the information of multiple wavelength-multiplexed holograms required for CCS is contained, based on space-division multiplexing of holograms. Instead of a micropolarizer array, a WPP array is inserted to apply both CCS and SSPS. De-mosaicking procedure used for pixelated/parallel PSI can also be applied to the recorded single image and then complex amplitude distributions at multiple wavelengths are retrieved using a CCS algorithm. A multiwavelength 3D image is reconstructed by numerical focusing such as diffraction integrals.

A WPP array was developed to combine the two IDH techniques. **Figure 11** shows the schematic of the WPP array and a photograph of the image sensor with the WPP array. Each WPP cell is composed of a photonic crystal, and a photonic-crystal array is fabricated by the self-cloning technique (Sato et al., 2007). The phase shifts of cells A, C, D, and E at the wavelength of 532 nm are 240, 107, 213, and 320°. Wavelength dependency of the phase shift of the photonic crystal fabricated is used for a CCS algorithm. More detail of the developed image sensor is described in ref. (Tahara et al., 2020c). We have constructed an SS-CCS IDHM system to experimentally show its validity, which is the combination of a fluorescence microscope, a CCS-IDH system, and the image sensor. Detailed experimental conditions are described in (Tahara et al., 2020c). Experimental results shown in **Figure 12** indicate that fluorescence object waves at different wavelength bands are selectively extracted, and 3D information at respective wavelength bands is reconstructed successfully. Different types of fluorescence particles are identified using wavelength separations with CCS. Experimental results show that SS-CCS IDHM performs color 3D imaging of fluorescence light from the single wavelength-multiplexed hologram. Improvements of image quality and frame rate are ongoing, and color 3D motion-picture recording of incoherent holograms with more than 70 fps and 4 megapixels has been performed to date (Tahara et al., 2021).

3.2 Compact Hologram Recorder—Holosensor–

As described in the **section 2**, an IDH system can be constructed with a small-size optical setup. A compact and portable hologram recorder is strongly desired in many fields of scientific research and industry. We introduce our compact hologram recorders, which is termed holosensor.

3.2.1 Multiplexed Holosensor Based on CCS-IDH

CCS-IDH is implemented with a compact optical system by adopting CH without an amplitude mask. In previous sections, we have shown how a compact system can be constructed in comparison with a two-arm laser interferometer. However, a more compact optical system can be constructed. **Figure 13A** shows the schematic of the basic concept of the ultimately compact hologram recorder based on CCS-IDH (Tahara, 2021; Tahara et al., 2021; Tahara et al., 2021c). Such a hologram recorder is composed of the integrations of the optical elements shown in **Figure 4B**. As a first step, we have succeeded in designing and constructing the holosensor as shown in **Figures 13B,C**. Experimental results with the prototypes of the CCS-holosensor can be seen in (Tahara et al., 2021; Tahara et al., 2021c).

Color imaging and 3D imaging have been performed using the developed CCS-holosensors (Tahara et al., 2021; Tahara et al., 2021c). However, several research topics are raised. Measurement speed is closely related to the speed of phase shifts and the frame rate. A compact and transparent polarimetric phase modulator is commercially available. A liquid crystal is used for such a phase

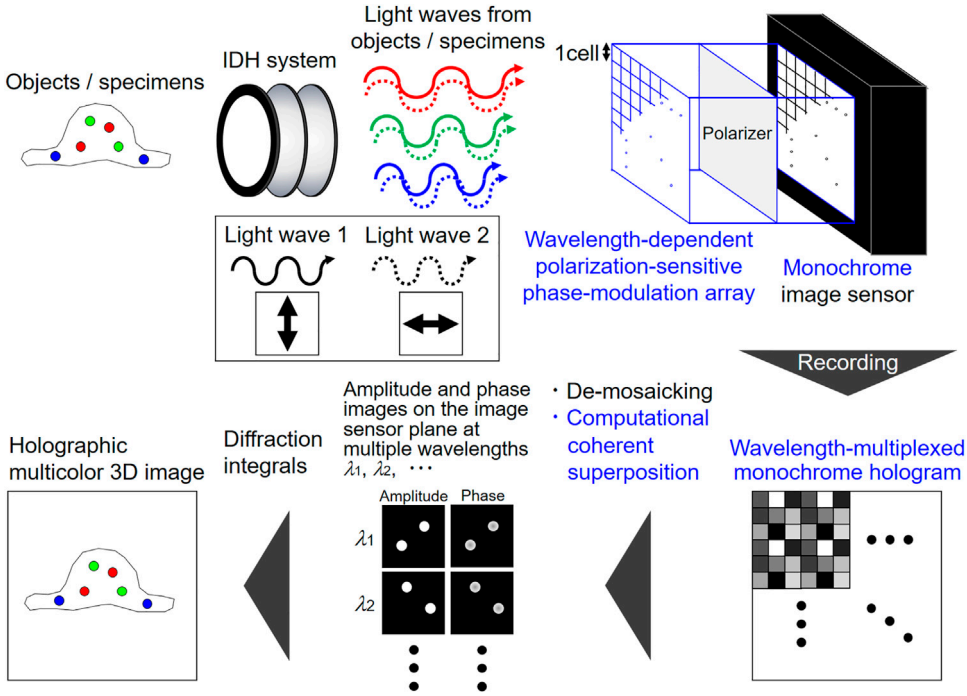

FIGURE 10 | Schematic of SS-CCS IDH.

modulator, and its working speed is much lower than the video rate. Although the working speed is much improved by using a high-speed LCoS-SLM, the size of the CCS-holosensor is increased. The size is also increased when using a Faraday rotator (Ueda and Takuma, 1984). A high-speed, compact, and transparent polarimetric phase modulator is strongly desired for the CCS-holosensor. Otherwise, an architectural design for constructing a compact optical system with an LCoS-SLM is required. As another research theme, careful design of birefringent materials is important. The resolution of IDH is closely related to the pitch of interference fringes. A curvature-radius difference between the two object waves should be large to generate a fine interference fringe image. A transparent material with a large birefringence is effective for the generation of a fine interference fringe image. However, the optical-path-length difference increases as the curvature-radius difference increases. The coherence length is small in IDH and interference fringes easily disappear. Therefore, the optical-path-length difference is adjusted by inserting a birefringent phase plate. After that, an image sensor to record a fine interference fringe image should be selected, considering the sampling theorem.

The initially developed wavelength-multiplexed holosensor is palm-sized. Phase-shift error owing to vibrations was a serious problem in two-arm laser holography with CCS. Accurate phase shifts are mandatory for CCS, and object-wave extraction at the desired wavelength easily fails if a phase-shift error occurs. A single-path IDH system achieved high tolerance against vibrations and reduction of phase-shift error during recording of holograms. Integrations of optical elements and construction of an extremely compact optical system will further help to achieve accurate multidimensional measurement with CCS. A chip-sized hologram recorder will be realized in the near future by integrating the optical elements.

3.2.2 Single-Shot Holosensor Based on IDH With SSPS and SS-CCS

A single-shot multidimensional compact hologram recorder can be fabricated using IDH with SSPS and SS-CCS. **Figure 14** illustrates the schematics. These systems can be constructed by integrating optical elements in the optical systems of SSPS and SS-CCS IDH. **Figure 14A** shows the integrated system shown in **Figure 5**. **Figure 14B** is the combination of **Figure 13A** and the image sensor with a WPP array. The finest pitch of interference fringes is determined by the design of birefringent materials and the pixel pitch of each phase-shifted holograms. A palm-sized single-shot holosensor can be constructed using commercially available optical elements and a polarization-imaging camera. As an experimental demonstration, we have developed a prototype of a single-shot holosensor based on SSPS as shown in **Figure 15A** (Tahara and Oi, 2021). With this single-shot holosensor, an object wave generated with an LED is recorded with a single-shot exposure of an image sensor as shown in **Figure 15B**. A focused object image is successfully reconstructed from a pixelated incoherent image as shown in **Figure 15C**. Detailed experimental conditions are described in (Tahara and Oi, 2021).

4 DISCUSSION AND CONCLUSION

Various IDH techniques have been proposed and continuously researched to date. We discuss the comparative merits of the introduced multidimensional IDH techniques. **Table 1** shows the

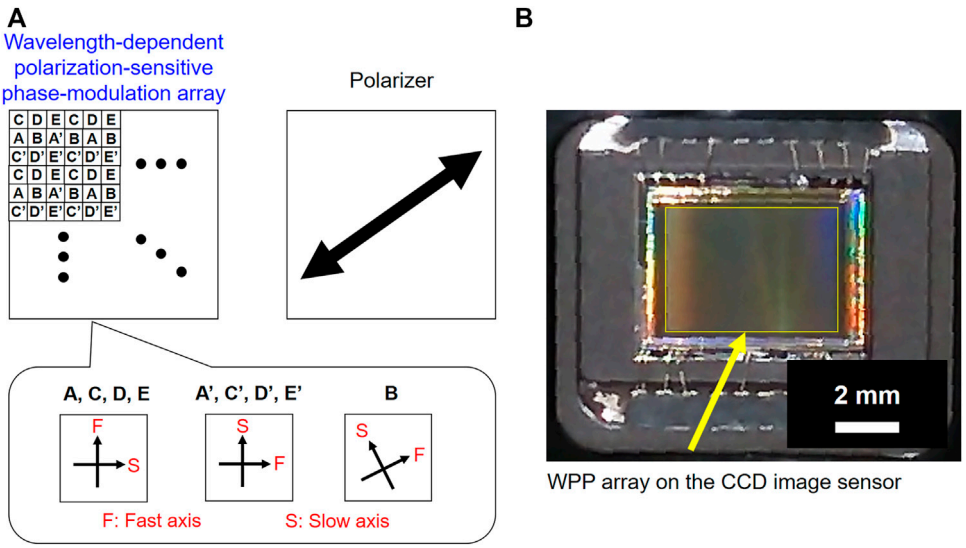

FIGURE 11 | WPP array and image sensor developed. **(A)** Schematic of the designed WPP array and **(B)** photograph of the CCD image sensor developed with the WPP array. Adapted with permission from (Tahara et al., 2020c)© AIP Publishing.

characteristics of various IDH techniques on tolerance against vibrations and information capacities for spatial, temporal, and wavelength imaging. Firstly, we discuss tolerance against vibrations and spatial and temporal information capacities. Spatial and temporal specifications of OSH depend on the range and speed of scan of illumination light and pitch of a GZP pattern. Tolerance against external vibrations is improved using a temporal heterodyne technique. CH is a spatially incoherent polarimetric phase-shifting DH technique. However, the use of a birefringent lens is not adopted. As a result, the resolution is limited although 3D imaging has been performed successfully. IDH has been implemented with various two-arm interferometers and many research achievements have been reported. However, tolerance against external vibrations is a problem. Coherence holography adopts Sagnac interferometer and is highly tolerant to external vibrations. Single-shot holographic imaging of spatially incoherent light has been demonstrated experimentally using an off-axis interferometer (Takeda et al., 2005; Naik et al., 2009) and therefore high temporal information capacity is obtained. On the other hand, spatial information capacity is limited owing to the use of an off-axis geometry. FINCH has clarified that, light sources with limited temporal coherency such as a lamp and an LED are recorded with a bandpass filter as holograms and in-plane PSF is improved at the cost of depth resolution. FINCH has been combined with PSI and off-axis holography. Therefore, spatial and temporal information capacities are flexibly designed. COACH improves depth resolution in comparison to self-interference DH with radial shearing. However, the acquisition of a PSF library on the measured 3D area is required. In IDH with a spatially incoherent light source containing single wavelength band, SSPS-IDH has contributed to the improvement of the product of spatial and temporal information capacities. Single-shot imaging can be conducted with an in-line configuration by using SSPS. In comparison to the off-axis geometry, space-bandwidth product (SBWP) is improved, and the visibility of interference fringes is improved by using an in-line configuration. As a result, field of view (FOV) extension owing to the increase of the SBWP and image-quality improvement owing to the enhancement of visibility are achieved in principle.

IDH for speckleless color holographic 3D imaging is a highly interested research theme. Using such an IDH technique, spatially and temporally incoherent light is recorded as incoherent hologram (s). Wavelength information is recorded using various wavelength-sensing techniques presented in DH (Tankam et al., 2010; Tahara et al., 2018b) and IDH adopts the techniques as shown in **Table 1**. Simultaneous RGB color sensing can be conducted using the principle of the Fourier spectroscopy. In OSH, when using a temporal heterodyne technique, different temporal frequencies of respective color GZP patterns are introduced and RGB information of the object is separated in the temporal frequency domain. The Fourier spectroscopy is also adopted to IDH with a two-arm interferometer. However, more than 250 exposures are required to conduct RGB color 3D imaging, and to reduce the number of exposures is a research problem when the number of the wavelength bands is small. FINCH adopts a diffractive phase lens and such a lens correctly works for the designed wavelength. Therefore, FINCH is not suitable for simultaneous multiwavelength measurement, and multiple bandpass filters and diffractive phase lenses are changed to obtain wavelength information sequentially. The filters should be sequentially changed using a filter wheel and this procedure loses temporal information capacity. The use of a color camera is straightforward and effective for color holographic imaging. On the other hand, spatial information capacity is partly lost when using a color camera with a color-filter

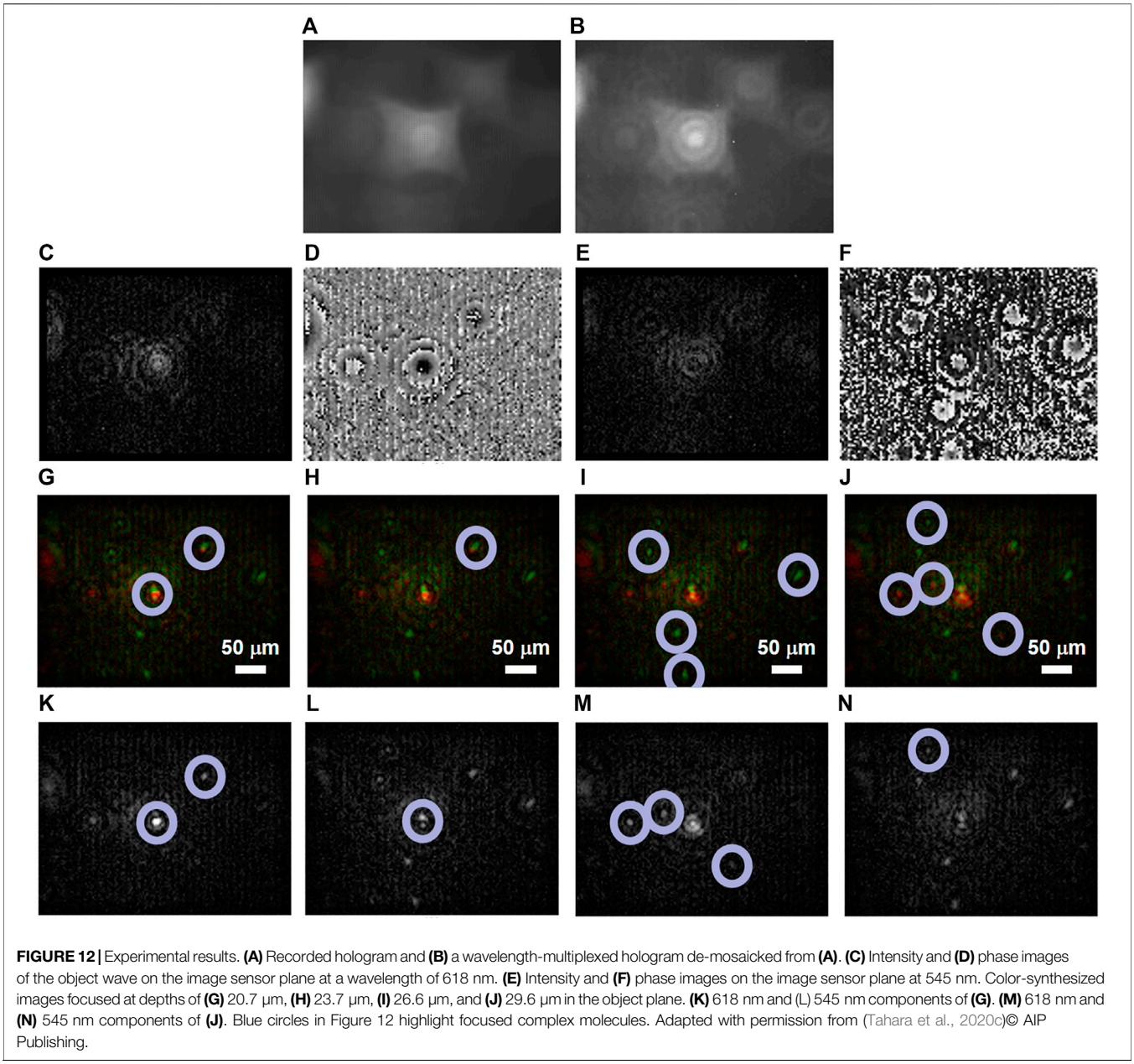

FIGURE 12 | Experimental results. **(A)** Recorded hologram and **(B)** a wavelength-multiplexed hologram de-mosaicked from **(A)**. **(C)** Intensity and **(D)** phase images of the object wave on the image sensor plane at a wavelength of 618 nm. **(E)** Intensity and **(F)** phase images on the image sensor plane at 545 nm. Color-synthesized images focused at depths of **(G)** 20.7 μm, **(H)** 23.7 μm, **(I)** 26.6 μm, and **(J)** 29.6 μm in the object plane. **(K)** 618 nm and (L) 545 nm components of **(G)**. **(M)** 618 nm and **(N)** 545 nm components of **(J)**. Blue circles in Figure 12 highlight focused complex molecules. Adapted with permission from (Tahara et al., 2020c)© AIP Publishing.

array. COACH utilizes wavelength dependency of a diffractive phase lens to separate wavelength information. The difference of the PSFs between different wavelength bands is used for the wavelength separation. FOV in the depth direction was limited but many researches are conducted to solve the problem. The main features of CCS-IDH are the single-path spectroscopic holographic interferometer with a phase modulator and wavelength separation with a small number of wavelength-multiplexed holograms. RGB holographic imaging has been conducted with seven wavelength-multiplexed holograms without a mechanical movement. The number of exposures is much less than that required for IDH adopting the Fourier spectroscopy when conducting RGB holographic imaging. Single-shot CCS is implemented using a WPP array, and temporal information capacity is enhanced at the partly cost of spatial information capacity owing to space-division multiplexing. In comparison to IDH using an RGB color camera, SS-CCS IDH can improve the SBWP available for recording an RGB object wave. This is because the number of multiplexing is reduced, and spatial density of respective phase-shifted holograms is increased.

However, there are problems to limit the specifications of CCS-IDH, SSPS-IDH, and SS-CCS IDH. The research topics of CCS-IDH are described in the **section 3.2.1**. CCS-IDH will proceed toward a highly stable hyperspectral holographic 3D imaging technique and a phase modulator to enhance the specification of the technique will be a key optical device. An advanced signal-processing algorithm in CCS is also important to

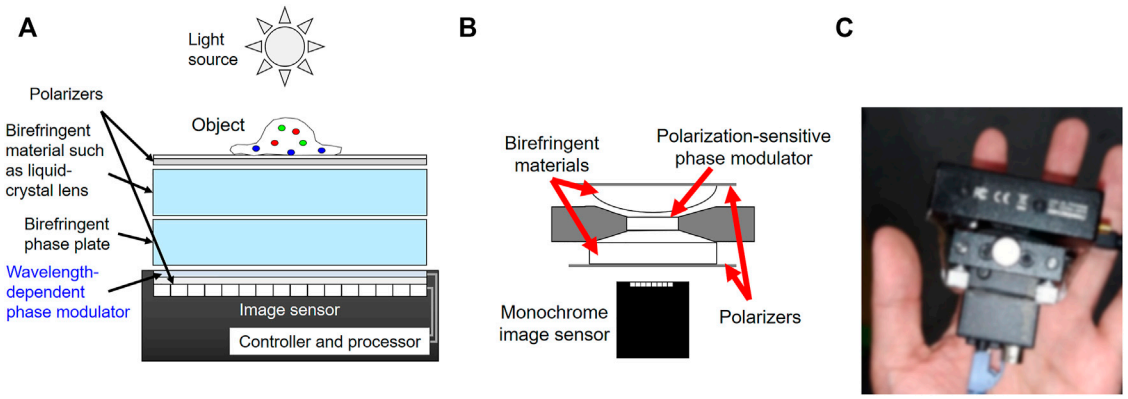

FIGURE 13 | Schematics of compact incoherent hologram recorders. **(A)** Basic concept of the ultimately compact chip-sized hologram recorder (Tahara et al., 2015b). **(B)** Design of a palm-sized hologram recorder "Holosensor" based on CCS-IDH. **(C)** Photograph of the initially developed CCS-holosensor.

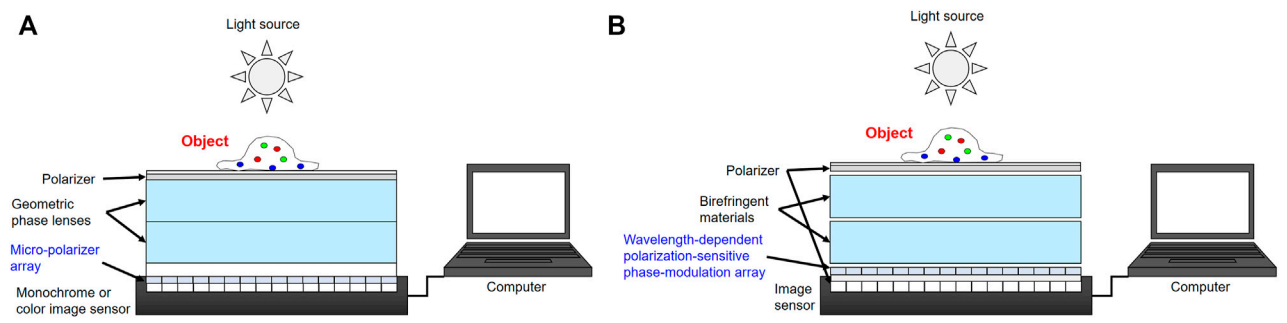

FIGURE 14 | Schematics of compact hologram recorders for single-shot multidimensional image sensing. The recorders are based on **(A)** SSPS-IDH and **(B)** SS-CCS.

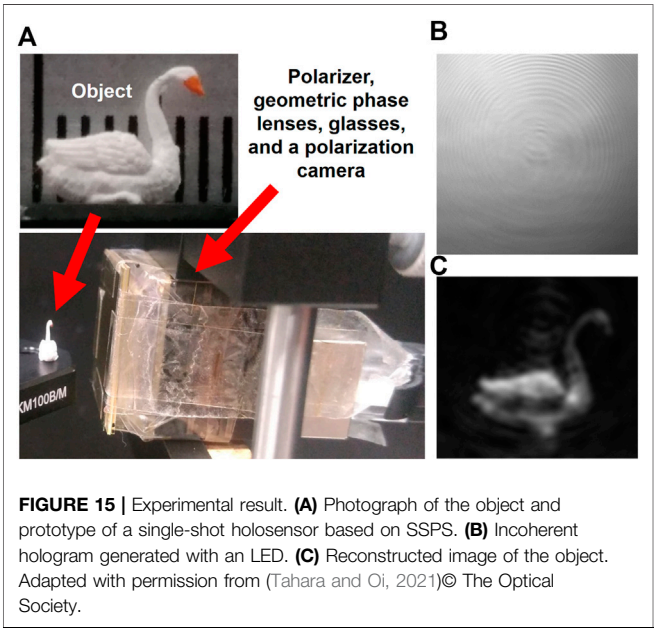

FIGURE 15 | Experimental result. **(A)** Photograph of the object and prototype of a single-shot holosensor based on SSPS. **(B)** Incoherent hologram generated with an LED. **(C)** Reconstructed image of the object. Adapted with permission from (Tahara and Oi, 2021)© The Optical Society.

enhance wavelength-sensing ability for IDH. In SSPS-IDH, a geometric phase lens is particularly useful for constructing a compact IDH system. A commercially available geometric phase lens is usable for white light. However, an undesired-order diffraction wave generated from the lens is not completely avoidable to date. Figure 9 shows an example. The residual light seen in the centers of **Figures 9A–G** is owing to the wave generated from the lens. Developments of some algorithms to remove such light are important to apply the SSPS-IDH system for scientific research. In SS-CCS IDH, the development of an advanced WPP array is important. Until now, it is difficult to attach an image sensor and a WPP array with a large number of cells and high spatial density.

Many IDH techniques have been proposed and developed as listed in **Table 1**. Experimental demonstrations of IDH techniques have been performed and various applications have been indicated with experimental results. However, researches and enhancements on IDH should be conducted toward applications to both scientific research and industry. Firstly, light-use efficiency should be improved toward the applications to fluorescence, Raman scattering, or other weak-

TABLE 1 | Comparisons of various IDH. *N* means the number of the wavelength bands measured.

	Tolerance against external vibrations	Monochrome imaging		Method to obtain wavelength information	RGB color imaging		Challenge to spectroscopic measurement
		Spatial information	Temporal information		Spatial information	Temporal information	
Optical scanning holography Poon and Korpel. (1979), Poon (1985)	High	Dependent on scan	Dependent on scan	Temporal frequency-division multiplexing	Dependent on scan	Dependent on scan	Requirement of multiple lasers
Conoscopic holography Sirat and Psaltis (1985), Mugnier and Sirat (1992), Mugnier et al. (1993), Mugnier (1995)	High	Difficulty in high resolution	Several exposures	—	—	—	—
IDH with a two-arm interferometer							
Rotational shearing Yoshimori (2001), Teeranutranont and Yoshimori (2013) and Mach-Zehnder-type Pedrini et al. (2012), Naik et al. (2014)	Low	Full bandwidth	Several exposures	Temporal frequency-division multiplexing	Full bandwidth	More than 250 exposures	Acceleration of the measurement
Michelson-type with a concave mirror Kim (2012), Kim (2013), Clark and Kim (2015)	Low	Full bandwidth	Several exposures	Color camera with a color-filter array	A quarter of full bandwidth	Several exposures	Requirement of hyperspectral camera
Off-axis Michelson-type with a concave mirror Hong and Kim (2013)	Low	A ninth of full bandwidth	Single-shot exposure	—	—	—	—
Coherence holography Takeda et al. (2005), Naik et al. (2009) that adopts Sagnac interferometer	High	A ninth of full bandwidth	Single-shot exposure	—	—	—	—
Fresnel incoherent correlation holography Rosen and Brooker (2007), Rosen et al. (2011), Rosen et al. (2019)	High	Full bandwidth and PSF improvement	Several exposures	Use of multiple bandpass filters	Full bandwidth	3*N*–4*N* exposures	Requirement of multiple filters
Fourier incoherent single channel holography Kelner and Rosen (2012) and single-shot off-axis FINCH Quan et al. (2017)	High	A ninth of full bandwidth	Single-shot exposure	—	—	—	—
Coded aperture correlation holography Vijayakumar et al. (2016), Vijayakumar and Rosen (2017)	High	Full bandwidth	Several exposures	PSF engineering and a diffractive phase lens	FOV limited in the depth direction	Several exposures	Requirement of additional/modified signal processing
CCS-IDH Tahara et al. (2019), Tahara et al. (2020b), Hara et al. (2020), Tahara et al. (2021a), Tahara et al. (2021b)	High	—	—	Wavelength-dependent phase shifts	Full bandwidth	2*N* + 1 exposures	Speed and range of phase modulation
SSPS-IDH Tahara et al. (2017a), Nobukawa et al. (2018), Choi et al. (2019), Tahara et al. (2020a), Liang et al. (2020)	High	A fourth of full bandwidth	Single-shot exposure	Color camera with a color-filter array	A 16th of full bandwidth	Single-shot exposure	Requirement of hyperspectral polarization-imaging camera
SS-CCS IDH Tahara et al. (2020c), Tahara et al. (2021)	High	—	—	Monochrome camera with a WPP array	A seventh of full bandwidth	Single-shot exposure	Development of an advanced WPP array

light nonlinear microscopy, and night-vision sensor. A polarimetric interferometer and a two-arm interferometer are frequently adopted in IDH. However, only a quarter of the intensity of the object wave can be utilized for the generation of an incoherent hologram in generally proposed IDH. An advanced optical system is effective for the improvement of the light-use efficiency. Furthermore, in the application to 3D fluorescence microscopy, light intensity is severely limited, and the number of photons in hologram recording should be considered when conducting holographic measurements. The importance of quantum optics on weak-light holographic sensing for the estimation of holographic measurement accuracy (Okamoto and Tahara, 2021) will be further increased, particularly in IDH. Image-quality improvement is also important research theme. In IDH, visibility of a recorded incoherent hologram decreases as the size of the object increases. An image sensor with high dynamic range is used to obtain a high-quality incoherent hologram. However, higher dynamic

range is required to record an incoherent hologram of larger size of the object. As another research problem, most of self-interference incoherent DH has the problem of the depth resolution. PSF of the IDH system is generally not the same as that of DH with a plane reference wave. This is because a spherical wave whose wavefront curvature depends on the depth position of the object point is used to generate interference fringes in IDH. COACH can obtain higher depth resolution than FINCH and other many self-interference IDH techniques. However, PSF library is required in advance. Depth-resolution improvement by a simple method will extend applicability of IDH. As a demonstration for the applicability of IDH to depth imaging, the generation of a depth map from the recorded incoherent hologram(s) is also highly desired research topic. Quantitative visualization of depth information as a depth map was not strongly required in the field of IDH. In contrast, such a depth map has been generated in laser DH by using quantitative phase information and phase unwrapping. The importance on the generation of a depth map will be increased to indicate applicability to other research fields such as 3D particle and flow measurements, 3D surface inspection, and machine vision. The problem on the depth resolution will be indicated when the generation of a depth map.

As an additional discussion, we analyze the composition of the CCS-holosensor. The CCS-holosensor shown in Figure 13 is the combinations of CH, single-path spectroscopy exploiting polarization (Ueda and Takuma, 1984), and a PSI technique. Instead of a Faraday rotator used in ref. (Ueda and Takuma, 1984), a liquid crystal phase retarder is utilized as a wavelength-dependent polarization-sensitive phase modulator. Using a liquid crystal, the CCS-holosensor can work with low voltage and without additional controller. Instead of the use of single-wavelength PSI in IDH, which has been successfully performed by CH and FINCH (Mugnier and Sirat, 1992; Mugnier et al., 1993; Mugnier, 1995; Rosen and Brooker, 2007), multidimensional-multiplexed PSI termed CCS is adopted to conduct simultaneous multiwavelength holographic image sensing without changing optical filters such as color filters. The proposed CCS-holosensor is based on many pioneers including Lohman's idea for the use of a birefringent dual-focus lens. Considering the applications, the CCS-holosensor will be effective particularly for holographic sensing of multicolor self-luminous light. This is because one of the merits in IDH is to be able to acquire digital holograms of self-luminous light such as fluorescence light, which was initially performed by Poon *et al.* with OSH. Furthermore, CCS can perform the recording of multicolor fluorescence light as wavelength-multiplexed fluorescence digital holograms with a monochrome image sensor and no change of wavelength filters. Therefore, the CCS-holosensor will be able to work as an ultimately compact holographic fluorescence microscopy system. As another aspect, the CCS-holosensor can work as a compact spectroscopic hologram recorder with self-luminous light including sunlight and Moon light. Compact IDH systems have been proposed using various IDH techniques, which is described in this review and ref. (Rosen et al., 2021). It is now possible to realize portable holographic imaging systems for sensing outdoor 3D scenes with IDH techniques. Using CCS-holosensor, spectroscopic holographic 3D imaging of outdoor 3D scenes will be realized without mechanically moving parts.

We have reviewed progress on IDH with an image sensor and its applications to microscopy and compact hologram recorders. Improvements of specifications such as measurement speed, image quality, and further downsizing are important next steps in IDH. Dynamic range, sensitivity, and low noise of an image sensor are now particularly important to obtain an incoherent digital hologram because the visibility and light intensity of such a hologram are lower than those of a hologram generated with a laser. Its importance on advanced digital signal processing techniques based on informatics such as deep learning and compressive sensing will also be increased (Wu et al., 2020; Wu et al., 2021). Algorithms for accelerating holographic image reconstruction are continuously developed and these will lead to real-time holographic measurement (Tsuruta et al., 2021; Shimobaba et al., 2022). Applications to the development of multidimensional imaging and measurement apparatus will be realized with the advancements in state-of-the art optics, photonics, optical devices, and information science.

AUTHOR CONTRIBUTIONS

The author has written the review article. The experimental results shown in this review article were obtained with the co-authors of the related papers.

FUNDING

This study is partially supported by The Mitsubishi Foundation (No. 202111007), Japan Science and Technology Agency (JST) Precursory Research for Embryonic Science and Technology (PRESTO) (JPMJPR16P8), Japan Society for the Promotion of Science (JSPS) (JP18H01456), and Cooperative Research Program of "Network Joint Research Center for Materials and Devices" (No. 20211086).

ACKNOWLEDGMENTS

TT sincerely thank co-workers and co-authors of the research studies related to this review.

REFERENCES

Awatsuji, Y., Sasada, M., and Kubota, T. (2004). Parallel Quasi-Phase-Shifting Digital Holography. *Appl. Phys. Lett.* 85, 1069–1071. doi:10.1063/1.1777796

Brooker, G., Siegel, N., Wang, V., and Rosen, J. (2011). Optimal Resolution in Fresnel Incoherent Correlation Holographic Fluorescence Microscopy. *Opt. Express* 19, 5047–5062. doi:10.1364/oe.19.005047

Bruning, J. H., Herriott, D. R., Gallagher, J. E., Rosenfeld, D. P., White, A. D., and Brangaccio, D. J. (1974). Digital Wavefront Measuring Interferometer for

Testing Optical Surfaces and Lenses. *Appl. Opt.* 13, 2693–2703. doi:10.1364/ao.13.002693

Choi, K., Yim, J., and Min, S.-W. (2018). Achromatic Phase Shifting Self-Interference Incoherent Digital Holography Using Linear Polarizer and Geometric Phase Lens. *Opt. Express* 26, 16212–16225. doi:10.1364/oe.26.016212

Choi, K., Joo, K.-I., Lee, T.-H., Kim, H.-R., Yim, J., Do, H., et al. (2019). Compact Self-Interference Incoherent Digital Holographic Camera System with Real-Time Operation. *Opt. Express* 27, 4818–4833. doi:10.1364/oe.27.004818

Clark, D. C., and Kim, M. K. (2015). Nonscanning Three-Dimensional Differential Holographic Fluorescence Microscopy. *J. Electron. Imaging* 24, 043014. doi:10.1117/1.jei.24.4.043014

Hara, T., Tahara, T., Ichihashi, Y., Oi, R., and Ito, T. (2020). Multiwavelength-multiplexed Phase-Shifting Incoherent Color Digital Holography. *Opt. Express* 28, 10078–10089. doi:10.1364/oe.383692

Hong, J., and Kim, M. K. (2013). Single-shot Self-Interference Incoherent Digital Holography Using off-axis Configuration. *Opt. Lett.* 38, 5196–5199. doi:10.1364/ol.38.005196

Imbe, M. (2019). Radiometric Temperature Measurement by Incoherent Digital Holography. *Appl. Opt.* 58, A82–A89. doi:10.1364/ao.58.000a82

Jang, C., Kim, J., Clark, D. C., Lee, S., Lee, B., and Kim, M. K. (2015). Holographic Fluorescence Microscopy with Incoherent Digital Holographic Adaptive Optics. *J. Biomed. Opt.* 20, 111204. doi:10.1117/1.jbo.20.11.111204

Kalenkov, S. G., Kalenkov, G. S., and Shtanko, A. E. (2019). Self-reference Hyperspectral Holographic Microscopy. *J. Opt. Soc. Am. A.* 36, A34–A38. doi:10.1364/josaa.36.000a34

Kelner, R., and Rosen, J. (2012). Spatially Incoherent Single Channel Digital Fourier Holography. *Opt. Lett.* 37, 3723–3725. doi:10.1364/ol.37.003723

Kim, M. K. (2012). Adaptive Optics by Incoherent Digital Holography. *Opt. Lett.* 37, 2694–2696. doi:10.1364/ol.37.002694

Kim, M. K. (2013). Full Color Natural Light Holographic Camera. *Opt. Express* 21, 9636–9642. doi:10.1364/oe.21.009636

Kumar, M., Quan, X., Awatsuji, Y., Cheng, C., Hasebe, M., Tamada, Y., et al. (2020). Common-path Multimodal Three-Dimensional Fluorescence and Phase Imaging System. *J. Biomed. Opt.* 25, 1–15. doi:10.1117/1.JBO.25.3.032010

Liang, D., Zhang, Q., Wang, J., and Liu, J. (2020). Single-shot Fresnel Incoherent Digital Holography Based on Geometric Phase Lens. *J. Mod. Opt.* 67, 92–98. doi:10.1080/09500340.2019.1695970

Liebel, M., Pazos-Perez, N., van Hulst, N. F., and Alvarez-Puebla, R. A. (2020). Surface-enhanced Raman Scattering Holography. *Nat. Nanotechnol.* 15, 1005–1011. doi:10.1038/s41565-020-0771-9

Liebel, M., Ortega Arroyo, J., Beltrán, V. S., Osmond, J., Jo, A., Lee, H., et al. (2020). 3D Tracking of Extracellular Vesicles by Holographic Fluorescence Imaging. *Sci. Adv.* 6, eabc2508. doi:10.1126/sciadv.abc2508

Liu, J.-P., Tahara, T., Hayasaki, Y., and Poon, T.-C. (2018). Incoherent Digital Holography: a Review. *Appl. Sci.* 8, 143. doi:10.3390/app8010143

Lohmann, A., and Bryngdahl, O. (1968). One-dimensional Holography with Spatially Incoherent Light. *J. Opt. Soc. Am.* 58, 625–628.

Lohmann, A. W. (1965). Wavefront Reconstruction for Incoherent Objects. *J. Opt. Soc. Am.* 55, 1555–1556. doi:10.1364/josa.55.1555_1

Marar, A., and Kner, P. (2020). Three-dimensional Nanoscale Localization of point-like Objects Using Self-Interference Digital Holography. *Opt. Lett.* 45, 591–594. doi:10.1364/ol.379047

Millerd, J., Brock, N., Hayes, J., Morris, M. N., Novak, M., and Wyant, J. (2004). Pixelated Phase-Mask Dynamic Interferometer. *Proc. SPIE* 5531, 304–314. doi:10.1117/12.560807

Mugnier, L. M., and Sirat, G. Y. (1992). On-axis Conoscopic Holography without a Conjugate Image. *Opt. Lett.* 17, 294–296. doi:10.1364/ol.17.000294

Mugnier, L. M., Sirat, G. Y., and Charlot, D. (1993). Conoscopic Holography: Two-Dimensional Numerical Reconstructions. *Opt. Lett.* 18, 66–68. doi:10.1364/ol.18.000066

Mugnier, L. M. (1995). Conoscopic Holography: toward Three-Dimensional Reconstructions of Opaque Objects. *Appl. Opt.* 34, 1363–1371. doi:10.1364/ao.34.001363

Naik, D. N., Ezawa, T., Miyamoto, Y., and Takeda, M. (2009). 3-D Coherence Holography Using a Modified Sagnac Radial Shearing Interferometer with Geometric Phase Shift. *Opt. Express* 17, 10633–10641. doi:10.1364/oe.17.010633

Naik, D. N., Pedrini, G., Takeda, M., and Osten, W. (2014). Spectrally Resolved Incoherent Holography: 3D Spatial and Spectral Imaging Using a Mach-Zehnder Radial-Shearing Interferometer. *Opt. Lett.* 39, 1857–1860. doi:10.1364/ol.39.001857

Nobukawa, T., Muroi, T., Katano, Y., Kinoshita, N., and Ishii, N. (2018). Single-shot Phase-Shifting Incoherent Digital Holography with Multiplexed Checkerboard Phase Gratings. *Opt. Lett.* 43, 1698–1701. doi:10.1364/ol.43.001698

Nobukawa, T., Katano, Y., Muroi, T., Kinoshita, N., and Ishii, N. (2019). Bimodal Incoherent Digital Holography for Both Three-Dimensional Imaging and Quasi-Infinite-Depth-Of-Field Imaging. *Sci. Rep.* 9, 3363. doi:10.1038/s41598-019-39728-8

Okamoto, R., and Tahara, T. (2021). Precision Limit for Simultaneous Phase and Transmittance Estimation with Phase-Shifting Interferometry. *Phys. Rev. A.* 104, 033521. doi:10.1103/physreva.104.033521

Pedrini, G., Li, H., Faridian, A., and Osten, W. (2012). Digital Holography of Self-Luminous Objects by Using a Mach-Zehnder Setup. *Opt. Lett.* 37, 713–715. doi:10.1364/ol.37.000713

Poon, T. C., and Korpel, A. (1979). Optical Transfer Function of an Acousto-Optic Heterodyning Image Processor. *Opt. Lett.* 4, 317–319. doi:10.1364/ol.4.000317

Poon, T.-C. (1985). Method of Two-Dimensional Bipolar Incoherent Image Processing by Acousto-Optic Two-Pupil Synthesis. *Opt. Lett.* 10, 197–199. doi:10.1364/ol.10.000197

Poon, T.-C. (2007). *Optical Scanning Holography with MATLAB*. New York: Springer.

Poon, T.-C. (2009). Optical Scanning Holography - A Review of Recent Progress. *J. Opt. Soc. Korea* 13, 406–415. doi:10.3807/josk.2009.13.4.406

Potcoava, M., Mann, C., Art, J., and Alford, S. (2021). Spatio-temporal Performance in an Incoherent Holography Lattice Light-Sheet Microscope (IHLLS). *Opt. Express* 29, 23888–23901. doi:10.1364/OE.425069

Quan, X., Matoba, O., and Awatsuji, Y. (2017). Single-shot Incoherent Digital Holography Using a Dual-Focusing Lens with Diffraction Gratings. *Opt. Lett.* 42, 383–386. doi:10.1364/ol.42.000383

Rosen, J., and Brooker, G. (2007). Digital Spatially Incoherent Fresnel Holography. *Opt. Lett.* 32, 912–914. doi:10.1364/ol.32.000912

Rosen, J., and Brooker, G. (2008). Non-scanning Motionless Fluorescence Three-Dimensional Holographic Microscopy. *Nat. Photon* 2, 190–195. doi:10.1038/nphoton.2007.300

Rosen, J., Siegel, N., and Brooker, G. (2011). Theoretical and Experimental Demonstration of Resolution beyond the Rayleigh Limit by FINCH Fluorescence Microscopic Imaging. *Opt. Express* 19, 26249–26268. doi:10.1364/oe.19.026249

Rosen, J., Vijayakumar, A., Kumar, M., Rai, M. R., Kelner, R., Kashter, Y., et al. (2019). Recent Advances in Self-Interference Incoherent Digital Holography. *Adv. Opt. Photon.* 11, 1–66. doi:10.1364/aop.11.000001

Rosen, J., Alford, S., Anand, V., Art, J., Bouchal, P., Bouchal, Z., et al. (2021). Roadmap on Recent Progress in FINCH Technology. *J. Imaging* 7, 197. doi:10.3390/jimaging7100197

Sato, T., Araki, T., Sasaki, Y., Tsuru, T., Tadokoro, T., and Kawakami, S. (2007). Compact Ellipsometer Employing a Static Polarimeter Module with Arrayed Polarizer and Wave-Plate Elements. *Appl. Opt.* 46, 4963–4967. doi:10.1364/ao.46.004963

Schilling, B. W., Poon, T.-C., Indebetouw, G., Storrie, B., Shinoda, K., Suzuki, Y., et al. (1997). Three-dimensional Holographic Fluorescence Microscopy. *Opt. Lett.* 22, 1506–1508. doi:10.1364/ol.22.001506

Shimobaba, T., Tahara, T., Hoshi, I., Shiomi, H., Wang, F., Hara, T., et al. (2022). Real-valued Diffraction Calculations for Computational Holography [Invited]. *Appl. Opt.* 61, B96–B102. doi:10.1364/ao.443439

Sirat, G., and Psaltis, D. (1985). Conoscopic Holography. *Opt. Lett.* 10, 4–6. doi:10.1364/ol.10.000004

Tahara, T., and Oi, R. (2021). Palm-sized Single-Shot Phase-Shifting Incoherent Digital Holography System. *OSA Continuum* 4, 2372–2380. doi:10.1364/osac.431930

Tahara, T., and Sato, I. (2019). "Single-shot Color Digital Holographic Microscopy with white Light," in Proceedings of 3D Image Conf. 2019, in Japanese, 4–1.

Tahara, T., Mori, R., Kikunaga, S., Arai, Y., and Takaki, Y. (2015). Dual-wavelength Phase-Shifting Digital Holography Selectively Extracting Wavelength

Information from Wavelength-Multiplexed Holograms. *Opt. Lett.* 40, 2810–2813. doi:10.1364/ol.40.002810

Tahara, T., Mori, R., Arai, Y., and Takaki, Y. (2015). Four-step Phase-Shifting Digital Holography Simultaneously Sensing Dual-Wavelength Information Using a Monochromatic Image Sensor. *J. Opt.* 17, 125707–126110. doi:10.1088/2040-8978/17/12/125707

Tahara, T., Kanno, T., Arai, Y., and Ozawa, T. (2017). Single-shot Phase-Shifting Incoherent Digital Holography. *J. Opt.* 19, 065705. doi:10.1088/2040-8986/aa6e82

Tahara, T., Otani, R., Omae, K., Gotohda, T., Arai, Y., and Takaki, Y. (2017). Multiwavelength Digital Holography with Wavelength-Multiplexed Holograms and Arbitrary Symmetric Phase Shifts. *Opt. Express* 25, 11157–11172. doi:10.1364/oe.25.011157

Tahara, T., Kikunaga, S., and Arai, Y. (2018). *Digital Holography Apparatus and Digital Holography Method*. Japanese patent No. JP6308594.

Tahara, T., Quan, X., Otani, R., Takaki, Y., and Matoba, O. (2018). Digital Holography and its Multidimensional Imaging Applications: a Review. *Microscopy* 67, 55–67. doi:10.1093/jmicro/dfy007

Tahara, T., Hara, T., Ichihashi, Y., Oi, R., and Ito, T. (2019). "Simultaneous Holographic Multicolor Sensing of Multiple Natural Light Sources Based on Computational Coherent Superposition," in *Proceedings of Optics and Photonics Japan 2019 (OPJ)* (in Japanese: Optical Society of Japan OSJ), PDP6.

Tahara, T., Ito, T., Ichihashi, Y., and Oi, R. (2020). "Single-shot Incoherent Digital Holographic Microscopy System without a Spatial Light Modulator," in *Digital Holography and Three-Dimensional Imaging 2020 (DH), OSA Technical Digest* (Optical Society of America). HF3D.5.

Tahara, T., Ito, T., Ichihashi, Y., and Oi, R. (2020). Single-shot Incoherent Color Digital Holographic Microscopy System with Static Polarization-Sensitive Optical Elements. *J. Opt.* 22, 105702. doi:10.1088/2040-8986/abb007

Tahara, T., Ito, T., Ichihashi, Y., and Oi, R. (2020). Multiwavelength Three-Dimensional Microscopy with Spatially Incoherent Light, Based on Computational Coherent Superposition. *Opt. Lett.* 45, 2482–2485. doi:10.1364/ol.386264

Tahara, T., Ishii, A., Ito, T., Ichihashi, Y., and Oi, R. (2020). Single-shot Wavelength-Multiplexed Digital Holography for 3D Fluorescent Microscopy and Other Imaging Modalities. *Appl. Phys. Lett.* 117, 031102. doi:10.1063/5.0011075

Tahara, T., Koujin, T., Matsuda, A., Ishii, A., Ito, T., Ichihashi, Y., et al. (2021). Incoherent Color Digital Holography with Computational Coherent Superposition for Fluorescence Imaging [Invited]. *Appl. Opt.* 60, A260–A267. doi:10.1364/ao.406068

Tahara, T., Kozawa, Y., Ishii, A., Wakunami, K., Ichihashi, Y., and Oi, R. (2021). Two-step Phase-Shifting Interferometry for Self-Interference Digital Holography. *Opt. Lett.* 46, 669–672. doi:10.1364/ol.414083

Tahara, T., Kozawa, Y., Koujin, T., Matsuda, A., and Oi, R. (2021). Incoherent Digital Holographic Microscopy for High-Speed Three-Dimensional Motion-Picture Sensing. *Proc. SPIE* 11898, 118980D. doi:10.1117/12.2599725

Tahara, T., Kozawa, Y., Matsuda, A., and Oi, R. (2021). Quantitative Phase Imaging with Single-Path Phase-Shifting Digital Holography Using a Light-Emitting Diode. *OSA Continuum* 4, 2918–2927. doi:10.1364/osac.435949

Tahara, T., Koujin, T., Matsuda, A., Kozawa, Y., and Oi, R. (2021e). "72 Fps Incoherent Two-Color Digital Motion-Picture Holography System for Fluorescence Cell Imaging," in *Digital Holography and Three-Dimensional Imaging 2021 (DH), OSA Technical Digest* (Optical Society of America). DTu6H.5. doi:10.1364/dh.2021.dtu6h.5

Tahara, T., Okamoto, R., Ishii, A., Kozawa, Y., Koujin, T., Matsuda, A., et al. (2021f). Phase-shifting Interferometry for Multidimensional Incoherent Digital Holography and toward Ultimately Low Light Sensing. *Proc. SPIE*, 1205752. doi:10.1117/12.2607197

Tahara, T., Kozawa, Y., and Oi, R. (2022). Single-path Single-Shot Phase-Shifting Digital Holographic Microscopy without a Laser Light Source. *Opt. Express* 30. (in press). 1182–1194. doi:10.1364/OE.442661

Tahara, T. (2021). Discussions and Visions for Multidimension-Multiplexed Incoherent Digital Motion-Picture Holography. *Rev. Laser Eng.* 49, 321–324.

Takeda, M., Wang, W., Duan, Z., and Miyamoto, Y. (2005). Coherence Holography. *Opt. Express* 13, 9629–9635. doi:10.1364/opex.13.009629

Tankam, P., Picart, P., Mounier, D., Desse, J. M., and Li, J.-C. (2010). Method of Digital Holographic Recording and Reconstruction Using a Stacked Color Image Sensor. *Appl. Opt.* 49, 320–328. doi:10.1364/ao.49.000320

Teeranutranont, S., and Yoshimori, K. (2013). Digital Holographic Three-Dimensional Imaging Spectrometry. *Appl. Opt.* 52, A388–A396. doi:10.1364/ao.52.00a388

Ting-Chung Poon, T. C., Ming Hsien Wu, M. H., Shinoda, K., and Suzuki, Y. (1996). Optical Scanning Holography. *Proc. IEEE* 84, 753–764. doi:10.1109/5.488744

Tsuruta, M., Fukuyama, T., Tahara, T., and Takaki, Y. (2021). Fast Image Reconstruction Technique for Parallel Phase-Shifting Digital Holography. *Appl. Sci.* 11, 11343. doi:10.3390/app112311343

Ueda, K., and Takuma, H. (1984). A Novel Spectrometric Technique Based on Fourier Transformation of Transmission Signal of Faraday Rotator. *Rev. Laser Eng.* 12, 41. (in Japanese). doi:10.2184/lsj.12.652

Vijayakumar, A., and Rosen, J. (2017). Spectrum and Space Resolved 4D Imaging by Coded Aperture Correlation Holography (COACH) with Diffractive Objective Lens. *Opt. Lett.* 42, 947–950. doi:10.1364/ol.42.000947

Vijayakumar, A., Kashter, Y., Kelner, R., and Rosen, J. (2016). Coded Aperture Correlation Holography-A New Type of Incoherent Digital Holograms. *Opt. Express* 24, 12430–12441. doi:10.1364/oe.24.012430

Wu, J., Zhang, H., Zhang, W., Jin, G., Cao, L., and Barbastathis, G. (2020). Single-shot Lensless Imaging with Fresnel Zone Aperture and Incoherent Illumination. *Light Sci. Appl.* 9, 53. doi:10.1038/s41377-020-0289-9

Wu, J., Cao, L., and Barbastathis, G. (2021). DNN-FZA Camera: a Deep Learning Approach toward Broadband FZA Lensless Imaging. *Opt. Lett.* 46, 130–133. doi:10.1364/ol.411228

Yamaguchi, I., and Zhang, T. (1997). Phase-shifting Digital Holography. *Opt. Lett.* 22, 1268–1270. doi:10.1364/ol.22.001268

Yanagawa, T., Abe, R., and Hayasaki, Y. (2015). Three-dimensional Mapping of Fluorescent Nanoparticles Using Incoherent Digital Holography. *Opt. Lett.* 40, 3312–3315. doi:10.1364/ol.40.003312

Yoneda, N., Saita, Y., and Nomura, T. (2021). Three-dimensional Fluorescence Imaging through Dynamic Scattering media by Motionless Optical Scanning Holography. *Appl. Phys. Lett.* 119, 161101. doi:10.1063/5.0066358

Yoshimori, K. (2001). Interferometric Spectral Imaging for Three-Dimensional Objects Illuminated by a Natural Light Source. *J. Opt. Soc. Am. A.* 18, 765–770. doi:10.1364/josaa.18.000765

Zhu, B., and Ueda, K.-i. (2003). Real-time Wavefront Measurement Based on Diffraction Grating Holography. *Opt. Commun.* 225, 1–6. doi:10.1016/j.optcom.2003.07.025

Conflict of Interest: The author declares that the research was conducted in the absence of any commercial or financial relationships that could be construed as a potential conflict of interest.

Publisher's Note: All claims expressed in this article are solely those of the authors and do not necessarily represent those of their affiliated organizations, or those of the publisher, the editors and the reviewers. Any product that may be evaluated in this article, or claim that may be made by its manufacturer, is not guaranteed or endorsed by the publisher.

frontiers in Photonics

ORIGINAL RESEARCH
published: 18 February 2022
doi: 10.3389/fphot.2022.848453

Elimination of Quadratic Phase Aberration in Digital Holographic Microscopy by Using Transport of Intensity

Wenjing Zhou[1], Shili Liu[1], Chen Wang[1], Hongbo Zhang[2], Yingjie Yu[1] and Ting-Chung Poon[3]*

[1]Department of Precision Mechanical Engineering, Shanghai University, Shanghai, China, [2]Department of Engineering Technology, Middle Tennessee State University, Murfreesboro, TN, United States, [3]Bradley Department of Electrical and Computer Engineering, Virginia Tech, Blacksburg, VA, United States

We propose to reconstruct 3D images by combining the merits of transport of intensity and digital holography. The proposed method solves the transport-of-intensity equation by using digital holographic reconstructed images as inputs. Our simulation and experimental results show that this method can eliminate quadratic phase aberration introduced by the microscope objective in digital holographic microscopy. This proposed phase retrieval method is free of phase unwrapping process. It is thus efficient in removing quadratic phase aberration introduced by the microscope objective.

Keywords: phase retrieval, aberration elimination, digital holography, transport of intensity, phase unwrapping

OPEN ACCESS

Edited by:
Yaping Zhang,
Kunming University of Science and Technology, China

Reviewed by:
Chao Zuo,
Nanjing University of Science and Technology, China
Naveen Nishchal,
Indian Institute of Technology Patna, India

****Correspondence:***
Wenjing Zhou
lazybee@shu.edu.cn

Specialty section:
This article was submitted to Optical Information Processing and Holography, a section of the journal Frontiers in Photonics

Received: *04 January 2022*
Accepted: *28 January 2022*
Published: *18 February 2022*

Citation:
Zhou W, Liu S, Wang C, Zhang H, Yu Y and Poon T-C (2022) Elimination of Quadratic Phase Aberration in Digital Holographic Microscopy by Using Transport of Intensity. Front. Photonics 3:848453. doi: 10.3389/fphot.2022.848453

1 INTRODUCTION

Holography was invented in 1948 by Dennis Gabor (1948) to improve the resolution of an electron microscope. Leith and Upatnieks (1964) proposed off-axis illumination with an off-axis reference beam, thus eliminating the spectral overlap of the zeroth-order beam and the twin image inherent in Gabor's in-line configuration. Schnars and Jüptner (1994) first used a CCD camera to capture a hologram and subsequently reconstruct the hologram numerically. They termed the technique as Digital Holography (DH).

In order to improve the transverse resolution of holographic measurements, digital holographic microscopy (DHM) was developed. In combination with microscopy, DHM provides label-free, quantitative phase imaging (Cuche et al., 1999; Mann et al., 2005). Even though DHM has significant advantages such as being simple, non-intrusive, and dynamic. However, quadratic phase aberration introduced by the microscope objective is a great issue (Zuo et al., 2013a). In addressing this issue, quadratic error compensation method has been applied (Zhou et al., 2009). It includes an optical design compensation (Rappaz et al., 2005) such as the use of a telecentric architecture (Sánchez-Ortiga et al., 2011) and a tunable lens compensation (Deng et al., 2017). The removal of quadratic phase aberration by software-based methods has also been investigated (Liu et al., 2018). Computer simulations of quadratic phase compensation (Colomb et al., 2006; Wang et al., 2019), least squares surface fitting compensation (Di et al., 2009), and automatic spectral energy analysis (Liu et al., 2014) have also been proven successfully. Most recently, deep learning compensation based on convolutional neural network has also shown great success (Nguyen et al., 2017). While these methods are promising, they mostly involve post processing steps for the quadratic phase removal, e.g., after holographic reconstruction. It is also feasible that intensity images can be reconstructed from a digital hologram to provide inputs for the transport-of-intensity equation

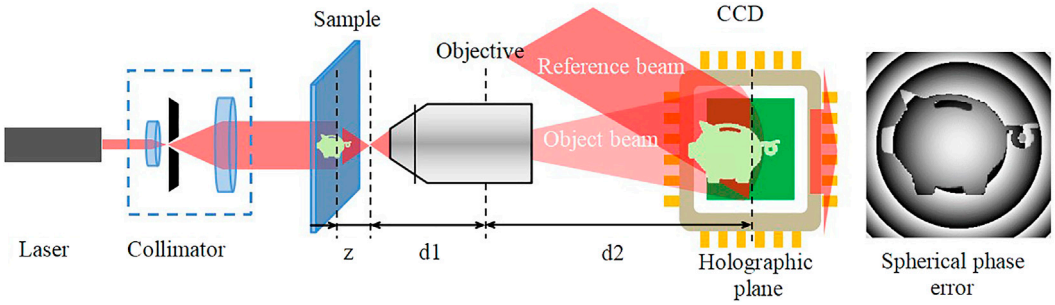

FIGURE 1 | Diagram of digital holographic plane microscopy.

(TIE) for unwrapped phase recovery. By doing this, we avoid shifting the sample or the camera in the experiment (Yan et al., 2019). In this research, we combine DH and TIE (DH-TIE) algorithm with regularization parameters. The TIE is a second-order elliptic partial differential equation for the phase φ. We use a fast method based on *FFT* to solve the TIE. Within the method of DH-TIE, a single hologram can provide phase retrieval without phase unwrapping (Zhou et al., 2018; Yan et al., 2019; Zuo et al., 2020; Lu et al., 2021).

Many scholars have combined digital holography and TIE in many applications. In the works by Zuo et al., TIE was invoked following the numerical reconstruction and propagation of the digital hologram, and the absolute phase without 2π discontinuities has been directly recovered (Zuo et al., 2013b). Whittkopp et al. described a microscopic setup implementing phase imaging by DHM and TIE, which allowed the results of both measurements to be quantitatively compared for either live cell or static samples (Wittkopp et al., 2020). Gupta et al. combined TIE with DH to overcome the artifacts caused by TIE phase recovery under low-light conditions by reconstructing the desired multiple out-of-focus intensity maps from the captured coaxial digital holograms (Gupta et al., 2020; Gupta and Nishchal, 2021). Kelly et al. (2013) compared Fresnel-based digital holography and phase retrieval from TIE. All these studies provide a lot of new ideas and methods for DH-TIE applications. In this paper, we employ the technique of DH-TIE to eliminate quadratic phase aberration introduced by a microscope objective in DHM. However, a suitable regularization parameter γ needs to be selected during the TIE phase retrieval process. By simulating the quadratic phase with different curvature factors, we provide some analysis for the appropriate selection of the regularization parameter. We will also present experimental results to verify our idea. In **Section 2**, we present some of the key formulas of the DH-TIE algorithm. In **Section 3**, a simulated phase object is used for the demonstration of the removal of quadratic phase aberration caused by a microscope objective in the DH system. In particular, we compare results using the DH-TIE and DH methods. We also analyze the effect of zero padding on phase retrieval. In **Section 4**, experimental results on a USAF resolution chart as a sample are presented to show the effectiveness of quadratic phase aberration removal. In the last section, we make some concluding remarks.

2 KEY FORMULAS OF DH-TIE ALGORITHM

In DH, a laser beam illuminates an object and the amplitude (A_o) and phase (φ_o) of the light waves on the holographic plane form the object wave are as follows:

$$O_o(x,y) = A_o(x,y)\,exp[i\varphi_o(x,y)]. \tag{1}$$

In DHM (**Figure 1**), the object wave is magnified on the holographic plane by a microscope objective (MO), and the image of the object beam satisfies the rule of lens imaging. The wavefront of the object wave therefore contains an additional quadratic phase aberration introduced by the microscope objective and is given by

$$O(x,y) = A_o\left(\frac{x}{M},\frac{y}{M}\right) exp\left[i\varphi_o\left(\frac{x}{M},\frac{y}{M}\right)\right] exp\left\{\frac{ik}{2\mu}\left[x^2+y^2\right]\right\}, \tag{2}$$

where M is the magnification of the microscope objective, μ is the radius of curvature of quadratic phase aberration (also called the quadratic phase aberration factor) introduced by the microscope objective, and k is the wave number of the laser. In off-axis holography, there is an angle between the reference beam and the holographic plane, which generates a linear phase reference wave on the holographic plane:

$$R(x,y) = A_r\,exp\left[ik\left(t_x x + t_y y\right)\right], \tag{3}$$

where t_x and t_y are the inclination factors along the x and y directions, respectively.

For off-axis holography, the digital hologram is generated through the interference between the object wave and the reference wave given by

$$H(x,y) = |R(x,y)|^2 + |O(x,y)|^2 + R^*(x,y)O(x,y) + R(x,y)O^*(x,y), \tag{4}$$

where $R^*(x,y)O(x,y)$ and $R(x,y)O^*(x,y)$ are the positive and negative first order images, respectively (Nguyen et al., 2017). We

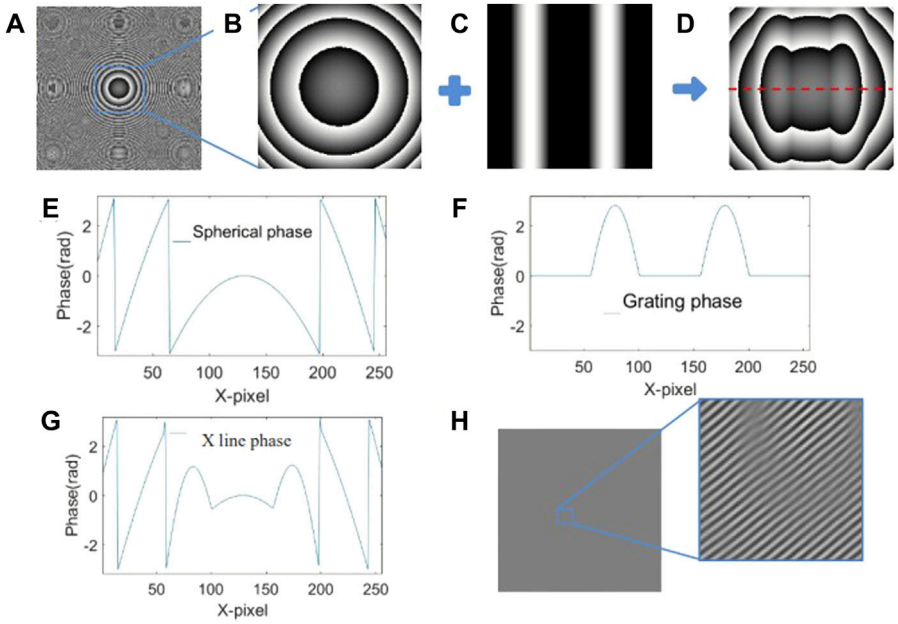

FIGURE 2 | Simulation of object wave and digital hologram. **(A)** Quadratic phase aberration simulated as the effect due to the microscope objective (wrapped), **(B)** Spherical phase map in center 256 × 256 region, **(C)** Object phase (sine grating function of two periods) located at the center of 256 × 256 region, **(D)** Wrapped phase map of quadratic phase combined with object. **(E)** Line trace of the quadratic phase extracted from the red line in **(B)**. **(F)** Line trace of the sine grating object from **(C)**, **(G)** Line trace of the combined phase extracted from the red line of **(D)**. **(H)** Simulated off axis digital hologram map with 50 mm recording distance.

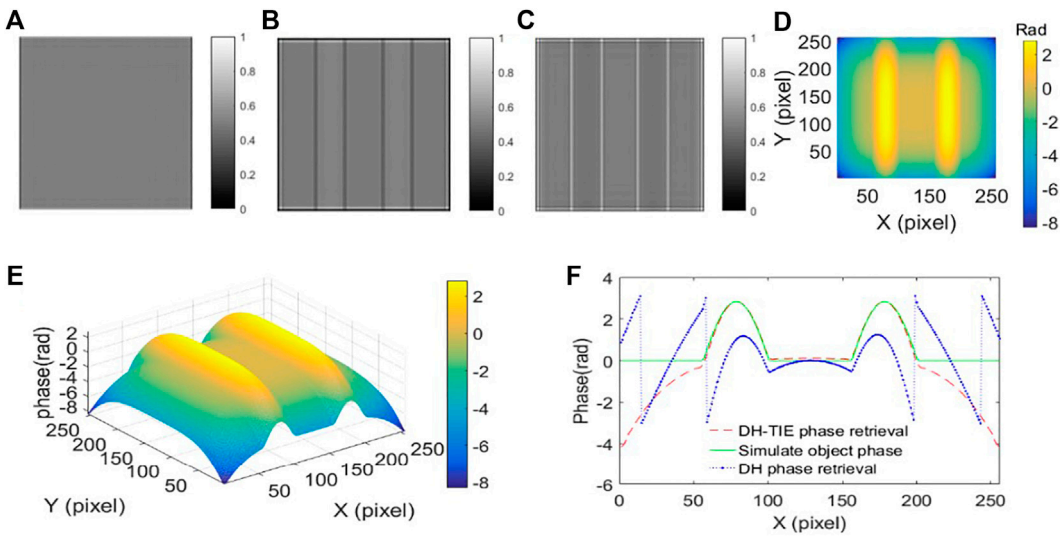

FIGURE 3 | Holographic reconstruction intensity images and TIE phase retrieval results. **(A)** Reconstruction intensity image (256 × 256 size of the center of the region) with 50 mm reconstruction distance. **(B)** Reconstruction intensity image with 49 mm reconstruction distance. **(C)** Reconstruction intensity image with 51 mm reconstruction distance. **(D)** Phase retrieval by DH-TIE with 1 mm Δz (vertical view). **(E)** 3D profile view of **(D)**. **(F)** Line traces of simulated object (Green), DH (Blue) and DH-TIE (Red) retrieval phase.

have used a Fourier spectrum window filter to extract the positive first order image of the hologram. Moreover, the tilted phase (with factors t_x, t_y) of the reference light can be eliminated by a Fourier frequency shift. The distribution of the filtered complex amplitude ($H^F(x, y)$) on the holographic plane is then given by

$$H^F(x,y) = F^{-1}\left\{F^{filter}\left[R^*(x,y)\cdot O(x,y)\right]\right\} = A_r A_0\left(\frac{x}{M},\frac{y}{M}\right) exp\left[i\varphi_0\left(\frac{x}{M},\frac{y}{M}\right)\right] exp\left[\frac{ik}{2\mu}\left(x^2+y^2\right)\right]. \quad (5)$$

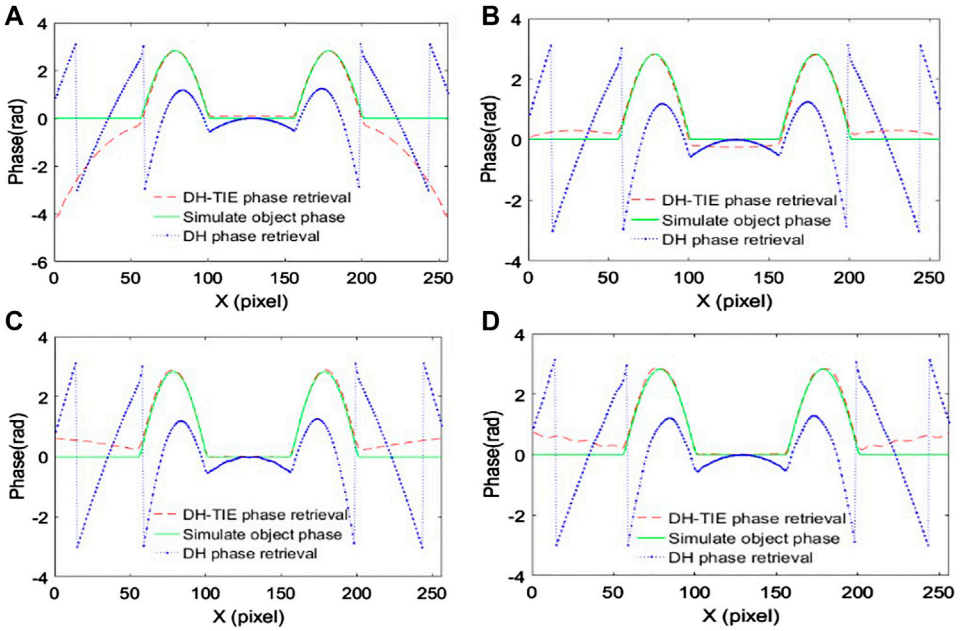

FIGURE 4 | Reconstruction under zero padding of different sizes and the line traces of simulated object (Green), DH (Blue) and DH-TIE (Red) phase retrieval. Reconstruction intensity images are with Δz = 1 mm. **(A)** The image file is 256 × 256. **(B)** The image file is 512 × 512. **(C)** The image file is 768 × 768. **(D)** The image file is 1,024 × 1,024.

Finally, the complex amplitude distribution of the original sample needs to be calculated by a convolution formula under paraxial approximations based on Kirchhoff scalar diffraction (Poon and Liu, 2014). The diffraction process can be regarded as a linear and space invariant system. After illuminating the hologram with $\boldsymbol{R}$. The reconstructed image is given by

$$\boldsymbol{O}'(\boldsymbol{x},\boldsymbol{y}) = \int\int \boldsymbol{R}\cdot\boldsymbol{H}^{\boldsymbol{F}}\cdot\boldsymbol{g}_{\boldsymbol{z}}(\boldsymbol{x}-\boldsymbol{x}_{\boldsymbol{z}},\boldsymbol{y}-\boldsymbol{y}_{\boldsymbol{z}};\boldsymbol{z})d\boldsymbol{x}_{\boldsymbol{z}}d\boldsymbol{y}_{\boldsymbol{z}}, \quad (6)$$

where

$$\boldsymbol{g}_{\boldsymbol{z}}(\boldsymbol{x},\boldsymbol{y};\boldsymbol{z}) = \frac{1}{\boldsymbol{i}\boldsymbol{\lambda}}\frac{\boldsymbol{exp}\left(\boldsymbol{ik}\sqrt{\boldsymbol{x}^2+\boldsymbol{y}^2+\boldsymbol{z}^2}\right)}{\sqrt{\boldsymbol{x}^2+\boldsymbol{y}^2+\boldsymbol{z}^2}}, \quad (7)$$

is the point spread function in free space. Note that the quadratic phase aberration, $\boldsymbol{exp}\{\frac{\boldsymbol{ik}}{2\boldsymbol{\mu}}[\boldsymbol{x}^2+\boldsymbol{y}^2]\}$, is contained in $\boldsymbol{H}^{\boldsymbol{F}}$. The angular spectrum numerical propagation method is used to propagate a small distance Δz, the value of Δz cannot be too small in the case of intensity measurement noise, otherwise the differential estimation of the light intensity will be drowned by the noise. However, when the value of Δz is too large, the phase ambiguity effect will become more obvious. In light of this, we choose Δz between the intensity measurement noise and nonlinear error as follows:

$$\frac{\boldsymbol{k\sigma}}{\sqrt{2}\boldsymbol{I}\nabla^2\boldsymbol{\varphi}} < \Delta\boldsymbol{Z} \ll \frac{1}{\boldsymbol{\pi\lambda f}_{\boldsymbol{max}}^2}, \quad (8)$$

where $\boldsymbol{I}(\boldsymbol{x},\boldsymbol{y};\boldsymbol{z})$ is the intensity distribution around the image plane, and $\boldsymbol{\varphi}(\boldsymbol{x},\boldsymbol{y};\boldsymbol{z})$ is the corresponding phase distribution of the phase object. The upper limit of the defocused distance is determined by the highest spatial frequency of the object $\boldsymbol{f}_{\boldsymbol{max}}$, and the lower limit is determined by the intensity measurement noise (assuming Gaussian noise of standard deviation $\boldsymbol{\sigma}$). The next two defocused intensities from the focal plane are generated by the angular spectrum method (ASM) numerically, giving $\mathbf{I}(\mathbf{x},\mathbf{y};\mathbf{z}+\boldsymbol{\Delta}\mathbf{z})$ and $\mathbf{I}(\mathbf{x},\mathbf{y};\mathbf{z}-\boldsymbol{\Delta}\mathbf{z})$. The two intensities are used as input data to solve the TIE. The axial differential intensity $\frac{\partial \mathbf{I}}{\partial \mathbf{Z}}$ is estimated by the following central finite difference method:

$$\frac{\partial \boldsymbol{I}}{\partial \boldsymbol{Z}} \approx \frac{\boldsymbol{I}(\boldsymbol{x},\boldsymbol{y};\boldsymbol{z}+\Delta\boldsymbol{z})-\boldsymbol{I}(\boldsymbol{x},\boldsymbol{y};\boldsymbol{z}-\Delta\boldsymbol{z})}{2\Delta\boldsymbol{z}}. \quad (9)$$

Figure 1 shows a diagram of the digital holographic microscopy system. The laser passes through the beam collimator and is divided into two beams, one of which passes through the object sample and is magnified by the microscope, and the other, which does not pass through the object, is served as a reference beam at the CCD to obtain the hologram of the sample. Furthermore in **Figure 1**, z is the reconstruction distance, d1 is the object distance, and d2 is the image distance.

The transport-of-intensity equation (TIE) is an elliptic partial differential equation (Zuo et al., 2014). In order to improve the speed of solving the equation, it can be approximated by the following Poisson equation:

$$\nabla(\boldsymbol{I}\nabla\boldsymbol{\varphi}) = -\frac{2\boldsymbol{\pi}}{\boldsymbol{\lambda}}\frac{\partial \boldsymbol{I}}{\partial \boldsymbol{z}}, \quad (10)$$

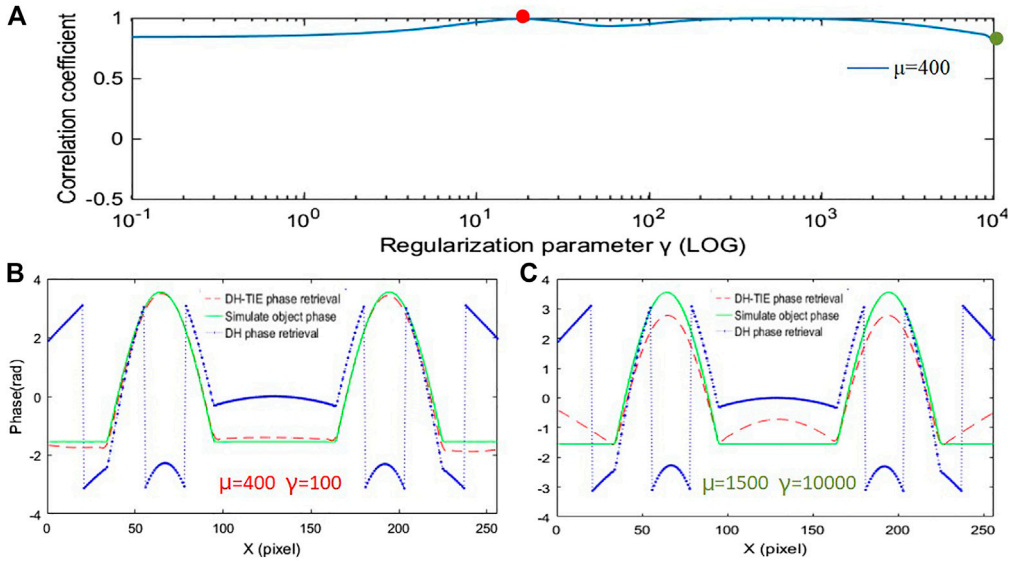

FIGURE 5 | (A) Correlation coefficient plots corresponding to different regularization parameters when the quadratic phase aberration factor μ = 400. **(B)** Reconstruction results, line traces when the value of the regularization parameter γ is taken as 100. **(C)** Reconstruction results, line traces when the value of the regularization parameter γ is taken as 10,000.

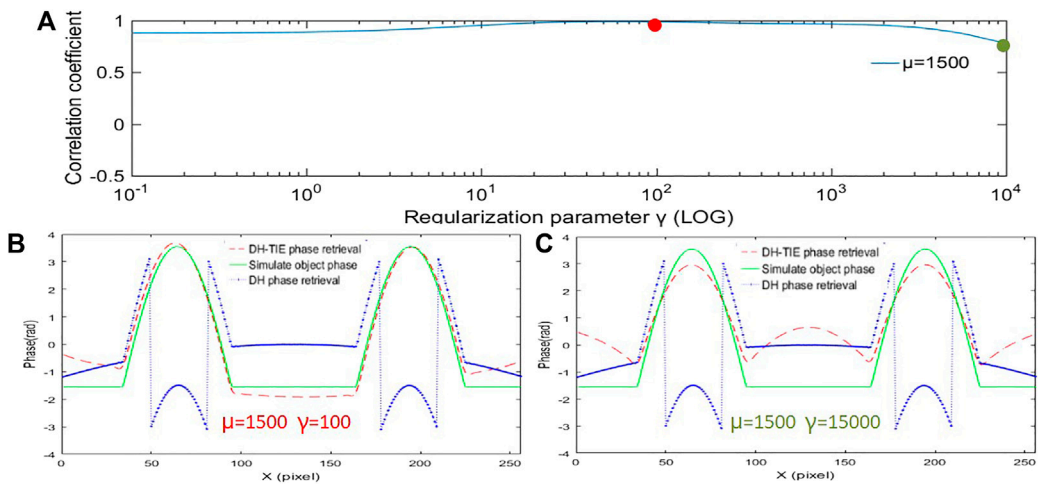

FIGURE 6 | (A) Correlation coefficient plots corresponding to different regularization parameters when the quadratic phase aberration factor μ = 1,500. **(B)** Reconstruction results, line traces when the value of the regularization parameter γ is taken as 100. **(C)** Reconstruction results, line traces when the value of the regularization parameter γ is taken as 15,000.

where $\frac{\partial I}{\partial Z}$, as shown in **Eq. 9**, can be approximated as the difference of defocused image intensities in two planes. The phase of the object can be reconstructed using the FFT-based Poisson solver (Teague, 1983; Zhou et al., 2018):

$$\boldsymbol{\varphi} = \mathcal{F}^{-1}\left\{\frac{f_x^2 + f_y^2}{\left(f_x^2 + f_y^2\right)^2 + \boldsymbol{\gamma}}\mathcal{F}\left\{\frac{\boldsymbol{k}}{\boldsymbol{I_o}}\cdot\frac{\partial \boldsymbol{I}}{\partial \boldsymbol{z}}\right\}\right\}, \tag{11}$$

where $\mathcal{F}$ and $\mathcal{F}^{-1}$ denotes forward and inverse Fourier transform notations, respectively. $\boldsymbol{\gamma}$ is the regularization parameter, an important factor under the Tikhonov-regularization treatment. $\boldsymbol{f_x}$ and $\boldsymbol{f_y}$ are the spatial frequencies in the $\boldsymbol{x}$ and $\boldsymbol{y}$ directions, respectively. $\boldsymbol{I_o}$ is the intensity distribution at the focused plane and usually can be taken as the average intensities of the two defocused planes. Since the TIE is being solved using Fourier transforms, the boundary conditions are implicitly assumed as the same as that for the existence of the Fourier transform of the function (Banerjee, 2022). The Tikhonov-regularization treatment is commonly used to remove very low frequency artifacts, and

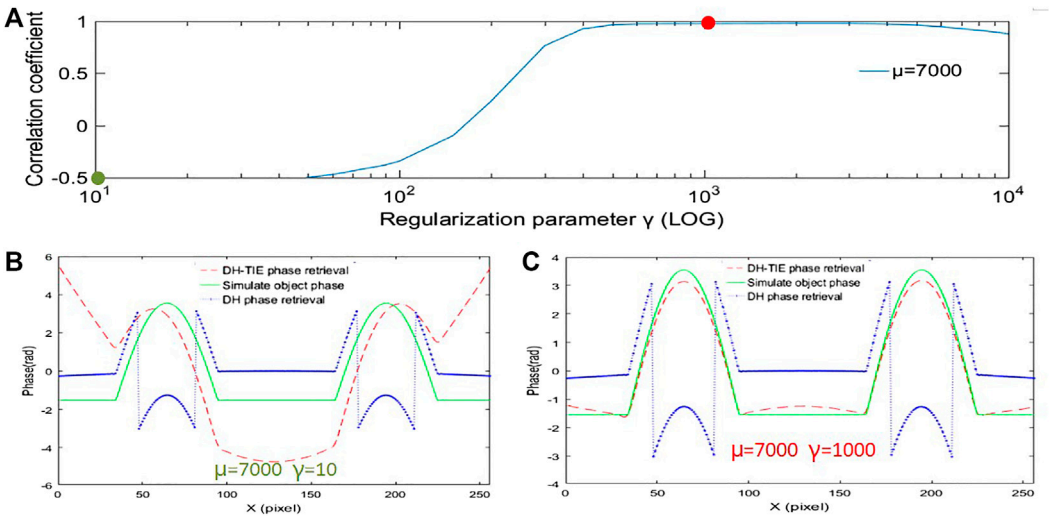

FIGURE 7 | (A) Correlation coefficient plots corresponding to different regularization parameters when the quadratic phase aberration factor μ = 7,000. **(B)** Reconstruction results, line traces when the value of the regularization parameter is taken as 10. **(C)** Reconstruction results when taking the red point in **(A)**, line trace when the value of the regularization parameter is taken as 1,000.

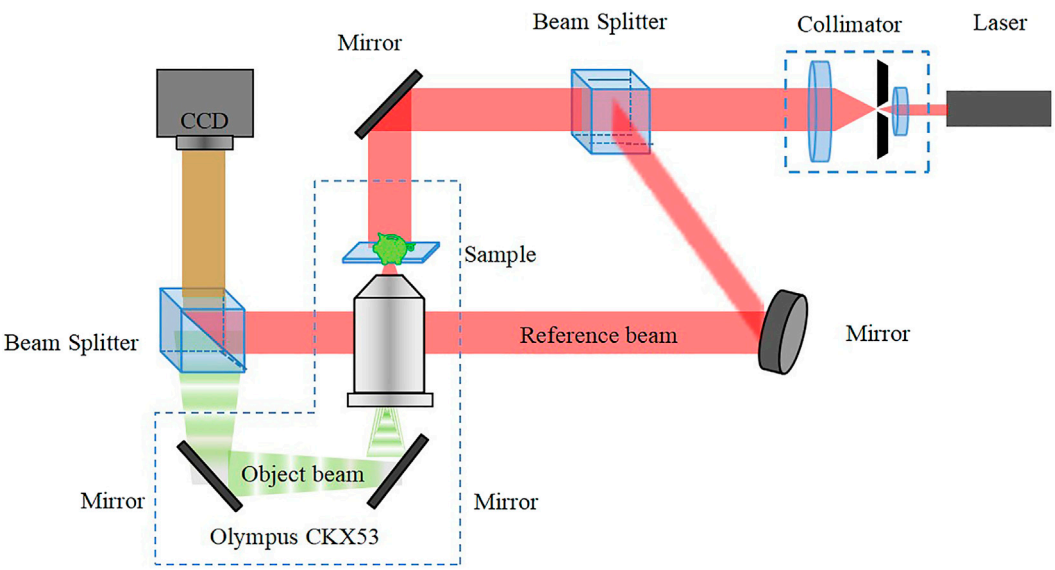

FIGURE 8 | Diagram of off-axis digital holographic microscopy system setup.

in the next Sections, we will demonstrate that the treatment can also filter out the slowly varying feature corresponding to spherical phase aberration introduced by the microscope objective in the DH system.

3 SIMULATION ANALYSIS

We have simulated a sine grating as a sample. The sinusoidal grating is expressed as follows:

$$t(x,y) = \begin{cases} e^{j\sin \omega x} & \sin \omega x > 0 \\ 0 & \sin \omega x \le 0 \end{cases}. \quad (12)$$

The wavelength used is 632.8 *nm*. The square size of the hologram is 1,024 pixels ×1,024 pixels with the pixel size of 4.65 μm. The defocused distances are Δz = ±1 mm. Quadratic phase aberration with spherical factor μ = 150 is shown in **Figure 2A**. We add quadratic phase aberration on the object phase (sine grating of two periods) shown in **Figure 2C**, to simulate the object after imaged by the microscope objective, as

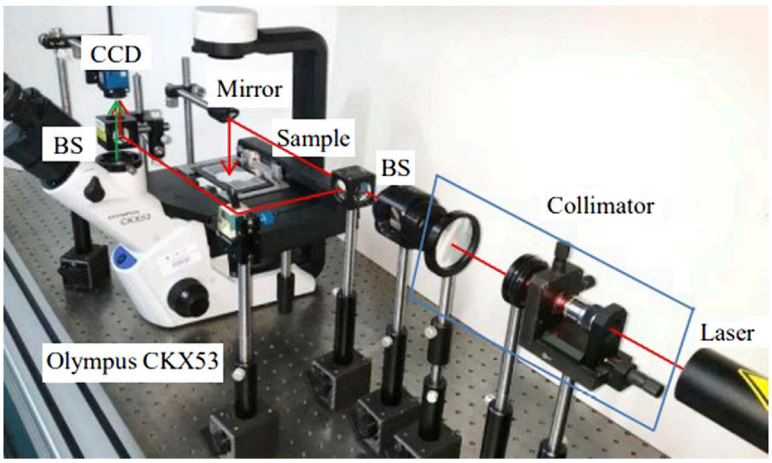

FIGURE 9 | Experimental setup diagram of off-axis digital holographic microscopy system.

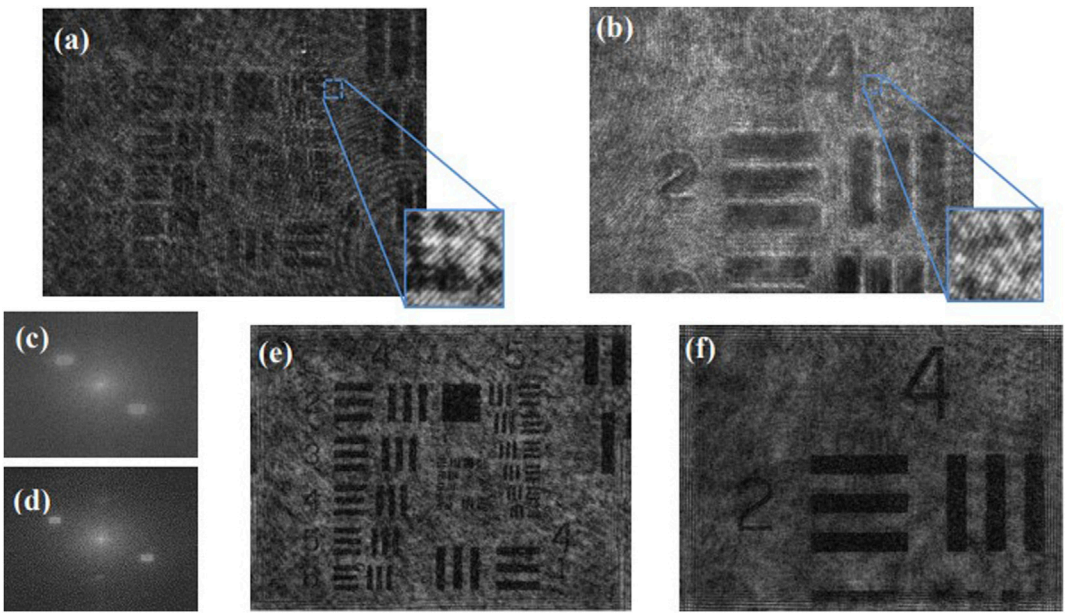

FIGURE 10 | Recorded holograms, two-dimensional spectra and reconstructed intensity images. **(A)** Hologram under X4 MO with 20 mm recording distance, **(B)** Hologram under ×10 MO with 30 mm recording distance, **(C,D)** are the two-dimensional spectra of holograms **(A,B)**, respectively, **(E)** Focused intensity reconstructed image of **(A)**, **(F)** Focused intensity reconstructed image of **(B)**.

shown in **Figure 2D**. **Figure 2E** is a line trace across center of wrapped quadratic phase aberration from **Figure 2B**. **Figure 2F** is the line trace of the object phase from **Figure 2C**. **Figure 2G** shows the line trace of the wrapped object phase mixed with quadratic phase aberration. An off-axis reference beam is simulated to interfere with the aberrated object complex amplitude. The digital hologram is shown in **Figure 2H**, with 50 mm recording distance and the zeroth-order term in the hologram has been eliminated. The complex amplitude distributions of the focal plane and the defocused planes can be obtained by multiplying the digital hologram with the reconstructed reference light and perform the convolution reconstruction process for different distances.

As shown in **Figures 3A–C**, in the holographic reconstruction process, the simulated phase of the object wave modulates the intensity image, but quadratic phase aberration added to the object only affects the boundary region of the phase retrieval. **Figure 3A** is the intensity image with 50 mm reconstruction distance equal to the recording distance. **Figures 3B,C** are the intensity image with 49 and 51 mm reconstruction distance, respectively. We solve the TIE to calculate the object phase with three intensity images. **Figures 3D,E** show the phase retrieval by DH-TIE with Δz = ±1 mm from vertical view and the 3-D profile view, respectively. In general, we observe that the center area of phase retrieval yields fairly accurate results. Around the boundary region phase retrieval

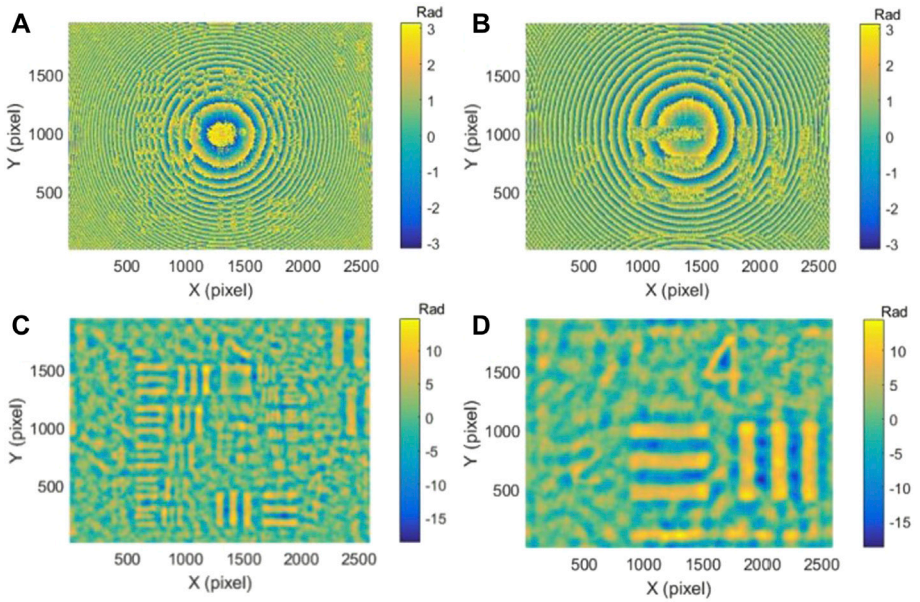

FIGURE 11 | Phase retrievals of DH and DH-TIE. **(A,B)** are the DH phase map retrievals from **Figures 10A,B**, respectively. **(C,D)** are the DH-TIE phase map retrievals from **Figures 10A,B**.

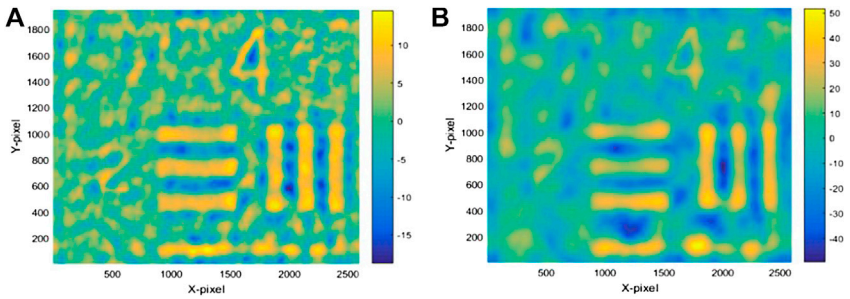

FIGURE 12 | Phase retrievals of DH-TIE under ×10 MO. **(A)** Phase map retrieval when γ = 1,000 **(B)** Phase map retrieval when γ = 10,000.

is, however, associated with large errors as evidenced by **Figure 3F**, where we present line traces of simulated object (Green), DH (Blue) and DH-TIE (Red) phase results.

As it turns out, the DH-TIE phase retrieval is improved drastically by zero padding. We summarize the results in **Figure 4**. In **Figure 4A**, we have used a 256 × 256 image. In **Figures 4B–D**, we perform zero padding on the image file in **Figure 4A** to have 512 × 512, 768 × 768, 1,024 × 1,024 image files, respectively. It is evident that phase retrieval of using 512 × 512, 768 × 768, 1,024 × 1,024 image files are better than that from the 256 × 256 image file, and the reconstruction effect of 512 × 512 image file is the best among them. It is also clear that quadratic phase aberration added to the object does not impact phase retrieval using the DH-TIE method. Simulation results show that the DH-TIE method can effectively eliminate quadratic phase aberration in DHM, greatly simplifying the phase reconstruction process of real objects. Zero padding provides a larger uniform background on the original image file and can achieve better retrieval results.

We also study the reconstruction effectiveness due to the regularization parameter under different severities of quadratic phase aberration. A two-dimensional correlation coefficient $\boldsymbol{r}(\boldsymbol{A},\boldsymbol{B})$ can effectively represent the similarity between the retrieved phase and the original phase (ground truth) and it is given by

$$\boldsymbol{r}(\boldsymbol{A},\boldsymbol{B}) = \frac{\sum_m \sum_n \left(\boldsymbol{A}_{mn} - \bar{\boldsymbol{A}}\right)\left(\boldsymbol{B}_{mn} - \bar{\boldsymbol{B}}\right)}{\sqrt{\left(\sum_m \sum_n \left(\boldsymbol{A}_{mn} - \bar{\boldsymbol{A}}\right)\right)^2 \left(\sum_m \sum_n \left(\boldsymbol{B}_{mn} - \bar{\boldsymbol{B}}\right)\right)^2}}, \qquad (13)$$

where $\boldsymbol{A}$, $\boldsymbol{B}$ are two arrays in the same size, $\bar{\boldsymbol{A}}$ is the mean of $\boldsymbol{A}$, and $\bar{\boldsymbol{B}}$ is the mean of $\boldsymbol{B}$. When the correlation coefficient is closer to one, DH-TIE achieves better phase reconstruction. **Figure 5A** shows that when the quadratic phase aberration factor μ = 400, the correlation coefficient is higher when the regularization parameter is 100–1,000, and the reconstruction effect is better. When the regularization parameter is 0.1–90 or more than 1,000, the correlation coefficient becomes lower with adverse reconstruction quality. **Figure 6A** shows that when the

quadratic phase aberration factor μ = 1,500, the regularization parameter is optimized around 100. **Figure 7A** shows that when the quadratic phase aberration factor μ = 7,000, the regularization parameter is optimized around 1,000.

4 EXPERIMENT AND RESULTS

To verify the effectiveness of the proposed method, a DHM system of off-axis Mach-Zehnder interferometer combined with an inverted microscopy (Olympus CKX53) has been constructed. The wavelength of He-Ne laser source (Da Heng DH-NH250) is 632.8 nm*nm*. The resolution of the CCD (Da Heng MER-500-7UM) is 2592(H)×1944(V) with single pixel size 2.2 $\mu m \times 2.2\ \mu m$. The off-axis digital holographic system setup is shown in **Figure 8**.

A collimated laser beam is divided into two beams after passing through a laser collimator and a beam-splitting prism. One of the beams is reflected by a reflector mirror and modulated by the sample phase to become the object beam, where the object wavefront (green) is magnified by an Olympus microscope and diffracted onto the CCD plane. The other beam is used as the reference light. An off-axis angle between the two beams is created to form an interference between the object and reference light waves on the CCD plane.

The actual off-axis digital holographic system is shown in **Figure 9**. The light beam emitted by the laser passes through a collimator and then passes through a beamsplitter (BS) which is divided into an object beam and a reference beam. The object beam passes through another beamsplitter and passes down through the object and the microscope, while the reference beam passes through the two beamsplitters and is incident onto the CCD together with the object beam (green arrow) to form an interference beam. In the system, the laser enters the Olympus microscope through a mirror, and by this way, the laser replaces the original light source of the microscope with vertical incidence, and the inverted microscope has been used to form a post-amplification digital holographic microscope. The merit of using an inverted microscope is that the microscope objective lens can be flexibly switched to change the magnification of the system.

We have obtained the holograms of a USAF 1951 resolution chart (Edmund Optics) using the holographic microscope. The digital holograms that we have captured under ×4 and ×10 microscope objectives are shown in **Figures 10A,B**, respectively. **Figures 10C,D** are the spectra of these two holograms, respectively, and **Figures 10E,F** are the focused intensity reconstructed images of **Figures 10A,B**, respectively.

In the DH-TIE phase retrieval process, we have used a focused image and two defocused images with 1 mm away from the focused image. We have reconstructed two holograms (**Figures 10A,B**) by the DH and DH-TIE methods. **Figures 11A,B** are the DH retrieved phase, and **Figures 11C,D** are the DH-TIE retrieved phase. In the DH-TIE phase reconstruction, the regulation parameter has been set to 5,000.

It can be seen in **Figures 11A,B** that quadratic phase aberration is sharp in the DH reconstruction. Quadratic phase aberration introduced by the microscope objective is so strong that the phase information of the objects have been completely buried. Under the ×4 and ×10 microscope objective, quadratic phase aberration has different curvatures. The quadratic phase factor in **Figure 11A** is μ = 200, and the quadratic phase factor in **Figure 11B** is μ = 400. This problem does not exist in the phase retrieval process using DH-TIE as quadratic phase aberration has been eliminated and the object phase has been retrieved successfully as shown in **Figures 11C,D**. In order to verify the effect of different regularization parameters on the reconstruction phase, we compare reconstructions when γ = 1,000 and γ = 10,000 under the ×10 microscope objective. It can be seen from **Figure 12** that reconstruction is worse when γ = 10,000 as compared to that when γ = 1,000. Clearly, regularization parameter plays an important role in reconstruction.

5 CONCLUDING REMARKS

Off-axis DHM simulation results show that, for quadratic phase aberration generated by a microscope objective, the DH-TIE method along with regularization can effectively eliminate quadratic phase aberration. The unique advantage of DH-TIE is that phase unwrapping is not needed. In contrast, conventional DH phase retrieval method is not able to remove quadratic phase aberration since there is no such process (regularization within TIE) for the removal of the quadratic phase. We have performed simulations that provide guidance for the proper selection of the regularization process under the TIE.

Through optical experimental results, along with regularization the DH-TIE method shows consistency in phase retrieval under quadratic phase aberration introduced by the microscope objective in the DH system. It should be noted that the uniformity of the beam brightness in the holographic plane should affect the accuracy of the DH-TIE reconstruction, because only when the light intensity is uniformly distributed on the hologram plane, the TIE equation can then be directly reduced to a Poisson equation, which can be solved directly by using Fourier transforms. This aspect should be further studied.

DATA AVAILABILITY STATEMENT

The original contributions presented in the study are included in the article/supplementary material, further inquiries can be directed to the corresponding author.

AUTHOR CONTRIBUTIONS

WZ, HZ, and T-CP contributed to conception and design of the study. CW organized the database. YY performed the statistical analysis. SL wrote the first draft of the manuscript. All authors contributed to manuscript revision, read, and approved the submitted version.

FUNDING

This project was supported by the National Natural Science Foundation of China (No.51775326 and No.61975112); the Major State Research Development Program of China (2020YFE024600); Shanghai Key Laboratory of Intelligent Manufacturing and Robotics.

REFERENCES

Banerjee, P. P. (2022). *University of Dayton.[Private Communications]*. Dayton, Ohio: University of Dayton.

Colomb, T., Kühn, J., Charrière, F., Depeursinge, C., Marquet, P., and Aspert, N. (2006). Total Aberrations Compensation in Digital Holographic Microscopy with a Reference Conjugated Hologram. *Opt. Express* 14, 4300. doi:10.1364/oe.14.004300

Cuche, E., Marquet, P., and Depeursinge, C. (1999). Simultaneous Amplitude-Contrast and Quantitative Phase-Contrast Microscopy by Numerical Reconstruction of Fresnel off-axis Holograms. *Appl. Opt.* 38, 6994–7001. doi:10.1364/ao.38.006994

Deng, D., Peng, J., Qu, W., Wu, Y., Liu, X., He, W., et al. (2017). Simple and Flexible Phase Compensation for Digital Holographic Microscopy with Electrically Tunable Lens. *Appl. Opt.* 56, 6007. doi:10.1364/AO.56.006007

Di, J., Zhao, J., Sun, W., Jiang, H., and Yan, X. (2009). Phase Aberration Compensation of Digital Holographic Microscopy Based on Least Squares Surface Fitting. *Opt. Commun.* 282, 3873–3877. doi:10.1016/j.optcom.2009.06.049

Gabor, D. (1948). A New Microscopic Principle. *Nature.* 161, 777–778. doi:10.1038/161777a0

Gupta, A. K., Nishchal, N. K., and Banerjee, P. P. (2020). Transport of Intensity Equation Based Photon-Counting Phase Imaging. *OSA Continuum.* 3, 236–245. doi:10.1364/OSAC.383527

Gupta, A. K., and Nishchal, N. K. (2021). Low-light Phase Imaging Using In-Line Digital Holography and the Transport of Intensity Equation. *J. Opt.* 23, 025701. doi:10.1088/2040-8986/abe18a

Kelly, D. P., Megel, L., Meinecke, T., and Sinzinger, S. (2013). A Theoretical Comparison of Fresnel Based Digital Holography and Phase Retrieval from the Transport of Intensity Equation. *Proc. SPIE.* 8833, 88330G. doi:10.1117/12.2024855

Leith, E. N., and Upatnieks, J. (1964). Wavefront Reconstruction with Diffused Illumination and Three-Dimensional Objects*. *J. Opt. Soc. Am.* 54, 1295–1301. doi:10.1364/JOSA.54.001295

Liu, S., Xiao, W., and Pan, F. (2014). Automatic Compensation of Phase Aberrations in Digital Holographic Microscopy for Living Cells Investigation by Using Spectral Energy Analysis. *Opt. Laser Technology.* 57, 169–174. doi:10.1016/j.optlastec.2013.10.014

Liu, Y., Wang, Z., and Huang, J. (2018). Recent Progress on Aberration Compensation and Coherent Noise Suppression in Digital Holography. *Appl. Sci.* 8, 444. doi:10.3390/app8030444

Lu, L., Fan, Y., Sun, J., Zhang, J., Wu, X., Chen, Q., et al. (2021). Accurate Quantitative Phase Imaging by the Transport of Intensity Equation: a Mixed-Transfer-Function Approach. *Opt. Lett.* 46, 1740–1743. doi:10.1364/OL.422095

Mann, C. J., Yu, L., Lo, C.-M., and Kim, M. K. (2005). High-resolution Quantitative Phase-Contrast Microscopy by Digital Holography. *Opt. Express.* 13, 8693–8698. doi:10.1364/opex.13.008693

Nguyen, T., Bui, V., Lam, V., Raub, C. B., Chang, L.-C., and Nehmetallah, G. (2017). Automatic Phase Aberration Compensation for Digital Holographic Microscopy Based on Deep Learning Background Detection. *Opt. Express.* 25, 15043–15057. doi:10.1364/OE.25.015043

Poon, T.-C., and Liu, J.-P. (2014). *Introduction to Modern Digital Holography with MATLAB*. Cambridge, UK: Cambridge University Press.

Rappaz, B., Marquet, P., Cuche, E., Emery, Y., Depeursinge, C., and Magistretti, P. J. (2005). Measurement of the Integral Refractive index and Dynamic Cell Morphometry of Living Cells with Digital Holographic Microscopy. *Opt. Express.* 13, 9361–9373. doi:10.1364/opex.13.009361

Sánchez-Ortiga, E., Ferraro, P., Martínez-Corral, M., Saavedra, G., and Doblas, A. (2011). Digital Holographic Microscopy with Pure-Optical Spherical Phase Compensation. *J. Opt. Soc. Am. A.* 28, 1410–1417. doi:10.1364/JOSAA.28.001410

Schnars, U., and Jüptner, W. (1994). Direct Recording of Holograms by a CCD Target and Numerical Reconstruction. *Appl. Opt.* 33, 179–181. doi:10.1364/AO.33.000179

Teague, M. R. (1983). Deterministic Phase Retrieval: a Green's Function Solution. *J. Opt. Soc. Am.* 73, 1434–1441. doi:10.1364/JOSA.73.001434

Wang, H., Dong, Z., Wang, X., Lou, Y., and Xi, S. (2019). Phase Compensation in Digital Holographic Microscopy Using a Quantitative Evaluation Metric. *Opt. Commun.* 430, 262–267. doi:10.1016/j.optcom.2018.08.061

Wittkopp, J. M., Khoo, T. C., Carney, S., Pisila, K., Bahreini, S. J., Tubbesing, K., et al. (2020). Comparative Phase Imaging of Live Cells by Digital Holographic Microscopy and Transport of Intensity Equation Methods. *Opt. Express* 28, 6123–6133. doi:10.1364/OE.385854

Yan, K., Yu, Y., Huang, C., Sui, L., Qian, K., and Asundi, A. (2019). Fringe Pattern Denoising Based on Deep Learning. *Opt. Commun.* 437, 148–152. doi:10.1016/j.optcom.2018.12.058

Zhou, W.-J., Guan, X., Liu, F., Yu, Y., Zhang, H., Poon, T.-C., et al. (2018). Phase Retrieval Based on Transport of Intensity and Digital Holography. *Appl. Opt.* 57, A229. doi:10.1364/AO.57.00A229

Zhou, W., Yu, Y., and Asundi, A. (2009). Study on Aberration Suppressing Methods in Digital Micro-holography. *Opt. Lasers Eng.* 47, 264–270. doi:10.1016/j.optlaseng.2008.04.026

Zuo, C., Chen, Q., Li, H., Qu, W., and Asundi, A. (2014). Boundary-artifact-free Phase Retrieval with the Transport of Intensity Equation II: Applications to Microlens Characterization. *Opt. Express* 22, 18310–18324. doi:10.1364/OE.22.018310

Zuo, C., Chen, Q., Qu, W., and Asundi, A. (2013a). Direct Continuous Phase Demodulation in Digital Holography with Use of the Transport-Of-Intensity Equation. *Opt. Commun.* 309, 221–226. doi:10.1016/j.optcom.2013.07.013

Zuo, C., Chen, Q., Qu, W., and Asundi, A. (2013b). Phase Aberration Compensation in Digital Holographic Microscopy Based on Principal Component Analysis. *Opt. Lett.* 38, 1724–1726. doi:10.1364/OL.38.001724

Zuo, C., Li, J., Sun, J., Fan, Y., Zhang, J., Lu, L., et al. (2020). Transport of Intensity Equation: a Tutorial. *Opt. Lasers Eng.* 135, 106187. doi:10.1016/j.optlaseng.2020.106187

Conflict of Interest: The authors declare that the research was conducted in the absence of any commercial or financial relationships that could be construed as a potential conflict of interest.

frontiers in Photonics

BRIEF RESEARCH REPORT
published: 25 February 2022
doi: 10.3389/fphot.2022.835962

Compact Computational Holographic Display

Ni Chen[1]*, *Congli Wang*[1,2] *and Wolfgang Heidrich*[1]

[1]Visual Computing Center, King Abdullah University of Science and Technology, Thuwal, Saudi Arabia, [2]Department of Electrical Engineering & Computer Sciences, University of California, Berkeley, Berkeley, CA, United States

Holographic display is an ultimate three-dimensional (3D) display technique that can produce the wavefront of 3D objects. The dynamic holographic display usually requires a spatial light modulator (SLM) with a following 4*f* system to eliminate the unnecessary orders produced by the grating structure of the SLM. We present a technique that displays the images without the 4*f* system. We detect the unnecessary wavefield by phase-shifting holography and suppress it using computational optimization. Experimental results are presented to verify the proposed method.

Keywords: holography, computational display, optimization, display, imaging

OPEN ACCESS

Edited by:
Yaping Zhang,
Kunming University of Science and Technology, China

Reviewed by:
Jia Jia,
Independent Researcher, Shenzhen, China
Tomasz Kozacki,
Warsaw University of Technology, Poland

***Correspondence:**
Ni Chen
ni.chen@kaust.edu.sa

Specialty section:
This article was submitted to Optical Information Processing and Holography, a section of the journal Frontiers in Photonics

Received: *15 December 2021*
Accepted: *31 January 2022*
Published: *25 February 2022*

Citation:
Chen N, Wang C and Heidrich W (2022) Compact Computational Holographic Display. Front. Photonics 3:835962. doi: 10.3389/fphot.2022.835962

1 INTRODUCTION

Holography could create a light field identical to the one generated by a real three-dimensional (3D) object. Thus, it is regarded as the ultimate display technique for 3D displays (Hong et al., 2011). One of the most challenging issues in holographic displays is modulating the complex wavefield at wavelength-scale, pixel by pixel, yielding ultra-high spatial resolution. The typical light modulation devices are spatial light modulators (SLMs) or digital micromirror devices (DMDs). The commercial SLMs or DMDs are mainly phase-only or amplitude-only, and the practical realization of a complex one is challenging. Various approaches have been reported to conduct complex field modulation in optical or computational manners (Hsueh and Sawchuk, 1978; Juday et al., 1991; Gregory et al., 1992; Neto et al., 1996; de Bougrenet de la Tocnaye and Dupont, 1997; Arrizón et al., 1998; Birch et al., 2000; Hsieh, 2007; Bingxia Wang et al., 2021). The optical approaches usually achieve complex modulation by integrating and controlling phase-only or amplitude-only SLMs in different ways (Juday et al., 1991; Gregory et al., 1992; Neto et al., 1996; de Bougrenet de la Tocnaye and Dupont, 1997; Hsieh, 2007), while the computational techniques convert the complex field into equivalent phase-only (Hsueh and Sawchuk, 1978; Birch et al., 2000) or amplitude-only (Arrizón et al., 1998; Bingxia Wang et al., 2021) ones that adapt to the physical constraints of commercial light modulators. The latter is also referred to as hologram encoding. Analytical solutions and computational optimization are two main approaches for hologram encoding. Detour phase (Arrizón et al., 1998; Bingxia Wang et al., 2021) and double-phase methods (Hsueh and Sawchuk, 1978; Song et al., 2012; Mendoza-Yero et al., 2014) are typical analytical techniques, which are fast but with compromised qualities, and can be easily applied to arbitrary complex holograms. Optimization techniques such as Gerchberg–Saxton (GS) (Gerchberg, 2002; Sun et al., 2018; Chen et al., 2020; Wu et al., 2021) are time-consuming with improved image quality. However, these are difficult to be applied to arbitrary complex fields (Chakravarthula et al., 2019). The rasterization structure of SLM or DMD also introduces multiple orders. The fill factor of the pixels results in the zero-order issue, which interferes with and distorts the modulated light wave. To improve the displayed image quality, it requires suppression of the zero-order. The 4*f* optical filter system (Arrizón et al., 2007; Liang et al., 2012; Ronzitti et al., 2012; Siemion et al., 2012; Improso et al.,

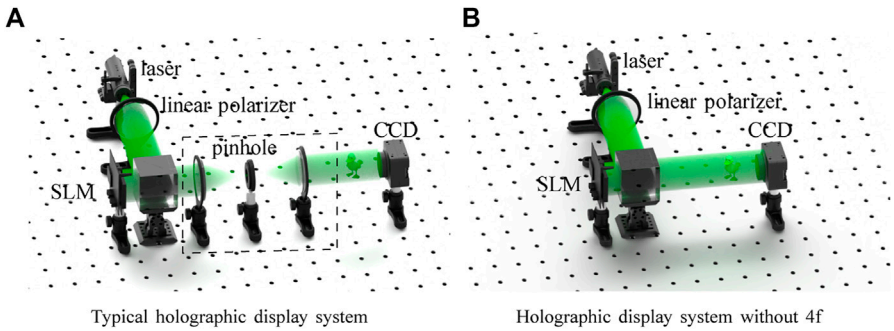

FIGURE 1 | Holographic display with **(A)** and without **(B)** 4*f* system.

2014) is a common approach that can block the zero-order in the Fourier plane. The 4*f* system and other variants of zero-order blocking techniques result in a non-accessible region in the final reconstruction because any part of the desired pattern near the zero-order area would also be affected. An ideal solution would be to create a correction beam with the same profile as the zero-order together with the desired target (Palima and Daria, 2007), which could create a destructive interference with the unwanted beam. However, developing complex field optimization may be the barrier to this approach (Improso et al., 2017).

Herein, we propose a computational holographic display technique that integrates phase-shifting holography and automatic differentiable (AD) optimization. The former helps us detect the unwanted complex wavefield in a holographic display system, and the latter achieves complex field optimization to suppress the unwanted wavefields. It shows that optimization through AD can obtain a phase-only hologram that acts equally as a complex field in an efficient way. In the simulation, the peak signal-to-noise (PSNR) and structural similarity index measure (SSIM) can reach 50 dB and 0.9 in around one second. Thanks to the powerful AD optimization, we can achieve comparable image quality in hologram display while deputing the 4*f* system. We present the methodology in **Section 2** and experimental results in **Section 3**.

2 METHODS

Figure 1A represents a typical holographic display system, wherein a laser light beam illuminates an SLM that shows the holograms. The diffracted light goes through a 4*f* system and reproduces the desired objects. The 4*f* system, as denoted by the dashed rectangle in **Figures 1A**, is used to block unwanted terms induced by the rasterized SLM and its limited fill factor. It usually keeps only the first order of the diffraction (Zaperty et al., 2018). The 4*f* makes the system bulky and may introduce extra aberrations if the focal lengths of the lenses are small. Therefore, it is demanded to be eliminated. The ideal display system is shown in **Figure 1B**.

However, without the 4*f* system, the detected images along the optical axis is an interference pattern between the directly reflected beam and the diffracted beam from the SLM, as shown in **Figure 2** and **Eq. 1**:

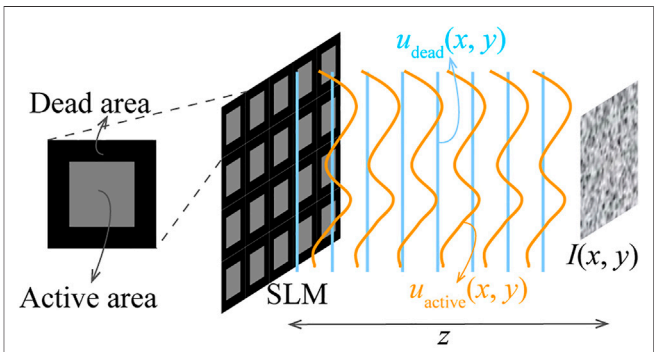

FIGURE 2 | Zero-order issue in holographic display systems with an SLM.

$$I(x, y) = |\mathcal{P}(u_{dead}(x, y), z) + \mathcal{P}(u_{active}(x, y), z)|^2, \quad (1)$$

where $u_{dead}(x, y) = A(x, y)e^{j\phi_{dead}(x,y)}$ and $u_{active}(x, y) = A(x, y)e^{j\phi_{active}(x,y)}$ are the beams from the dead area and activate area of the SLM, respectively, $\mathcal{P}(\cdot, z)$ is the free-space propagator of a complex amplitude of a wavefield with a distance z (described in **Section 2.3**), and $I(x, y)$ is the detected image in the camera sensor. The proposed method detects the complex amplitude of the wavefield $u_{dead}(x, y)$ and eliminates it with a computational optimization approach. It should be mentioned that $u_{dead}(x, y)$ is not only the directly reflected beam from the SLM but also contains some system aberrations. We obtain it through phase-shifting holography. With the known $u_{dead}(x, y)$, the computationally designed phase hologram displayed by the active area of the SLM can cancel it in the camera plane. We achieve this by automatic differentiable complex field optimization. The following two sub-sections describe the proposed method in more detail.

2.1 Unwanted Wavefront Detection

Figure 2 and **Eq. 1** show the unwanted complex amplitude of the wavefield we want to suppress is an interference pattern. Obtaining it is a holographic imaging problem. Therefore, we

introduce the four-step phase-shifting holography (Yamaguchi and Zhang, 1997; Jeong et al., 2008) to measure it. We treat the wavefield $u_{dead}(x, y)$ at the camera sensor plane as the target and the wavefield from the SLM active area as the reference beam and perform phase-shifting hologram recording. The four holograms are taken by shifting the reference beams' phase with a step of 0.5π; that is, α is of 0π, 0.5π, π and 1.5π, respectively. Thus, the captured holograms under phase-shifting α can be represented by

$$\begin{aligned} I(x, y; \alpha) &= |u_{dead}(x, y) + u_{active}(x, y; \alpha)|^2 \\ &= |A_{dead}(x, y)|^2 + |A_{active}(x, y; \alpha)|^2 + \\ &= 2A_{dead}(x, y)A_{active}(x, y; \alpha)\cos(\phi_{dead}(x, y) - \phi_{active}(x, y) - \alpha). \end{aligned} \tag{2}$$

Thus, the phase and amplitude of the light beam of $u_{dead}(x, y) = A_{dead}e^{j\phi_{dead}(x,y)}$ can be obtained by (Jeong et al., 2008)

$$\phi_{dead}(x, y) = \tan^{-1}\left(\frac{I(x, y; 0.5\pi) - I(x, y; 1.5\pi)}{I(x, y; 0) - I(x, y; \pi)}\right), \tag{3}$$

$$A_{dead}(x, y) = \frac{1}{4}\frac{I(x, y; 0) - I(x, y; \pi)}{\cos(\phi_{dead}(x, y) - \phi_{active}(x, y))}. \tag{4}$$

It should be mentioned that we suppose the dead area of the SLM acts as a "mirror." However, the cover glass of the SLMs may be imperfect, which could result in an inaccurate estimation of the zero-order.

2.2 Unwanted Wavefront Suppression Through Automatic Differentiable Optimization

With the detected complex amplitude of the wavefield $u_{dead}(x, y)$, we need to calculate a desired phase only hologram that can be loaded into the active area of the SLM to produce the desired image after interfering with $u_{dead}(x, y)$. Suppose b is the known target, the problem is to find a phase $\phi(x, y)$, such that for a known distance z, the interference between the propagated wavefield and $u_{dead}(x, y)$ approaches the target b, which can be presented as

$$\min_{\phi} \quad \mathcal{L}(\phi) = \||\mathcal{P}(e^{j\phi}, z) + u_{dead}(x, y)|^2 - b\|^2, \tag{5}$$

We can optimize the above equation using a gradient descent. At iteration n, update ϕ^{n+1} given a step size τ:

$$\phi^{n+1} \leftarrow \phi^n - \tau\nabla\mathcal{L}(\phi^n), \tag{6}$$

with the derivatives of

$$\nabla\mathcal{L}(\phi^n) = \frac{\partial\mathcal{L}}{\partial\phi}\bigg|_{\phi=\phi^n}. \tag{7}$$

Computing $\frac{\partial\mathcal{L}}{\partial\phi}$ is critical because the partial derivatives indicate how the phase affects the error metric locally. The analytic expression of **Eq. 7** is typically derived by writing an explicit expression for the error metric $\mathcal{L}(\phi)$ and symbolically differentiating with respect to each of the input parameters. Herein, we can expand **Eq. 7** using the chain rule as follows:

$$\frac{\partial\mathcal{L}}{\partial\phi} = \frac{\partial\mathcal{L}}{\partial x_7}\frac{\partial x_7}{\partial x_6}\frac{\partial x_6}{\partial x_5}\frac{\partial x_5}{\partial x_4}\frac{\partial x_4}{\partial x_3}\frac{\partial x_3}{\partial x_2}\frac{\partial x_2}{\partial x_1}\frac{\partial x_1}{\partial\phi}, \tag{8}$$

where

$$\begin{aligned} x_1 &= \exp(j\phi) \\ x_2 &= \mathcal{F}\{x_1\} \\ x_3 &= x_2 \circ H \\ x_4 &= \mathcal{F}^{-1}\{x_3\} \\ x_5 &= x_4 + u_{dead} \\ x_6 &= |x_5|^2 \\ x_7 &= x_6 - y \\ \mathcal{L} &= |x_7|^2, \end{aligned} \tag{9}$$

where H is the transfer function of free-space wave propagation, $\circ$ is the element-wise product, and $\mathcal{F}$ and $\mathcal{F}^{-1}$ are the Fourier and inverse Fourier operator, respectively. Calculating **Eq. 8** is mathematically straightforward, but somewhat laborious. Herein, we apply the reverse-mode AD (Griewank and Walther, 2008), which is a cheap technique for a computing derivative of a scalar function with many variables by the chain rule (Blennow, 2018; Congli Wang et al., 2021). From **Eqs 8**, **9**, it is clear that we need to optimize real-valued loss functions with complex variables, that is, $f(z)$: $\mathbb{C} \to \mathbb{R}$. However, a non-constant real-valued function of a complex variable is not (complex) analytic and therefore is not differentiable. Generally, the same real-valued function viewed as a function of the real-valued real and imaginary components of the complex variable can have a (real) gradient when partial derivatives are taken with respect to those two (real) components, that is, $f(z) = f(x, y)$: $\mathbb{R}^2 \to \mathbb{R}$. However, taking the real or imaginary part of a complex number (Peng et al., 2020; Chen et al., 2021), do not satisfy the Cauchy–Riemann equations and cannot be addressed via a complex differentiation. In this work, we use the Wirtinger derivative (Remmert, 1991; Kreutz-Delgado, 2009), which can rewrite a real differentiable function $f(z)$ as two-variable holomorphic function $f(z, z^\star)$, where $z = x + jy$ and $z^\star = x - jy$. We can use the chain rule to establish a relationship between partial derivatives of $\frac{\partial}{\partial z}$, $\frac{\partial}{\partial z^\star}$ and the partial derivatives with respect to the real and imaginary components of z:

$$\begin{aligned} \frac{\partial}{\partial x} &= \frac{\partial z}{\partial x}\frac{\partial}{\partial z} + \frac{\partial z^\star}{\partial x}\frac{\partial}{\partial z^\star} = \frac{\partial}{\partial z} + \frac{\partial}{\partial z^\star} \\ \frac{\partial}{\partial y} &= \frac{\partial z}{\partial y}\frac{\partial}{\partial z} + \frac{\partial z^\star}{\partial y}\frac{\partial}{\partial z^\star} = 1j \times \left(\frac{\partial}{\partial z} + \frac{\partial}{\partial z^\star}\right) \end{aligned} \tag{10}$$

From the aforementioned equations, we get the classic definition of Wirtinger calculus:

$$\begin{aligned} \frac{\partial}{\partial z} &= \frac{1}{2}\left(\frac{\partial}{\partial x} - 1j \times \frac{\partial}{\partial y}\right) \\ \frac{\partial}{\partial z^\star} &= \frac{1}{2}\left(\frac{\partial}{\partial x} + 1j \times \frac{\partial}{\partial y}\right) \end{aligned} \tag{11}$$

For step s and loss L, we have $z_{n+1} = z_n - s \times \frac{\partial L}{\partial z^\star}$. This tells us that we can simplify the complex variable update formula above to only refer to the conjugate Wirtinger derivative $\frac{\partial L}{\partial z^\star}$, giving us exactly the step we take in optimization.

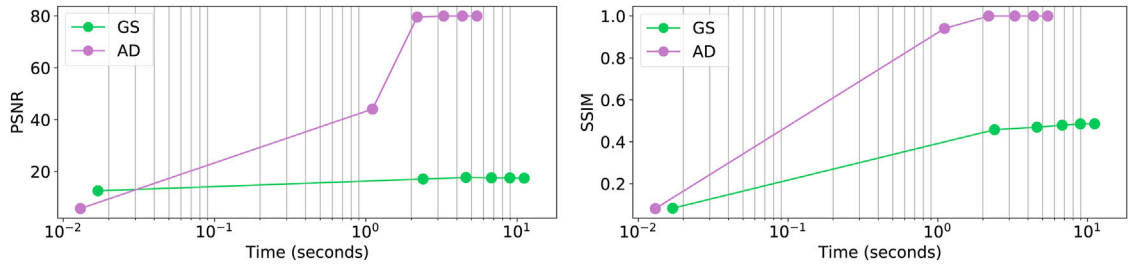

FIGURE 3 | Image quality of the proposed AD and the traditional Gerchberg–Saxton (GS) versus computation time.

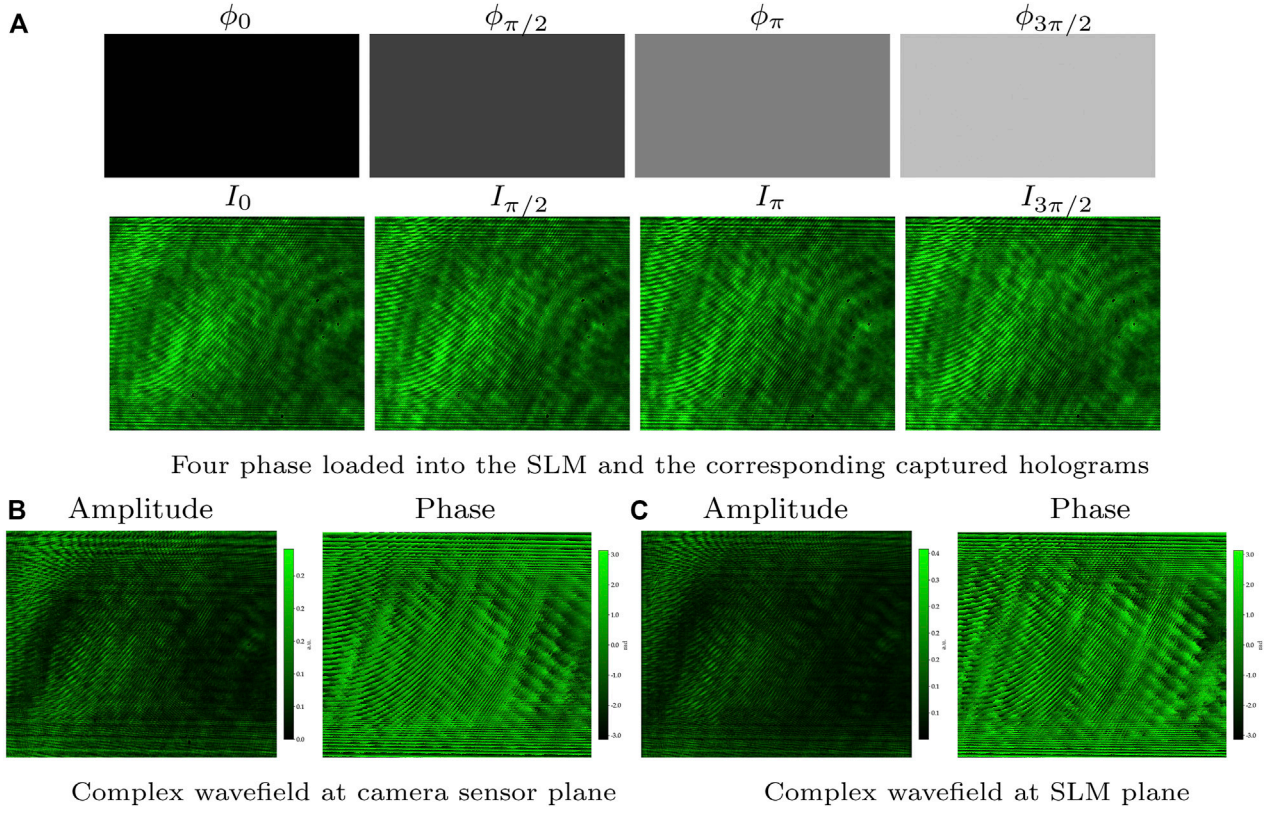

FIGURE 4 | Four phases and the holograms **(A)**, and the calculated wavefield at the image sensor **(B)** and SLM **(C)** planes.

The complex numbers are represented by the cascading of real and imaginary parts in the last dimension. The derivative implementation of the complex elementary functions follows the gradient rules in Table 1 of Jurling and Fienup (2014). We implement the proposed method with PyTorch 1.8 (Chilamkurthy and Tanamala, 2019), while the derivatives are calculated automatically. All presented results in the following sections were performed on a workstation with an Intel Core i7-6820 CPU and an NVIDIA GTX1080 GPU. **Figure 3** shows the image quality of the proposed AD and the traditional Gerchberg–Saxton (GS) concerning the computation time. It takes around one second to optimize one 1,024 × 1,024 hologram with a PSNR ratio more significant than 70 dB and SSIM larger than 0.8. In comparison, the GS method can hardly reach a PSNR larger than 20 dB and SSIM larger than 0.6.

2.3 Free-Space Wavefield Diffraction

The wave propagation mentioned in the previous sections is free-space diffraction and is implemented with the angular spectrum method (ASM) of the Rayleigh–Sommerfeld diffraction (Goodman, 2005):

$$u(x,y) = \int_{z_1}^{z_2} \mathcal{F}^{-1}\left\{\mathcal{F}\{u(x,y,z)\}H(f_x,f_y,z-z_1)\right\}dz, \quad (12)$$

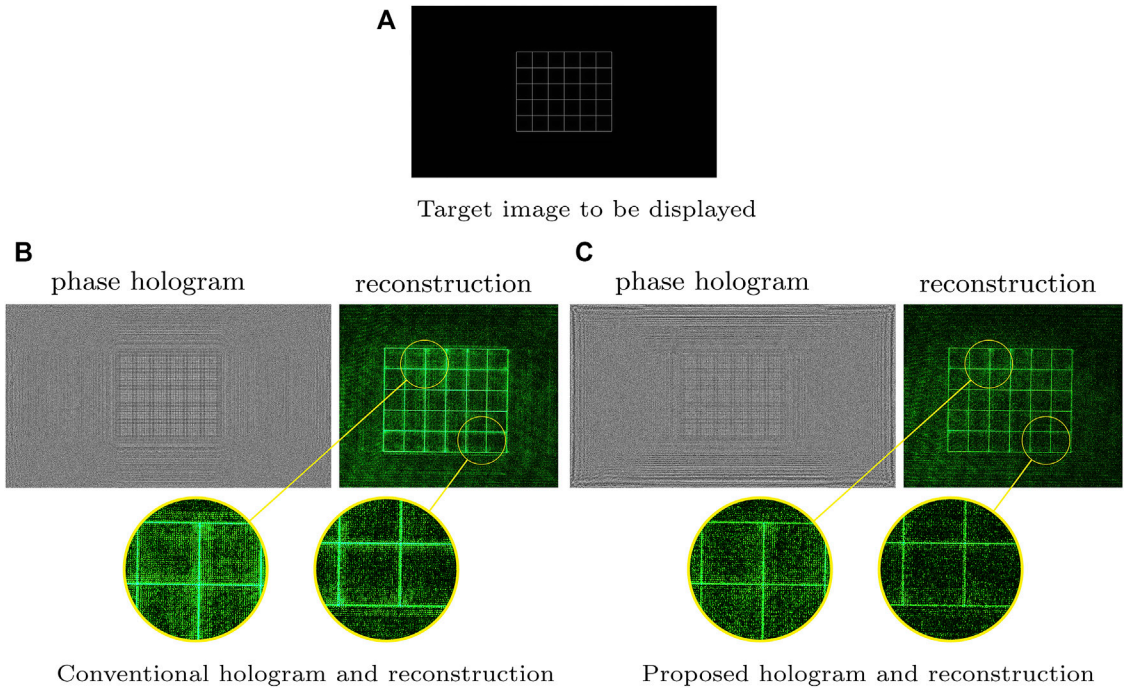

FIGURE 5 | Experimental results of conventional **(B)** and proposed **(C)** methods for displaying a target image **(A)**.

where $u(x, y, z)$ is the complex amplitude at a plane located at z, $\mathcal{F}$ is the Fourier transform, and H is the ASM transfer function given by

$$H(f_x, f_y, z) = \begin{cases} \exp\left(j2\pi z\sqrt{\frac{1}{\lambda^2} - (f_x^2 + f_y^2)}\right), & \sqrt{f_x^2 + f_y^2} < \frac{1}{\lambda}, \\ 0, & \text{otherwise.} \end{cases} \tag{13}$$

3 EXPERIMENTS

The SLM in the experiment is HOLOEYE PLUTO with a full resolution of 1,920 × 1,080 pixels and 8 μm pixel pitch. Moreover, the image sensor is Point Grey Research GS3-U3-50S5C, with a resolution of 2,248 × 2,048 pixels and 3.45 μm pixel pitch. The light source was a laser diode with a center wavelength of 532 nm, and the image sensor distance was 250 mm away from the SLM. The four phases used for detection $u_{dead}(x, y)$ are shown in the above row of **Figure 4A**, and the corresponding captured holograms are shown in the below row. The phase-shifting hologram reconstruction is shown in **Figure 4B**, and the propagated wavefield at the SLM plane is shown in **Figure 4C**. We conducted a calibration to match the size difference between the image sensor and the SLM.

For a target image shown in **Figure 5A**, we calculated the phase-only holograms without and with the unwanted term suppression, which are shown in the left column of **Figures 5B,C**. Whether the difference between the conventional and the proposed method is optimizing the zero-order term or not, the computational calculation time is the same. However, we conducted the phase-shifting holography in the proposed method to obtain the zero-order field. The calculation time can be overlooked, but the capture takes time. This can be improved by automatically synchronizing and controlling the SLM and the camera. The corresponding experimentally reconstructed images are shown in the right columns. Comparing the proposed method with the conventional one, we can observe less background noise in **Figure 5C**, indicating that the proposed technique suppresses some of the unwanted terms. However, some noise still exists, which may be due to the inaccurate modeling of the optical system. This could be improved if we further consider the laser speckle and the SLM's fill factor that reflects only part of the incident light wave.

4 DISCUSSION AND CONCLUSION

We presented a computational holographic display technology that can achieve a lightweight holographic display with high quality. The results show that the automatic differentiable complex wavefield optimization can suppress the unwanted wavefield with the assistance of phase-shifting holography. The automatic differentiable complex wavefield optimization can also

be applied to other optical systems requiring aberration or system error corrections.

DATA AVAILABILITY STATEMENT

The original contributions presented in the study are included in the article/Supplementary Material, further inquiries can be directed to the corresponding author.

AUTHOR CONTRIBUTIONS

NC proposed the idea and conducted the simulation and experiments. CW and WH worked together on the manuscript writing.

FUNDING

This work was supported by the KAUST individual baseline funding.

REFERENCES

Arrizón, V., Kinne, S., and Sinzinger, S. (1998). Efficient Detour-phase Encoding of One-Dimensional Multilevel Phase Diffractive Elements. *Appl. Opt.* 37, 5454. doi:10.1364/ao.37.005454

Arrizón, V., Ruiz, U., Carrada, R., and González, L. A. (2007). Pixelated Phase Computer Holograms for the Accurate Encoding of Scalar Complex fields. *J. Opt. Soc. Am. A.* 24, 3500. doi:10.1364/josaa.24.003500

Birch, P., Young, R., Chatwin, C., Farsari, M., Budgett, D., and Richardson, J. (2000). Fully Complex Optical Modulation with an Analogue Ferroelectric Liquid crystal Spatial Light Modulator. *Opt. Commun.* 175, 347–352. doi:10.1016/s0030-4018(00)00478-810.1016/s0030-4018(00)00478-8

Blennow, M. (2018). *Mathematical Methods for Physics and Engineering*. New York, NY: CRC Press. doi:10.1201/b22209

Chakravarthula, P., Peng, Y., Kollin, J., Fuchs, H., and Heide, F. (2019). Wirtinger Holography for Near-Eye Displays. *ACM Trans. Graph.* 38, 1–13. doi:10.1145/3355089.3356539

Chen, C., Lee, B., Li, N.-N., Chae, M., Wang, D., Wang, Q.-H., et al. (2021). Multi-depth Hologram Generation Using Stochastic Gradient Descent Algorithm with Complex Loss Function. *Opt. Express*, 29, 15089. doi:10.1364/oe.425077

Chen, L., Zhang, H., Cao, L., and Jin, G. (2020). Non-iterative Phase Hologram Generation with Optimized Phase Modulation. *Opt. Express* 28, 11380. doi:10.1364/oe.391518

Chilamkurthy, S., and Tanamala, S. (2019). Deep Learning and Medical Diagnosis - Authors' Reply. *The Lancet* 394, 1711. doi:10.1016/s0140-6736(19)32614-510.1016/s0140-6736(19)32614-5

de Bougrenet de la Tocnaye, J. L., and Dupont, L. (1997). Complex Amplitude Modulation by Use of Liquid-crystal Spatial Light Modulators. *Appl. Opt.* 36, 1730. doi:10.1364/ao.36.001730

Gerchberg, R. W. (2002). A New Approach to Phase Retrieval of a Wave Front. *J. Mod. Opt.* 49, 1185–1196. doi:10.1080/09500340110114425

Goodman, J. (2005). *Introduction to Fourier Optics*. Englewood, Colo: Roberts & Co.

Gregory, D. A., Kirsch, J. C., and Tam, E. C. (1992). Full Complex Modulation Using Liquid-crystal Televisions. *Appl. Opt.* 31, 163. doi:10.1364/ao.31.000163

Griewank, A., and Walther, A. (2008). *Evaluating Derivatives: Principles and Techniques of Algorithmic Differentiation*. University City, Philadelphia: Society for Industrial and Applied Mathematics. doi:10.1137/1.9780898717761

Hong, J., Kim, Y., Choi, H.-J., Hahn, J., Park, J.-H., Kim, H., et al. (2011). Three-dimensional Display Technologies of Recent Interest: Principles, Status, and Issues [invited]. *Appl. Opt.* 50, H87. doi:10.1364/ao.50.000h87

Hsieh, M.-L. (2007). Improvement of the Complex Modulated Characteristic of Cascaded Liquid crystal Spatial Light Modulators by Using a Novel Amplitude Compensated Technique. *Opt. Eng.* 46, 070501. doi:10.1117/1.2750658

Hsueh, C. K., and Sawchuk, A. A. (1978). Computer-generated Double-phase Holograms. *Appl. Opt.* 17, 3874. doi:10.1364/ao.17.00387410.1364/ao.17.003874

Improso, W. D. G. D., Tapang, G. A., and Saloma, C. A. (2017). "Suppression of Zeroth-Order Diffraction in Phase-Only Spatial Light Modulator via Destructive Interference with a Correction Beam," in *Proceedings of the 5th International Conference on Photonics, Optics and Laser Technology* (Porto, Portugal: SCITEPRESS - Science and Technology Publications). doi:10.5220/0006129802080214

Improso, W. D. G., Hilario, P. L. A., and Tapang, G. (2014). "Zero Order Diffraction Suppression in a Phase-Only Spatial Light Modulator via the GS Algorithm," in *Frontiers in Optics 2014* (Tucson, AZ: OSA). doi:10.1364/fio.2014.ftu4c.3

Jeong, M.-O., Kim, N., and Park, J.-H. (2008). Elemental Image Synthesis for Integral Imaging Using Phase-Shifting Digital Holography. *J. Opt. Soc. Korea* 12, 275–280. doi:10.3807/josk.2008.12.4.275

Juday, R. D., and Florence, J. M. (1991). "Full-complex Modulation with Two One-Parameter Slms," in *Wave Propagation and Scattering in Varied Media II*. Editor VK. Varadan (San Diego, CA: SPIE). doi:10.1117/12.49656

Jurling, A. S., and Fienup, J. R. (2014). Applications of Algorithmic Differentiation to Phase Retrieval Algorithms. *J. Opt. Soc. Am. A.* 31, 1348. doi:10.1364/josaa.31.001348

[Dataset] Kreutz-Delgado, K. (2009). *The Complex Gradient Operator and the Cr-Calculus*. ArXiv.

Liang, J., Wu, S.-Y., Fatemi, F. K., and Becker, M. F. (2012). Suppression of the Zero-Order Diffracted Beam from a Pixelated Spatial Light Modulator by Phase Compression. *Appl. Opt.* 51, 3294. doi:10.1364/ao.51.003294

Mendoza-Yero, O., Mínguez-Vega, G., and Lancis, J. (2014). Encoding Complex fields by Using a Phase-Only Optical Element. *Opt. Lett.* 39, 1740. doi:10.1364/ol.39.001740

Neto, L. G., Roberge, D., and Sheng, Y. (1996). Full-range, Continuous, Complex Modulation by the Use of Two Coupled-Mode Liquid-crystal Televisions. *Appl. Opt.* 35, 4567. doi:10.1364/ao.35.004567

Palima, D., and Daria, V. R. (2007). Holographic Projection of Arbitrary Light Patterns with a Suppressed Zero-Order Beam. *Appl. Opt.* 46, 4197. doi:10.1364/ao.46.004197

Peng, Y., Choi, S., Padmanaban, N., Kim, J., and Wetzstein, G. (2020). "Neural Holography," in *ACM SIGGRAPH 2020 Emerging Technologies* (Virtual Event, United States: ACM). doi:10.1145/3388534.3407295

Remmert, R. (1991). *Theory of Complex Functions*. New York, NY: Springer New York.

Ronzitti, E., Guillon, M., de Sars, V., and Emiliani, V. (2012). LCoS Nematic SLM Characterization and Modeling for Diffraction Efficiency Optimization, Zero and Ghost Orders Suppression. *Opt. Express* 20, 17843. doi:10.1364/oe.20.017843

Siemion, A., Sypek, M., Suszek, J., Makowski, M., Siemion, A., Kolodziejczyk, A., et al. (2012). Diffuserless Holographic Projection Working on Twin Spatial Light Modulators. *Opt. Lett.* 37, 5064. doi:10.1364/ol.37.005064

Song, H., Sung, G., Choi, S., Won, K., Lee, H.-S., and Kim, H. (2012). Optimal Synthesis of Double-phase Computer Generated Holograms Using a Phase-Only Spatial Light Modulator with Grating Filter. *Opt. Express* 20, 29844. doi:10.1364/oe.20.029844

Sun, P., Chang, S., Liu, S., Tao, X., Wang, C., and Zheng, Z. (2018). Holographic Near-Eye Display System Based on Double-Convergence Light Gerchberg-saxton Algorithm. *Opt. Express* 26, 10140. doi:10.1364/oe.26.010140

Wang, B., Hong, X., Wang, K., Chen, X., Liu, S., Krolikowski, W., et al. (2021). Nonlinear Detour Phase Holography. *Nanoscale* 13, 2693–2702. doi:10.1039/d0nr07069f

Wang, C., Chen, N., and Heidrich, W. (2021). Towards Self-Calibrated Lens Metrology by Differentiable Refractive Deflectometry. *Opt. Express* 29, 30284–30295. doi:10.1364/oe.433237

Wu, Y., Wang, J., Chen, C., Liu, C.-J., Jin, F.-M., and Chen, N. (2021). Adaptive Weighted Gerchberg-saxton Algorithm for Generation of Phase-Only

Hologram with Artifacts Suppression. *Opt. Express* 29, 1412. doi:10.1364/oe.413723

Yamaguchi, I., and Zhang, T. (1997). Phase-shifting Digital Holography. *Opt. Lett.* 22, 1268. doi:10.1364/ol.22.001268

Zaperty, W., and Kozacki, T. (2018). "Numerical Model of Diffraction Effects of Pixelated Phase-Only Spatial Light Modulators," in *Speckle 2018: VII International Conference on Speckle Metrology*. Editors M Józwik, L. R Jaroszewicz, and M Kujawińska (Janów Podlaski, Poland: SPIE). doi:10.1117/12.2319739

Conflict of Interest: The authors declare that the research was conducted in the absence of any commercial or financial relationships that could be construed as a potential conflict of interest.

Publisher's Note: All claims expressed in this article are solely those of the authors and do not necessarily represent those of their affiliated organizations or those of the publisher, the editors, and the reviewers. Any product that may be evaluated in this article, or claim that may be made by its manufacturer, is not guaranteed or endorsed by the publisher.

frontiers in Photonics

ORIGINAL RESEARCH
published: 04 March 2022
doi: 10.3389/fphot.2022.846731

Compressive Interferenceless Coded Aperture Correlation Holography With High Imaging Quality

*Chao Liu, Tianlong Man and Yuhong Wan**

Department of Physics and Optoelectronics, Faculty of Science, Beijing University of Technology, Beijing, China

Interferenceless coded aperture correlation holography (I-COACH) provides an alternative way for the 3D imaging of spatial incoherent illuminated or fluorescent sample. However, the low imaging signal-to-noise ratio (SNR) is one of the bottlenecks that restrict the application of I-COACH. The limitation is mainly originated from the strong bias level that presents in the recorded holograms. Phase shifting methods were implemented in I-COACH to eliminate the background noise while the multiple-exposures recording mechanism significantly reduces the temporal resolution of the system. In this paper, we proposed a compressive I-COACH imaging method with high reconstruction quality and without the sacrifice of the imaging speed. The 3D holographic image reconstruction was implemented under compressive sensing framework while only one single-exposure object hologram and one point spread hologram are necessary. High quality reconstructions were obtained using the proposed method, even for the down-sampled holograms. The imaging SNR of the I-COACH system was improved by a factor of more than 16.5% when comparing with the imaging SNR obtained by the conventional cross-correlation reconstruction method. The proposed method provides a fast and high-fidelity imaging method that can potentially benefit the imaging through scattering medium, partial aperture imaging, and other fields.

Keywords: incoherent holography, coded aperture imaging, 3D imaging, compressive sensing, high quality reconstruction

OPEN ACCESS

Edited by:
Yaping Zhang,
Kunming University of Science and Technology, China

Reviewed by:
Jianglei Di,
Guangdong University of Technology, China
Shuming Jiao,
Peng Cheng Laboratory, China

****Correspondence:***
Yuhong Wan
yhongw@bjut.edu.cn

Specialty section:
This article was submitted to Optical Information Processing and Holography, a section of the journal Frontiers in Photonics

Received: *31 December 2021*
Accepted: *25 January 2022*
Published: *04 March 2022*

Citation:
Liu C, Man T and Wan Y (2022) Compressive Interferenceless Coded Aperture Correlation Holography With High Imaging Quality. Front. Photonics 3:846731. doi: 10.3389/fphot.2022.846731

INTRODUCTION

Holography based on two-beam mutual-coherent and interference has unique advantages in the field of quantitative phase contrast imaging and 3D imaging because it can record and reconstruct not only the amplitude but also the phase of the light that emitted or reflected from the object. However, coherent sources are not always practically available, especially in some important applications such as astronomical imaging and fluorescence microscopy. In addition, the coherent speckle noise in the reconstructed images has significantly affected the imaging performance of the holographic system (Men et al., 2017). On the other hand, incoherent holography that first was proposed by Mertz and Young in 1961 has extended the application of holography to the field of spatial incoherent imaging (Rogers, 1950; Mertz et al., 1961). The basic idea of original incoherent holography is that the spatial incoherent objects can be 3D reconstructed from their Fresnel zone plate projection patterns (hologram). The incoherent holographic techniques were then further developed and improved by Lohmann, Stroke, and Cochran (Lohmann, 1965; Stroke and Restrick, 1965; Cochran, 1966). One significant difference between incoherent holography and conventional holography is that the

mutual coherence between any two different points on the sample is no longer necessary for holographic recording. Instead, the holographic recording scheme was based on the characteristics of spatial self-coherence by splitting the light that emitted from each point on the object into two beams and then recording the resulting interference patterns. However, incoherent holographic methods are normally failed in providing images with sufficient SNR. The problems are mainly arising from the strong bias in the recorded holograms as the results of the incoherent superposition of all the point holograms.

A new type of incoherent digital holography, coined as coded aperture correlation holography (COACH), was proposed in 2016 (Vijayakumar et al., 2016), which originated from Fresnel incoherent correlation holography (FINCH) (Men et al., 2017). COACH possesses the advantages of higher axial-resolution and higher spectral-resolution when comparing with FINCH. In COACH, the pseudorandom coded phase mask (CPM) generated using Gerchberg-Saxton (GS) algorithm is loaded onto the spatial light modulator (SLM), and the self-interference holographic recording is realized based on the beam splitting using the polarization sensitive characteristics of the SLM (Vijayakumar et al., 2016). The 3D reconstruction of the object is realized by cross-correlating the object hologram (OH) with the point spread holograms (PSHs) that have been recorded at all possible axial planes. That the 3D information of an object can be encoded and decoded even without the use of self-interference recording was found by later research. The interferenceless coded aperture correlation holography (I-COACH) was proposed for 3D imaging without any two-wave interference (Vijayakumar and Rosen, 2017). Comparing with COACH, I-COACH has a much simpler optical setup and improved photon-energy efficiency. However, the temporal resolution of the system is sacrificed because multi-exposure phase shifting technique and image averaging method were used to suppress the background noise that dominates the reconstructed images. Different techniques such as phase filtering (PF) (RatnamRai et al., 2017), non-linear reconstruction (NLR) (Rai and Rosen, 2019; Liu et al., 2020), and adaptive reconstruction (Wan et al., 2021) were used to suppress the background noise and improve the temporal resolution of the I-COACH system. However, the increases of temporal resolution normally come with the decreases of reconstruction quality. On the other hand, compressive sensing (CS) theory has demonstrated that signals, assumed to be sparse in some basis and sampled by multiplex encoding systems, may be accurately inferred with high probability from much fewer measurements than suggested by Nyquist's sampling theorem. In digital holography, the CS technique provides a high-efficiency way for 3D object reconstruction from single real-valued (intensity) hologram. Specifically, the 3D sample is modulated by the optical system to form a 2D hologram, and the reconstruction process is implemented under the CS framework to achieve 3D tomographic imaging of the sample (Zhang et al., 2018). In compressive digital holography, the theoretical model of the holographic recording procedure of a 3D object was first established based on vector diffraction theorem. The forward and backward propagation models, with sparsity regularization imposed on the object, were then used to solve the so-called under-determined inverse problem that will be met when trying to reconstruct 3D objects from their single-exposure digital hologram. As a result, the bias and twin-images can be suppressed (Brady et al., 2009; Lim et al., 2011; Brady et al., 2015; Zhang et al., 2018).

In this paper, inspired by the basic idea of compressive holography, we propose a compressive I-COACH 3D imaging method with high imaging quality and most importantly without the sacrifice of the system temporal resolution. In CS-I-COACH, only single-exposure PSH and OH are necessary for the 3D reconstruction of the object. The imaging model under the CS frame of the I-COACH was first discussed, followed by the preliminary experimental results on 2D and 3D objects that demonstrate the validity of the proposed method. The dependence of the CS reconstruction accuracy in I-COACH on the scattering degree of the CPM was analyzed. The implementation of CS high fidelity reconstruction for under-sampled holograms was also discussed. We believe the proposed method provides a powerful research tool and benefits the optical research fields such as 3D tracking, imaging through scattering medium, and partial aperture imaging.

THE SENSING MODEL OF THE I-COACH SYSTEM

Nyquist sampling frequency is a sufficient but not necessary condition for the high-fidelity retrieval of a discrete signal. CS theory demonstrates that if the signal is sparse itself or can be represented sparse in a certain domain (i.e., Fourier domain or wavelet domain), the original signal can be reconstructed with high probability using numerical optimization approaches, even when the sampling rate is much lower than the value required by the Nyquist criterion. CS can be used for image reconstruction in imaging systems because most natural images are sparse or have sparsity in some transform domains. Assume the image f can be expressed on the orthogonal base $\varphi = \{\varphi_1,\varphi_2\ldots,\varphi_n\}$ as:

$$f = \sum_{i=1}^{n} \varphi_i \mu_i = \varphi\mu \tag{1}$$

where the coefficient $u = [u_1, u_2 \ldots u_n]^T \in \Re^{n\times n}$. If $\|\mu\|_0 \le k$, ($\|\cdot\|_0$ is defined as the l_0-norm and k is the number of non-zero elements in u, $k \ll n$), then f is a k-sparse under matrix φ, while φ is a sparse operator. Given the measurement matrix $R \in \mathbb{C}^{m\times n}$, the matrix that describes the imaging procedure and details of object-image transformation, the measured image g can be expressed as:

$$g = Rf = R\sum_{i=1}^{n} \varphi_i \mu_i = R\varphi\mu = \Theta\mu \tag{2}$$

where $\Theta \in \mathbb{C}^{m\times n}$ is the sensing operator, $g \in \mathbb{C}^{m\times 1}$ is the measurement, and the dimension m of g is much smaller than the dimension n of f. Then an accurate reconstruction can be obtained with high probability by solving:

$$\hat{\mu} = \arg\min_{u} \left\| g - \Theta\mu \right\|_{l_1} \qquad s.t. \quad g = \Theta\mu \tag{3}$$

An I-COACH optical setup is shown in **Figure 1**. The object or pinhole is critically illuminated with spatial incoherent light, the

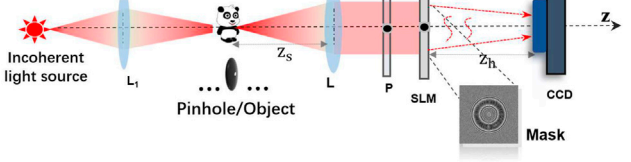

FIGURE 1 | Optical setup of the I-COACH system.

diffracted light is collected and collimated by the lens L, and then modulated by the phase mask which comprises pseudorandom CPM and a quadratic phase mask (QPM) with focal length f_s. The light scattered by the phase mask is then projected to the sensor plane by the QPM. The hologram of the object is recorded by the image sensor.

In the system as show in **Figure 1**, for a point object at the position of (x_s,y_s,z_s), the intensity distribution I_{psh} on the CCD plane can be calculated and given as (Wan et al., 2021):

$$\begin{aligned} & I_{psh}\left(\overline{r_h};\overline{r_s},z_s\right) \\ & == \left|C\sqrt{A_s\left(\overline{r_s};z_s\right)}L\left(\frac{\overline{r_s}}{z_s}\right)Q\left(\frac{1}{z}\right)\exp\left[i\varphi\left(\overline{r}\right)\right]\otimes Q\left(\frac{1}{z_h}\right)\right|^2 \\ & = I_{psh}\left(\overline{r_h}-\frac{z_h}{z_s}\overline{r_s};z_s\right) \end{aligned} \tag{4}$$

where the sign $\otimes$ is 2D convolution, $z = z_s f_L f_s/(f_L f + z_s f_L - z_s f_s)$, and $\sqrt{A_s(\overline{r_s};z_s)}$ is the amplitude of the object point at (x_s, y_s, z_s). C is a complex constant. $\overline{r_s} = (x_s, y_s)$ is the transverse location vector. $\overline{r_h} = (x_h, y_h)$ is the transverse location vector on the CCD. z_h/z_s is the transverse magnification. The function $\varphi(\bar{r})$ represents the phase of the pseudorandom CPM calculated by the GS algorithm. L and Q are linear and quadratic phase functions, given by $L(\bar{r}_s/z) = \exp[i2\pi(b_x x + b_y y)/\lambda z]$ and $Q(b) = \exp[-i\pi b(x^2 + y^2)/\lambda]$, respectively. In the I-COACH system, the point spread function of the imaging system is actually the point spread hologram (PSH) of the point object.

The system of I-COACH is treated as a linear space-invariant imaging system (Wan et al., 2021). Assume that the intensity response of the *K-th* axial position plane of the 3D object at $z_s = z_k$ to the CCD plane is the convolution of the system point spread function and the 2D object plane. Therefore, the intensity pattern of the object at a certain depth level on the CCD and the hologram reconstruction with pure phase filtering can be given as **Eqs. 5**, **6**, respectively, which show the sensing model under the CS frame of I-COACH.

$$\begin{aligned} I_{oh}\left(\overline{r_h};z_k\right) &= O\left(\overline{r_s};z_k\right)\otimes I_{psh}\left(\overline{r_h};z_k\right) \\ &= \sum_j^n a_j\delta\left(\overline{r_s}-\bar{r}_j\right)\otimes I_{psh}\left(\overline{r_h}-\frac{z_h}{z_s}\bar{r}_s;z_k\right) \\ &= \sum_j^n a_j I_{psh}\left(\overline{r_h}-\left(1+\frac{z_h}{z_s}\right)\bar{r}_j;z_k\right) \end{aligned} \tag{5}$$

$$\begin{aligned} O'\left(\overline{r_s};z_k\right) &= I_{oh}\left(\overline{r_h};z_k\right)\otimes I^*_{psh}\left(\overline{r_h};z_k\right) \\ &= \mathfrak{F}_{2D}^{-1}\left\{\mathfrak{F}_{2D}\left(I_{oh}\right)\cdot\mathfrak{F}_{2D}\left(I^*_{psh}\right)\right\} \\ &= \left[\mathfrak{F}_{2D}^{-1}E\mathfrak{F}_{2D}\right]\mu = \Theta\mu \end{aligned} \tag{6}$$

where $\mathfrak{F}_{2D}\mu$ corresponds to the calculation of $\mathfrak{F}_{2D}(I_{oh})$, $\mathfrak{F}_{2D}$ represents the 2D discrete Fourier transform matrix, and $\mathfrak{F}_{2D}^{-1}$ represents the inverse 2D discrete Fourier transform matrix. The sensing matrix of CS-I-COACH can be obtained from **Eq. 6**:

$$\Theta = \mathfrak{F}_{2D}^{-1}E\mathfrak{F}_{2D} = \mathfrak{F}_{2D}^{-1}\exp\left(-i\arg\left(\bar{I}_{psh}\right)\right)\mathfrak{F}_{2D} \tag{7}$$

The matrix $\Theta = \mathfrak{F}_{2D}^{-1}E\mathfrak{F}_{2D}$ denotes the I-COACH reconstruction process of the hologram. The object reconstruction is done with the pure phase filtering of $\boldsymbol{E}$ given by $E = \exp[-i\arg(\mathfrak{F}_{2D}(I_{psh}(\overline{r_h};z_k)))]$. The compressed reconstruction problem of I-COACH can be denoted as an optimal solution problem, which is solved by the TwIST algorithm (Bioucas-Dias and Figueiredo, 2007). Further considering that the fluctuation of high frequency noise in the reconstructed image is small in the space domain, the total variable (TV) algorithm is chosen to suppress the reconstructed image noise:

$$\hat{u} = \arg\min_u \left\|g-\Theta u\right\|_2^2 + \tau\|u\|_{TV} \tag{8}$$

As described above, the CS model of I-COACH and the optimized solution algorithm are established, combined with the sensing matrix to suppress the influence of the bias term on the reconstructed image, which is expected to obtain a high quality reconstructed image quickly by single exposure of PSH and OH.

EXPERIMENTS AND RESULTS

Preliminary experiments were carried out to demonstrate the validity and imaging performance of the proposed CS-I-COACH system. In the first experiment, the transmitted object was imaged, and the imaging performances of the CS-I-COACH were quantitatively evaluated and compared with conventional I-COACH methods. The next experiment verified the high SNR imaging capabilities of CS-I-COACH for under-sampled holograms.

As shown in **Figure 2**, the pinhole or object was illuminated by the incoherent light emitting diode (LED) (Thorlabs LED 625L4, 700 mW, center wavelength of $\lambda = 625$ nm, $\Delta\lambda = 17$ nm) placed at the front focal plane of the lens L_0 with focal length $f_0 = 150$ mm. The light from the beam splitter BS_1 was collimated by the lens L_0 and passed through a polarizer P. The polarizer P polarizes the light along the orientation of the active axis of the spatial light modulator (SLM, Holoeye PLUTO, 1,080 × 1920 pixels, 8 μm pixel pitch, phase-only modulation) located at a distance of 55 mm from the L_0. On the SLM, a phase mask is displayed whereas its phase is the combination of a CPM and a QPM with a focal length of $f_s = 150$ mm. The light modulated by the SLM was

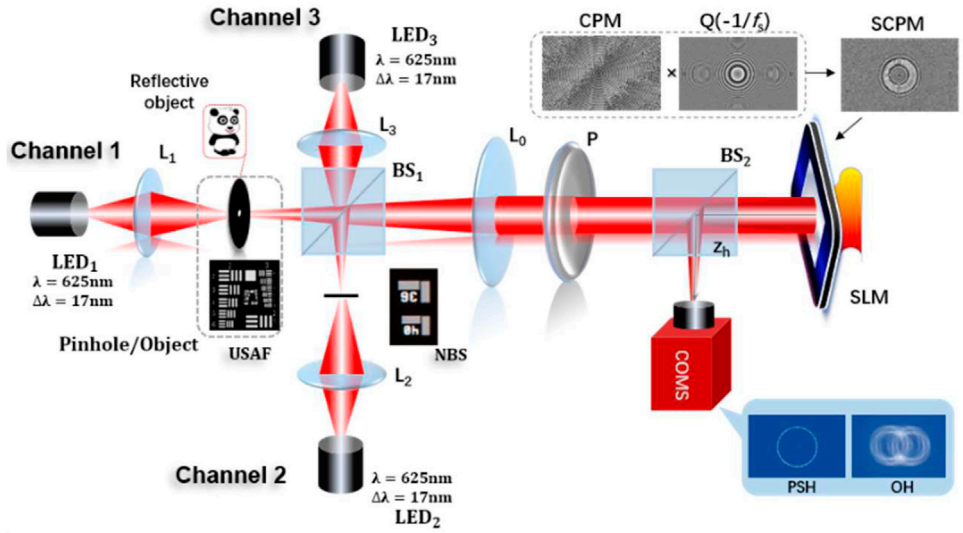

FIGURE 2 | Experimental setup of the CS-I-COACH.

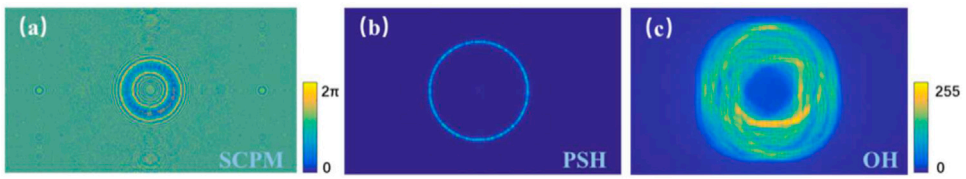

FIGURE 3 | The SCPM used in hologram recording and experimentally recorded holograms. **(A)** Phase of the SCPM; **(B)** the Point spread hologram; **(C)** the object hologram.

collected by a Charge Coupled Device (CCD, Thorlabs CS235MU,1,200 × 1920 pixels, 5.86 μm pixel pitch, and monochrome) located at a distance of z_h = 171 mm from the SLM.

In the first experiment, the ability of CS-I-COACH to image two-dimensional transmissive objects was demonstrated. Similar with our work before (Wan et al., 2021; Liu et al., 2022), the scattering degree $\sigma = 0.167$ and the annular width ω = 1 pixel were chosen as the optimization parameters of the CPM in the modified GS algorithm. The PSH was recorded by placing in Channel-1 a 20 μm diameter pinhole at the front focal plane of the input lens L_0. Channel-2 was blocked during the recording of PSH. Then with Channel-1 blocked, the object hologram OH was recorded with a United States Air Force resolution chart (USAF 1951 RES-1, Newport, placed at the front focal plane of the L_0, line-groups of 4 and 5 have been illuminated) as the 2D object. The synthesized coded phase mask (SCPM), the hologram of a 20 μm diameter pinhole (PSH), and the hologram of a USAF target chart (OH) are shown in **Figure 3**, respectively.

The reconstructed images of the single-exposure PSH and OH were obtained using different traditional reconstruction methods and the CS-I-COACH reconstruction method, respectively, and the results are shown in **Figure 4**. The reconstructed images from the single-exposure PSH and OH as shown in **Figures 3B,C** were obtained using different methods of cross-correlation (CC), pure phase filtering (PF), non-linear reconstruction (NLR), and CS-I-COACH, respectively. The results are shown in **Figure 4**. For the CS-I-COACH, **Eq. 8** was solved using the TwIST algorithm with $\lambda_{\mathrm{TwIST}} = 0.001$ (iteration = 50). Regularization parameter of $\tau_{TV} = 0.01$ was used. For comparison, the direct imaging result obtained in the same system (by using the SLM as a lens) is shown in **Figure 4A**. The strong background noise that presents in the CC results (**Figure 4B**) was suppressed partially by the PF (**Figure 4C**) and more effectively by the NLR (**Figure 4D**) reconstruction method. However, the imaging performances of the I-COACH system, especially the background noise level, were still much worse than the direct imaging (**Figure 4A**). The CS-based methods, on the other hand, provide results with much better quality (**Figure 4E**) than their conventional reconstruction counterparts. The improvements on the imaging quality can be seen more clearly from the inserted line profiles and the peak-signal-to-noise-ratio (PSNR) (Bioucas-Dias and Figueiredo, 2007) data of the reconstructions (**Figure 4F**).

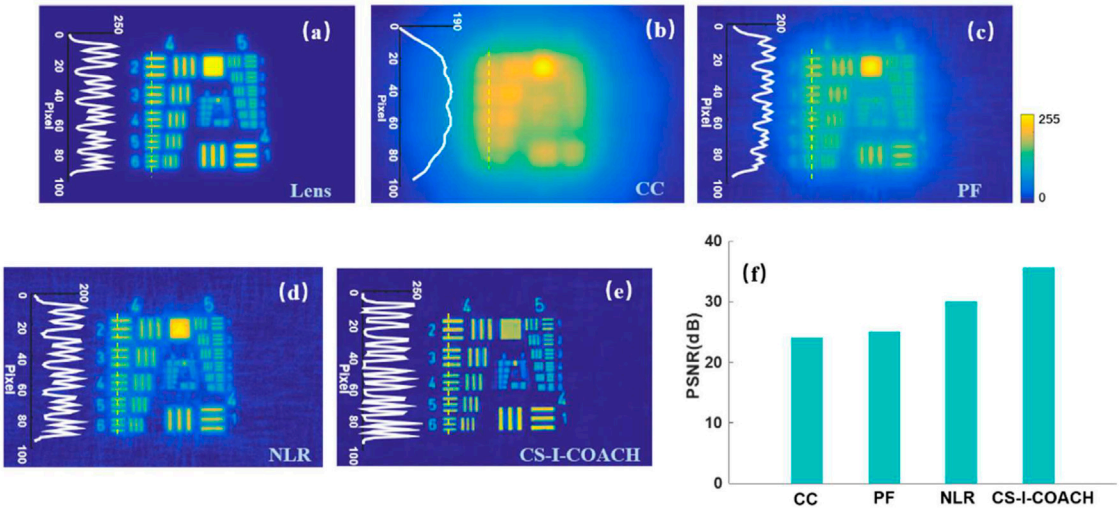

FIGURE 4 | Comparison of the results of different reconstruction methods of PSH and OH for single exposure. **(A)** Lens imaging; **(B)** cross-correlation; **(C)** phase filtered cross-correlation; **(D)** non-linear reconstruction with parameters $o = 0.8$ and $p = -0.2$; **(E)** our proposed CS-I-COACH compression reconstruction method; **(F)** the PSNR of the reconstructed images from different methods.

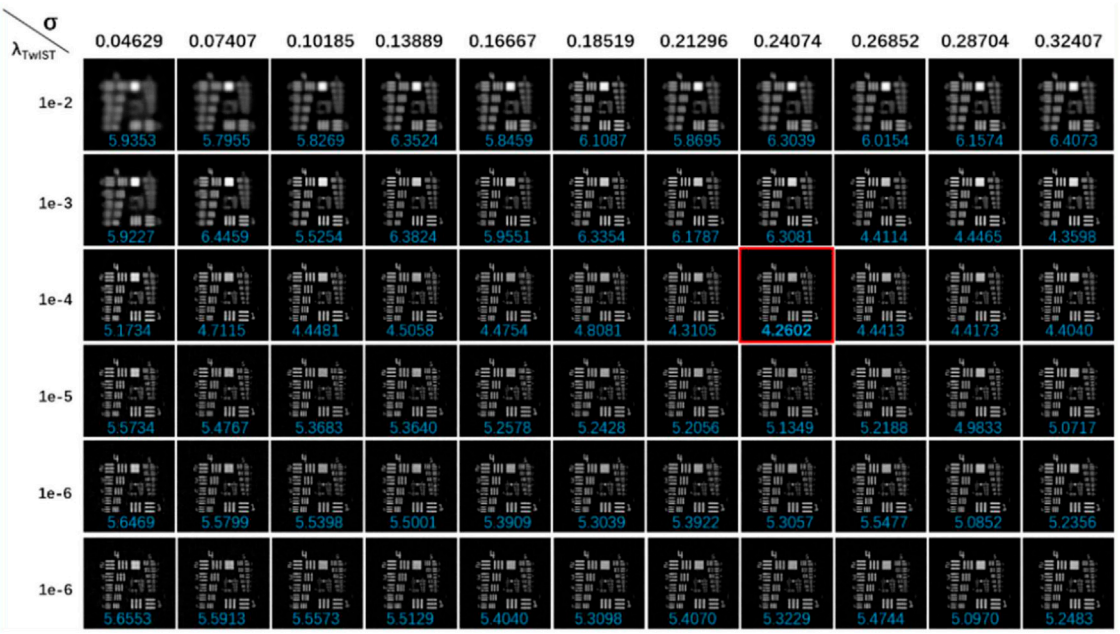

FIGURE 5 | The dependence of CS-I-COACH reconstruction accuracy on the scattering degrees σ of the CPM. Inserted blue-colored numbers indicate the entropy of the corresponding image.

Among those, one can notice that the CS-I-COACH reconstruction has better SNR than all the conventional I-COACH reconstruction methods and direct imaging results. It turned out to be that for all the different methods, CS-based I-COACH reconstructions can always have an improved PSNR by a factor of 45.8% (CC), 42% (PF), and 16.5% (NLR). Since additional processing is required in NLR methods to find the optimal modulation parameters (o and p in **Eq. 7**) (Liu et al., 2020), the more time-efficient phase-filtering-based methods (PF and CS-I-COACH) that provide similar imaging performance were used in the following experiments on 3D objects.

The CS reconstruction accuracy is highly correlated with the incoherence between the sparse operator (i.e., the sparsity transform matrix that has been applied on the object) and the imaging modal of the system (i.e., the matrix that describes the

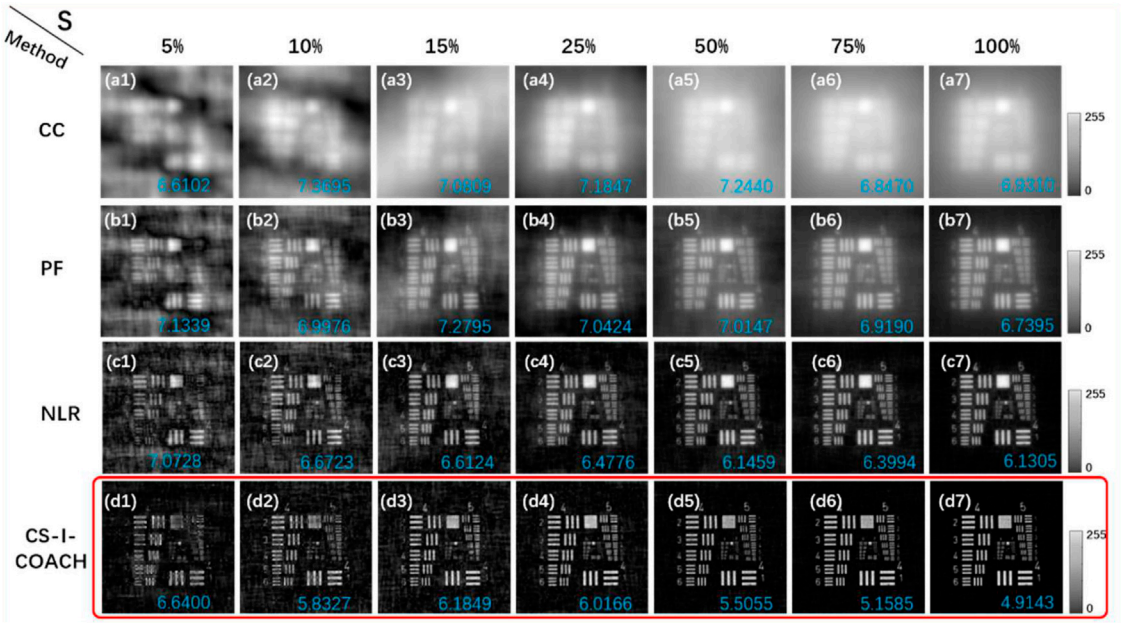

FIGURE 6 | Reconstructed images from under-sampled holograms using different methods. (a_1-a_7) Cross-correlation (CC), (b_1-b_7) phase filtering (PF), (c_1-c_7) non-linear reconstruction (NLR) with parameters o = 0.8 and p = −0.2, and (d_1-d_7) CS-I-COACH reconstructions.

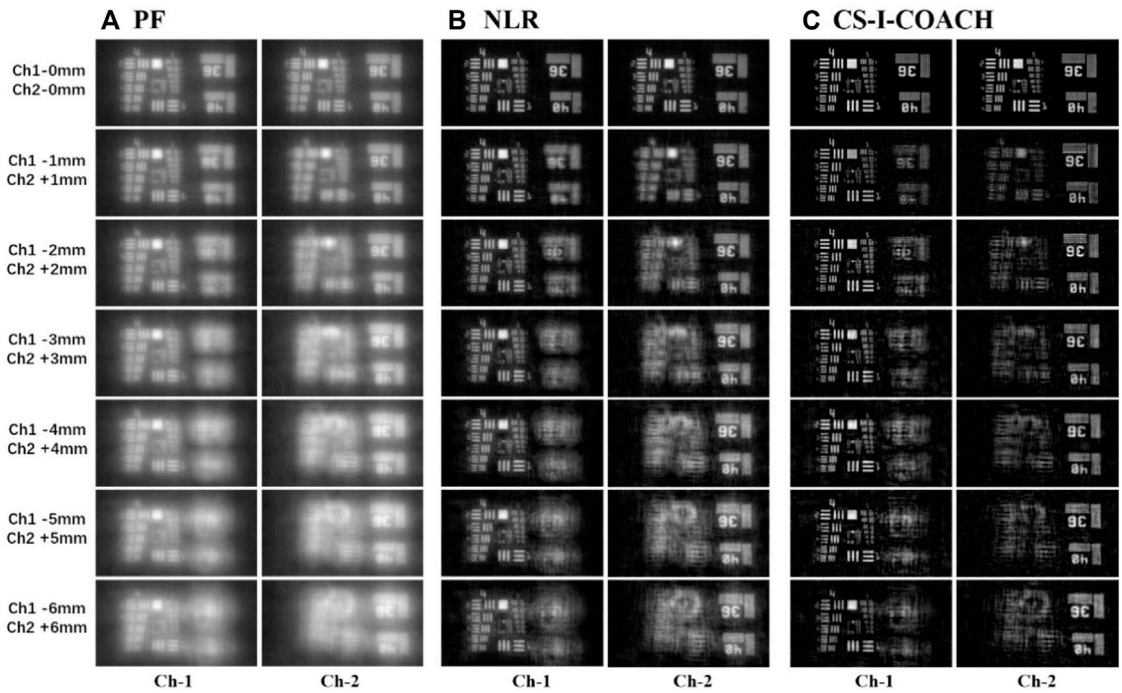

FIGURE 7 | Reconstructions of the 3D objects with different axial spaces in between using **(A)** PF, **(B)** NLR, and **(C)** CS methods.

transform relationship between the object and the measurement). The incoherence can be described theoretically by the number of the non-zero off-diagonal elements in the autocorrelation of the sensing matrix. In the I-COACH system, the incoherence can be controlled by using different scattering degrees σ of the CPM. To obtain the optimal scattering degree σ in the modified GS algorithm (Liu et al., 2020) corresponding to the best imaging quality

of the CS-I-COACH system, the entropy merit was used to quantitatively evaluate the quality of the reconstructed images in this paper (Men et al., 2017). Entropy is a measure of the disorder in a system, which in this case is maximized when the magnitude of the reconstructed image is distributed over the entire image plane and minimized when the entire image points are accumulated in the smallest area as possible. Therefore, for the relatively simple objects that have been used in the following experiments, a minimum entropy is expected to yield the reconstruction with the optimal SNR. From the intensity distribution function of the reconstructed image $O'(m,n)$, the entropy can be calculated as:

$$\mathfrak{R}_{en} = -\sum_{m}\sum_{n}\psi(m,n)\log[\psi(m,n)] \tag{9}$$

where m and n are the pixel coordinates of the image and $\psi(m,n) = \frac{|Q'(m,n)|}{\sum_m\sum_n Q'(m,n)}$. The dependence of the CS reconstruction accuracy (evaluated by the entropy of the reconstructed images, inserted blue-colored numbers) on the scattering degree σ of the CPM is shown in **Figure 5**. It was expected that higher accuracy would be obtained under higher σ. However, we found that this is not always true in our experiments and there exists an optimal value of σ that provides the reconstructed image with the relative optimal quality (indicated by the red rectangle in **Figure 5**). These can be explained by the fact that the imaging performances of the CS-I-COACH system are not disrupted only by the above-mentioned mathematical coherence, but also by physical factors such as the read-out noise of the camera and numerical factors in the reconstruction algorithm such as the coefficient of the regulator and iteration times.

We further demonstrated in our system one of the most interesting applications of CS in holography, i.e., the high-fidelity image retrieval from under-sampled holograms. The recorded holograms of the PSH and OH were down-sampled randomly in the spatial frequency domain, and then used to reconstruct the object image. The dependence of the reconstruction accuracy (again evaluated by the entropy of the image, inserted blue-colored values) on the sampling rate S is shown in **Figure 6**. That the CS reconstructed images still preserve a reasonable quality until S = 10% was found in the results. Meanwhile, under the sample condition, the reconstructions obtained using conventional reconstruction methods were dominated by the strong background noise.

In the next experiment the proposed method was used for 3D imaging. The 20 μm diameter pinhole was moved within a range of 12 mm (6 mm above and 6 mm below) around the front focal plane of L_0, with 1 mm step interval. The PSHs library at 13 different axial positions were then recorded. To simulate a 3D object, two transmission resolution targets (NBS, 1963A 1X R2L2S1N, and USAF 1951 1X, USAF GO Edmund optics), with an axial distance of 6 mm, were placed at the front focal plane of L_0, in Channel-1 and Channel-2, respectively. The line-groups of 4, 5 of the USAF targets, and the line-groups of 36 and 40 of the NBS target, were illuminated by the LED source. Initially, two targets were placed in the front focal plane of the lens L_0. Then, the two targets in Channels 1 and 2 are moved simultaneously in reverse directions at 1 mm step, and the corresponding 7 object holograms are recorded to simulate 13 different depth planes of the 3D objects. The reconstructed images obtained using different reconstruction methods are shown in **Figure 7**. It can be seen from the results that 3D imaging performances of I-COACH can be improved by the proposed method since the defocus images attenuate more quickly with the increase of the axial space in the CS reconstructions when comparing it with PF and NLR results.

CONCLUSION

In this paper, we have successfully suppressed the background noise and improved the reconstruction quality of the conventional I-COACH methods without sacrificing the imaging speed. This was achieved by establishing the compressive sensing model and then by numerically reconstructing the holograms under the CS framework. Our experimental results have demonstrated that the PSNR of the reconstructed images can be improved by a factor of 16.5% via the proposed method. Meanwhile, CS reconstructions can still preserve reasonable quality for a 10% under-sampled hologram. In our method, the 3D imaging performance of I-COACH was improved by suppressing the effects of out-of-focus images that are present in the reconstructions. With those improved system imaging performances, we believe the proposed CS-I-COACH method will benefit the research areas such as imaging through scattering medium and partial aperture imaging.

DATA AVAILABILITY STATEMENT

The original contributions presented in the study are included in the article/Supplementary Material, further inquiries can be directed to the corresponding author.

AUTHOR CONTRIBUTIONS

YW: Conceptualization, Methodology, Supervision, Writing-Reviewing and Editing, Project administration, Funding acquisition. CL: Software, Writing-Original draft preparation, Methodology, Investigation. TM: Conceptualization, Methodology, Software, Investigation.

FUNDING

National Natural Science Foundation of China (61575009); Natural Science Foundation of Beijing Municipality (4182016).

REFERENCES

Bioucas-Dias, J. M., and Figueiredo, M. A. T. (2007). A New TwIST: Two-step Iterative Shrinkage/Thresholding Algorithms for Image Restoration. *IEEE Trans. Image Process.* 16 (12), 2992–3004. doi:10.1109/tip.2007.909319

Brady, D. J., Choi, K., Marks, D. L., Horisaki, R., and Lim, S. (2009). Compressive Holography. *Opt. Express* 17 (15), 13040–13049. doi:10.1364/oe.17.013040

Brady, D. J., Mrozack, A., MacCabe, K., and Llull, P. (2015). Compressive Tomography. *Adv. Opt. Photon.* 7, 756–813. doi:10.1364/aop.7.000756

Cochran, G. (1966). New Method of Making Fresnel Transforms with Incoherent Light*. *J. Opt. Soc. Am.* 56 (11), 1513–1517. doi:10.1364/josa.56.001513

Lim, S. D., Marks, D. L., and Brady, D. J. (2011). Sampling and Processing for Compressive Holography [Invited]Sampling and Processing for Compressive Holography. *Appl. Opt.* 50 (34), H75–H86. doi:10.1364/ao.50.000h75

Liu, C., Man, T. L., and Wan, Y. H. (2020). Optimized Reconstruction with Noise Suppression for Interferenceless Coded Aperture Correlation Holography. *Appl. Opt.* 59 (6), 1769–1774.

Liu, C., Man, T. L., and Wan, Y. H. (2022). High-quality Interferenceless Coded Aperture Correlation Holography with Optimized High SNR Holograms. *Appl. Opt.* 61 (3), 661–668. doi:10.1364/ao.444783

Lohmann, A. W. (1965). Wavefront Reconstruction for Incoherent Objects. *J. Opt. Soc. Am.* 55 (11), 1555–1556. doi:10.1364/josa.55.1555_1

Men, G. F., Pascal, P., and Wang, H. Y. (2017). .Research Progress of Fresnel Incoherent Correlation Digital Holography. *Imaging Sci. Photochem.* 35 (2), 199–207.

Mertz, L., and Young, N. O. (1961). "Fresnel Transform of Images,". Editor K. J. Habell.Proceedings of the International Conference on Optical Instruments and Techniques.London: Chapman Hall, 305.

Rai, M. R., and Rosen, J. (2019). Noise Suppression by Controlling the Sparsity of the point Spread Function in Interferenceless Coded Aperture Correlation Holography (I-COACH). *Opt. Express* 27 (17), 24311–24323. doi:10.1364/oe.27.024311

Ratnam Rai, M., Vijayakumar, A., and Rosen, J. (2017). Single Camera Shot Interferenceless Coded Aperture Correlation Holography. *Opt. Lett.* 42 (19), 3992–3995. doi:10.1364/ol.42.003992

Rogers, G. L. (1950). .Gabor Diffraction Microscopy: the Hologram as a Generalized Zone-Plate. *Nature*, 166,237. doi:10.1038/166237a0

Stroke, G. W., and Restrick, R. C. (1965). Holography with Spatially Noncoherent Light. *Appl. Phys. Lett.* 7 (9), 229–231. doi:10.1063/1.1754392

Vijayakumar, A., Kashter, Y., Kelner, R., and Rosen, J. (2016). Coded Aperture Correlation Holography-A New Type of Incoherent Digital Holograms. *Opt. Express* 24 (11), 12430–12441. doi:10.1364/oe.24.012430

Vijayakumar, A., and Rosen, J. (2017). Interferenceless Coded Aperture Correlation Holography-A New Technique for Recording Incoherent Digital Holograms without Two-Wave Interference. *Opt. Express* 25 (12), 13883–13896. doi:10.1364/oe.25.013883

Wan, Y., Liu, C., Ma, T., Qin, Y., and Lv, S. (2021). Incoherent Coded Aperture Correlation Holographic Imaging with Fast Adaptive and Noise-Suppressed Reconstruction. *Opt. Express* 29, 8064–8075. doi:10.1364/oe.418918

Zhang, H., Cao, L. C., and Jin, G. F. (2018). Applications and Challenges of Compressed Imaging. *Sci. &Technology Rev.* 36 (10), 20–29.

Conflict of Interest: The authors declare that the research was conducted in the absence of any commercial or financial relationships that could be construed as a potential conflict of interest.

frontiers in Photonics

ORIGINAL RESEARCH
published: 28 March 2022
doi: 10.3389/fphot.2022.843860

Development of a Fringe Printer With 0.35 µm Pixel Pitch

Takeshi Yamaguchi and Hiroshi Yoshikawa*

Department of Computer Engineering, College of Science and Technology, Nihon University, Chiba, Japan

The development of computational devices can provide computer-generated holograms (CGH) of over 100 Giga-pixel easily. The performance improvement of the graphical processing unit makes calculations faster with a normal personal computer. In contrast, the output device of CGH is not reported much. Since CGH is a fringe pattern, high resolution and fine pixel pitch are required for the output device. We have been developing a direct fringe printer, which consists of a laser, an X-Y stage, an SLM, and optical parts available on the market. Our previous report presented a liquid crystal panel, which was used for SLM that had full HD resolution and 7 µm pixel pitch. Since the Pixel pitch of the liquid crystal panel is not small enough for CGH, the optical setup works to demagnify the pixel pitch of the printed fringe pattern. To record high resolution CGH, the calculated fringe pattern is split and exposed in tiles by the X–Y stage. The results showed a 0.44 µm pixel pitch and over 100 Gpixel CGHs. However, to output more high-quality CGH, the development of pixel pitch and resolution is very important. In this paper, we review the optical system of a fringe printer that achieved an output of 0.35 µm pixel pitch CGH. We also investigate the performance of the new fringe printer.

Keywords: Holography, computer-generated hologram, fringe pattern, high resolution, pixel pitch

OPEN ACCESS

Edited by:
Peter Wai Ming Tsang, City University of Hong Kong, Hong Kong SAR, China

Reviewed by:
Tomasz Kozacki, Warsaw University of Technology, Poland
Hongbo Zhang, Virginia Military Institute, United States

****Correspondence:***
Takeshi Yamaguchi
yamaguchi.takeshi89@nihon-u.ac.jp

Specialty section:
This article was submitted to Optical Information Processing and Holography, a section of the journal Frontiers in Photonics

Received: *27 December 2021*
Accepted: *02 March 2022*
Published: *28 March 2022*

Citation:
Yamaguchi T and Yoshikawa H (2022) Development of a Fringe Printer With 0.35 µm Pixel Pitch. Front. Photonics 3:843860. doi: 10.3389/fphot.2022.843860

INTRODUCTION

A holographic display can reconstruct true 3-D images that have the binocular parallax, convergence, accommodation, and so on. The hologram records the wavefront of the object beam as the interference fringe pattern with the reference beam. The fringe pattern can be calculated by the computer and is called a computer-generated hologram (CGH). As the recording wavefront, CGH is usually calculated from the virtual object. Calculated CGH is displayed on a spatial light modulator (SLM) and reconstructs the 3D image. However, there are two problems in the reconstruction with the conventional SLM. One is low pixel resolution, and the other is large pixel pitch. Both parameters are related to the viewing angle and size of the reconstructed 3D image. Therefore, commercially available SLM could not reconstruct a practical 3D image.

Some reports outline that the output high resolution CGH can be achieved with special devices. Reference (Hamano and Yoshikawa, 1998) uses an electron beam writer, which provides an excellent quality CGH. CGHs output using a laser lithography system has also been reported (Nishi and Matsushima, 2017). The quality of both CGHs is good, but both the equipment and running costs of the electron beam writer are very expensive. On the other hand, Sakamoto et al. have proposed a CGH printer with a CD-R writer (Sakamoto et al., 2004). The running cost of this system is very low, but the size of this CGH is limited by the size of the CD-R.

We have been developing a CGH output device named a fringe printer since 2004 (Yoshikawa et al., 2004). The fringe printer consists of a laser, an SLM, X-Y moving stage, and optical components available on the market. Since output CGH is recorded to the holographic plate or

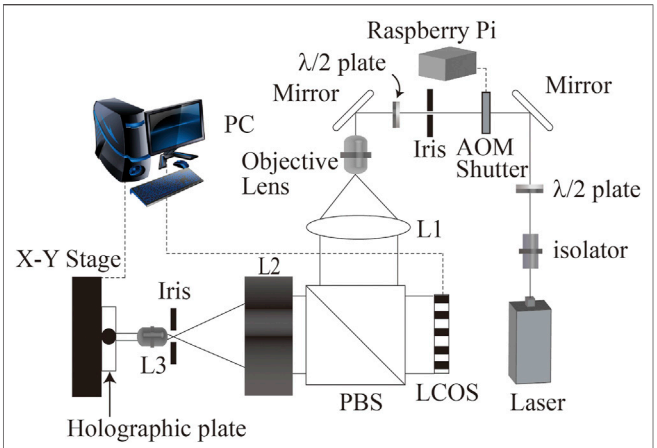

FIGURE 1 | Schematic of the fringe printing system. L1 is a collimator lens. Lenses L2 and L3 work as the telecentric imaging system to demagnify the image of LCOS. PBS is a polarizing beam splitter.

film, the running cost of the fringe printer is not expensive. Our previous paper, discusses a printed CGH of 129 Gpixels (412,800 × 307,200) with a pixel resolution of 0.44 μm and 8 bits gray-scale level (Nakaguchi et al., 2010; Yoshikawa et al., 2013). In the present paper, we achieved and developed fringe printer outputs of 0.35 μ m pixel pitch CGH by changing the lens pair of the optical reduction system. Additionally, we confirmed the specification of the developed fringe printer.

COMPUTER-GENERATED HOLOGRAM

CGH is usually defined as the numerical simulation of the interference fringe pattern or its output. The interference fringe pattern is formed by the wavefront of the object beam and the wavefront of the reference beam. Since no material can record optical phase information directly, it is necessary to introduce the reference beam to encode the phase information as an interference fringe pattern that is represented as the intensity distribution. The pixel pitch d of the interference fringe pattern is described as

$$d = \frac{\lambda}{2\left(\sin\theta_{obj} - \sin\theta_{ref}\right)}, \tag{1}$$

where λ is the free space wavelength of the light, θ_{obj} and θ_{ref} are the incident angles of the object beam and the reference beam, respectively.

Geometrical 3D models are usually employed to record the object of CGH. To calculate the wavefront of the object beam, a 3D model was supposed to be a collection of the self-illuminated points. Each point has 3D coordinates, real-valued amplitudes of three primary colors of light, and relative phase. The fringe pattern is calculated by the collection of spherical waves from each object point. It is, therefore, necessary to set several parameters, such as object size and position, pixel pitch, resolution, reference beam, and so on, to be determined. Each parameter is also suitable for **Eq. 1**. In the CGH, fine pixel pitch and high resolution provide

TABLE 1 | Components of the fringe printer.

(0.1em) component Name	Parameter name	Value
Blue laser [BLK73100TS (LASOS)]	Wavelength (nm)	473
	Power (mW)	100
L2 [TTL200 (Thorlabs)]	focal length (mm)	200
L3 [CFI Plan Apo λ 20x (Nikon)]	focal length (mm)	10
X Stage [KXL06300-C2-FC (Suruga Seiki Co.)]	Moving area (mm)	300
Y Stage [KXL06200-N2-FC (Suruga Seiki Co.)]	Moving area (mm)	200
AOM [AOMO 3080-125 (Gooch and Housego)]	Operating Frequency (MHz)	80
LCOS [Video Projector VPL-VW50 (Sony)]	Resolution (pixels)	1,920 × 1,080
	Pixel pitch (μm)	7.0

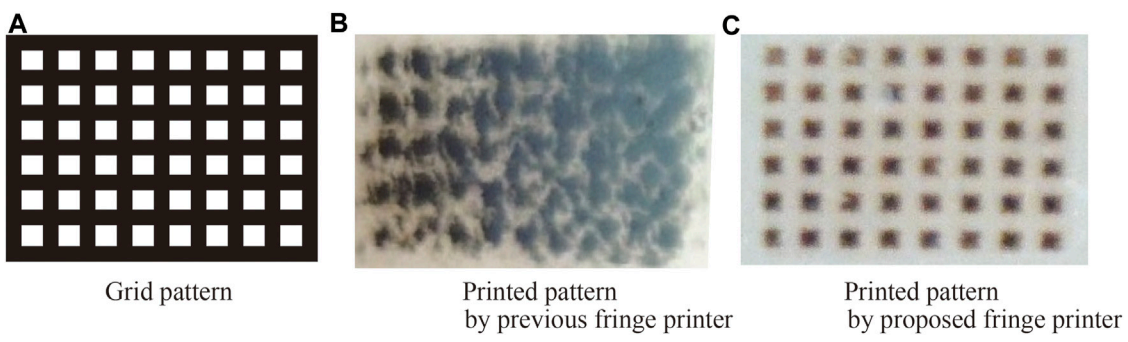

FIGURE 2 | Comparison of the printed patterns according to the lens distortion(White areas are printed block as negative image.)

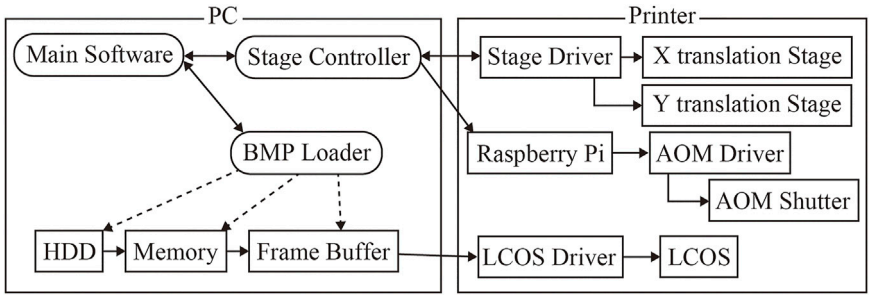

FIGURE 3 | Block diagram of the fringe printer system.

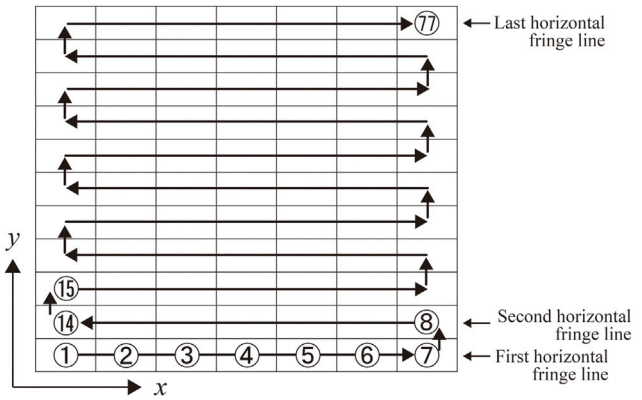

FIGURE 4 | Exposure order on the X-Y stage.

a wide viewing angle and a large image size of reconstructed image.

CGH can be categorized into two types: one is the plane type on which the fringe pattern is constructed into the surface direction; the other is volume type which the fringe pattern is constructed into thickness direction. The fringe printer can output the plane type CGH. We have also developed a volume type CGH printer (Yamaguchi et al., 2017). Due to the difference in shape or position of the reconstructed image, there are many plane type CGHs. Our group has published several plane type CGH such as Fresnel type, image type (Yamaguchi and Yoshikawa, 2011), rainbow type (Yoshikawa and Taniguchi, 1999), cylindrical type (Yamaguchi et al., 2008) and alcove type (Yamaguchia et al., 2011). Image type and rainbow type CGHs reconstruct a 3D image that is placed on or close to the hologram, and these holograms are collectively referred to as image type CGH. The pixel pitch of image type CGH affects the viewing angle of the reconstructed image, and the size of image type CGH affects the size of the reconstructed image. On the other hand, the pixel pitch of Fresnel type CGH affects the size of the reconstructed image, and the size of the Fresnel type CGH affects the viewing angle of the reconstructed image. Therefore, the output device of plane type CGH requires fine pixel pitch and high resolution.

OPTICAL SYSTEM OF FRINGE PRINTER

The optical system of the fringe printer is shown in **Figure 1** The fringe printer has a laser (473 nm), an LCOS (a liquid crystal on silicon) as an SLM, an X-Y translation stage, an acousto-optic modulator (AOM) shutter with Raspberry Pi, optics, and a control computer. The AOM is used together with the iris. It can be used as a shutter by transmitting the first-order diffracted light that is generated when the modulation signal is turned on. The LCOS used in this study is a disassembled projector. Therefore, when displaying a calculated fringe pattern on the LCOS, it can be displayed through the hardware of the projector.

Important parameters of output CGH are pixel pitch and resolution. A lens pair of L2 and L3 are used for fine pixel pitch. Since the pixel pitch of LCOS is not small enough for practical CGH for 3D display, the reflected beam from LCOS is reduced by a lens pair of L2 and L3. Demagnification ratio M is described as,

$$M = \frac{f_3}{f_2}, \tag{2}$$

where f_2 and f_3 are focal length of L2 and L3, respectively. In our system, a part of the computed fringe pattern is displayed on the LCOS that gives the intensity modulation to the illuminated light, and a plane hologram can be output by reducing and exposing it with this optical system.

In our previous report, the demagnification ratio was 1/16 and the pixel pitch of output CGH was 0.44 μm (Yamaguchi et al., 2009b). **Table 1** shows the specifications of the printer components. In this paper, we changed lenses L2 and L3 whose focal length is 200 and 10 mm, respectively. The new demagnification ratio is 1/20 and the pixel pitch of output CGH is 0.35 μm. An iris, which is located between L2 and L3, filtered the high order diffraction and the diffraction due to the LCOS structure. Many lens pairs show a better demagnification ratio. However, each lens must pass not only the non-diffracted beam but also the diffracted beam, large ±1-st order diffraction image occurs around L3. Therefore, L3 requires a small F-number. In the previous fringe printer, a Fresnel lens was employed to fulfill the small F-number. **Figure 2** shows the output patterns by the previous and proposed fringe printer. Since the previous system employs the Fresnel lens, the output pattern by the previous system was not printed sharply by the lens distortion. On the

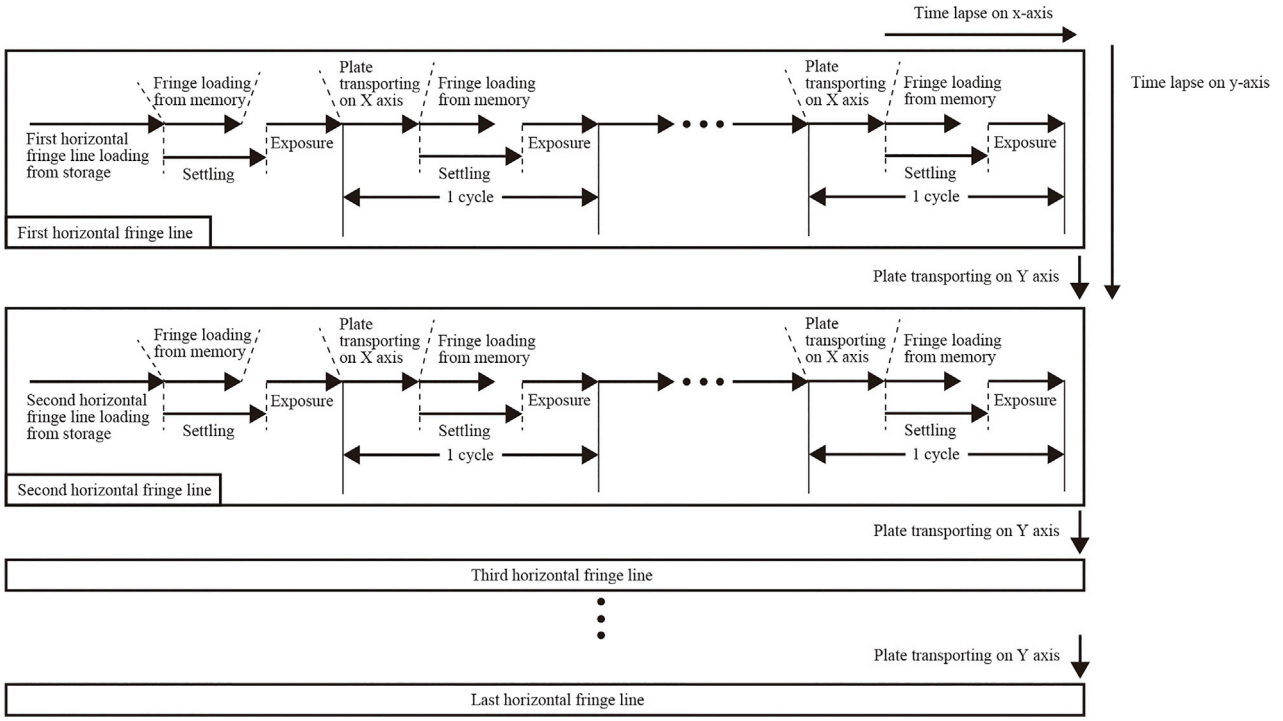

FIGURE 5 | Recording process timechart for the fringe printer.

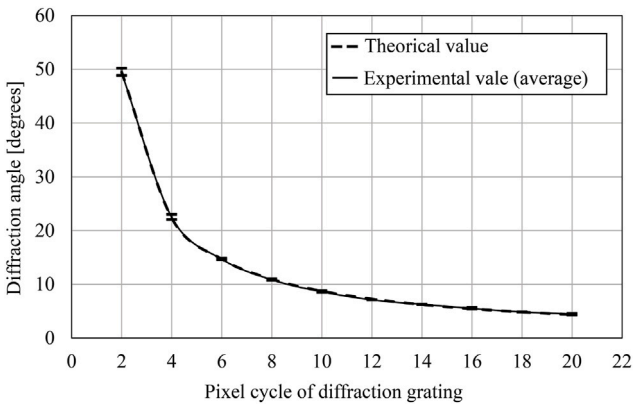

FIGURE 6 | A variation of the diffraction angle according to the pixel pitch of the diffraction grating.

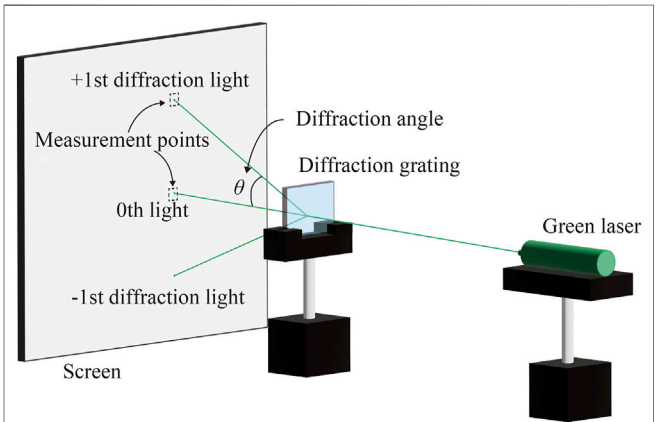

FIGURE 7 | Schematic of the measurement system.

other hand, the output pattern by the proposed system is printed sharply.

The X-Y stage is used for tiling of fringe pattern which is displayed on LCOS. Since the resolution of LCOS is not suitable for CGH, the fringe printer repeats exposure. The AOM with Raspberry Pi are used as a shutter. The Raspberry Pi sends a signal to control an open/close operation. Since the number of shutter operations necessary to output one CGH exceed 10,000, for example, 300,000 × 150,000 pixels CGH requires 10,981 times shutter operations, the fringe printer does not employ a mechanical shutter. In our previous fringe printer, a mechanical shutter is used. However, since the durable number of the mechanical shutter is around one million, around 100 times the output exceeds the shutter's durable number. On the other hand, the AOM shutter is an electronic shutter, so it is suitable for a fringe printer.

COMPUTATIONAL OPERATION

Three software packages control the fringe printer. The first software, named BMP Loader, displays part of the fringe

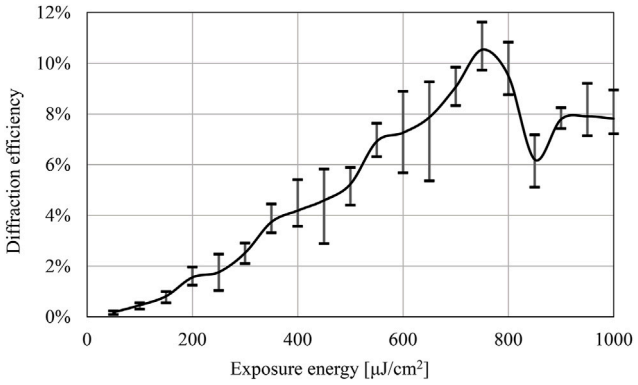

FIGURE 8 | A variation of the diffraction efficiency according to exposure energy (Settling time: 1,500 msec)

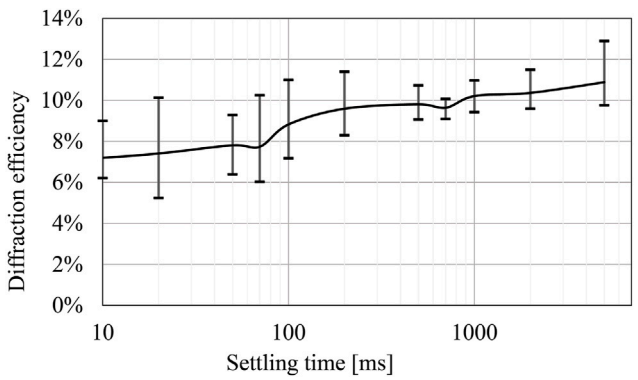

FIGURE 9 | A variation of the diffraction efficiency according to the settling time (Sutter time: 1.3 msec)

pattern on the LCOS panel. The second software, named the Stage Controller, controls the X-Y stage and the AOM shutter. The third software, named the Main Software, manages and connects each software. **Figure 3** shows a simple block diagram of the proposed fringe printing system. These software perform serial communication, and each software runs independently.

Tiling exposure sequence requires a computational operation. **Figure 4** shows the exposure order of divided fringe pattern on the X-Y stage. **Figure 5** shows the exposure and translation timing for the tiling exposure cycle. Since the image capacity of the fringe pattern sometimes exceeds 100 GB, the whole fringe pattern cannot be stored in the main memory. Therefore, the fringe printer stores a single fringe line, for example, a single fringe line of 300,000 × 150,000 pixels CGH is 300,000 × 1,080, which is determined by the vertical resolution of LCOS. Each fringe pattern is displayed on LCOS and is stored in the frame buffer before exposure. There is also a settling time after stage translation to suppress the stage vibration. As an example, when the exposure time was 15 msec and the settling time was 900 msec, the duration of one cycle was 1.49 msec, although it depended on the exposure conditions.

PERFORMANCE OF FRINGE PRINTER

To verify the specification of proposed fringe printer, several experiments were performed. The first parameter is the diffraction angle. The demagnification ratio of the proposed fringe printer has been improved from 1/16 to 1/20. Therefore, diffracted light by the output CGH is measured. The second parameter is the diffraction efficiency. The fringe printer uses the recording material that is VRP–M manufactured by Slavich. The VRP-M is silver halide photomaterial and green–blue sensitive. In the usual holographic recording, the proper exposure energy of VRP-M is 75–100 μJ/cm^2. However, single exposure of the fringe printer is a small area, and exposure time is very short compared with usual holographic recordings. Therefore, the diffraction grating is used for the measurement of the diffraction efficiency. Enough settling time is also revealed by the experimental result. In each measurement, the output pattern of the fringe printer is bleached and turns into the phase hologram from the amplitude hologram.

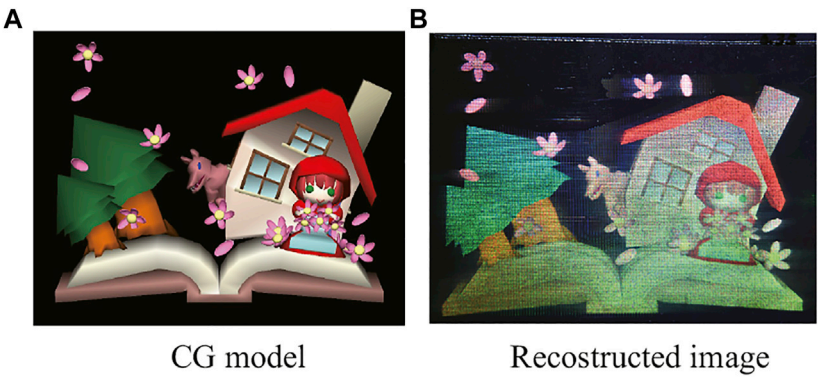

FIGURE 10 | Reconstructed image of computer-generated rainbow hologram.288,080 × 194,560 pixels. **A**: Perspective image of the object. **B**: Photo of the optically reconstructed image.

Diffraction Angle

To measure the diffraction angle, the diffraction gratings of the different cycles are prepared. These diffraction gratings have 9,600 × 6,480 pixels and are output by the fringe printer. **Figure 6** shows the experimental result of the diffraction angle against the cycle of the diffraction grating. A schematic of the measurement system is shown in **Figure 7**. The theoretical value in **Figure 6** is defined as follows,

$$\sin\theta = \frac{\lambda}{2d}, \tag{3}$$

The graph shows the experimental result is almost the same as the theoretical value. Therefore, the proposed system can output finer pixel pitch CGH than the previous system. The larger diffraction angle makes it possible to reproduce a larger image in general Fresnel holograms when the incident angle of the reference beam is the same. On the other hand, image-type holograms can provide a wider viewing area when the incident angle of the reference beam is the same.

Diffraction Efficiency

To obtain the optimum exposure parameter of the fringe printer, the exposure energy and the settling time are measured. **Figure 8** shows the variation of the relative diffraction efficiency (International Organization for Standardization, 2015) according to the single exposure energy of the fringe printer. The diffraction grating had enough settling time when it was output. **Figure 9** shows the variation of diffraction efficiency according to the settling time. The X-Y stage is used to change the exposure position during the output. If there is any vibration left after the movement, the fringe pattern cannot be recorded correctly, so sufficient settling time is required. Both measurements used **Figure 7**, and the diffraction efficiency is obtained from the ratio of the transmitted laser power and the +first order diffraction light power. **Figure 8** shows the proper exposure energy is about 750 μJ/cm^2. **Figure 9** shows the stable settling time is over 700 ms.

Reconstructed Image

Figure 10 shows the reconstructed image of the computer-generated rainbow hologram (CGRH) by the proposed fringe printer. The computational method of CGRH is described in detail in Ref. (Yamaguchi and Yoshikawa, 2018).

CONCLUSION

This paper has proposed an improved fringe printer with new lens pair to reduce pixel pitch. The new fringe printer can output CGH with a pixel pitch of 0.35 μm. We measured the diffraction angle of the output diffraction grating and confirmed the accuracy of the optical system. We also measured the suitable condition of the exposure. The new fringe printer can provide a large 3D image or a wide viewing area compared with the previous fringe printer. The authors have output various other holograms, such as a computer-generated disk hologram (Yamaguchi et al., 2009a), a holographic stereogram, a computer-generated image hologram (Yamaguchi and Yoshikawa, 2011), and a computer-generated alcove hologram (Yamaguchia et al., 2011), and plan to output them with the new fringe printer in the future.

DATA AVAILABILITY STATEMENT

The original contributions presented in the study are included in the article/Supplementary Material, further inquiries can be directed to the corresponding author.

AUTHOR CONTRIBUTIONS

Conceptualization, TY and HY; methodology, TY and HY; software, TY; validation, TY and HY; formal analysis, TY and HY; investigation, TY; resources, TY and HY; data curation, TY; writing—original draft preparation, TY; writing—review and editing, TY and HY; visualization, TY; supervision, TY; All authors contributed to manuscript revision, read, and approved the submitted version.

ACKNOWLEDGMENTS

The authors would like to thank T. Iwamoto and M. Miyazawa for technical assistance with the experiments. The authors also thank Team–Opt Corp. for technical advice with the optical design.

REFERENCES

Hamano, T., and Yoshikawa, H. (1998). Image-type CGH by Means of E-Beam Printing. *Proc. SPIE* 3293, 2–14.doi:10.1117/12.303638

International Organization for Standardization (2015). *Optics and Photonics – Holography – Part 1: Methods of Measuring Diffraction Efficiency and Associated Optical Characteristics of Holograms*. Geneva. ISO 17901-1:2015.

Nakaguchi, Y., Yamaguchi, T., and Yoshikawa, H. (2010). Computer-generated Rainbow Hologram over 100 Giga-Pixel. *Int. Conf. 3D Syst. Appl.*, 107–110.

Nishi, H., and Matsushima, K. (2017). Rendering of Specular Curved Objects in Polygon-Based Computer Holography. *Appl. Opt.* 56, F37–F44. doi:10.1364/ao.56.000f37

Sakamoto, Y., Morishima, M., and Usui, A. (2004). Computer-generated Holograms on a CD-R Disk. *SPIE Proc. Pract. Holography XVIII* 5290, 28–34. doi:10.1117/12.526504

Yamaguchi, T., Fujii, T., and Yoshikawa, H. (2009a). Disk Hologram Made from a Computer-Generated Hologram. *Appl. Opt.* 48, H16–H22. doi:10.1364/ao.48.000h16

Yamaguchi, T., Matuoka, M., Fujii, T., and Yoshikawa, H. (2009b). "Development of Fringe Printer and its Practical Applications," in Proceedings of the 8th International Symposium on Display Holography.

Yamaguchi, T., Fujii, T., and Yoshikawa, H. (2008). Fast Calculation Method for Computer-Generated Cylindrical Holograms. *Appl. Opt.* 47, D63–D70. doi:10.1364/ao.47.000d63

Yamaguchi, T., Miyamoto, O., and Yoshikawa, H. (2012). Volume Hologram Printer to Record the Wavefront of Three-Dimensional Objects. *Opt. Eng.* 51 (1–7), 075802.doi:10.1117/1.OE.51.7.075802

Yamaguchi, T., and Yoshikawa, H. (2011). Computer-generated Image Hologram. *Chin. Opt. Lett.* 9 (1–4), 120006. doi:10.3788/COL201109.120006

Yamaguchi, T., and Yoshikawa, H. (2018). High Resolution Computer-Generated Rainbow Hologram. *Appl. Sci.* 8, 1955. doi:10.3390/app8101955

Yamaguchia, T., Ozawa, H., and Yoshikawaa, H. (2011). Computer-generated Alcove Hologram to Display Foating Image with Wide Viewing Angle. *Proc. SPIE* 7959 (1–10), 795719.

Yoshikawa, H., and Takei, K. (2004). Development of a compact direct fringe printer for computer-generated holograms,. *Proc. SPIE* 5290, 114–121.doi:10.1117/12.526516

Yoshikawa, H., and Taniguchi, H. (1999). Computer Generated Rainbow Hologram. *Opt. Rev.* 6, 118–123. doi:10.1007/s10043-999-0118-0

Yoshikawa, H., Yamaguchi, T., and Kajiro, S. (2013). Direct Fringe Printer for Computer-Generated Holograms: Improvement of Printing Speed. *SPIE Proc. Pract. Holography XXVII* 8644, 12–15. doi:10.1117/12.2002023

Conflict of Interest: The authors declare that the research was conducted in the absence of any commercial or financial relationships that could be construed as a potential conflict of interest.

frontiers in Photonics

REVIEW
published: 28 March 2022
doi: 10.3389/fphot.2022.854391

Deep-Learning Computational Holography: A Review

Tomoyoshi Shimobaba[1]*, *David Blinder*[2,3], *Tobias Birnbaum*[2,3], *Ikuo Hoshi*[1], *Harutaka Shiomi*[1], *Peter Schelkens*[2,3] *and Tomoyoshi Ito*[1]

[1]Graduate School of Engineering, Chiba University, Chiba, Japan, [2]Department of Electronics and Informatics (ETRO), Vrije Universiteit Brussel, Brussel, Belgium, [3]IMEC, Leuven, Belgium

Deep learning has been developing rapidly, and many holographic applications have been investigated using deep learning. They have shown that deep learning can outperform previous physically-based calculations using lightwave simulation and signal processing. This review focuses on computational holography, including computer-generated holograms, holographic displays, and digital holography, using deep learning. We also discuss our personal views on the promise, limitations and future potential of deep learning in computational holography.

Keywords: computer-generated hologram, deep learning, digital holography, digital holographic microscopy, microscopy, neural network, three-dimensional display

OPEN ACCESS

Edited by:
Peter Wai Ming Tsang, City University of Hong Kong, Hong Kong SAR, China

Reviewed by:
Ni Chen, King Abdullah University of Science and Technology, Saudi Arabia
Inkyu Moon, Daegu Gyeongbuk Institute of Science and Technology (DGIST), South Korea
Prathan Buranasiri, King Mongkut's Institute of Technology Ladkrabang, Thailand

***Correspondence:**
Tomoyoshi Shimobaba
shimobaba@faculty.chiba-u.jp

Specialty section:
This article was submitted to Optical Information Processing and Holography, a section of the journal Frontiers in Photonics

Received: *13 January 2022*
Accepted: *28 February 2022*
Published: *28 March 2022*

Citation:
Shimobaba T, Blinder D, Birnbaum T, Hoshi I, Shiomi H, Schelkens P and Ito T (2022) Deep-Learning Computational Holography: A Review. Front. Photonics 3:854391. doi: 10.3389/fphot.2022.854391

1 INTRODUCTION

Holography (Gabor, 1948) can record three-dimensional (3D) information of light waves on a two-dimensional (2D) hologram as well as reproduce the 3D information from the hologram. Computer-generated holograms and holographic 3D measurements (digital holography) can be realized by simulating this physical process on a computer. Computer-generated holograms can be generated by calculating light wave propagation (diffraction) emitted from 3D objects. If this hologram is displayed on a spatial light modulator (SLM), the 3D image can be reproduced in space. Holographic displays can successfully reproduce the wavefront of 3D objects, making them ideal 3D displays (Hilaire et al., 1990; Takaki and Okada, 2009; Chang et al., 2020).

In contrast, digital holography (Goodman and Lawrence, 1967; Kim, 2010; Liu et al., 2018; Tahara et al., 2018) is a technique that uses an image sensor to capture a hologram of real macroscale objects or cells. Diffraction calculations are used to obtain numerically reproduced images from the hologram. Digital holography has been the subject of much research in 3D sensing and microscopy. In addition to coherent light, the technique of capturing holograms with incoherent light has been actively studied in recent years (Liu et al., 2018; Rosen et al., 2019).

Computational holography is the general term for handling holography on a computer. It has been widely used in 3D display, projection, measurement, optical cryptography, and memory. The following are common problems of computational holography that need to be addressed:

(1) A high computational complexity for hologram and diffraction calculations.
(2) A limited image quality of the reproduced images from holograms, due to speckle noise, optical abberations, etc.
(3) A large amount of data required to store holograms.

The computational complexity of hologram calculations increases with the complexity of 3D objects and the resolution of a hologram. Digital holography requires diffraction calculations to obtain the complex amplitude of object light, followed by aberration correction of the optical system,

and phase unwrapping, if necessary. Additionally, autofocusing using an object position prediction may be necessary. These are time-consuming calculations.

The quality of the reproduced images from a hologram is also a critical issue in holographic displays and digital holography. The following factors degrade reproduced images: high-order diffracted light due to the pixel structure of SLMs, quantized and non-linear light modulation of SLMs, alignment accuracy, and aberration of optical systems.

The amount of data in holograms is also a major problem. Data compression is essential for real-time hologram transmission and wide-viewing-angle holographic displays, which require holograms with a large spatial bandwidth product (Blinder et al., 2019). Hologram compression using existing data compression methods, such as JPEG and JPEG2000, and original compression methods for hologram have been investigated (Blinder et al., 2014; Birnbaum et al., 2019; Stepien et al., 2020) and recently the JPEG committee (ISO/IEC JTC 1/SC 29/WG 1) initated the standardization of compression technology for holographic data.

Many studies have developed algorithms based on the physical phenomena of holography (diffraction and interference of light) and signal processing. In this paper, we refer to these algorithms as physically-based calculation. In 2012, AlexNet (Krizhevsky et al., 2012), which uses deep neural networks (DNNs), achieved an improvement of more than 10% over conventional methods in the ImageNet large-scale visual recognition challenge, a competition for object recognition rates. This led to a great deal of interest in deep learning (LeCun et al., 2015). In 2017, research using deep learning started increasing in computational holography. Initially, simple problems using deep learning, such as the hologram identification problem and restoration of holographic reproduced images, were investigated (Shimobaba et al., 2017a; Shimobaba et al., 2017b; Jo et al., 2017; Muramatsu et al., 2017; Pitkäaho et al., 2017). Currently, more complex deep-learning-based algorithms have been developed, and many results have been reported that outperform physically-based calculations.

This review presents an overview of deep-learning-based computer-generated hologram and digital holography. In addition, we outline diffractive neural networks, which are closely related to holography. It is worth noting that deep learning outperforms conventional physically-based calculations in terms of computational speed and image quality in several holographic applications. Additionally, deep learning has led to the development of techniques for inter-converting images captured by digital holographic and other microscopes, blurring the boundaries between research areas. Furthermore, we will discuss our personal views on the relationship between physically-based calculations and deep learning in the future.

2 HOLOGRAM COMPUTATION USING DEEP LEARNING

Computer-generated holography has many applications, such as 3D display (Hilaire et al., 1990; Takaki and Okada, 2009; Chang et al., 2020), projection (Buckley, 2011; Makowski et al., 2012), beam generation (Yao and Padgett, 2011), and laser processing (Hasegawa et al., 2006). This section focuses on hologram calculations for holographic display applications.

Figure 1 shows the data processing pipeline of holographic displays. From 3D data, acquired using computer graphics and 3D cameras, the distribution of light waves on a hologram is calculated using diffraction theory. The generated hologram is usually complex-valued data (complex holograms); however, SLMs can only modulate amplitude or phase. Therefore, we must encode the complex hologram into amplitude or phase-only holograms. The encoded hologram can be displayed on the SLM and the 3D image can be observed through the optical system.

The 3D data format handled in physically-based hologram calculations can be classified into four main categories: point cloud (Lucente, 1993; Yamaguchi et al., 1993; Kang et al., 2008; Shimobaba et al., 2009; Hiroshi Yoshikawa and Yoshikawa, 2011; Blinder and Schelkens, 2020), polygon (Ahrenberg et al., 2008; Matsushima and Nakahara, 2009; Zhang et al., 2018a), layered (RGBD images) (Okada et al., 2013; Chen et al., 2014; Chen and Chu, 2015; Zhao et al., 2015), and light field (multiviewpoint images) (Yatagai, 1976; Zhang et al., 2015). Fast computation methods for each 3D data format have been proposed (Shimobaba et al., 2015; Nishitsuji et al., 2017; Tsang et al., 2018; Blinder et al., 2019). For the hologram computation using deep learning, some research has been conducted on the point cloud method (Kang et al., 2021). However, the layer method has been the focus of research using deep learning. To the best of our knowledge, polygon and light-field methods using deep learning have not been investigated yet.

2.1 Supervised Learning

In 1998, hologram generation using a neural network with three fully-connected layers was investigated (Yamauchi et al., 1998). However, this is not deep learning, but it is similar to current deep-learning-based hologram calculations. To the best of our knowledge, this is the pioneering work using neural networks for hologram computation. It performed end-to-end learning to train the neural network using a dataset consisting of 16 × 16-pixel input images and holograms. The end-to-end learning method is a supervised learning technique and allows a DNN to learn physical processes used in physically-based calculations from a dataset alone. This study showed that the neural network could optimize holograms faster than direct binary search (Seldowitz et al., 1987). It was impossible to adopt the current deep network structure due to poor computing resources. Additionally, even if DNN could be created, there was no algorithm (optimizer) to optimize its large number of parameters. For a while, neural networks were not the mainstream in hologram calculation, and physically-based calculations were actively studied. However, since 2018, hologram calculations have developed rapidly using deep learning.

Figure 2 shows the DNN-based hologram computation using supervised learning. Horisaki et al. (2018) designed a DNN that directly infers holograms from input 2D images using end-to-end learning. For end-to-end learning, it is necessary to prepare a large dataset of input images $\mathcal{X}$ and their holograms $\mathcal{Y}$. DNNs can be represented as an arbitrary function by combining

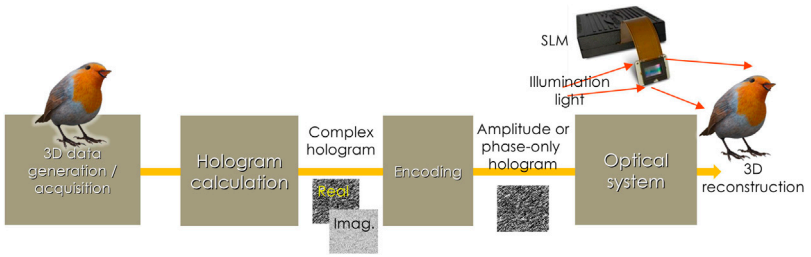

FIGURE 1 | Data processing pipeline for holographic displays.

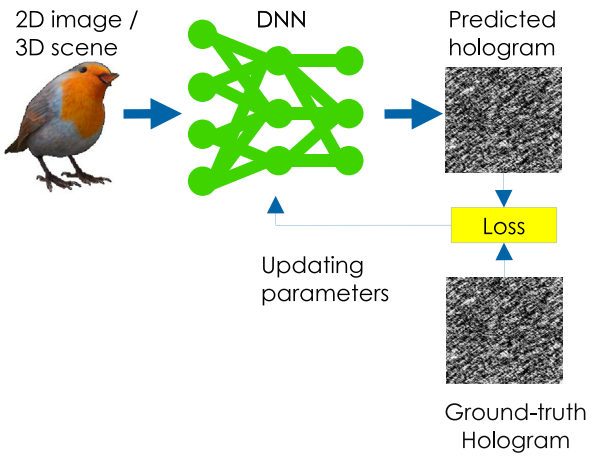

FIGURE 2 | Deep neural network-based hologram computation using supervised learning.

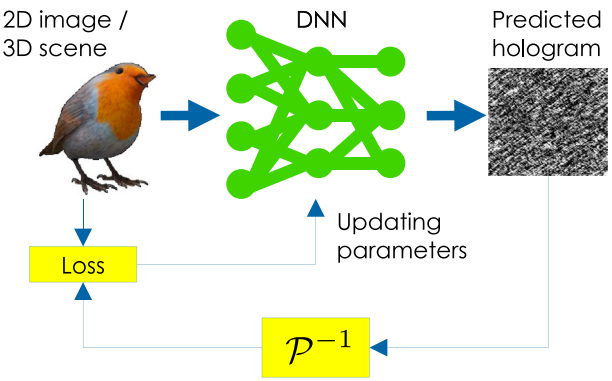

FIGURE 3 | Deep neural network-based hologram calculation using unsupervised learning.

convolutional and other layers with nonlinear activation functions. In this paper, a DNN function is represented as $\mathcal{N}(\mathcal{X};\Theta)$, where Θ are the network parameters. The parameters Θ of the DNN in Horisaki et al. (2018) are updated by solving the minimization problem:

$$\underset{\Theta}{\text{minimize}}\ \mathcal{L}(\mathcal{N}(\mathcal{X};\Theta),\mathcal{Y}), \tag{1}$$

where $\mathcal{L}$ is the loss function for calculating the error between the predicted hologram output from the DNN ($\mathcal{N}(\mathcal{X};\Theta)$) and the ground-truth hologram ($\mathcal{Y}$). This DNN can infer a hologram from a 64×64-pixel 2D image several times faster, and the image quality is the same as obtained with the Gerchberg–Saxton (GS) algorithm (Gerchberg, 1972; FienupFienup, 1982).

Goi et al. (2020) proposed a method for generating binary holograms from 2D images directly using DNN. This study prepared a dataset of binary random patterns (binary holograms) and its reproduced images (original objects). The DNN was trained using end-to-end learning with the reproduced images as input of the DNN and the binary holograms as output. The output layer of the DNN should be a step function since it should be able to output binary values; however, this is not differentiable. The study Goi et al. (2020) used a differentiable activation function that approximates the step function.

2.2 Unsupervised Training

Unsupervised learning does not require the preparation of a dataset consisting of original images and its holograms, as discussed in **Section 2.1**. **Figure 3** shows the DNN-based hologram calculation using unsupervised learning (Hossein Eybposh et al., 2020; Horisaki et al., 2021; Wu et al., 2021). We input the original 3D scene (or 2D image) $\mathcal{X}$ into the DNN and compute an inverse diffraction calculation ($\mathcal{P}^{-1}$) from the predicted hologram to the location of the original object to obtain the reproduced image. We calculate a loss function between the reproduced image and the original data. Then, we update the DNN parameters by solving the following minimization problem:

$$\underset{\Theta}{\text{minimize}}\ \mathcal{L}(|\mathcal{P}^{-1}(\mathcal{N}(\mathcal{X};\Theta))|,\mathcal{X}). \tag{2}$$

We can use any diffraction calculation for the propagation calculation, provided that it is differentiable. We usually use the angular spectrum method (Goodman and Goodman, 2005). The lightwave distribution on a plane u_d, which is z away from a plane u_s, can be calculated using the angular spectrum method expressed as follows:

$$u_d = \mathcal{P}(u_s) = \mathcal{F}^{-1}\left(\mathcal{F}(u_s)\exp\left(2\pi i z\sqrt{\frac{1}{\lambda^2}-\left(f_x^2+f_y^2\right)}\right)\right), \tag{3}$$

where $i = \sqrt{-1}$, $\mathcal{F}$ and $\mathcal{F}^{-1}$ are the forward and inverse Fourier transforms, respectively; λ is the wavelength, and (f_x, f_y) represent the spatial frequencies.

Wu et al. (2021) showed that a hologram of a 4K 2D image could be generated in 0.15 s using unsupervised learning. The network structure of the issued DNN is U-Net (Ronneberger et al., 2015). Instead of the angular spectrum method, an inverse diffraction calculation to obtain the reproduced images was a single fast Fourier transform (FFT) Fresnel diffraction, which is computationally light. The DNN was trained using **Eq. 2** a weighted combination of a negative Pearson correlation coefficient and a perceptual loss function (Johnson et al., 2016). The DNN method is superior to the GS method and Wirtinger holography (Chakravarthula et al., 2019) in computational speed; i.e., ×100 faster for the same reconstruction quality (Wu et al., 2021).

Hossein Eybposh et al. (2020) developed an unsupervised method called DeepCGH to generate holograms of 3D scenes using DNN. They have developed this method for two-photon holographic photostimulation, which can also be used for holographic displays. The network structure is U-Net. When 3D volume data $\mathcal{X}(x, y, z)$ representing a 3D scene are input to the DNN, the DNN outputs its hologram. From the output hologram, multiple inverse propagations ($\mathcal{P}^{-1}$) are performed to compute the 3D reproduced image $\mathcal{X}'_{(x,y,z)} = |\mathcal{P}(\mathcal{N}(\mathcal{X}(x, y, z)))|$. The DNN was trained by **Eq. 2** with a loss function using the following cosine similarity

$$\mathcal{L}(\mathcal{X}, \mathcal{X}') = 1 - \frac{\sum_{x,y,z} \mathcal{X}(x, y, z)\mathcal{X}'(x, y, z)}{\sqrt{\sum_{x,y,z} \mathcal{X}^2(x, y, z)}\sqrt{\sum_{x,y,z} \mathcal{X}'^2(x, y, z)}}. \quad (4)$$

Since 3D volume data requires much memory, DNNs tend to be large. Therefore, the study Hossein Eybposh et al. (2020) used a method called interleaving (Shi et al., 2016) to reduce the DNN size.

By employing the method of **Figure 3**, Horisaki et al. (2021) trained an U-Net-based DNN using the following 3D mean squared root error (MSE) for the loss function,

$$\mathcal{L}(\mathcal{X}, \mathcal{X}') = \sqrt{\sum_{x,y,z} (\mathcal{X}(x, y, z) - \mathcal{X}'(x, y, z))^2}. \quad (5)$$

The hologram computation using DNN (Wu et al., 2021) introduced in this subsection showed that it can produce higher quality reproductions than conventional methods. However, the reproduced images were limited to two dimensions. The Methods (Hossein Eybposh et al., 2020; Horisaki et al., 2021) for calculating holograms of 3D objects using DNNs were also proposed, but the number of layers was limited to a few due to the resources of the computer hardware. A method introduced in the next subsection solves these limitations.

2.3 Layer Hologram Calculation Using the Deep Neural Network

Generally, layer-based hologram calculations (Okada et al., 2013; Chen et al., 2014; Chen and Chu, 2015; Zhao et al., 2015) generate

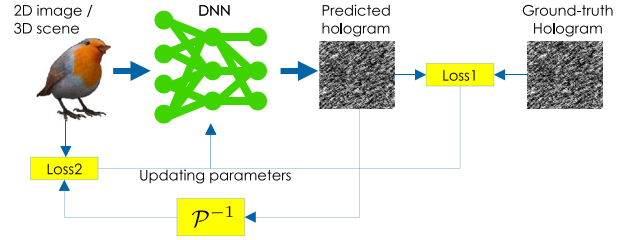

FIGURE 4 | Layer-based hologram calculation using deep neural network (Shi et al., 2021).

sectional images at each depth from RGB and depth images. We compute diffraction calculations to the sectional images. Consequently, we employ these results to obtain the final hologram. Although the diffraction calculation can be accelerated using FFTs, the computational complexity of the layer method is still large, making it difficult to calculate 2K size holograms at video rate.

Layer-based hologram calculations using DNN have been investigated in Hossein Eybposh et al. (2020) and Horisaki et al. (2021). The study by Shi et al. (2021) published in Nature in 2021 had a great impact on holographic displays using the layer method. **Figure 4** shows the outline of layer-based hologram calculations using DNN. This result significantly outperforms the computational speed and image quality of existing physically-based layer methods. The network structure was similar to that of ResNet (He et al., 2016). Additionally, DNNs were trained using two types of label data: RGBD images and their holograms. Since DNNs are suitable for 2D images, they work well with RGBD images used in layer hologram calculations.

This DNN was trained using two loss functions. The first loss function, $\mathcal{L}_1$, calculates the error between the hologram output from the DNN and the ground-truth hologram. The second loss function, $\mathcal{L}_2$, calculates the error between a reproduced image, obtained by an inverse diffraction calculation ($\mathcal{P}^{-1}$) with the propagation distance z from the predicted hologram, and its corresponding sectional image at z. Here, the hologram output from the DNN is in complex amplitude at an intermediate position between the 3D scene and final hologram. The study Shi et al. (2021) explained the reason for using intermediate holograms as follows:

The convolutional layers of DNN use a 3 × 3 filter. If a 3D scene and hologram are far apart, it is impossible to represent the spread light waves without connecting many convolution layers, making the DNN very large. The DNN outputs a complex hologram at an intermediate position to alleviate the above problem. In the middle position, the light wave does not spread; thus, reducing the number of convolution layers.

Additionally, if the 3D scene and intermediate hologram are sufficiently close, these images will be similar, facilitating the DNN training. The intermediate hologram is propagated to the final hologram plane using the angular spectrum method and converted to an anti-aliased double phase hologram (Hsueh and Sawchuk, 1978; Shi et al., 2021). By displaying the anti-aliased double phase hologram on a phase-only SLM, speckle-free,

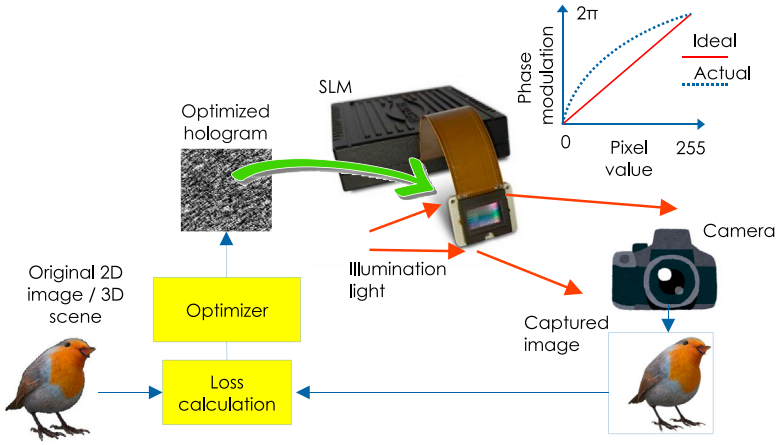

FIGURE 5 | Camera-in-the-loop holography.

natural, and high-resolution 3D images can be observed at video rates.

The study trained the DNN using their RGBD image dataset called MIT-CGH-4K. This dataset consists of 4,000 sets of RGBD images and intermediate holograms. It allows DNNs to work well with RGBD images rendered by computer graphics and real RGBD images captured by RGBD cameras. In many DNN-based color 3D reproductions, including this study, the time-division method (Shimobaba and Ito, 2003; Oikawa et al., 2011) is employed. The time-division method enables color reproduction by displaying the holograms of the three primary colors synchronously with the RGB illumination light. However, it requires an SLM capable of high-speed switching.

The trained DNN can generate 1,920, ×, 1,080 pixel holograms at a rate of 60 Hz using a graphics processing unit. It can also generate holograms interactively at 1.1 Hz on a mobile device (iPhone 11 Pro) and at 2.0 Hz on an edge device with Google tensor processing unit (TPU). For the TPU a float 32 precision DNN was compressed into an Int8 precision DNN using quantization, which is one of the model compression methods for DNNs.

2.4 Camera-in-the-Loop Holography

The quality of reproduced images of holographic displays will be degraded because of the following factors: misalignment of optical components (beam splitters and lenses), SLM cover glass, aberrations of optical components, uneven light distribution of a light source on the SLM, and quantized and non-linear light modulation of SLM, as shown in the graph of **Figure 5**.

The GS algorithm, Wirtinger holography, and stochastic gradient methods (Chakravarthula et al., 2019) determine a hologram that yields the desired reproduced image using $\underset{\phi}{minimize}\ \mathcal{L}(\mathcal{P}_{ideal}(\phi), a_o)$. Here ϕ, a_o, and $\mathcal{L}$ represent a hologram, target image, and loss function (defined as the error between the target and reproduced images). Successful optimization with this method will be achieved when the actual optical system and ideal light wave propagation model $\mathcal{P}_{ideal}$ are consistent.

Although some studies have been conducted to manually correct aberrations to get closer to the ideal propagation model $\mathcal{P}_{ideal}$, the camera-in-the-loop holography (Peng et al., 2020) has been proposed to automatically correct these image quality degrading factors. **Figure 5** shows the outline of the camera-in-the-loop holography. The camera-in-the-loop holography differs from the GS algorithms, Wirtinger holography, and gradient descent methods because it uses actual reproduced images in the optimization loop.

In the camera-in-the-loop holography, a gradient descent method was used to find an ideal hologram as $\phi \leftarrow \phi - \alpha\partial\mathcal{L}/\partial\phi$, where α is the learning rate, $\mathcal{L}$ is the loss function used to calculate the error between an actual reproduced image captured by a camera and target image, and $\frac{\partial\mathcal{L}}{\partial\phi} = \frac{\partial\mathcal{L}}{\partial\mathcal{P}}\frac{\partial\mathcal{P}}{\partial\phi}$, where $\mathcal{P}$ represents the actual optical system, including unknown aberrations. However, the gradient $\frac{\partial\mathcal{P}}{\partial\phi}$ cannot be calculated due to the unknown parameter. The camera-in-the-loop holography approximates the unknown gradient as follows

$$\frac{\partial\mathcal{L}}{\partial\phi} = \frac{\partial\mathcal{L}}{\partial\mathcal{P}}\frac{\partial\mathcal{P}}{\partial\phi} \approx \frac{\partial\mathcal{L}}{\partial\mathcal{P}}\frac{\partial\mathcal{P}'}{\partial\phi}, \tag{6}$$

where $\mathcal{P}'$ is a known propagation model. For example, if $\mathcal{P}'$ is a free-space propagation between the SLM and reproduced image, it can simply use a diffraction calculation as $\mathcal{P}' = \mathcal{P}_{ideal}$. The gradient $\frac{\partial\mathcal{L}}{\partial\mathcal{P}}$ can be calculated using reproduced images captured by a camera.

The following research is an extension of the camera-in-the-loop holography: high-quality holographic display using partially coherent light (LED light source) (Peng et al., 2021), holographic display using Michelson setup to eliminate undiffracted light of SLM (Choi et al., 2021), optimizing binary phase holograms (Kadis et al., 2021), holographic display that suppresses high-order diffracted light using only computational processing without any physical filters (Gopakumar et al., 2021), and

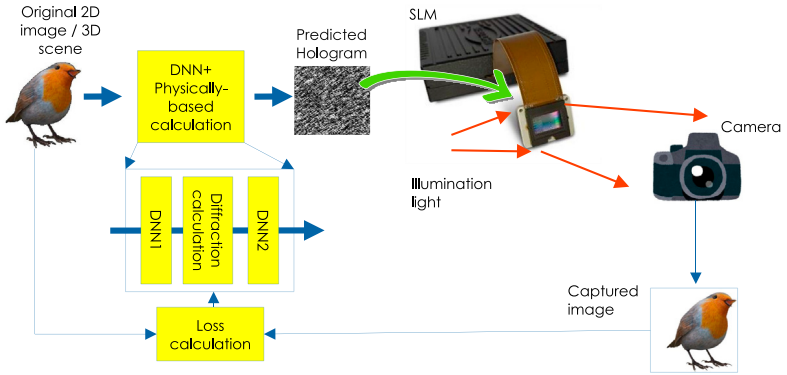

FIGURE 6 | HoloNet: a combination of camera-in-the-loop holography and deep neural network (Peng et al., 2020).

further improvement of image quality by using a Gaussian filter to remove noise that is difficult to optimize (Chen et al., 2022).

The above camera-in-the-loop holography needs to be re-optimized for each target image, which can take several minutes. To solve this problem, HoloNet, a combination of camera-in-the-loop holography and DNN, was proposed (Peng et al., 2020). **Figure 6** shows a schematic of HoloNet. HoloNet consists of two DNNs and a physically-based calculation (diffraction calculation). The camera is required for the training stage of the DNN; however, it is not required for the inference stage. DNN1 outputs the optimal phase distribution of the target image. The phase distribution and target image are combined to form a complex amplitude. Then, a Zernike-compensated diffraction calculation is performed by considering the aberrations of the optical system. DNN2 transforms the complex amplitude obtained by the diffraction calculation into a phase-only hologram suitable for SLM. HoloNet can generate full-color holograms with 2K resolution at 40 frames per second.

Chakravarthula et al. (2020) proposed an aberration approximator. The aberration approximator uses a U-Net-based DNN. The DNN infers the aberrations of an optical system to obtain holograms that are corrected for the aberrations. The conditional GAN (Isola et al., 2017) was used to train the DNN, and the training datasets were numerical reproduced images of holograms generated assuming an ideal optical system and reproduced images from the actual optical system captured by a camera.

Kavaklı et al. (2022) pointed out that the algorithms of Wu et al. (2021) and Peng et al. (2020) are complex processing. The study Kavaklı et al. (2022) obtained an optimized point spread function for diffraction calculation from the error between numerically reproduced images from holograms calculated from the ideal diffraction calculation and the actual reproduced images captured by a camera. It is worth noting that the optimized point spread function has an asymmetric distribution different from the point spread function in the ideal case. Additionally, the optimized point spread function reflects the aberrations of the optical system. We can obtain holograms that give an ideal reproduction image by calculating holograms with the optimized point spread function.

2.5 Other Applications Using Deep Neural Network

2.5.1 Image Quality Enhancement

A reproduced image of a hologram calculated using random phase will have speckle noise. Park and Park (2020) proposed a method for removing speckle noise from random phase holograms. In this method, the reproduced image (light-field data) is first numerically computed from a random phase hologram. Since the reproduced light-field data also contains speckle noise, this method employs a denoising convolutional neural network (Zhang et al., 2017a) to remove this noise. Furthermore, a speckle-free reproduction image can be observed by recalculating the hologram from the speckle-free light-field data.

Ishii et al. (2022) proposed the image quality enhancement of zoomable holographic projections using DNNs. To obtain a reproduced image larger than the hologram size, it is necessary to use a random phase; however, this gives rise to speckle noise. The random phase-free method (Shimobaba and Ito, 2015), which applies virtual spherical waves to the original image and calculates the hologram using a scaled diffraction calculation (Shimobaba et al., 2013), can avoid this problem. However, it does not apply well to phase-only holograms. A DNN of (Ishii et al., 2022) converts a phase-only hologram computed using the random phase-free method in an optimized phase-only hologram. Two layers for computing the forward and inverse scaled diffraction (Shimobaba et al., 2013) are introduced before and after DNN. Then, the DNN is trained using unsupervised learning, as discussed in **Section 2.2**. In the inference, the two layers are removed, and a phase-only hologram is computed using the random phase-free method and a scaled diffraction calculation is input to the DNN to optimize a zoomable phase-only hologram.

2.5.2 Hologram Compression

The amount of data in holograms is a major problem. Data compression is essential for real-time hologram transmission and wide-viewing-angle holographic displays, which require holograms with large spatial bandwidth products. Existing

compression techniques [e.g., JPEG, JPEG 2000, and high-efficiency video coding (HEVC)] and distinctive compression techniques have been proposed (Blinder et al., 2014; Birnbaum et al., 2019; Stepien et al., 2020), which aim to take the distinctive signal properties of digital holograms into account. Compression of hologram data is not easy because holograms have different statistical properties from general natural images, so standard image and video codecs will achieve sub-optimal performance. Several DNN-based hologram data compression algorithms have been proposed to address this matter.

When JPEG or other compression algorithms targeted to natural image date are used for hologram compression, essential high-frequency components are lost, and block artefacts will perturb the hologram viewing. In Jiao et al. (2018), a simple DNN with three convolution layers was used to restore the JPEG-compressed hologram close to the original one. The DNN learns the relationship between the JPEG-degraded hologram and the original hologram using end-to-end learning. Although it was tested on JPEG, it can easily be applied to other compression methods, making it highly versatile.

In Shimobaba et al. (2019a) and Shimobaba et al. (2021a), holograms were compressed through binarization using the error diffusion method (Floyd, 1976). The U-Net-based DNN restored binary holograms to the original grayscale. If the input hologram is 8 bits, the data compression ratio is 1/8. DNN can obtain better reproduction images than JPEG, JPEG2000, and HEVC at the same bit rate.

2.5.3 Hiding of Information in Holograms

Steganography is a technique used to hide secret images in a host image (also called cover image). The hidden images must not be known to others. A closely related technique is watermarking: it embeds copyright information (e.g., a copyright image) in the host image. The copyright information can be known by others, but it must be impossible to remove. These techniques are collectively referred to as information hiding. Many holographic information hiding techniques have been proposed (Jiao et al., 2019). For example, the hologram of a host image can be superimposed on that of a hidden image to embed hidden information (Kishk and Javidi, 2003). The hidden information should be encrypted with double random phase encryption (Refregier and Javidi, 1995) to prevent it from being read. An important difference with digital information hiding is that holographic information hiding allows for optical encryption and decryption of the hidden image, and handling 3D host and hidden information.

The combination of holographic information hiding and DNN can improve the resistance to attacks and the quality of decoded images. In Wang et al. (2021), the holograms of host and hidden images were superimposed on a single hologram using a complementary mask image. Each hologram was converted into a phase-only hologram by patterned-phase-only holograms (Tsang et al., 2017). The hologram of the hidden image is encrypted with double random phase encryption (Refregier and Javidi, 1995). When the final hologram is reconstructed, we can observe only the host image. Since the mask image is the key, we can observe the hidden image when the mask image is multiplied with the hologram, but the image quality is considerably degraded. This degradation is recovered using a DNN; DenseNet (Huang et al., 2017) was used as the DNN. It is trained by end-to-end learning using the dataset of degraded and ground-truth hidden images.

In Shimobaba et al. (2021b), a final hologram u recorded a hologram u_h of a host image and a hologram u_e of a hidden image was calculated as $u = \mathcal{P}_{z_1}\{u_h\} + \alpha\mathcal{P}_{z2}\{u_e\}$. Here, $\mathcal{P}_z$ is the diffraction calculation of the propagation distance z; z_1 and z_2 are the distance between the hologram and each image; α is the embedding strength of the hidden hologram. We can make the reproduced hidden image less noticeable by making α sufficiently small. Here, it was set to 4% of the amplitude of the host hologram. It is not easy to identify the reproduced hidden image at this value. Therefore, if we want to identify it, DNN recovers the hidden image. The DNN was trained using reproduced hidden and ground-truth hidden images. U-Net and ResNet were used as the network structure. Both networks could recover the hidden images.

3 DIGITAL HOLOGRAPHY USING DEEP LEARNING

In digital holography (Goodman and Lawrence, 1967; Kim, 2010; Liu et al., 2018; Tahara et al., 2018) image sensors are used to capture holograms of real macroscale objects and cells. It is possible to obtain a reproduced image from the hologram using diffraction calculation. Digital holography has been the subject of much research in 3D sensing and microscopy. **Figure 7** shows the process of digital holography. We calculate a diffraction calculation from a hologram captured by an image sensor to obtain a reproduction image in a computer. If the reconstructed position of the target object needs to be known accurately, autofocusing is required to find the focus position by repeating diffraction calculations. Autofocusing looks for a position where the reconstructed image is sharp. Aberrations are superimposed due to optical components and alignment errors. Meanwhile, it is necessary to correct this aberration. Since digital holography can obtain complex amplitudes, simultaneous measurement of amplitude and phase is possible. The phase can be obtained by calculating the argument of a complex value using the arctangent function, but its value range is wrapped into $[-\pi, +\pi)$. Therefore, phase unwrapping is required to reproduce the thickness of an object from its phase.

However, the above processes are time-consuming computations. In this section, we introduce digital holography using DNNs. We can speed up some (or all) of the time-consuming processing using DNNs. Furthermore, DNNs have successfully obtained reproduced images with better image quality than conventional methods. For a more comprehensive and detailed description of digital holography using DNNs, see review papers Rivenson et al. (2019), Javidi et al. (2021), and Zeng et al. (2021).

3.1 Depth Estimation

A general method for estimating the focus position is to obtain the most focused position by calculating reproduced images at

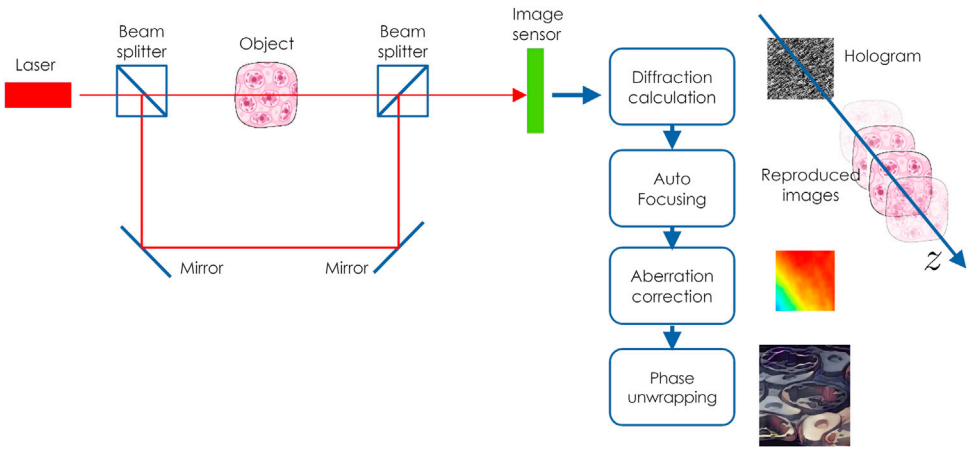

FIGURE 7 | Process flow of digital holography.

different depths from the hologram. The focus position is determined using metrics, such as entropy, variance, and Tamura coefficient (Zhang et al., 2017b). This process requires an iterative diffraction calculation, which is computationally time-consuming. An early investigation of autofocusing using DNNs was to estimate the depth position of a target object from a hologram. The depth prediction can be divided into two categories: classification and regression problems.

Pitkäaho et al. (2019) proposed the depth position prediction as a classification problem. They showed that DNNs for classification commonly used in the MNIST classification problem could classify the range of 260–272 mm, where the target object is located, into five depths at 3 mm intervals.

DNNs for estimating the depth location as a regression problem (Ren et al., 2018; Shimobaba et al., 2018) infer a depth value z directly from a hologram image (or its spectrum) H. This network is similar to that of the classification problem but with only one neuron in the output layer. The training is performed using end-to-end learning as $\underset{\Theta}{minimize}\ \mathcal{L}(\mathcal{N}(H;\Theta),z)$, where z is the ground-truth depth value. The MSE and other metrics are usually used as loss functions. We can obtain a focused reproduced image through a diffraction calculation using the estimated depth distance from a hologram.

3.2 Phase Unwrapping

Phase unwrapping in physically-based calculation (Ghiglia and Pritt, 1998) connects wrapped phases to recover the thickness (or optical path length) of a target object. Phase unwrapping algorithms have global, region, path-following, and quality-guided algorithms. Additionally, a method that applies the transport intensity equation has been proposed (Martinez-Carranza et al., 2017). These methods are computationally time-consuming.

Many methods have been proposed to perform phase unwrapping by training DNNs with end-to-end learning using a dataset of wrapped phase and their unwrapping images (Wang et al., 2019a; Qin et al., 2020). Once trained, DNNs can rapidly generate unwrapped phase images. Phase unwrapping using Pix2Pix (Isola et al., 2017), a type of generative adversarial network (GAN) (Goodfellow et al., 2014), has been proposed (Park et al., 2021). Pix2Pix can be thought of as a supervised GAN. This study prepared a dataset of wrapped phase and their unwrapped phase images generated using the quality-guided algorithm (Herráez et al., 2002). The U-Net-based generator employs this dataset to generate a realistic unwrapped phase image from the unwrapped phase image to fool the discriminator. The discriminator is trained to detect whether it concerns a generated or real unwrapped phase image. Such adversarial learning can produce high-quality unwrapped images.

3.3 Direct Reconstruction Using the Deep Neural Network

As a further development, research has been conducted to obtain aberration-eliminated, autofocusing, and phase unwrapping images directly by inputting holograms into DNNs.

3.3.1 Supervised Learning

A reproduced image can be obtained by propagating holograms captured by inline holography back to the object plane. However, since the reproduced image contains a twin image and direct light, it is necessary to remove unwanted lights using physically-based algorithms, e.g., phase recovery algorithms. This requires multiple hologram recordings and computational costs for diffraction calculations.

Rivenson et al. (2018) inputs a reproduced image obtained using an inverse diffraction calculation ($\mathcal{P}^{-1}$) to the object plane into a DNN ($\mathcal{N}$) to obtain a twin image-free reproduced image. The prepared dataset consists of a hologram H and a ground-truth complex amplitude field $\mathcal{Y}$. Then, they trained the DNN using end-to-end learning as $\underset{\Theta}{minimize}\ \mathcal{L}(\mathcal{N}(\mathcal{P}^{-1}(H);\Theta),\mathcal{Y})$. They used MSE as the loss function $\mathcal{L}$. The ground-truth complex amplitudes were obtained from eight holograms with different recording positions using the multiheight phase retrieval algorithm (Greenbaum and Ozcan, 2012). This study showed

that this DNN could reproduce images comparable to those obtained using the multiheight phase retrieval algorithm without time-consuming phase recovery.

Although the study of Rivenson et al. (2018) required the results of propagation calculations from a hologram to be input to the DNN, eHoloNet (Wang et al., 2018) developed DNN that does not require propagation calculations and directly infers object light from a hologram. They created a dataset consisting of a hologram $\mathcal{H}$ and its ground-truth object light $\mathcal{Y}$. The DNN was trained with the following end-to-end learning: $\underset{\Theta}{minimize}\ \mathcal{L}(\mathcal{N}(H;\Theta),\mathcal{Y})$. MSE was used as the loss function $\mathcal{L}$. They employed phase distributions displayed on SLM for collecting ground-truth object lights instead of real objects.

Y-Net (Wang et al., 2019b) separates the upsampling path of U-Net (Ronneberger et al., 2015) into two parts and outputs the intensity and phase of a reproduced image. The dataset includes captured holograms and their ground-truth intensity and phase images. Y-Net is trained using end-to-end learning. Compared with the case where the output layer of U-Net has two channels, and each channel outputs an intensity image and a phase image, Y-Net has successfully obtained better reproduction images.

Y4-Net (Wang et al., 2020a) extends the Y-Net upsampling paths by four for use in dual-wavelength digital holography (Wagner et al., 2000). Dual-wavelength holography uses two wavelengths, λ_1 and λ_2, to make synthetic wavelength for long wavelength measurements $\lambda_1\lambda_2/(\lambda_1 - \lambda_1)$ and short wavelength measurements $\lambda_1\lambda_2/(\lambda_1 + \lambda_1)$. Y4-Net outputs the real and imaginary parts of the reproduced image at each wavelength by inputting holograms captured at λ_1 and λ_2.

The above researches are about digital holographic measurement of microorganisms and cells. However, 3D particle measurement is essential to understand the spatial behavior of tiny particles, such as bubbles, aerosols, and droplets. It is applied to flow path design of flow cytometers, environmental measurement, and 3D behavior measurement of microorganisms. Digital holographic particle measurement can measure one-shot 3D particles; however, it requires time-consuming post-processing using diffraction calculations and particle position detection. 3D particle measurement using holography and DNN has been proposed. The study Shimobaba et al. (2019b) prepared a dataset consisting of holograms and their particle position images, a 2D image showing the 3D position of the particle. The position of a pixel indicates the position of the particle in the plane, and its color indicates the depth position of the particle. U-Net was trained using end-to-end learning with the dataset. The DNN can transform holograms to particle position images. The effectiveness of the method was confirmed by simulation.

The study of Shimobaba et al. (2019b) was conducted using simple end-to-end learning. However, Shao et al. (2020) inputs two more pieces of information (depth map and maximum phase projection, both obtained by preprocessing the hologram) to their U-Net in addition to holograms. Additionally, by developing a loss function, this study successfully obtained 3D particle images with a particle density 300 times higher than that of Shimobaba et al. (2019b).

Chen et al. (2021) incorporated compressive sensing into DNN and trained it using end-to-end learning. The input of the DNN were 3D particle holograms, whereas the output was 3D volume data of the particles. Unlike (Shimobaba et al., 2019b; Shao et al., 2020), Zhang et al. (2022) used the Yolo network (Joseph et al., 2016). When a hologram is an input to the DNN, it outputs a 6D vector containing a boundary box that indicates the location of the particle, its objectiveness confidence, and the depth position of the particle.

3.3.2 Unsupervised Learning

End-to-end learning requires a dataset consisting of a large amount of paired data (captured hologram and object light recovered using physically-based algorithms). Since the interference fringes of holograms vary significantly depending on the holographic recording conditions and target objects, there is no general-purpose hologram dataset. Therefore, it is necessary to create an application-specific datasets, which requires much effort. Unsupervised learning is also used for DNNs for digital holography.

Li et al. (2020) showed that using a deep image prior (Ulyanov et al., 2018), a twin image-free reproduced image can be obtained using only a captured inline hologram without large datasets. Furthermore, an auto-encoder was used for the DNN network structure. The deep image prior (Ulyanov et al., 2018) initializes the DNN with random values and inputs a fixed image to the DNN for training. For example, the deep image prior can be used to denoise an image from noisy input. This technique works due to the fact that DNNs are not good at representing noise. The deep image prior is also useful for super-resolution and in-painting. In Li et al. (2020), DNN was trained using the following unsupervised learning: $\underset{\Theta}{minimize}\ \mathcal{L}(\mathcal{P}(\mathcal{N}(\mathcal{P}^{-1}(H_{\mathrm{fix}});\Theta)),H_{\mathrm{fix}})$, where H_{fix} is a captured inline hologram, and $\mathcal{N}$ is the DNN with the network parameter Θ. The reproduced image of an inline hologram $(\mathcal{P}^{-1}(H_{\mathrm{fix}}))$ includes a twin image, which can be considered noise. By inputting the noisy reproduced image into the DNN, the DNN outputs the complex amplitude field of the target object with reduced twin image using the principle of the deep image prior. This study conducted a diffraction calculation $(\mathcal{P})$ of the DNN output to generate a hologram. It learns Θ to minimize the error between computed and captured holograms. Consequently, the study obtained that the quality of a reproduced image is better than using a state-of-the-art compressed sensing (Zhang et al., 2018b).

PhysenNet (Wang et al., 2020b) was also inspired by the deep image prior. PhysenNet can infer the phase image of a phase object by inputting its hologram into a DNN. The network is a U-Net, trained using the following unsupervised learning: $\underset{\Theta}{minimize}\ \mathcal{L}(\mathcal{P}(\mathcal{N}(H_{\mathrm{fix}}));\Theta),H_{\mathrm{fix}}$. The phase distribution output from the DNN is computed by diffraction to generate holograms. The DNN is trained to minimize the error between the measured and generated holograms. The minimization formula is slightly different from Li et al. (2020).

3.3.3 Generative Adversarial Network

GANs (Goodfellow et al., 2014), one of the training methods for DNNs, have been widely used in computational holography because of their excellent image transformation capabilities.

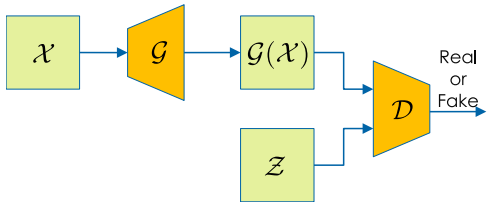

FIGURE 8 | Architecture of a conditional generative adversarial network.

Liu et al. (2019a) used the conditional GAN for super-resolution in digital holographic microscopy. Conditional GAN is a method that adds ground-truth information to GAN; it is a supervised learning method. **Figure 8** shows a schematic of Liu et al. (2019a). As shown in the figure, $\mathcal{X}$ is the low-resolution hologram; $\mathcal{G}$ is the generating network (using U-Net); $\mathcal{G}(\mathcal{X})$ is the high-resolution hologram output from the generating network; $\mathcal{Z}$ is a ground-truth high-resolution hologram; $\mathcal{D}$ is a discriminating network that can distinguish whether a high-resolution hologram is a generated or a ground-truth hologram. The datasets of low- and high-resolution holograms are taken with on-chip digital holographic microscopy. The high-resolution holograms are captured by changing objective lenses with different numerical apertures. Alternatively, the image sensor can be laterally shifted to capture multiple low-resolution holograms, which are super-resolved using the physically-based algorithm (Greenbaum et al., 2014) to generate high-resolution holograms.

Similar to Liu et al. (2019a), Liu et al. (2019b) employed the conditional GAN to generate accurate color images from holograms captured at three wavelengths suitable for point-of-care pathology. Conditional GAN can produce holographic images with high accuracy. However, a dataset must be prepared since it is supervised learning, which requires much effort. To overcome this problem, holographic microscopy using cycle GANs with unsupervised learning has been investigated (Yin et al., 2019; Zhang et al., 2021).

3.4 Interconversion Between Holographic and Other Microscopes

Many microscopes, such as bright-field, polarized light, and digital holographic microscopes, have been developed, each with its strengths and weaknesses. Interconversion between the reproduced image of a holographic microscope and that of another microscope has been investigated using deep learning. It has become possible to overcome each other's shortcomings. In many cases, GANs, which are excellent at transforming images, are used to train DNNs.

Bright-field microscopy allows simple observation of specimens using a white light source; however, transparent objects must be stained. Additionally, only 2D amplitude information of a target object can be obtained due to the shallow depth of focus. Wu et al. (2019) showed that digital holographic reproduced images could be converted to bright-field images using GAN. In contrast, Go et al. (2020) converted an image taken by bright-field microscopy into a hologram. They showed that it is possible to recover the 3D positional information of particles from this hologram. Additionally, they developed a system that can capture bright-field and holographic images simultaneously to create a dataset. The GAN generator produces holograms from bright-field images, and the discriminator is trained to determine whether it is a generated or captured hologram.

Liu et al. (2020) converted the reproduced image of digital holographic microscopy into a polarized image of polarized light microscopy. Polarized light microscopy has problems, such as a narrow field of view and the need to capture several images with different polarization directions. The study Liu et al. (2020) showed that a DNN trained by a GAN could infer a polarization image from a single hologram. The dataset consists of data pairs of holograms taken using a holographic microscope and polarized light images taken with single-shot computational polarized light microscopy (Bai et al., 2020) of the same object.

3.5 Holographic Classification

Holographic digital microscopy can observe the phase of transparent objects, such as cells, allowing for label-free observation of cells. By using this feature, a rapid and label-free screening of anthrax using DNN and holographic microscopy has been proposed (Jo et al., 2017). The DNN consists of convolutional layers, MaxPoolings, and classifiers using fully-connected layers.

O'Connor et al. (2020) classified holographic time-series data. They employed a low-cost and compact shearing digital holographic microscopy (Javidi et al., 2018) made with a 3D printer to capture and classify holographic time-series data of blood cells in animals, and healthy individuals, and those with sickle cell disease in humans.

Figure 9 shows a schematic of O'Connor et al. (2020). In the second step of the off-axis phase reconstruction, only the object light component is Fourier filtered, as in a conventional off-axis hologram, to obtain the phase image in the object plane using a diffraction calculation (Takeda et al., 1982; Cuche et al., 2000). The feature extractor extracts features from the phase image. The manually extracted and automatically extracted features from DNNs, which are transfer-learned from DenseNet (Huang et al.,

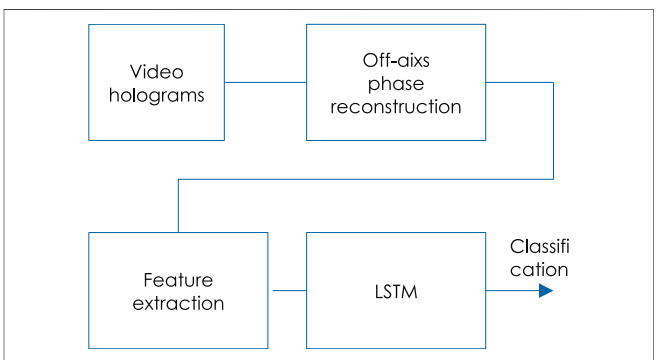

FIGURE 9 | Classification of time-series hologram of cells.

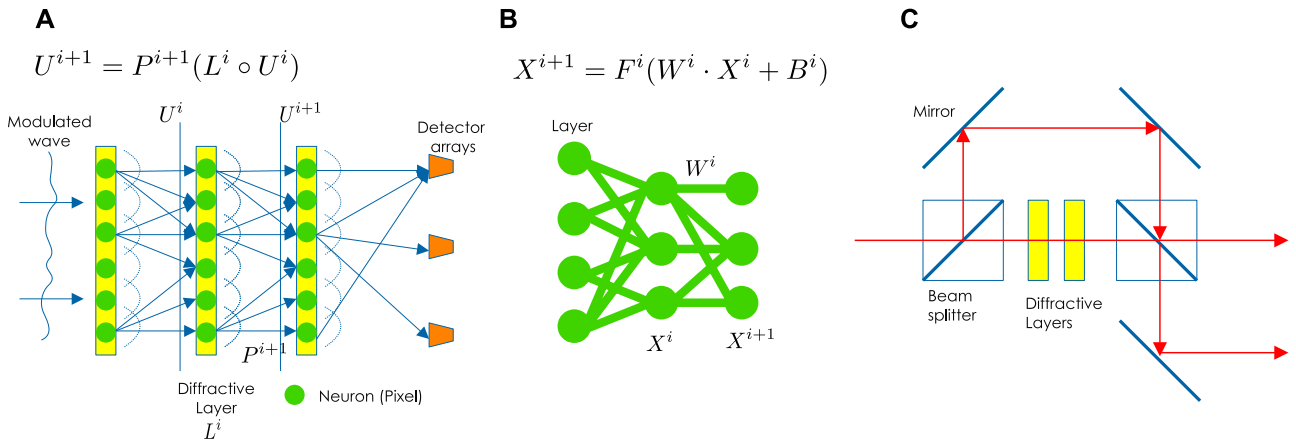

FIGURE 10 | Diffractive deep neural network: **(A)** D^{2}NN, **(B)** semiconductor-based DNN **(B)**, and **(C)** D^{2}NN incorporating the ideas of ResNet.

2017), are input to a long short-term memory network (LSTM) to classify the cells. LSTM is a recurrent neural network (RNN). RNNs have a gradient vanishing problem as the time-series data become longer; however, LSTMs can solve this problem. The study O'Connor et al. (2020) showed that LSTM significantly improved the classification rate of the cells compared to traditional machine learning methods, such as the random forest and support vector machine. The classification of spatiotemporal COVID-19 infected and healthy erythrocytes was reported (O'Connor et al., 2021) using this technique.

4 FASTER DEEP NEURAL NETWORKS

Deep learning, as introduced above, entails a neural network running on semiconductors. The switching speed of transistors governs its speed, and its power consumption is high. To solve this problem, an optical neural network has been proposed (Goodman and Goodman, 2005; Genty et al., 2021).

Research on optical computers has a long history. For example, pattern recognition by optical computing was reported in 1964 (Vander LUGH, 1964). This research used optical correlation to perform simple recognition. Optical computers use a passive hologram used as a modulator of light. Therefore, it requires little power and can perform the recognition process at exactly the speed of light. Research has been recently conducted on optical deep learning (Genty et al., 2021). In this study, we introduce one of them, the diffractive DNN (D^{2}NN), which is closely related to holography (Lin et al., 2018).

Figure 10 shows the D^{2}NN and semiconductor-based DNN. A D^{2}NN modulates the input light modulated by some information with multiple diffractive layers (holograms). It learns the amplitude and phase of the diffractive layers to strengthen the light intensity of the desired detector. For example, in the case of classification, the input light of the classification target is modulated in each diffractive layer, and the diffractive layer is learned to strengthen the light intensity of the detector corresponding to the target. Existing deep-learning frameworks, such as Keras, Tensorflow, or PyTorch, can be used to train the diffractive layers.

In **Figure 10A**, a light wave U^i is diffracted by ith diffractive layer. The propagated light wave U^{i+1} before the next diffractive layer is expressed as follows:

$$U^{i+1} = \mathcal{P}^{i+1}\left(L^i \circ U^i\right), \tag{7}$$

where $\mathcal{P}^{i+1}$ is the diffraction between the layers of i and $i+1$, and $\circ$ is the Hadamard product. For $\mathcal{P}^i$, general diffraction calculations, such as the angular spectrum method, can be used. The forward calculation of D^{2}NN is completed by iterating **Eq. 7** as many times as the number of diffractive layers.

Since the calculation of **Eq. 7** consists of the entirely differentiable operations, each diffractive layer can be optimized by automatic differentiation from the forward calculation. The D^{2}NN is trained on a computer, and the trained diffractive layers are recorded on an optical modulator (photopolymer or SLM). These optical modulators correspond to the layers of the semiconductor-based DNN. A D^{2}NN can be constructed by arranging these layers in equal intervals. The classification rate can be further improved (Watanabe et al., 2021) by arranging the diffractive layers in a non-equally spaced manner. The spacing of diffractive layers is a hyperparameter, which is not easy to tune manually. Watanabe et al. (2021) employed a Bayesian optimization technique, the tree-structured Parzen estimator (James et al., 2011), for hyperparameter tuning.

Figure 10B shows a semiconductor-based DNN. The output X^{i+1} of the input X^i at the ith layer of this DNN can be expressed by

$$X^{i+1} = F^i\left(W^i \cdot X^i + B^i\right), \tag{8}$$

where W^i is the weight parameters, B_i is the bias (not shown in the figure), $\cdot$ is the matrix product, and F^i is the activation function. Semiconductor-based DNNs can represent arbitrary functions because **Eq. 8** contains nonlinear activation functions. However,

Eq. 7 of D^2NN has no activation function; therefore, it can only handle linear problems. Still, there are many applications where D^2NNs work effectively for linear problems.

The study Lin et al. (2018) investigated the MNIST classification accuracy using D^2NN. When a five-layer D^2NN was validated through simulation, it achieved a 91.75% classification rate. Meanwhile, the classification rate improved to 93.39% for a seven-layer. The state-of-the-art classification rate for electrical DNNs was 99.77%. When the layers were 3D printed and optically tested, a classification rate of 88% was achieved despite the manufacturing and alignment errors of the layers.

D^2NNs are usually constructed with relatively shallow layers. Dou et al. (2020) applied the idea of ResNet (He et al., 2016) to D^2NN and reduced the gradient vanishing problem in deep diffractive layers. ResNet reduced gradient vanishing by introducing shortcuts, whereas Res-D^2NN (Dou et al., 2020) introduces optical shortcut connections, as shown in **Figure 10C**. When a 20-layer D^2NN and Res-D^2NN were run through the MNIST classification problem, the identification rates were 96.0% and 98.4%, respectively, with the Res-D^2NN showing superior performance.

Sakib Rahman and Ozcan (2021) showed through simulations that a twin image-free holographic reproduced image could be obtained using a D^2NN. When holograms captured by inline digital holography are reproduced, blurry conjugate light is superimposed on the object light. Phase recovery algorithms, compressive sensing, and deep learning are used to remove this conjugate light, all of which operate on semiconductors. The study Sakib Rahman and Ozcan (2021) trained a D^2NN to input light from a hologram into the D^2NN and pass it through several diffractive layers to obtain a twin image-free reproduced image. The loss function $\mathcal{L}$ is defined as follows:

$$\mathcal{L} = \|I - \mathcal{Y}\|_2 + \alpha_1 \|\mathcal{F}(I) - \mathcal{F}(\mathcal{Y})\|_2 + \alpha_2 \left(1 - P_I / P_{illum}\right), \quad (9)$$

where $\|\cdot\|_2$ denotes the $\ell 2$ norm, and the first term is the error between the inferred image I of D^2NN and the ground-truth image $\mathcal{Y}$; the second term is the spectral error; the third term is the diffraction efficiency defined as the ratio of the power P_I of the reproduced image to the total power P_{illum} of the illumination light. The third term subtracts the diffraction efficiency from 1 so that the loss function becomes smaller as the diffraction efficiency increases. α_1 and α_2 are hyperparameters. The amount of modulation of the diffractive layers is determined by minimizing this loss function.

5 OUR PERSONAL VIEW AND DISCUSSION

In previous sections, we introduced computational holography, including computer-generated holograms, holographic displays, digital holography, and D^2NN, using deep learning. Several studies have shown that deep learning outperforms existing physically-based calculations. In this section, we briefly discuss our personal view on deep learning.

Algorithms for computer-generated hologram in holographic display include point-cloud, polygon, layer, and light-field methods. Several physically-based algorithms have been proposed for layer methods (Okada et al., 2013; Chen et al., 2014; Chen and Chu, 2015; Zhao et al., 2015). The DNN-based method (Shi et al., 2021) proposed by Shi et al. (2021) has been a near-perfect layer method in computational speed and image quality. Physically-based layer methods are inherently computationally expensive due to the iterative use of diffraction calculations. The DNN in Shi et al. (2021) skips this computational process and can map input RGBD images directly to holograms. This study showed that DNN could generate holograms two orders of magnitude faster than sophisticated physically-based layer methods.

Holograms generated using the layer method are suitable for holographic near-eye display because a good 3D image can be observed from the front of holograms (Maimone et al., 2017). These holograms have a small number of hologram pixels. Additionally, since the holograms do not need to have a wide viewing angle, they have only low-frequency interference fringes, indicating low spatial bandwidth product (Blinder et al., 2019). These features are suitable for DNNs, which is why current hologram generation using DNNs is mainly for layer holograms. Holograms with a large spatial bandwidth product have a wide viewing angle, allowing a large 3D image to be observed by many people. However, this would require large-scale holograms. Such holograms require a pixel pitch of about a wavelength and billions to tens of billions of pixels (Matsushima and Sonobe, 2018; Matsushima, 2020). Holograms are formed from high-frequency interference fringes, and hologram patterns appear noisy at first glance. Current DNNs have difficulty handling such large-scale holograms due to memory issues and computational complexity. Additionally, deep image prior (Ulyanov et al., 2018) points out that current DNNs based on convolutions are not good at generating noisy patterns. Therefore, hologram generation with large spatial bandwidth products using DNNs is a big challenge.

Since DNNs were developed from image identification, RGBD images used in the layer method are suitable for DNNs. However, it is not easy for DNN to handle coordinate data formats used in the point cloud and polygon methods. So far, few studies exist on how to handle the point cloud method (Kang et al., 2021) using DNN. The authors look forward to further progress in these studies.

Deep learning is a general-purpose optimization framework that can be used in any application involving signals. However, it is difficult to answer whether it can outperform existing methods in all applications and use cases. Using optical cryptography and single-pixel imaging as examples, Jiao et al. (2020) compared a well-known linear regression method (GeorgeSeber and AlanLee, 2012) with deep learning. They concluded that the linear regression method is superior in both applications. DNNs require a lot of tuning: tuning the network structure and hyperparameters, selecting appropriate loss functions and optimizers, and preparing a large dataset. If we tune them properly, which is not necessary in existing physically-based methods, we may obtain excellent results. However, it requires much effort. Ultimately, deep learning is a sophisticated fitting technique, so analytical models matching the ground truth

physics may be favorable whenever knowable and efficiently computable. Thus, it is essential to choose appropriate physically-based methods and deep learning in the future.

Deep learning requires the preparation of a large number of datasets, which generally require much effort. Computer-generated holograms using DNNs also require the preparation of datasets; however, they can be generated on a computer. Therefore, there is no need to take holograms with an actual optical system, except for systems such as the camera-in-the-loop holography. Digital holography is more problematic, as it requires a great deal of effort to acquire information about target objects and their holograms. Unsupervised learning, as discussed in **Section 3.3**, is ideal. However, unlike DNNs trained in supervised and unsupervised manners, phase recovery algorithms and compressed sensing can recover target object lights using only few known information about the target objects. Thus, they do not require a dataset. For supervised learning, DNNs should be trained by generating data pairs of holograms and their object lights using phase recovery algorithms and compressed sensing, as stated in Rivenson et al. (2018).

The generalization performance of DNNs is also essential. For example, in the case of digital holography, there is no guarantee that a DNN trained on a dataset with a particular object and optical system will be able to accurately recover object lights from holograms captured in other situations. Therefore, to improve the generalization performance of DNNs, we can use datasets that include various types of data, and techniques such as domain adaptation (Tzeng et al., 2017), which has been the subject of much research in recent years.

Furthermore, DNNs have outperformed physically-based calculations in many applications of computational holography. So, will there still be a need for physically-based calculations in the future? The answer is yes, because DNNs require large datasets which need to be generated using sophisticated physically-based calculations. Additionally, the validity of the results generated using DNNs should be benchmarked with the results obtained using physically-based calculation. Meanwhile, several attempts have been made on introducing layers of physically-based calculations in DNNs (Rivenson et al., 2018; Wang et al., 2020b; Hossein Eybposh et al., 2020; Li et al., 2020; Chen et al., 2021; Horisaki et al., 2021; Shi et al., 2021; Wu et al., 2021; Ishii et al., 2022; Kavaklı et al., 2022). Therefore, it will be necessary to continue research on physically-based calculations in terms of speed and image quality to speed up these layers.

6 CONCLUSION

In this review, we comprehensively introduced computational holography, including computer-generated holography, holographic display, digital holography using deep learning, and D^2NNs using holographic technology. Computational holography using deep learning has outperformed conventional physically-based calculations in several applications. Additionally, we briefly discussed our personal view on the relationship between DNNs and physically-based calculations. Based on these discussions, we believe that we need to continue research on deep learning and physically-based calculations. The combination of deep learning and physically-based calculations will further lead to a groundbreaking computational holography research.

AUTHOR CONTRIBUTIONS

TS, DB, and TB wrote the manuscript. TS, DB, TB, IH, HS, PS, and TI also discussed the techniques introduced in the manuscript and reviewed the manuscript.

FUNDING

This research was funded by the joint JSPS–FWO scientific cooperation program (VS07820N), FWO Junior postdoctoral fellowship (12ZQ220N), and the Japan Society for the Promotion of Science (19H04132 and JPJSBP120202302).

REFERENCES

Ahrenberg, L., Benzie, P., Magnor, M., and Watson, J. (2008). Computer Generated Holograms from Three Dimensional Meshes Using an Analytic Light Transport Model. *Appl. Opt.* 47 (10), 1567–1574. doi:10.1364/ao.47.001567

Bai, B., Wang, H., Liu, T., Rivenson, Y., FitzGerald, J., and Ozcan, A. (2020). Pathological crystal Imaging with Single-Shot Computational Polarized Light Microscopy. *J. Biophotonics* 13 (1), e201960036. doi:10.1002/jbio.201960036

Birnbaum, T., Ahar, A., Blinder, D., Schretter, C., Kozacki, T., and Schelkens, P. (2019). Wave Atoms for Digital Hologram Compression. *Appl. Opt.* 58 (22), 6193–6203. doi:10.1364/AO.58.006193

Blinder, D., Ahar, A., Bettens, S., Birnbaum, T., Symeonidou, A., Ottevaere, H., et al. (2019). Signal Processing Challenges for Digital Holographic Video Display Systems. *Signal. Processing: Image Commun.* 70, 114–130. doi:10.1016/j.image.2018.09.014

Blinder, D., Bruylants, T., Ottevaere, H., Munteanu, A., and Schelkens, P. (2014). Jpeg 2000-based Compression of Fringe Patterns for Digital Holographic Microscopy. *Opt. Eng.* 53 (12), 123102. doi:10.1117/1.oe.53.12.123102

Blinder, D., and Schelkens, P. (2020). Phase Added Sub-stereograms for Accelerating Computer Generated Holography. *Opt. Express* 28 (11), 16924–16934. doi:10.1364/oe.388881

Buckley, E. (2011). Holographic Laser Projection. *J. Display Technol.* 7 (3), 135–140. doi:10.1109/jdt.2010.2048302

Chakravarthula, P., Peng, Y., Kollin, J., Fuchs, H., and Heide, F. (2019). Wirtinger Holography for Near-Eye Displays. *ACM Trans. Graph.* 38 (6), 1–13. doi:10.1145/3355089.3356539

Chakravarthula, P., Tseng, E., Srivastava, T., Fuchs, H., and Heide, F. (2020). Learned Hardware-In-The-Loop Phase Retrieval for Holographic Near-Eye Displays. *ACM Trans. Graph.* 39 (6), 1–18. doi:10.1145/3414685.3417846

Chang, C., Bang, K., Wetzstein, G., Lee, B., and Gao, L. (2020). Toward the Next-Generation Vr/ar Optics: a Review of Holographic Near-Eye Displays from a Human-Centric Perspective. *Optica* 7 (11), 1563–1578. doi:10.1364/optica.406004

Chen, C., Kim, D., Yoo, D., Lee, B., and Lee, B. (2022). Off-axis Camera-In-The-Loop Optimization with Noise Reduction Strategy for High. *Opt. Lett.* 44, 790–793. doi:10.1364/OL.447871

Chen, J.-S., and Chu, D. P. (2015). Improved Layer-Based Method for Rapid Hologram Generation and Real-Time Interactive Holographic Display Applications. *Opt. Express* 23 (14), 18143–18155. doi:10.1364/oe.23.018143

Chen, J.-S., Chu, D., and Smithwick, Q. (2014). Rapid Hologram Generation Utilizing Layer-Based Approach and Graphic Rendering for Realistic Three-Dimensional Image Reconstruction by Angular Tiling. *J. Electron. Imaging* 23 (2), 023016. doi:10.1117/1.jei.23.2.023016

Chen, N., Wang, C., and Heidrich, W. (2021). Holographic 3d Particle Imaging with Model-Based Deep Network. *IEEE Trans. Comput. Imaging* 7, 288–296. doi:10.1109/tci.2021.3063870

Choi, S., Kim, J., Peng, Y., and Wetzstein, G. (2021). Optimizing Image Quality for Holographic Near-Eye Displays with Michelson Holography. *Optica* 8 (2), 143–146. doi:10.1364/optica.410622

Cuche, E., Marquet, P., and Depeursinge, C. (2000). Spatial Filtering for Zero-Order and Twin-Image Elimination in Digital off-axis Holography. *Appl. Opt.* 39 (23), 4070–4075. doi:10.1364/ao.39.004070

Dou, H., Deng, Y., Yan, T., Wu, H., Lin, X., and Dai, Q. (2020). Residual D2NN: Training Diffractive Deep Neural Networks via Learnable Light Shortcuts. *Opt. Lett.* 45 (10), 2688–2691. doi:10.1364/ol.389696

FienupFienup, J. R. (1982). Phase Retrieval Algorithms: a Comparison. *Appl. Opt.* 21 (15), 2758–2769. doi:10.1364/ao.21.002758

Floyd, Robert. W. (1976). An Adaptive Algorithm for Spatial gray-scale. *Proc. Soc. Inf. Disp.* 17, 75–77.

Gabor, D. (1948). A New Microscopic Principle. *nature* 161, 777–778. doi:10.1038/161777a0

Genty, G., Salmela, L., Dudley, J. M., Brunner, D., Kokhanovskiy, A., Kobtsev, S., et al. (2021). Machine Learning and Applications in Ultrafast Photonics. *Nat. Photon.* 15 (2), 91–101. doi:10.1038/s41566-020-00716-4

GeorgeSeber, A. F., and AlanLee, J. (2012). *Linear Regression Analysis*. John Wiley & Sons.

Gerchberg, R. W. (1972). A Practical Algorithm for the Determination of Phase from Image and Diffraction Plane Pictures. *Optik* 35, 237–246.

Ghiglia, Dennis. C., and Pritt, Mark. D. (1998). *Two-dimensional Phase Unwrapping-Theory, Algorithms, and Software; Chapter 1, 2 and 3*. Wiley, 1–99.

Go, T., Lee, S., You, D., and LeeLee, S. J. (2020). Deep Learning-Based Hologram Generation Using a white Light Source. *Sci. Rep.* 10 (1), 8977. doi:10.1038/s41598-020-65716-4

Goi, H., Komuro, K., and Nomura, T. (2020). Deep-learning-based Binary Hologram. *Appl. Opt.* 59 (23), 7103–7108. doi:10.1364/ao.393500

Goodfellow, I., Pouget-Abadie, J., Mirza, M., Xu, B., Warde-Farley, D., Ozair, S., et al. (2014). Generative Adversarial Nets. *Adv. Neural Inf. Process. Syst.* 27.

Goodman, J. W. (2005). in *Introduction to Fourier Optics*. Editor J. W. Goodman. 3rd ed. (Englewood, CO: Roberts & Co. Publishers), 2005.

Goodman, J. W., and Lawrence, R. W. (1967). Digital Image Formation from Electronically Detected Holograms. *Appl. Phys. Lett.* 11 (3), 77–79. doi:10.1063/1.1755043

Gopakumar, M., Kim, J., Choi, S., Peng, Y., and Wetzstein, G. (2021). Unfiltered Holography: Optimizing High Diffraction Orders without Optical Filtering for Compact Holographic Displays. *Opt. Lett.* 46 (23), 5822–5825. doi:10.1364/ol.442851

Greenbaum, A., Zhang, Y., Feizi, A., Chung, P. L., Luo, W., Kandukuri, S. R., et al. (2014). Wide-field Computational Imaging of Pathology Slides Using Lens-free On-Chip Microscopy. *Sci. Transl Med.* 6 (267), 267ra175. doi:10.1126/scitranslmed.3009850

Greenbaum, A., and Ozcan, A. (2012). Maskless Imaging of Dense Samples Using Pixel Super-resolution Based Multi-Height Lensfree On-Chip Microscopy. *Opt. Express* 20 (3), 3129–3143. doi:10.1364/oe.20.003129

Hasegawa, S., Hayasaki, Y., and Nishida, N. (2006). Holographic Femtosecond Laser Processing with Multiplexed Phase Fresnel Lenses. *Opt. Lett.* 31 (11), 1705–1707. doi:10.1364/ol.31.001705

He, K., Zhang, X., Ren, S., and Sun, J. (2016). "Deep Residual Learning for Image Recognition," in *Proceedings of the IEEE Conference on Computer Vision and Pattern Recognition*, 770–778. doi:10.1109/cvpr.2016.90

Herráez, M. A., Burton, D. R., Lalor, M. J., and Gdeisat, M. A. (2002). Fast Two-Dimensional Phase-Unwrapping Algorithm Based on Sorting by Reliability Following a Noncontinuous Path. *Appl. Opt.* 41 (35), 7437–7444. doi:10.1364/ao.41.007437

Hilaire, P. S., Benton, S. A., Lucente, M. E., Jepsen, M. L., Kollin, J., Yoshikawa, H., et al. (1990). Electronic Display System for Computational Holography. *Pract. Holography IV Int. Soc. Opt. Photon.* 1212, 174–182.

Hiroshi Yoshikawa, T. Y. H. Y., and Yoshikawa, H. (2011). Computer-generated Image Hologram. 中国光学快报 9 (12), 120006–120009. doi:10.3788/col201109.120006

Horisaki, R., Nishizaki, Y., Kitaguchi, K., Saito, M., and Tanida, J. (2021). Three-dimensional Deeply Generated Holography [Invited]. *Appl. Opt.* 60 (4), A323–A328. doi:10.1364/ao.404151

Horisaki, R., Takagi, R., and Tanida, J. (2018). Deep-learning-generated Holography. *Appl. Opt.* 57 (14), 3859–3863. doi:10.1364/ao.57.003859

Hossein Eybposh, M., Caira, N. W., Atisa, M., Chakravarthula, P., and Pégard, N. C. (2020). Deepcgh: 3d Computer-Generated Holography Using Deep Learning. *Opt. Express* 28 (18), 26636–26650. doi:10.1364/oe.399624

Hsueh, C. K., and Sawchuk, A. A. (1978). Computer-generated Double-phase Holograms. *Appl. Opt.* 17 (24), 3874–3883. doi:10.1364/ao.17.003874

Huang, G., Liu, Z., Van Der Maaten, L., and Weinberger, K. Q. (2017). "Densely Connected Convolutional Networks," in *Proceedings of the IEEE Conference on Computer Vision and Pattern Recognition*, 4700–4708. doi:10.1109/cvpr.2017.243

Ishii, Y., Shimobaba, T., Blinder, D., Tobias, B., Schelkens, P., Kakue, T., et al. (2022). Optimization of Phase-Only Holograms Calculated with Scaled Diffraction Calculation through Deep Neural Networks. *Appl. Phys. B* 128 (2), 1–11. doi:10.1007/s00340-022-07753-7

Isola, P., Zhu, J. Y., Zhou, T., and Efros, A. (2017). "Image-to-image Translation with Conditional Adversarial Networks," in *Proceedings of the IEEE Conference on Computer Vision and Pattern Recognition*, 1125–1134. doi:10.1109/cvpr.2017.632

James, B., Bardenet, R., Bengio, Y., and Kégl, B. (2011). Algorithms for Hyper-Parameter Optimization. *Adv. Neural Inf. Process. Syst.* 24.

Javidi, B., Carnicer, A., Anand, A., Barbastathis, G., Chen, W., Ferraro, P., et al. (2021). Roadmap on Digital Holography [Invited]. *Opt. Express* 29 (22), 35078–35118. doi:10.1364/oe.435915

Javidi, B., Markman, A., Rawat, S., O'Connor, T., Anand, A., and Andemariam, B. (2018). Sickle Cell Disease Diagnosis Based on Spatio-Temporal Cell Dynamics Analysis Using 3d Printed Shearing Digital Holographic Microscopy. *Opt. Express* 26 (10), 13614–13627. doi:10.1364/oe.26.013614

Jiao, S., Gao, Y., Feng, J., Lei, T., and Yuan, X. (2020). Does Deep Learning Always Outperform Simple Linear Regression in Optical Imaging? *Opt. Express* 28 (3), 3717–3731. doi:10.1364/oe.382319

Jiao, S., Jin, Z., Chang, C., Zhou, C., Zou, W., and Li, X. (2018). Compression of Phase-Only Holograms with Jpeg Standard and Deep Learning. *Appl. Sci.* 8 (8), 1258. doi:10.3390/app8081258

Jiao, S., Zhou, C., Shi, Y., Zou, W., and Li, X. (2019). Review on Optical Image Hiding and Watermarking Techniques. *Opt. Laser Technology* 109, 370–380. doi:10.1016/j.optlastec.2018.08.011

Jo, Y., Park, S., Jung, J., Yoon, J., Joo, H., Kim, M. H., Kang, S. J., Choi, M. C., Lee, S. Y., and Park, Y.Myung Chul Choi, Sang Yup Lee (2017). Holographic Deep Learning for Rapid Optical Screening of Anthrax Spores. *Sci. Adv.* 3 (8), e1700606. doi:10.1126/sciadv.1700606

Johnson, J., Alahi, A., and Fei-Fei, L. (2016). "Perceptual Losses for Real-Time Style Transfer and Super-resolution," in *European Conference on Computer Vision* (Springer), 694–711. doi:10.1007/978-3-319-46475-6_43

Joseph, R., Divvala, S., Girshick, R., and Ali, F. (2016). "You Only Look once: Unified, Real-Time Object Detection," in *Proceedings of the IEEE Conference on Computer Vision and Pattern Recognition*, 779–788.

Kadis, A., Mouthaan, R., Dong, D., Wang, Y., Wetherfield, B., El Guendy, M., et al. (2021). "Binary-phase Computer-Generated Holography Using Hardware-In-The-Loop Feedback," in *Digital Holography and Three-Dimensional Imaging* (Optical Society of America), DW5E–1. doi:10.1364/dh.2021.dw5e.1

Kang, H., Yamaguchi, T., and Yoshikawa, H. (2008). Accurate Phase-Added Stereogram to Improve the Coherent Stereogram. *Appl. Opt.* 47 (19), D44–D54. doi:10.1364/ao.47.000d44

Kang, J.-W., Park, B-S., Park, B.-S., Kim, J.-K., Kim, D.-W., and Seo, Y.-H. (2021). Deep-learning-based Hologram Generation Using a Generative Model. *Appl. Opt.* 60 (24), 7391–7399. doi:10.1364/ao.427262

Kavaklı, K., Urey, H., and Akşit, K. (2022). Learned Holographic Light Transport: Invited. *Appl. Opt.* 61 (5), B50–B55. doi:10.1364/AO.439401

Kim, M. K. K. (2010). Principles and Techniques of Digital Holographic Microscopy. *J. Photon. Energ.* 1 (1), 018005. doi:10.1117/6.0000006

Kishk, S., and Javidi, B. (2003). 3d Object Watermarking by a 3d Hidden Object. *Opt. Express* 11 (8), 874–888. doi:10.1364/oe.11.000874

Krizhevsky, A., Sutskever, I., and Hinton, G. E. (2012). Imagenet Classification with Deep Convolutional Neural Networks. *Adv. Neural Inf. Process. Syst.* 25, 1097–1105.

LeCun, Y., Bengio, Y., and Hinton, G. (2015). Deep Learning. *nature* 521 (7553), 436–444. doi:10.1038/nature14539

Li, H., Chen, X., Chi, Z., Mann, C., and Razi, A. (2020). Deep Dih: Single-Shot Digital In-Line Holography Reconstruction by Deep Learning. *IEEE Access* 8, 202648–202659. doi:10.1109/access.2020.3036380

Lin, X., Rivenson, Y., YardimciYardimci, N. T., Veli, M., Luo, Y., Jarrahi, M., et al. (2018). All-optical Machine Learning Using Diffractive Deep Neural Networks. *Science* 361 (6406), 1004–1008. doi:10.1126/science.aat8084

Liu, J.-P., Tahara, T., Hayasaki, Y., and Poon, T.-C. (2018). Incoherent Digital Holography: a Review. *Appl. Sci.* 8 (1), 143. doi:10.3390/app8010143

Liu, T., De Haan, K., Rivenson, Y., Wei, Z., Zeng, X., Zhang, Y., et al. (2019). Deep Learning-Based Super-resolution in Coherent Imaging Systems. *Sci. Rep.* 9 (1), 3926. doi:10.1038/s41598-019-40554-1

Liu, T., Wei, Z., Rivenson, Y., de Haan, K., Zhang, Y., Wu, Y., et al. (2019). Deep Learning-Based Color Holographic Microscopy. *J. Biophotonics* 12 (11), e201900107. doi:10.1002/jbio.201900107

Liu, T., de Haan, K., Bai, B., Rivenson, Y., Luo, Y., Wang, H., et al. (2020). Deep Learning-Based Holographic Polarization Microscopy. *ACS Photon.* 7 (11), 3023–3034. doi:10.1021/acsphotonics.0c01051

Lucente, M. E. (1993). Interactive Computation of Holograms Using a Look-Up Table. *J. Electron. Imaging* 2 (1), 28–34. doi:10.1117/12.133376

Maimone, A., Georgiou, A., and KollinKollin, J. S. (2017). Holographic Near-Eye Displays for Virtual and Augmented Reality. *ACM Trans. Graph.* 36 (4), 1–16. doi:10.1145/3072959.3073624

Makowski, M., Ducin, I., Kakarenko, K., Suszek, J., Sypek, M., and Kolodziejczyk, A. (2012). Simple Holographic Projection in Color. *Opt. Express* 20 (22), 25130–25136. doi:10.1364/oe.20.025130

Martinez-Carranza, J., Falaggis, K., and Kozacki, T. (2017). Fast and Accurate Phase-Unwrapping Algorithm Based on the Transport of Intensity Equation. *Appl. Opt.* 56 (25), 7079–7088. doi:10.1364/ao.56.007079

Matsushima, K. (2020). *Introduction to Computer Holography: Creating Computer-Generated Holograms as the Ultimate 3D Image*. Springer Nature.

Matsushima, K., and Sonobe, N. (2018). Full-color Digitized Holography for Large-Scale Holographic 3d Imaging of Physical and Nonphysical Objects. *Appl. Opt.* 57 (1), A150–A156. doi:10.1364/AO.57.00A150

Matsushima, K., and Nakahara, S. (2009). Extremely High-Definition Full-Parallax Computer-Generated Hologram Created by the Polygon-Based Method. *Appl. Opt.* 48 (34), H54–H63. doi:10.1364/ao.48.000h54

Muramatsu, N., Ooi, C. W., Itoh, Y., and Ochiai, Y. (2017). "Deepholo: Recognizing 3d Objects Using a Binary-Weighted Computer-Generated Hologram," in SIGGRAPH Asia 2017 Posters, 1–2.

Nishitsuji, T., Shimobaba, T., Kakue, T., and Ito, T. (2017). Review of Fast Calculation Techniques for Computer-Generated Holograms with the point-light-source-based Model. *IEEE Trans. Ind. Inf.* 13 (5), 2447–2454. doi:10.1109/tii.2017.2669200

O'Connor, T., Anand, A., Andemariam, B., and Javidi, B. (2020). Deep Learning-Based Cell Identification and Disease Diagnosis Using Spatio-Temporal Cellular Dynamics in Compact Digital Holographic Microscopy. *Biomed. Opt. Express* 11 (8), 4491–4508.

O'Connor, T., Shen, J. B., Liang, B. T., and Javidi, B. (2021). Digital Holographic Deep Learning of Red Blood Cells for Field-Portable, Rapid Covid-19 Screening. *Opt. Lett.* 46 (10), 2344–2347.

Oikawa, M., Shimobaba, T., Yoda, T., Nakayama, H., Shiraki, A., Masuda, N., et al. (2011). Time-division Color Electroholography Using One-Chip Rgb Led and Synchronizing Controller. *Opt. Express* 19 (13), 12008–12013. doi:10.1364/oe.19.012008

Okada, N., Shimobaba, T., Ichihashi, Y., Oi, R., Yamamoto, K., Oikawa, M., et al. (2013). Band-limited Double-step Fresnel Diffraction and its Application to Computer-Generated Holograms. *Opt. Express* 21 (7), 9192–9197. doi:10.1364/oe.21.009192

Park, D.-Y., and Park, J.-H. (2020). Hologram Conversion for Speckle Free Reconstruction Using Light Field Extraction and Deep Learning. *Opt. Express* 28 (4), 5393–5409. doi:10.1364/oe.384888

Park, S., Kim, Y., and Moon, I. (2021). Automated Phase Unwrapping in Digital Holography with Deep Learning. *Biomed. Opt. Express* 12 (11), 7064–7081. doi:10.1364/boe.440338

Peng, Y., Choi, S., Kim, J., and Wetzstein, G. (2021). Speckle-free Holography with Partially Coherent Light Sources and Camera-In-The-Loop Calibration. *Sci. Adv.* 7 (46), eabg5040. doi:10.1126/sciadv.abg5040

Peng, Y., Choi, S., Padmanaban, N., and Wetzstein, G. (2020). Neural Holography with Camera-In-The-Loop Training. *ACM Trans. Graph.* 39 (6), 1–14. doi:10.1145/3414685.3417802

Pitkäaho, T., Aki, M., and Naughton, T. J. (2017). *Deep Convolutional Neural Networks and Digital Holographic Microscopy for In-Focus Depth Estimation of Microscopic Objects*.

Pitkäaho, T., Manninen, A., and Naughton, T. J. (2019). Focus Prediction in Digital Holographic Microscopy Using Deep Convolutional Neural Networks. *Appl. Opt.* 58 (5), A202–A208. doi:10.1364/ao.58.00a202

Qin, Y., Wan, S., Wan, Y., Weng, J., Liu, W., and Gong, Q. (2020). Direct and Accurate Phase Unwrapping with Deep Neural Network. *Appl. Opt.* 59 (24), 7258–7267. doi:10.1364/ao.399715

Refregier, P., and Javidi, B. (1995). Optical Image Encryption Based on Input Plane and Fourier Plane Random Encoding. *Opt. Lett.* 20 (7), 767–769. doi:10.1364/ol.20.000767

Ren, Z., Xu, Z., and Lam, E. Y. (2018). Autofocusing in Digital Holography Using Deep Learning. *Three-Dimensional Multidimensional Microsc. Image Acquisition Process. XXV* 10499, 104991V.

Rivenson, Y., Wu, Y., and Ozcan, A. (2019). Deep Learning in Holography and Coherent Imaging. *Light Sci. Appl.* 8 (1), 85–88. doi:10.1038/s41377-019-0196-0

Rivenson, Y., Zhang, Y., Günaydın, H., Teng, D., and Ozcan, A. (2018). Phase Recovery and Holographic Image Reconstruction Using Deep Learning in Neural Networks. *Light Sci. Appl.* 7 (2), 17141. doi:10.1038/lsa.2017.141

Ronneberger, O., Fischer, P., and Brox, T. (2015). "U-net: Convolutional Networks for Biomedical Image Segmentation," in *International Conference on Medical Image Computing and Computer-Assisted Intervention* (Springer), 234–241. doi:10.1007/978-3-319-24574-4_28

Rosen, J., Vijayakumar, A., Kumar, M., Rai, M. R., Kelner, R., Kashter, Y., et al. (2019). Recent Advances in Self-Interference Incoherent Digital Holography. *Adv. Opt. Photon.* 11 (1), 1–66. doi:10.1364/aop.11.000001

Sakib Rahman, M. S., and Ozcan, A. (2021). Computer-free, All-Optical Reconstruction of Holograms Using Diffractive Networks. *ACS Photon.* 8, 3375–3384. doi:10.1021/acsphotonics.1c01365

Seldowitz, M. A., Allebach, J. P., and Sweeney, D. W. (1987). Synthesis of Digital Holograms by Direct Binary Search. *Appl. Opt.* 26 (14), 2788–2798. doi:10.1364/ao.26.002788

Shao, S., Mallery, K., Kumar, S. S., and Hong, J. (2020). Machine Learning Holography for 3d Particle Field Imaging. *Opt. Express* 28 (3), 2987–2999. doi:10.1364/oe.379480

Shi, L., Li, B., Kim, C., Kellnhofer, P., and Matusik, W. (2021). Towards Real-Time Photorealistic 3d Holography with Deep Neural Networks. *Nature* 591 (7849), 234–239. doi:10.1038/s41586-020-03152-0

Shi, W., Caballero, J., Huszár, F., Totz, J., Aitken, A. P., Bishop, R., et al. (2016). "Real-time Single Image and Video Super-resolution Using an Efficient Sub-pixel Convolutional Neural Network," in *Proceedings of the IEEE Conference on Computer Vision and Pattern Recognition*, 1874–1883. doi:10.1109/cvpr.2016.207

Shimobaba, T., Kakue, T., and Ito, T. (2018). "Convolutional Neural Network-Based Regression for Depth Prediction in Digital Holography," in 2018 IEEE 27th International Symposium on Industrial Electronics (ISIE), Cairns, QLD, Australia, 13-15 June 2018 (IEEE), 1323–1326. doi:10.1109/isie.2018.8433651

Shimobaba, T., Kakue, T., and Ito, T. (2015). Review of Fast Algorithms and Hardware Implementations on Computer Holography. *IEEE Trans. Ind. Inform.* 12 (4), 1611–1622.

Shimobaba, T., Oshima, S., Kakue, T., and Ito, T. (2021). Image Quality Enhancement of Embedded Holograms in Holographic Information Hiding Using Deep Neural Networks. *Asian J. Phys.* in print.

Shimobaba, T., Blinder, D., Makowski, M., Schelkens, P., Yamamoto, Y., Hoshi, I., et al. (2019). Dynamic-range Compression Scheme for Digital Hologram Using a Deep Neural Network. *Opt. Lett.* 44 (12), 3038–3041. doi:10.1364/ol.44.003038

Shimobaba, T., Blinder, D., Schelkens, P., Yamamoto, Y., Hoshi, I., Shiraki, A., et al. (2021). "Deep-learning-based Dynamic Range Compression for 3d Scene Hologram," in *ICOL-2019: Proceedings of the International Conference on*

Optics and Electro-Optics (Dehradun, India: Springer Singapore), 41–44. doi:10.1007/978-981-15-9259-1_10

Shimobaba, T., Endo, Y., Hirayama, R., Nagahama, Y., Takahashi, T., Nishitsuji, T., et al. (2017). Autoencoder-based Holographic Image Restoration. *Appl. Opt.* 56 (13), F27–F30. doi:10.1364/ao.56.000f27

Shimobaba, T., and Ito, T. (2003). A Color Holographic Reconstruction System by Time Division Multiplexing with Reference Lights of Laser. *Opt. Rev.* 10 (5), 339–341. doi:10.1007/s10043-003-0339-6

Shimobaba, T., and Ito, T. (2015). Random Phase-free Computer-Generated Hologram. *Opt. Express* 23 (7), 9549–9554. doi:10.1364/oe.23.009549

Shimobaba, T., Kakue, T., Okada, N., Oikawa, M., Yamaguchi, Y., and Ito, T. (2013). Aliasing-reduced Fresnel Diffraction with Scale and Shift Operations. *J. Opt.* 15 (7), 075405. doi:10.1088/2040-8978/15/7/075405

Shimobaba, T., Kuwata, N., Homma, M., Takahashi, T., Nagahama, Y., Sano, M., et al. (2017). Convolutional Neural Network-Based Data page Classification for Holographic Memory. *Appl. Opt.* 56 (26), 7327–7330. doi:10.1364/ao.56.007327

Shimobaba, T., Masuda, N., and Ito, T. (2009). Simple and Fast Calculation Algorithm for Computer-Generated Hologram with Wavefront Recording Plane. *Opt. Lett.* 34 (20), 3133–3135. doi:10.1364/ol.34.003133

Shimobaba, T., Takahashi, T., Yamamoto, Y., Endo, Y., Shiraki, A., Nishitsuji, T., et al. (2019). Digital Holographic Particle Volume Reconstruction Using a Deep Neural Network. *Appl. Opt.* 58 (8), 1900–1906. doi:10.1364/ao.58.001900

Stepien, P., Muhamad, R. K., Blinder, D., Schelkens, P., and Kujawińska, M.(2020). Spatial Bandwidth-Optimized Compression of Image Plane off-axis Holograms with Image and Video Codecs. *Opt. Express* 28 (19), 27873–27892.

Tahara, T., Quan, X., Otani, R., Takaki, Y., and Matoba, O. (2018). Digital Holography and its Multidimensional Imaging Applications: a Review. *Microscopy* 67 (2), 55–67. doi:10.1093/jmicro/dfy007

Takaki, Y., and Okada, N. (2009). Hologram Generation by Horizontal Scanning of a High-Speed Spatial Light Modulator. *Appl. Opt.* 48 (17), 3255–3260. doi:10.1364/ao.48.003255

Takeda, M., Ina, H., and Kobayashi, S. (1982). Fourier-transform Method of Fringe-Pattern Analysis for Computer-Based Topography and Interferometry. *J. Opt. Soc. Am.* 72 (1), 156–160. doi:10.1364/josa.72.000156

Tsang, P. W. M., Chow, Y. T., and Poon, T.-C. (2017). Generation of Patterned-Phase-Only Holograms (Ppohs). *Opt. Express* 25 (8), 9088–9093. doi:10.1364/oe.25.009088

Tsang, P. W. M., Poon, T.-C., and Wu, Y. M. (2018). Review of Fast Methods for point-based Computer-Generated Holography [Invited]. *Photon. Res.* 6 (9), 837–846. doi:10.1364/prj.6.000837

Tzeng, E., Hoffman, J., Saenko, K., and Darrell, T. (2017). "Adversarial Discriminative Domain Adaptation," in *Proceedings of the IEEE Conference on Computer Vision and Pattern Recognition*, 7167–7176. doi:10.1109/cvpr.2017.316

Ulyanov, D., Vedaldi, A., and Lempitsky, V. (2018). "Deep Image Prior," in *Proceedings of the IEEE Conference on Computer Vision and Pattern Recognition*, 9446–9454.

Vander Lugh, A. (1964). Signal Detection by Complex Spatial Filtering. *IEEE Trans. Inf. Theor.* 10, 139.

Wagner, C., Osten, W., and Seebacher, S. (2000). Direct Shape Measurement by Digital Wavefront Reconstruction and Multiwavelength Contouring. *Opt. Eng.* 39 (1), 79–85. doi:10.1117/1.602338

Wang, F., Bian, Y., Wang, H., Lyu, M., Pedrini, G., Osten, W., et al. (2020). Phase Imaging with an Untrained Neural Network. *Light Sci. Appl.* 9 (1), 77–7. doi:10.1038/s41377-020-0302-3

Wang, H., Lyu, M., and Situ, G. (2018). Eholonet: a Learning-Based End-To-End Approach for In-Line Digital Holographic Reconstruction. *Opt. Express* 26 (18), 22603–22614. doi:10.1364/oe.26.022603

Wang, K., Dou, J., Kemao, Q., Di, J., and Zhao, J. (2019). Y-net: a One-To-Two Deep Learning Framework for Digital Holographic Reconstruction. *Opt. Lett.* 44 (19), 4765–4768. doi:10.1364/ol.44.004765

Wang, K., Kemao, Q., Di, J., and Zhao, J. (2020). Y4-net: a Deep Learning Solution to One-Shot Dual-Wavelength Digital Holographic Reconstruction. *Opt. Lett.* 45 (15), 4220–4223. doi:10.1364/ol.395445

Wang, K., Li, Y., Kemao, Q., Di, J., and Zhao, J. (2019). One-step Robust Deep Learning Phase Unwrapping. *Opt. Express* 27 (10), 15100–15115. doi:10.1364/oe.27.015100

Wang, X., Wang, W., Wei, H., Xu, B., and Dai, C. (2021). Holographic and Speckle Encryption Using Deep Learning. *Opt. Lett.* 46 (23), 5794–5797. doi:10.1364/ol.443398

Watanabe, S., Shimobaba, T., Kakue, T., and Ito, T. (2021). *Hyperparameter Tuning of Optical Neural Network Classifiers for High-Order Gaussian Beams*. arXiv preprint arXiv:2112.09872.

Wu, J., Liu, K., Sui, X., and Cao, L. (2021). High-speed Computer-Generated Holography Using an Autoencoder-Based Deep Neural Network. *Opt. Lett.* 46 (12), 2908–2911. doi:10.1364/ol.425485

Wu, Y., Luo, Y., Chaudhari, G., Rivenson, Y., Calis, A., De Haan, K., et al. (2019). Bright-field Holography: Cross-Modality Deep Learning Enables Snapshot 3d Imaging with Bright-Field Contrast Using a Single Hologram. *Light Sci. Appl.* 8 (1), 25–27. doi:10.1038/s41377-019-0139-9

Yamaguchi, M., Hoshino, H., Honda, T., and Ohyama, N. (1993). Phase-added Stereogram: Calculation of Hologram Using Computer Graphics Technique. *Pract. Holography VII: Imaging Mater.* 1914, 25–31. doi:10.1117/12.155027

Yamauchi, Ss., Chen, Y-W., and Nakao, Zensho. (1998). "Optimization of Computer-Generated Holograms by an Artificial Neural Network," in 1998 Second International Conference. Knowledge-Based Intelligent Electronic Systems. Proceedings KES'98 (Cat. No. 98EX111), Adelaide, SA, Australia, 21-23 April 1998 (IEEE), 220–223.

Yao, A. M., and Padgett, M. J. (2011). Orbital Angular Momentum: Origins, Behavior and Applications. *Adv. Opt. Photon.* 3 (2), 161–204. doi:10.1364/aop.3.000161

Yatagai, T. (1976). Stereoscopic Approach to 3-d Display Using Computer-Generated Holograms. *Appl. Opt.* 15 (11), 2722–2729. doi:10.1364/ao.15.002722

Yin, D., Gu, Z., Zhang, Y., Gu, F., Nie, S., Ma, J., et al. (2019). Digital Holographic Reconstruction Based on Deep Learning Framework with Unpaired Data. *IEEE Photon. J.* 12 (2), 1–12.

Zeng, T., Zhu, Y., and Lam, E. Y. (2021). Deep Learning for Digital Holography: a Review. *Opt. Express* 29 (24), 40572–40593. doi:10.1364/oe.443367

Zhang, H., Zhao, Y., Cao, L., and Jin, G. (2015). Fully Computed Holographic Stereogram Based Algorithm for Computer-Generated Holograms with Accurate Depth Cues. *Opt. Express* 23 (4), 3901–3913. doi:10.1364/oe.23.003901

Zhang, K., Zuo, W., Chen, Y., Meng, D., and Zhang, L. (2017). Beyond a Gaussian Denoiser: Residual Learning of Deep Cnn for Image Denoising. *IEEE Trans. Image Process.* 26 (7), 3142–3155. doi:10.1109/tip.2017.2662206

Zhang, W., Cao, L., Brady, D. J., Zhang, H., Cang, J., Zhang, H., et al. (2018). Twin-image-free Holography: a Compressive Sensing Approach. *Phys. Rev. Lett.* 121 (9), 093902. doi:10.1103/PhysRevLett.121.093902

Zhang, Y.-P., Wang, F., Poon, T.-C., Fan, S., and Xu, W. (2018). Fast Generation of Full Analytical Polygon-Based Computer-Generated Holograms. *Opt. Express* 26 (15), 19206–19224. doi:10.1364/oe.26.019206

Zhang, Y., Andreas Noack, M., Vagovic, P., Fezzaa, K., Garcia-Moreno, F., Ritschel, T., et al. (2021). Phasegan: a Deep-Learning Phase-Retrieval Approach for Unpaired Datasets. *Opt. Express* 29 (13), 19593–19604. doi:10.1364/oe.423222

Zhang, Y., Wang, H., Wu, Y., Tamamitsu, M., and Ozcan, A. (2017). Edge Sparsity Criterion for Robust Holographic Autofocusing. *Opt. Lett.* 42 (19), 3824–3827. doi:10.1364/ol.42.003824

Zhang, Y., Zhu, Y., and Lam, E. Y. (2022). Holographic 3d Particle Reconstruction Using a One-Stage Network. *Appl. Opt.* 61 (5), B111–B120. doi:10.1364/ao.444856

Zhao, Y., Cao, L., Zhang, H., Kong, D., and Jin, G. (2015). Accurate Calculation of Computer-Generated Holograms Using Angular-Spectrum Layer-Oriented Method. *Opt. Express* 23 (20), 25440–25449. doi:10.1364/oe.23.025440

Conflict of Interest: The authors declare that the research was conducted in the absence of any commercial or financial relationships that could be construed as a potential conflict of interest.

Publisher's Note: All claims expressed in this article are solely those of the authors and do not necessarily represent those of their affiliated organizations, or those of the publisher, the editors and the reviewers. Any product that may be evaluated in this article, or claim that may be made by its manufacturer, is not guaranteed or endorsed by the publisher.

frontiers in Photonics

REVIEW
published: 29 March 2022
doi: 10.3389/fphot.2022.845971

A Survey for 3D Flame Chemiluminescence Tomography: Theory, Algorithms, and Applications

Ying Jin[1]* *and Guohai Situ*[1,2]*

[1]Shanghai Institute of Optics and Fine Mechanics, Chinese Academy of Sciences, Shanghai, China, [2]Hangzhou Institute for Advanced Study, University of Chinese Academy of Sciences, Hangzhou, China

Combustion diagnostics play an essential role in energy engineering, transportation, and aerospace industries, which has great potential in combustion efficiency improvement and polluting emission control. The three-dimensional (3D) visualization of the combustion field and the measurement of key physical parameters such as temperature, species concentration, and velocity during the combustion process are important topics in the field of combustion diagnostics. Benefiting from the non-contact and non-intrusive advantages of the optical detection method as well as the advantages of the 3D full-field measurement of the measured field by computational tomography, flame chemiluminescence tomography (FCT) has the ability to realize non-intrusive and instantaneous 3D quantitative measurement and 3D full-field visualization of key physical parameters in the combustion process, which has crucial research significance in combustion diagnostics. In this study, we review the progress of FCT technique. First, we provide an extensive review of practical applications of FCT in state-of-the-art combustion diagnostics and research. Then, the basic concepts and mathematical theory of FCT are elaborated. Finally, we introduce the conventional reconstruction algorithm and proceed to more popular artificial intelligence-based algorithms.

Keywords: 3D optical computerized tomography, spectroscopy measurement, flame chemiluminescence, reconstruction algorithm, projection model, deep learning, combustion diagnostics

OPEN ACCESS

Edited by:
Peter Wai Ming Tsang,
City University of Hong Kong, Hong Kong SAR, China

Reviewed by:
Wen Chen,
Hong Kong Polytechnic University, Hong Kong SAR, China
Jianglei Di,
Guangdong University of Technology, China
Hongbo Zhang,
Virginia Military Institute, United States

***Correspondence:**
Ying Jin
yingjin@siom.ac.cn
Guohai Situ
ghsitu@siom.ac.cn

Specialty section:
This article was submitted to Optical Information Processing and Holography, a section of the journal Frontiers in Photonics

Received: *30 December 2021*
Accepted: *02 March 2022*
Published: *29 March 2022*

Citation:
Jin Y and Situ G (2022) A Survey for 3D Flame Chemiluminescence Tomography: Theory, Algorithms, and Applications. Front. Photonics 3:845971. doi: 10.3389/fphot.2022.845971

INTRODUCTION

As a kind of complex reaction process, combustion phenomenon combines chemical, physical, and mechanical knowledge, which is accompanied by the formation of a large number of intermediate products such as OH*, CH*, and C2* radicals. It has been reported that CH*, C2*, and OH* radicals can be considered the critical parameters in the combustion process of hydrocarbon fuels as well as be intimately related to the combustion status (Gaydon and Wolfhard, 1953; Nori and Seitzman, 2008; Alviso et al., 2017; Navakas et al., 2018). As a consequence, with the aid of the detection and measurement of OH*, CH*, and C2* radicals in the combustion process, the diagnosis of combustion characteristics such as combustion components, combustion structure, temperature, velocity, pollution emissions, and the heat release rate of the combustion field can be realized, which will further facilitate the control of the combustion process and gain an in-depth understanding of the combustion reaction mechanism in the industrial fields of aerospace and energy (Kojima et al., 2005; Jeong et al., 2006; Orain and Hardalupas, 2010; Hossain and Nakamura, 2014; Sun et al., 2015; Ax and Meier, 2016).

During the combustion process, the radicals emit spectra of specific wavelengths from the excited state to the ground state, which is defined as the flame chemiluminescence spectrum (Gupta et al., 1999). For instance, the chemiluminescence spectrum measurement of high-temperature propane flame has been provided in Gupta et al. (1999). On account of the flame chemiluminescence spectrum being the inherent optical property of flame in the combustion process, the measurement of flame chemiluminescence spectrum becomes the most straightforward strategy to analyze the combustion properties (Griffiths and Barnard, 1995; Kathrotia et al., 2012). Compared to the commonly employed methods in combustion diagnostics, such as the laser induced fluorescence (LIF) technique (Daniele et al., 2013; Wellander et al., 2014; Lee et al., 2015) and the particle image velocimetry (PIV) technique (Weinkauff et al., 2013; Liu et al., 2018; Liu and Ma, 2020), flame chemiluminescence spectrum technology eliminates the demand for an external detection source and the requirement of spreading tracer particles in the tested flame. Flame chemiluminescence spectrum technology focuses on the wavelength of specific radicals; the intensity of radicals can be accessed directly after filtering and acquiring *via* industrial cameras or optical fiber detectors. Furthermore, in contrast with spatial single-point or planar detection methods, the chemiluminescence 3D imaging strategy shows better performance in full-field 3D quantitative visualization and detection of crucial physical parameters in a complex combustion phenomenon, not only in modern aviation, aerospace, and military fields, for instance, the 3D combustion structure detection of rocket motor exhaust flames, but also for a wide range of industrial and civil applications, such as energy engineering of an industrial power plant boiler chamber and high-temperature cutting and smelting. As a consequence, benefited by the non-contact, easy implementation, and simple arrangement of the experiment setup as well as full-field measurement ability, chemiluminescence 3D imaging tactics has attracted a lot of attention in the field of combustion diagnostics.

In a bid to achieve 3D visualization as well as measurement of the combustion field, computerized tomography (CT) technology is used and integrated with the flame chemiluminescence spectrum method, and then the flame chemiluminescence tomography (FCT) technique is developed (Sebald, 1980; Melnikova and Pickalov, 1984; Iwama et al., 1989). With the advantages of the non-contact and non-intrusiveness of the optical detection method and the ability of 3D full-field measurement of CT, FCT is capable of achieving both instantaneous 3D quantitative measurement and full-field visualization of key physical parameters in the combustion field, which has essential research significance in combustion diagnostics. Recently, with the continuous advancement in the performance of photoelectric detection equipment and the tremendous improvement of computing power, numerous scholars have carried out extensive research in the acquisition and calibration of multidirectional projection data, the establishment of projection models, and the improvement of 3D reconstruction algorithms of FCT.

In order to provide a comprehensive review of flame chemiluminescence-based tomographic imaging and technology, the remainder of this article is organized as follows: the applications of FCT in practical combustion diagnostics are given in **Section 2**. **Section 3** focuses on background information of FCT and begins with concepts of the projection model before presenting an explanation of projection acquirement as well as multi-view calibration; **Section 4** depicts the mathematical formulation of the reconstruction algorithm of tomographic inverse problem; furthermore, **Section 5** concludes the review with a summary and an outlook on the potential developments of FCT in the future.

APPLICATION OF FCT

FCT technique has been extensively employed in practical combustion measurement of laboratory and industry to provide key insights into flame physics. This section surveys four main aspects of application of FCT, including combustion status, geometric measurement, temperature measurement, and propagation speed measurement.

Combustion Status

The chemiluminescence intensity of excited OH*, CH*, and C2* has been reported having maxima of the flame spectra at 309, 431.5, and 516.5 nm, respectively (Gupta et al., 1999). Many scholars focus on the measurement of OH*, CH*, and C2* concentration and pay extensive attention to figure out the relationship between the measured chemiluminescence and flame combustion status with various experimental conditions, such as the equivalence ratio and fuel type in practical systems.

The relationship between the intensity ratios (C2*/CH*, C2*/OH*, and CH*/OH*) of methane/air partially premixed flame with different equivalence ratios were investigated and compared with the results of a photomultiplier tube (PMT) in the study by Y. Jeong. Abel inversion was applied here to reconstruct cylindrically symmetric flame to yield 2D "slices" (Jeong et al., 2006). Likewise, Denisova et al. (2013) attempted to reconstruct the spatial distributions of CH*, OH*, and C2* chemiluminescence of axisymmetric as well as non-axisymmetric flames to further monitor the fuel–air ratio and completeness of combustion. Similarly, Liu et al. (2020) employed intensified-CCD and the Abel inversion method to retrieve 2D radial distribution of chemiluminescence characteristics of OH* and CH* in a low swirl burner with the equivalence ratio varying from 0.8 to 1.2. Analogous work has been mentioned in D. Sellan's research. The OH*/CH* signals of a swirl-stabilized axisymmetric flame with changing equivalence ratios were measured and reconstructed by Abel inversion (Sellan and Balusamy, 2021).

In contrast to aforementioned 2D reconstruction, taking the transmissivity of a customized double-channel band-pass filter and a color camera into account, Y. Jin et al. proposed a quantitative multispectral separation technique to realize both

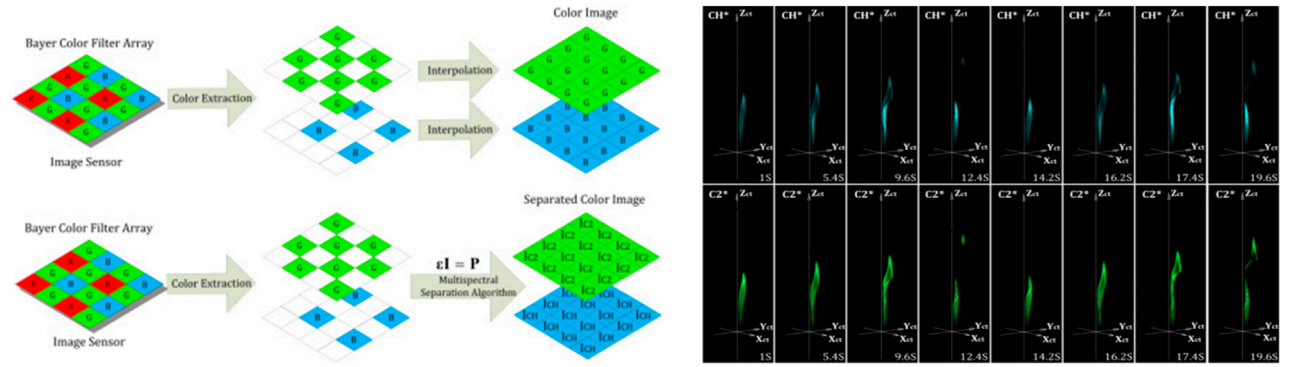

FIGURE 1 | Multispectral separation algorithm and 3D radical distribution of CH* and C2*. Adapted with permission from Jin et al. (2017) © The Optical Society.

CH* and C2* intensities. As seen in **Figure 1**, the dynamic 3D chemiluminescence emission structure of CH* and C2* were reconstructed simultaneously. Afterward, quantitative analysis of CH* and C2* components was conducted in details (Jin et al., 2017).

Temperature Measurement

The measurement of flame temperature plays an essential role in combustion diagnostics and is necessary to access an in-depth understanding of combustion physics. Several methods have been utilized for flame temperature measurements, such as LIF, moiré deflection, and tunable diode laser absorption spectroscopy (TDLAS) (Kaminski and Kaminski, 2014). However, limited by the complex arrangement of the aforementioned technique, they are somehow unsuitable for industrial requirement. With the increasing employment of the FCT method, it also gives a potential tactic for recovering 3D flame temperature distribution.

On the basis of two-color pyrometric techniques and optical CT theory, 3D temperature and emission distributions of propane flame were reconstructed simultaneously by M. M. Hossain. In their study, two RGB CCD cameras coupled with eight OFB were used to acquire flame images. Red and green components were extracted to further achieve temperature and emission measurements in view of the two-color method (Hossain et al., 2013). Similar methods were reported in Brisley et al. (2005). Also, double-wave spectral tomography was adopted to retrieve distribution features of the 3D temperature field. Different from the aforementioned studies, Gao et al. (2010) established an orthographic CCD array coupled with the narrowband filters (central wavelength: 696.5 and 763.5 nm) to acquire images *via* four views. Using 4D temperature measurements a weakly turbulent diffusion flame was studied in the same way in Yu et al. (2021). Recently, Y. Liu et al. proposed a light-field sectioning pyrometry (LFSP) method which combined light-field imaging and color ratio pyrometry (CRP) to achieve *in situ* temperature measurement of ethylene flame. Moreover, the spatial resolution of reconstruction was improved in lateral and depth directions based on their cage-typed light-field camera (Liu et al., 2021a; Shi et al., 2022).

Geometric Measurement

Flame geometrical characteristics give instantaneous information on the quality of the combustion process. The monitoring and measurement of flame geometric are essential for deepening the understanding and optimizing the combustion conditions. Benefiting from the rise of 3D tomography technology, FCT technique has been a promising tactic for providing 3D whole-field geometric measurement of the flame, which is generally impossible by using traditional 2D measurement methods.

Several parameters, such as orientation, volume, length, surface area, and circularity, were defined to characterize the flame geometry by H. C. Bheemul. Combined with the mesh-generating technique and the FCT method, a 'fishnet' was generated to cover the flame surface. The aforementioned geometric parameters were measured and analyzed based on 3D reconstruction results of the diffusion flame (Bheemul et al., 2002). By means of FCT, T. D. Upton investigated structural details of a turbulent, premixed propane/air flame. The 3D flame front and 2D contours were recovered with high resolution (Upton et al., 2011). It is worth pointing out that 3D flame topography and curvature were inspected in detail by L. Ma. The projections of premixed turbulent Bunsen flame were captured from six perspectives at a rate of 5 kHz. Probability density function (PDF) of flame topography was derived from a series of 3D reconstruction results, and the calculation of flame curvature was achieved in Ma et al. (2016). Recently, R. Dong focused on the relationship between flame edge deformations and oscillations. The 3D instantaneous flame edge structures with fine-scale corrugations were retrieved using the FCT tactic, which enabled the observation of small vortices' evolution (Dong et al., 2021a). An analogous strategy was employed in 4D fire events imaging for temporal evolution of flame (Windle et al., 2021).

Flame Propagation Speed Measurement

Flame propagation speed plays a crucial role in combustion diagnostics owing to the straightforward reflection of flame stabilization. Generally, flame propagation speed refers to the moving speed of the flame surface in the combustion process, which is also called the absolute flame velocity in some cases. In contrast to the commonly used tactic for velocity measurement, such as PIV and PLIF methods, the FCT technique shows

privileged advantages in the measurement of flame propagation speed, owing to the successful application in geometric measurement.

The flame propagation and local burning velocity of a propane/air turbulent flame were investigated in Ishino et al. (2009). A set of flame images were acquired from 40 views with a short time interval to reveal the 3D distributions of the turbulent flame and to further calculate the local burning velocity. On the basis of geometric measurement of two non-axisymmetric premixed flames, Wiseman et al. (2017) depicted the surface speed measurement algorithm and especially focused on the influence of the number of perspective. Considering the frequently used surface fitting and normal vectors methods being not suitable for turbulent flame of laboratory, Y. Chi proposed two novel methods to deal with this problem. Numerical and experimental validations on the turbulent jet flame were conducted. Meanwhile, the relationship between the flame curvature and the propagation speed was analyzed (Chi et al., 2021). Recently, Liu et al. (2021b) concentrated on the influence of the external direct current electric field on the propagation speed of swirl flames. With the help of FCT strategy, the velocity vectors and magnitude contours at various horizontal cross sections were accessed.

BACKGROUND INFORMATION

In this section, some background information about FCT are presented, including a brief demonstration of the acquirement of projections, an introduction to the multi-camera calibration method, and several kinds of projection models often employed for FCT research.

Acquirement of Projections

In FCT practical measurement, the acquirement of projections of the test field is the fundamental for further tomography reconstruction. According to the different combustion state of the test field, the achievement of projections acquisition in practical experiment can be divided into two categories: single directional arrangement and multidirectional arrangement.

A single directional arrangement can be utilized to reveal an axisymmetric flame. Based on the assumption of rotational symmetry of the laboratory-scale flame in their study, Brisley et al. (2004) developed a single monochromatic CCD camera instrumentation system to complete the 3D temperature measurement of a gaseous flame. Similarly, in order to investigate the partial premixing effects of a laminar CH4–air flames with different equivalence ratios, an intensified charge-coupled device (ICCD) system was presented by Jeong et al. (2006) to detect OH*, CH*, and C_2* radicals and tomographic reconstruction. Furthermore, the single directional acquirement assembly could be capitalized on stable flame tomographic measurement, which can be achieved by rotating the test flame. Hertz and Faris (1988) proposed a simple experiment setup and sequentially recorded the projections of a steady-state Bunsen flame by rotating for recovering CH* emission distribution. Although the single-direction projection acquisition system has a simple structure as well as low cost, it is only applicable for test flame with good axial symmetry or stable-state combustion measurement, which is not suitable for instantaneous non-axisymmetric and unstable flame tomographic experiments.

Benefited by the rapid development of optical sensing and computing power, simultaneous multidirectional projection acquirement can be realized. H. C. Bheemul and coworkers built a detection system with three monochromatic CCD cameras to visualize and quantitatively demonstrate the gaseous flames. In their study, three CCD enclosed the burner with equidistance and an equal angle and obtained the 2D projections of the flame simultaneously from three different views (Bheemul et al., 2002). Moreover, a 10 direction Kepler telescopes tomographic system was reported by Anikin et al. (2010) to measure the OH*-chemiluminescence distribution of diffusion as well as premixed flames, respectively. L. Ma et al. reported a five CMOS camera arrangement to record CH* chemiluminescence simultaneously and further retrieved the instantaneous structures of McKenna burner and jet flame volumetrically (Cai et al., 2013a; Li and Ma, 2014; Li and Ma, 2015). A 24-view acquirement setup was proposed by Mohri et al. (2017) to investigate the strengths of the FCT technique in a real highly turbulent swirl flame measurement. It is worth noting that a semicircular shape of cameras equipped with forty small high-performance lenses was designed by Ishino et al. (2005); Ishino and Ohiwa (2005); Ishino et al. (2007); and Ishino et al. (2009). On the basis of their famous forty-lens equipment, further expansion has been applied to achieve a 158-lens FCT system, which was awarded the Guinness world record in 2009 (Ishino et al., 2011).

Additionally, multidirectional capture could be accessed by the combination of a camera and a mirror. GilabertLuYan et al. (2007) established a special imaging system incorporating three identical RGB cameras and an optical transmission unit and captured flame projections concurrently from six perspectives. Similarly, combined with a mirror array, Upton et al. (2011) presented a six camera optical system to collect a turbulent premixed flame projection data from 12 views for 3D reconstruction. Floyd and Kempf (2011) demonstrated an instantaneous computed tomography of the chemiluminescence (CTC) experimental setup, which comprises five cameras and mirrors providing two perspectives for each camera. As demonstrated in **Figure 2C**, Wei presented a high-speed FCT system which included three customized mirror–prism–camera blocks to capture multiple projections of an unconfined turbulent swirl flame from distinct views (Yu et al., 2018a; Ruan et al., 2019).

With the expeditious development of optical fiber technology as well as the advantage of an excellent optical waveguide property, devices based on the optical fiber and industrial cameras have also become a way of multidirectional projection acquisition for FCT. Considering the complex arrangement of multi-camera system, G. Lu et al. designed an imaging fiber-based FCT system coupled with two cameras to acquire flame projections simultaneously from eight fiber bundles around the burner (Hossain et al., 2011; Moinul Hossain et al., 2012).

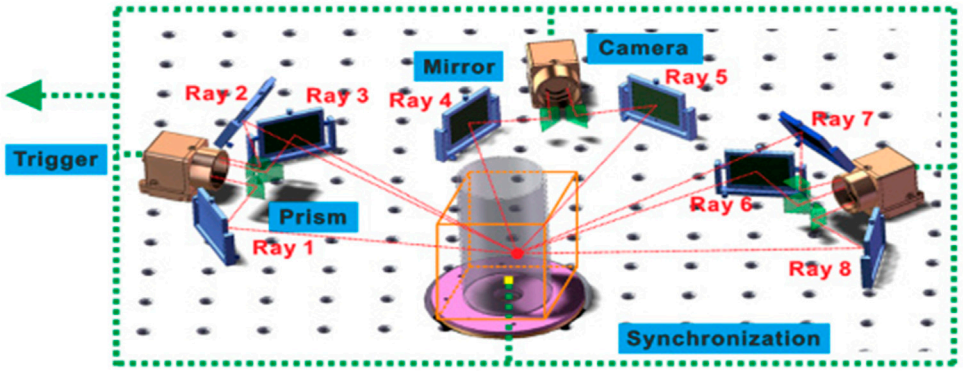

FIGURE 2 | Multidirectional system with mirror–prism–camera blocks. Adapted with permission from Yu et al. (2018a) © The Optical Society.

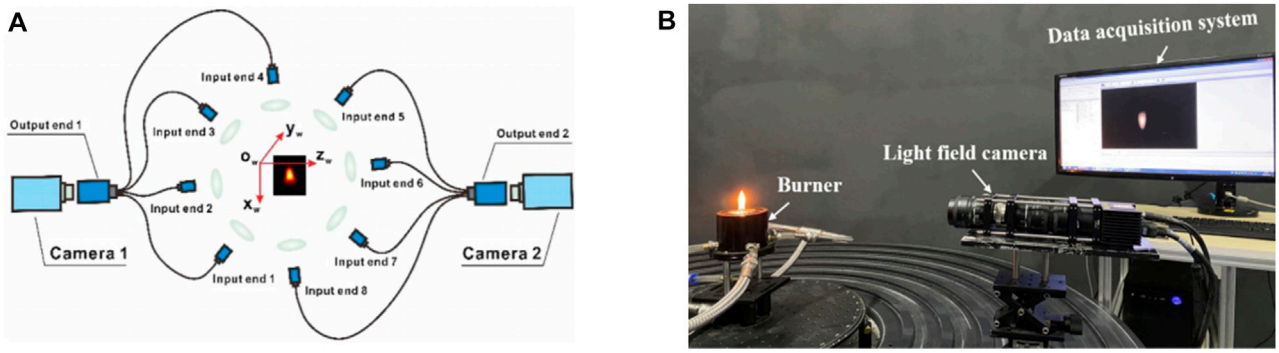

FIGURE 3 | (A) Schematic of the endoscopic multidirectional FCT system. Adapted with permission from Yu et al. (2018b) © The Optical Society. **(B)** Experimental setup of the light-field imaging system. Adapted with permission from Qi et al. (2021a) © The Optical Society.

Wan et al. (2009; Wan et al. (2013) established an optical fiber bundle tomography (OFBT) system consisting of four telecentric lens and a number of fiber bundle units. Similarly, W. Cai et al. developed a variety of endoscopy-based multidirectional FCT projection acquisition systems (Yu et al., 2018b; Liu et al., 2019a; Liu et al., 2019b; Yu et al., 2019a; Yu et al., 2019b). As indicated in **Figure 3A**, two synchronized cameras equipped with customized fiber bundles were utilized to obtain the Bunsen flame projections from eight views simultaneously. In order to maximize the differences between flame projections, eight input fiber bundles were arranged in nearly an equiangular manner in a circular shape (Yu et al., 2018b). A nine inputs optical fiber bundle-based experimental setup was proposed by Q. Lei et al. to transmit the CH* chemiluminescence signals of the swirl flame in the gas turbine to one high-speed camera (Dong et al., 2021b; Rising et al., 2021). Recently, considering the drawbacks of FBT of low SNR imaging and signal diminishment with various equivalence ratios, C. Rising et al. proposed a filter-intensified FBE approach to capture the CH* radical and obtained more precise reconstruction results (Ishino and Ohiwa, 2005).

Recently, taking into account the complexity of installing and operating multidirectional FCT system, as shown in **Figures 3B,C**. Xu et al. designed a cage-typed light-field camera (LFC) system and conducted a series of studies on 3D reconstruction of flame temperature distribution under different combustion operating conditions, including the improvement of spatial resolution as well as the reduction of sampling redundancy (Liu et al., 2017a; Zhao et al., 2018; Liu et al., 2021a; Qi et al., 2021a). Likewise, a light-field camera was used in H. Qi's study. Based on their light-field convolution imaging model, multidimensional radiation information of the flame was collected by LFC, and 3D temperature distribution was further retrieved (Qi et al., 2021b; Niu et al., 2021; Shi et al., 2022).

Calibration of Multi-Camera

The measurement of the spatial positions of multiple acquirement directions and the internal parameters of camera play a critical role in FCT research. View registration is able to unify the placement and orientation of each camera into the same world coordinate system, which have a significant effect on following reconstruction quality.

The spatial location of multiple cameras was generally roughly determined by a very simple angle determination device in previous research. An illuminated alignment tool was utilized in T. D. Upton's study to determine the angular viewing directions, image orientation, and image magnification of a 12

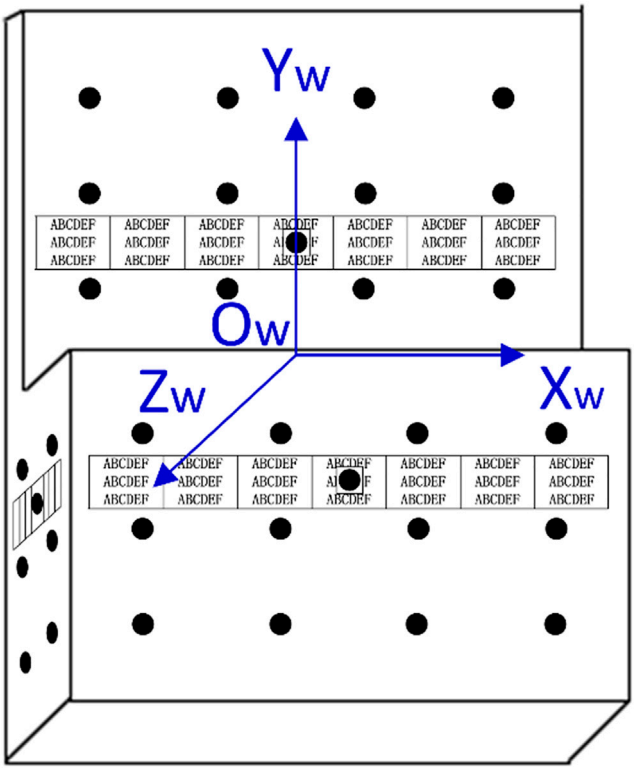

FIGURE 4 | 3D view registration object.

view FCT system. The numbers near the bottom of the tool was separated azimuthally by π/12 radians to indicate the orientation of different projections (Upton et al., 2011). Similarity, J. Floyd et al. employed a cylindrical calibration object to locate the view angles by the scale affixed around the circumference (Moinul Hossain et al., 2012). Additionally, the rectangular object in target contributed to locate the object domain center in each perspective. However, the aforementioned calibration methods can only roughly determine the spatial location of the camera. For the sake of improving the spatial resolution and reconstruction precision of FCT technology, there is an urgent need to develop a more flexible and accurate multi-camera calibration technology.

In the field of computer vision, a large number of studies have been reported on the camera calibration of internal and external parameters (Remondino and Fraser, 2006; Zhang, 2000; Zhang, 1999; Hwang et al., 2013; Huang et al., 2019a). Generally, the commonly used camera calibration method is mainly based on the pinhole camera model, and the spatial position as well as internal parameters of the camera is determined by 2D checkerboard. First, the world coordinate system is established. As a consequence, the position of the corner points of checkerboard in the world coordinate system can be determined. Next, the images of checkerboard are captured *via* camera from various views. On the basis of the image processing algorithm, the identification and location confirmation of the corner points in the camera image coordinate system are completed. Finally, the internal and external parameters of the camera are derived from the world coordinates and image coordinates of the corner points. Worth and Dawson (2012) utilized a custom-made calibration plate to accomplish the view registration in OH* chemiluminescence measurement of two interacting turbulent flames. Plate images were recorded at translation positions corresponding to the measurement volume. World and image coordinates for each camera were established and related *via* a third-order polynomial calibration function. L. Ma et al. adapted 2D check board and an open source camera calibration tool of MATLAB to complete the view registration of the multiple fiber-based endoscopes tomography system (Worth and Dawson, 2012; Kang et al., 2014). Likewise, in order to figure out the geometrical relationship between the reconstruction domain and flame projections, 2D check board was applied in W. Cai's research and placed in the burner's position to conduct the view registration process (Liu et al., 2019a; Yu et al., 2017). Furthermore, J. Wang et al. proposed a 3D pattern with dot arrays for the camera calibration of the multidirectional FCT system. As illustrated in **Figure 4**, three specified points on the surface were used to indicate the focus level of cameras (Wang et al., 2015; Wang et al., 2016a). Nonetheless, the accuracy of this approach is limited by the manufacturing precision of calibration object. Recently, without the special calibration object, Cai et al. (2020) developed a convenient multi-view registration method that capitalized on a synergistic combination of rotating calibration plate and multi-view stereo vision.

Additionally, a number of combustion phenomena of practical environment happen in a confined space, which means the light refractions fostered by the imaging through optical walls will seriously influence the imaging process, and further result in the degradation of calibration precision. As a consequence, the developed view registration method based on an open space will be not applicable for the confined-space problems. In view of this question, Falkhytten (2018) presented a polynomial camera calibration model to address view registration in the FCT system for annular combustion chambers. However, the polynomial calibration model does not indicate a clear physical meaning. Meanwhile, higher-order polynomial functions are often required to ensure higher calibration accuracy, which inevitably introduces a large number of fitting parameters and computational consumption in the computational model. On the basis of the calibration model that takes into account the refraction effect of cylindrical glass (Paolillo and Astarita, 2019), H. Liu et al. proposed a refined model combined with the pinhole camera model with Snell's laws in a swirl flame measurement confined within a 20 mm thick glass. In their strategy, the reverse ray-tracing approach was utilized to incorporate the effects of light refraction (Liu et al., 2019c). As indicated in **Figure 5**, inspired by the study of Liu, a new algorithm was built by Ling et al. (2020) to figure out the ray tracing of the reconstructed domain through the optical cylinder to overcome the time consumption of multiple iterations.

Projection Model of FCT

In order to describe the relationship between the reconstructed domain and the corresponding image, a large and growing body

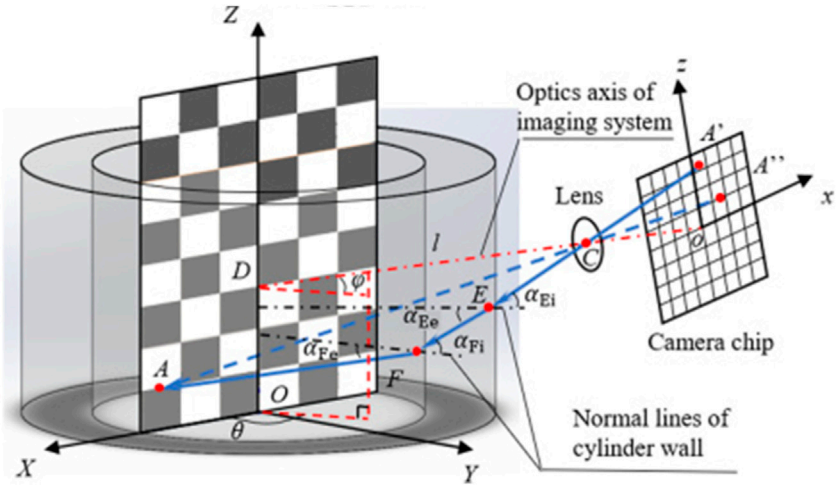

FIGURE 5 | Reversed ray-tracing model with the optical cylinder. Adapted with permission from Ling et al. (2020) © The Optical Society.

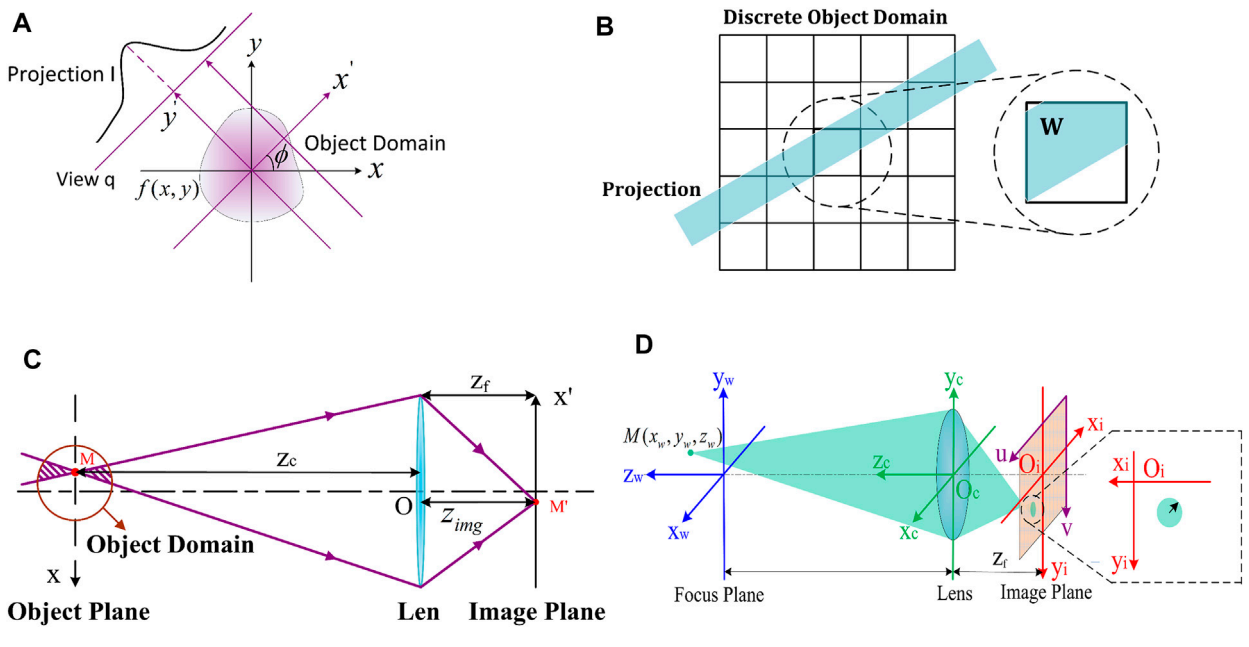

FIGURE 6 | (A) Schematic of projection based on line integrals. **(B)** Example of the calculation of weight factor by the exact intersection area. **(C)** Diagram of the conic projection model. **(D)** Light propagation of a single voxel to the image plane.

of literature has investigated the establishment of the projection model of FCT. Generally, the reconstructed domain is discretized into several voxels with equal size, and different projection models depict various calculation methods of the weight factor, which refer to the contribution by each voxel to the pixels of the image plane.

To date, the parallel projection model is one of methods adopted in FCT research. Based on the parallel projection model, the light intensity value of pixels on the camera image plane can be considered as a linear integration of the light intensity along the parallel projection direction, as shown in **Figure 6A** (Floyd, 2009). In this context, the weight factor represents the intersection length of the light line and the pixel. However, considering the discrete measurement of each perspective has an associated bin width, and strip integrals are a more appropriate way to calculate the weight factor. Taking into account the limitation of computing resources, the original calculation of the weight factor based on strip integration adopted a binary approximation tactic, which means when the center of a pixel was within the boundary of the strip, a unity

value was given to the weight factor; otherwise, the weight factor was set as zero. However, this assumption leads to salt and pepper noise in the reconstruction result. As indicated in **Figure 6B**, with the development of computer technology as well as the increase of computing power, the calculation of the weight factor becomes available by dealing with the exact intersection area (2D) or volume (3D) of the projection beam and pixels (Floyd, 2009). In 1990, Deutsch (1990) of Placer Dome Inc. designed the FORTRAN program to achieve the calculation process. In the light of the aforementioned theory and two-color pyrometric techniques, Hossain et al. (2013) investigated the 3D temperature and emissivity distribution of the laboratory-scale gas-fired flame.

However, the most widely used projection acquisition devices in FCT are industrial cameras, and the impact of the perspective effect of camera lens on the imaging process becomes particularly important and non-negligible, especially when the depth-of-field of the camera is small or the reconstruction domain is large. In this case, the description of the imaging process based on the parallel projection model is not suitable. An alternative projection model was presented in light of a weighted double cone, derived from geometric optics to provide a complimentary modification, which is able to use non-parallel projections to account for perspective effects. **Figure 6C** briefly demonstrates the light propagation of a point source in the reconstructed domain through the lens to the image plane (Floyd, 2009). It is noticeable that the light intensity of point p on the image plane can be obtained by summing the intensity in two conical regions before and after point v on the object plane, instead of the simple approximation of the linear integration of the light intensity along the projection ray (Floyd, 2009; Anikin et al., 2010). Walsh et al. (2000) paid special attention to analyze the influence of a perspective effect of the camera lens on the reconstruction results of an axisymmetric diffusion flame measurement. However, Walsh's study predominantly focused on considering the reconstruction field with axisymmetric distribution and within the depth-of-field of the camera; as a consequence, the weight factor of all voxels located within the cone region was uniformly simplified to 1. In essence, for the voxel located outside the depth-of-field of the camera, it cannot be clearly imaged on the image plane, and in this regard, the weight factor of this voxel can no longer be treated as 1.

In view of the perspective imaging effect, J. Floyd et al. established a 3D projection model considering the depth-of-field effect of lens, which involved the blurring effect of the reconstructed domain outside the depth-of-field range of lens in the imaging process. The weight factor in this projection model can be obtained as follows: first, the cone area of the 3D reconstructed domain corresponding to the pixel on the image plane is determined according to the ray-tracing method; secondly, the position on the image plane of each spatially discrete voxel within the cone area is analyzed; and finally, the weight factor of a voxel to the pixel on image plane is procured *via* estimating the intersection area of the imaging blur circle with the pixel. Their model was validated in the measurements of a methane–oxygen matrix burner as well as a turbulent opposed jet flame. Furthermore, the instantaneous flame-surface density, wrinkling factor, flame normal direction, and heat release were figured out (Floyd et al., 2009; Floyd and Kempf, 2011; Floyd et al., 20112011). As illustrated in **Figure 6D**, on the basis of Floyd's study, Wang et al. (2015) developed a 3D projection model including light collection effect of lens. Additionally, the relationship between the camera pixel and the blur circle was analyzed in detail to provide a more complete calculation of the weight factor, as can be seen in **Figure 7A**. However, it is inevitable that some image spots appear within a pixel while some out of the corresponding circle in the practical imaging process. As a result, the ignored weight factors in such circumstances always cause information missing, which influence the quality of further reconstructions. For the sake of overcoming the drawback of the simplified calculation model, Jin et al. (2016a) presented the equal area and the sub-pixel calculation model of weight factor, respectively, as demonstrated in **Figure 7B**. Moreover, K. Wang et al. further investigated the performance of clear-imaging, out-of-focus imaging, and deconvolution models, as indicated in **Figure 7C**. Considering the bokeh effect, the deconvolution model provided the best precision with low computational time (Wang et al., 2017). However, the aforementioned models are on the basis of the uniform distribution of voxel, which further leads to the large gradient between neighboring voxels and certain discretization errors. In light of the finite element and interpolation operation, Liu et al. (2021c) estimated the distribution within each voxel to defeat uniform voxel problem.

Likewise, the point spread function (PSF) was utilized in W. Cai's study to represent the projection formed by a point-source located at the reconstruction domain, which was only related to the location angle and position of the acquisition device rather than the intensity distribution of the reconstruction domain. Meanwhile, the projections that the camera acquired in the image plane were composed of the summation of all voxels in the reconstruction domain with the interplay of respective PSF (Cai et al., 2013b). A large number of statistical calculations were carried out that capitalized on the Monte Carlo statistical method, and finally the weight factor of one voxel was figured out (Cai et al., 2013a; Li and Ma, 2014). However, the tremendous demand of computing power and relatively low computational efficiency inevitably become the drawback of the Monte Carlo statistical method. In contrast to Cai's method, M. Wan et al. applied the low-discrepancy sequence of the Monte Carlo method instead of the pseudorandom sequence to achieve the Meker burner flame measurement with higher reconstruction accuracy (Wan et al., 2015). Furthermore, by combining the ray-tracing technique and the Monte Carlo method, Wan and Zhuang (2018) took the inhomogeneous distribution of captured radiance on the image plane into account and analyzed the performance numerically.

RECONSTRUCTION ALGORITHM

Apart from the projections acquirement and imaging model establishment, another research focus is the reconstruction algorithm of FCT. As a branch of optical tomography, the reconstruction algorithm of FCT is also derived from the

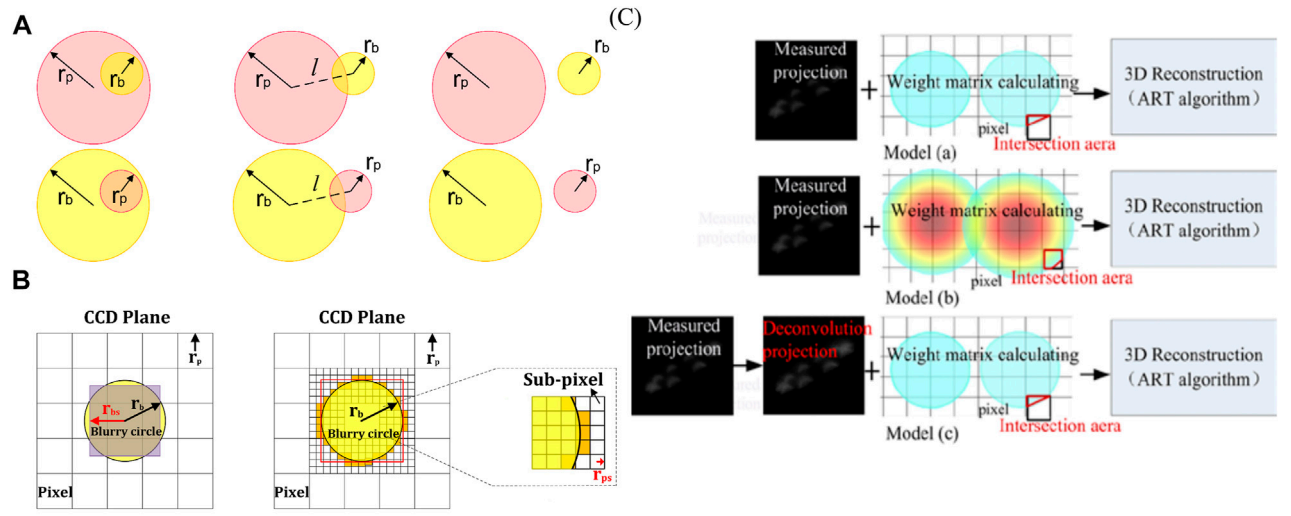

FIGURE 7 | (A) Diagram of the relationship between camera pixel and the blur circle. **(B)** Demonstration of the equal area and the sub-pixel calculation model of weight factor. **(C)** Schematic diagram of clear imaging, out-of-focus imaging, and deconvolution imaging projection models. Adapted with permission from Wang et al. (2017) © The Optical Society.

algorithm study of X-ray CT (Beister et al., 2012). On the other hand, due to the different experimental conditions of practical combustion diagnostics and limitation of optical access, the reconstruction of FCT belongs to incomplete data reconstruction problem. Numerous scholars have conducted extensive research in reconstruction algorithm of FCT. This section reviews the mainly employed reconstruction algorithm: analytical and iterative types. Finally, the emerging artificial intelligence-based reconstruction algorithm of FCT is depicted as well.

Analytical Reconstruction Algorithm

Analytical reconstruction algorithm is separated into Abel Inverse Transform, Radon Inverse Transform and Filtered Back Projection (FBP) method. Abel Inverse Transform is commonly utilized to tackle axisymmetric reconstruction fields. For instance, Y. K. Jeong et al. investigated the combustion structure of axisymmetric methane flame relied on Abel Inverse Transform (Jeong et al., 2006). The traditional 2D Radon Inverse Transform is usually divided into three steps: partial differentiation, Hilbert Transform and inverse projection. On the basis of Radon Inverse Transform, S. Cha and C. M. Vest reconstructed the asymmetric refractive index fields (Vest, 1974; Cha and Vest, 1979). Meanwhile, it was proven that the reconstruction process of Abel Inverse Transform and Radon Inverse Transform are equivalent on the condition of axisymmetric field.

In contrast to the Radon Inverse Transform, the FBP method is more representative of analytical reconstruction algorithm. The FBP method introduces Fourier Transform in Radon Inverse Transform to reduce this blurring in the reconstruction by filtering each perspective before the back projection step. **Eq. 1** describes how a point $(\boldsymbol{x}, \boldsymbol{y})$ in the back projection reconstruction $f_a(x, y)$ is given by the accumulation of the integral values of projections I that intersect with that point. This accumulation is performed over all view angle θ. Z is the propagation length of light. $\hat{I}$ is the filtered version of I. The FBP method was utilized by R. N. Bracewell and A. C. Riddle in the study of radio astronomy (Bracewell and Riddle, 1967). Moreover, G. N. Ramachandran et al. applied the FBP method for medical X-ray CT issue (Ramachandran and Lakshminarayanan, 1971; Shepp and Logan, 1974). G. W. Fairs et al. employed the FBP method for deflection tomography successfully (Faris and Byer, 1988). Furthermore, the application of the FBP reconstruction method in moire deflection tomography has been investigated in detail by Song et al. (2016).

$$\boldsymbol{f_a(x,y)} = \int_0^{\pi} \hat{\boldsymbol{I}}(\boldsymbol{Z}, \boldsymbol{\theta}) \boldsymbol{d\theta}. \tag{1}$$

The analytical reconstruction algorithm generally requires numerous low noise views for successful reconstruction. In consequence, it is utilized extensively in applications where static subjects and good access are available, which means many measurements can be taken and is generally less favored in the incomplete data reconstruction problem. In contrast, the iterative class reconstruction algorithm is more robust to the effect of noise in the reconstructed data and is therefore more favored by scholars in the field of CT reconstruction. In contrast, the iterative reconstruction algorithm is more robust to the effect of noise in data and is therefore more commonly utilized in FCT reconstruction.

Iterative Reconstruction Algorithm

The fundamental of iterative reconstruction algorithm is discrete reconstruction domain $\boldsymbol{F}$ as well as the projection data $\boldsymbol{I}$. According to the weight matrix $\boldsymbol{W}$, the connection between the reconstruction domain and projection data could

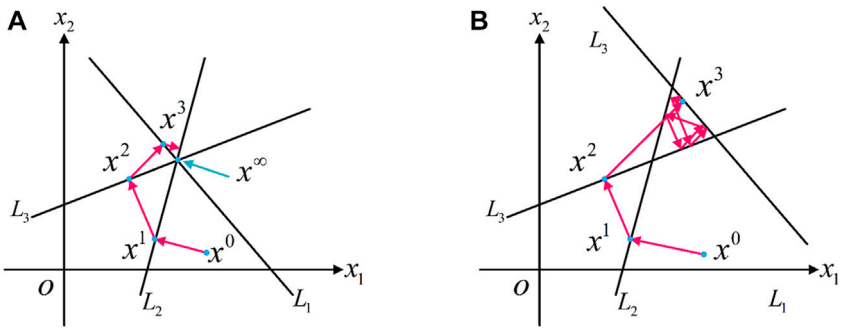

FIGURE 8 | (A) Diagram of compatible equations. **(B)** Diagram of incompatible equations.

be established in **Eq. 2**. *F* is divided into N discrete voxels in the reconstruction domain. The voxel indices are represented by the single index *i*, *j* is defined as the index of projection direction of *q* views and *p* pixels of each view. *Ij*. is regarded as the projection of the direction *j*, and *fi* refers to the intensity of the voxel *i*. Weight factor *wij* can be considered as the contribution coefficient of the voxel *i* to the direction *j* (Jin et al., 2016b), as follows:

$$\boldsymbol{I}_j = \sum_{i=1}^{N_i} \boldsymbol{w}_{j,i}\boldsymbol{f}_i. \tag{2}$$

Equation 2 can recast the reconstruction problem as a system of linear equations as indicated in the matrix form in **Eq. 3**. It is worth noting that the weight matrix $\boldsymbol{W}$ has as many rows as the projection number and as many columns as the reconstructed voxel numbers.

$$\boldsymbol{I} = \boldsymbol{W}\boldsymbol{F}. \tag{3}$$

In accordance with the solution method of the system of equations, iterative reconstruction algorithms are divided into direct algebraic and algebraic iterative methods. Meanwhile, the direct algebraic methods consist of inverse and decomposition methods. The inverse method refers to reconstructing the field by computing the inverse of the weight matrix (Hartley, 1994), while the decomposition method decomposes the weight matrix into several specific matrices and recovers the reconstruction field in view of the properties of these specific matrices, such as singular value decomposition (SVD) (Selivanov and Lecomte, 2001) and QR decomposition (Iborra et al., 2015). Considering that the dimension of the weight matrix $\boldsymbol{W}$ is determined by both the number of voxels in the reconstruction domain and the number of projection data, which is too large to apply direct algebraic methods, it is more practical to use an algebraic iterative method to find an approximate solution for system of equations.

The most widely used iterative algorithm is called the algebraic reconstruction technique (ART). The original ART algorithms were proposed by Gordon and Herman (1971), and it was found to be a special case of the well-known Kaczmarz algorithm of integral equation (Guenther et al., 1974). In concept of ART, I*j* is treated as a hyperplane in the solution space of the system of equations. Therefore, the number of projections determines the number of hyperplanes. If the system of linear equations is noiseless and compatible, the unique solution could be accessed when all hyperplanes intersect at a point. As seen in **Figure 8A**, the three projection rays, L_1, L_2, and L_3, represent three equations. The intersection point of three rays is the solution of the system of equations. An arbitrary initial value x^0 is given and projected onto L_1 in the light of **Eq. 2** to obtain an update value x^1 in the iteration process. Next, x^1 is projected onto L_2 in the same way and the updated value x^2 is determined. Eventually, the iterative process converges to the solution of the system of equations. However, the noise influence is inevitable in a practical experiment, as a consequence the system of equations is incompatible and the solution of equations cannot converge to a point. As illustrated in **Figure 8B**, the iteration process of incompatible equations converges to a small region of solution space. In this case, iteration continues until some convergence criteria is achieved.

Figure 9 indicates the working principle of the ART algorithm on a simple 2 × 2 tomographic problem with four perspectives. FCT problem is demonstrated in upper left panel, where the numbers represent the measured projections and the values of object domain are calculated according to the measured projections. In step 1, the initialization of object domain is completed and the values are designed as 0; next, the differences between the initial and measured projections are defined as e and calculated for each view; in step 3, e is distributed evenly along the perspective to update the value of object domain; the calculation and distribution of e are repeated in step 4 and step 5 until the termination criterion is met. Generally, the update of object domain can stop when the difference e is smaller than the designed error, while the ART algorithm can be considered as convergence.

The iteration process of ART is shown in **Eq. 4**. $f^{(0)}$ represents the initial value. Projection error is defined as the difference between the measured projection *Ij* and equivalent projection estimated by f of current iteration. This error is following normalized and back projected into the reconstruction domain via *wij*, and then the next projection is addressed. The next iteration begins once all projections have been considered. In general, the higher accuracy is available with more iterations.

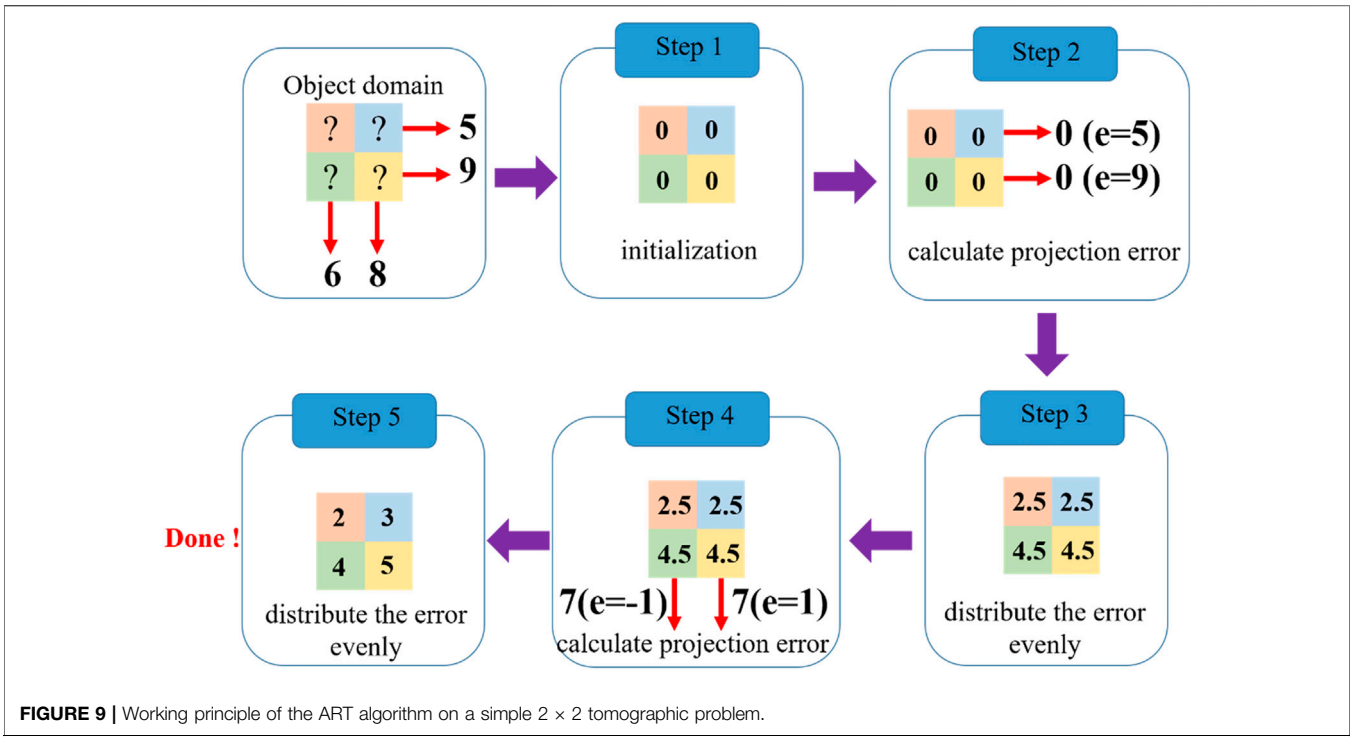

FIGURE 9 | Working principle of the ART algorithm on a simple 2 × 2 tomographic problem.

$$\begin{cases} f^{(0,0)} = f^{(0)} \\ f_i^{(k,j+1)} = f_i^{(k,j)} + \varepsilon \dfrac{I_j - \sum_i^N w_{j,i} f_i^{(k,j)}}{\sum_i^N \left(w_{j,i}\right)^2} w_{j,i}, \\ f^{(k+1,0)} = f^{(k,p\times q)} \end{cases} \tag{4}$$

where ε refers to the laxation factor. The choice of relaxation factor affects the convergence speed and iteration accuracy during the iterative process. The small relaxation factor leads to a low convergence speed with high iteration accuracy; on the contrary, the relaxation factor is large and its convergence speed is fast, but the iteration accuracy is low. Generally, $\varepsilon \in (0,2)$ (Herman et al., 1978).

Furthermore, the pseudo-code for the ART algorithm is provided to illustrate the work process.

Initialization: $k = 0, \varepsilon = 0.6, f^{(0)} = 0$
Repeat:
$k = k + 1$
for $j = 1$ to $p \times q$ do
  for $i = 1$ to N do
$$f_i^{(k,j+1)} = f_i^{(k,j)} + \varepsilon \frac{I_j - \sum_i^N w_{j,i} f_i^{(k,j)}}{\sum_i^N (w_{j,i})^2} w_{j,i}$$
  end for
end for
until the termination criterion is met
Stop

As a variation of ART, multiplicative algebraic reconstruction technique (MART) not only changes the correction method of the initial value, which means the iterative results can be updated multiplicatively during the iteration process, but also maximizes the entropy of reconstruction domain. It is worth noting that the entropy mentioned here is in the context of information theory not thermodynamic entropy (Floyd, 2009). MART shows better performance on improving iteration speed. Especially for reconstruction fields with high gradient, MART is capable of giving superior reconstruction quality (Verhoeven, 1993). **Eq. 5** shows the expression of MART given by Verhoeven (1993), as follows:

$$\begin{cases} f^{(0,0)} = f^{(0)} \\ f_i^{(k,j+1)} = f_i^{(k,j)} \times \left(1 - \dfrac{\varepsilon w_{j,i}}{\sum_i^N \left(w_{j,i}\right)^2} \left(1 - \dfrac{I_j}{\sum_i^N w_{j,i} f_i^{(k,j)}}\right)\right). \\ f^{(k+1,0)} = f^{(k,p\times q)} \end{cases} \tag{5}$$

It is worth mentioning that the multiplicative correction of MART causes the values of the voxels with zero in the reconstructed domain to remain unchanged. Therefore, the widely used initial estimate of zero in ART is not appropriate and the mean value of projections is suggested to be more suitable for MART (Floyd, 2009).

Additionally, another kind of ART algorithm called simultaneous algebraic reconstruction technique (SART) is proposed by A. H. Aderson. Compared with standard ART algorithm, SART tackles all the error from a single projection simultaneously, instead of view-by-view. This operation averagely reduces the error oscillation when two adjacent projections consecutive correct the same pixel and shows better noise immunity (Andersen and Kak, 1984). As seen in

Eq. 6, SART can be achieved by correcting standard ART of one view q, as follows:

$$f_i^{(k+1)} = f_i^{(k)} + \frac{1}{\sum_i^N w_{j,i}} \sum_1^p w_{j,i} \frac{I_j - w_{j,i} f_i^{(k)}}{\sum_i^N w_{j,i}}. \quad (6)$$

The ART algorithm has been extensively used in reconstruction problem of FCT. Numerous scholars (L. Ma, Y. Ishino, G. Lu, M. M. Hossain, W. Cai, to name a few) have conducted comprehensive research in the feasibility and reliability of ART via numerical simulation as well as practical experiments (Wang et al., 2016b; Lei, 2016; Ma et al., 2016). For instance, T. Yu investigated multiple kinds of series expansion reconstruction algorithm on the basis of previous study of ART (Liu et al., 2017b). S. M. Wiseman and J. Zhuan employed MART as well as SART separately to inspect the 3D combustion structure (Wiseman et al., 2017; Wan and Zhuang, 2018).

Although the ART algorithm has become the conventional method for FCT reconstruction, but the limited optical accessibility of practical applications results in the inversion problem of FCT is ill-posed mathematically. As a consequence, the inevitable line artifacts introduced by ART will certainly affect the further reconstruction quality. It is worth mention that novel reconstruction algorithms have been developed in terms of the utilization of the additional information on the reconstruction field, which can be treated as the a priori information incorporating into the iteration algorithm to mitigate the ill-posed problem (Ma and Cai, 2008). For instance, profited by Tikhonov's regularization, Zhou et al. measured the 3D temperature distribution of a large-scale furnace numerically and experimentally (Zhou et al., 2005). Similarly, Daun et al. applied Tikhonov's regularization to reconstruct the axisymmetric flame properties (Daun et al., 2006). Häber et al. retrieved the tomographic multispecies visualization of laminar and turbulent methane/air diffusion flames based on a kind of variation Tikhonov's regularization (Häber et al., 2020a; Häber et al., 2020b). As another type of priori information of temperature field, Total Variance (TV) indicates the sparseness of field (Cai et al., 2013b; Yu and Cai, 2017; Dai et al., 2018). Compared with Tikhonov's regularization, TV regularization shows better performance in preserving sharp discontinuities between distinct regions of reconstruction domain, which is capable for providing representative features of combustion such as the flame front (Rudin et al., 1992; Strong and Chan, 2003). TV regularization was utilized for practical FCT applications and its ability of significantly reducing the typical line artifacts was proved numerically and experimentally (Jin et al., 2021). Furthermore, the regularization minimizing p-norm ($0 < p < 1$) was applied to enhance the spatial resolution in photoacoustic (PA) tomography (Okawa et al., 2020). A weighted Schatten p-norm minimization was proposed by Xu et al. for reconstruction issue of sparse-view cone beam computed tomography (CBCT) (Xu et al., 2020a). A compression sensing-based algorithm was employed by G. -J. Yoon et al. to achieve simplification of amount of data in reconstruction process. On the condition of limit-view, they proved the feasibility of this method experimentally (Yoon et al., 2019). Analogous method was mentioned and validated in single-pixel laminar flames reconstruction (Zhang et al., 2019). Moreover, Bayesian optimization is also proficient in integrating the measurement data with prior information by a statistically robust method (Jin et al., 2021). In light of Bayesian framework, S. Grauer et al. recovered the instantaneous refractive index distribution of a turbulent flame (Grauer et al., 2018).

In addition, A. Unterberger et al. developed an evolutionary reconstruction technique (ERT), which integrated a genetic algorithm (GA) with a ray-tracing software. Evaluations were carried on the reconstruction results of three different kinds of flames, and the reconstruction ability of ERT was proved to be consonant with ART (Unterberger et al., 2019). Besides, several types of reconstruction algorithm have also been reported in CT problem, for instance, Landweber algorithm (Rossberg and Funke, 2010), maximum entropy algorithm (Denisova, 2004), maximum likelihood estimation algorithm (Busa et al., 2014) and maximum expectation algorithm (Dey and King, 2009), to name a few. Meanwhile, some research focused on the comparisons of various algorithms have been reported, such as (Yu and Cai, 2017) and (Shui et al., 2021).

Although iterative reconstruction algorithms (such as ART) are extensively used in FCT problem, it is still important to note that the major drawback of iteration algorithm is semi-convergence, which means the true solution may be figured out at an early stage while diverges away as the iteration steps increase. As a consequence, the iteration number and termination criterion play essential part in FCT. However, the iteration number as well as termination criterion of iterative reconstruction algorithms are usually determined by experience, which will influence the accuracy of reconstruction results evidently. Moreover, on account of the time consuming and high data throughput of conventional iteration methods, it causes the FCT technique hard to be utilized for online combustion monitor and diagnostics in practical environment. As a result, the 3D reconstructions in FCT are generally conducted off-line.

Artificial Intelligence-Based Reconstruction Algorithm

In the last few years, with the rapid development of the artificial intelligence-based technique, deep learning method has aroused extensive attention in academia and industry, which leads to excellent performance on sorts of problems, such as image classification (Colburn et al., 2019), object detection (Ren et al., 2017), face recognition (Yu and Tao, 2019) and natural language processing (Agrawal et al., 2019), to name a few. Especially in the field of computational optical imaging, the artificial intelligence-based technique has been effectively applied in ghost imaging (Lyu et al., 2017), digital holography (Ren et al., 2018; Wang et al., 2018) and phase retrieve (Wu et al., 2018). Meanwhile, a variety of neural network frameworks have developed, for example, LeNet-5 (LeCun et al., 1998), AlexNet (Krizhevsky et al., 2017), VGG (Simonyan and Zisserman, 2014) and GoogLeNet (Szegedy et al., 2015). In addition, deep learning methods are induced to handle CT reconstruction in medical field

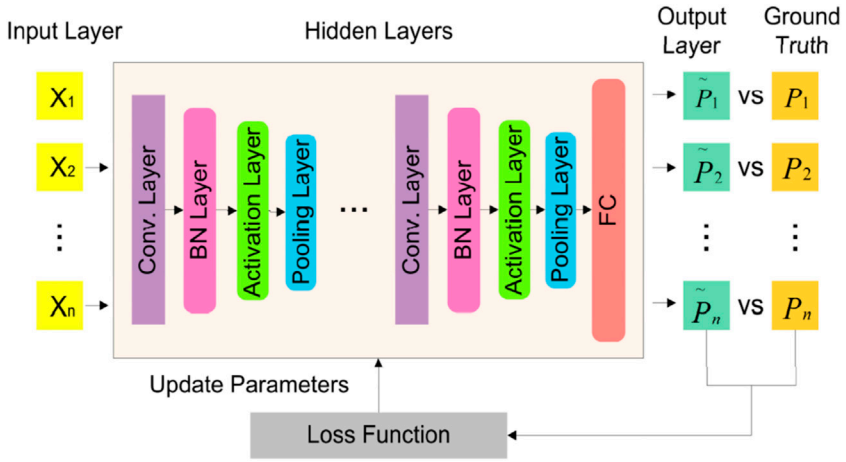

FIGURE 10 | Demonstration of convolutional natural networks (CNN). Adapted with permission from Jin et al. (2017) © The Optical Society.

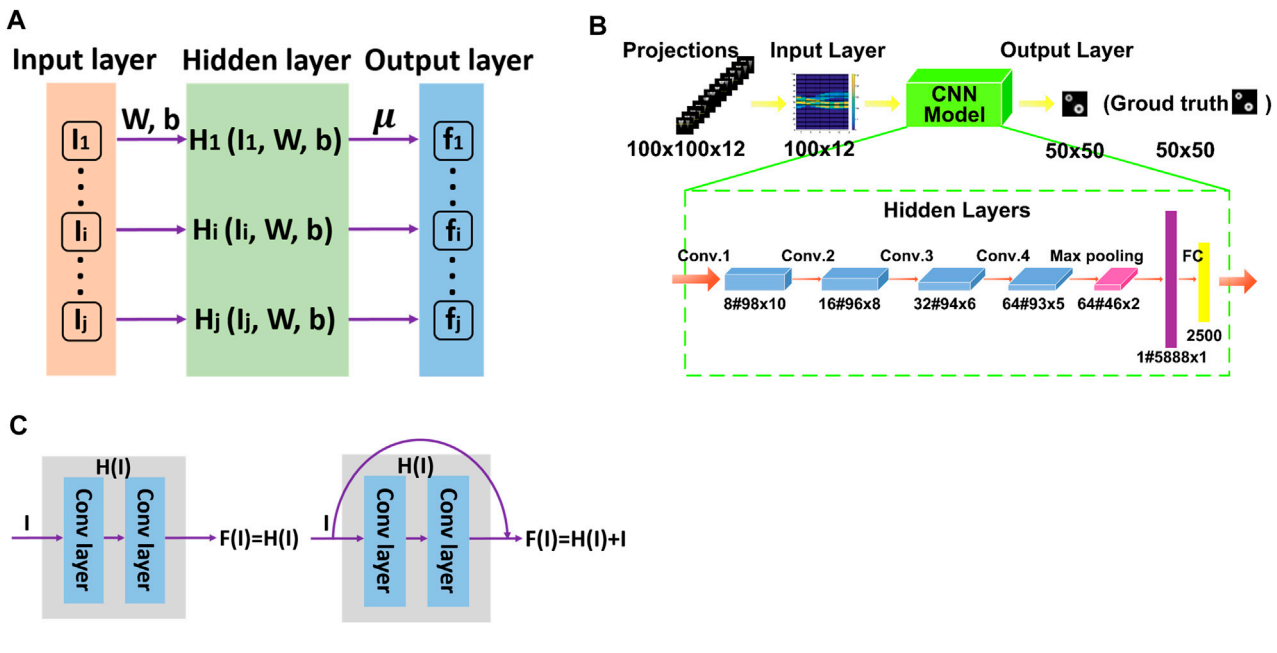

FIGURE 11 | (A) ELM-based neural network for CT inversion. **(B)** Diagram of CNN architecture for FCT. Adapted with permission from Jin et al. (2019) © The Optical Society. **(C)** Two parts of VT-Net in Huang's study.

(Wang, 2016). A new noise reduction method and residual encoder-decoder convolutional neural network were presented by Wang et al. to tackle low-dose CT imaging problem with high computed speed (Chen et al., 2017). Besides, DD-Net (Zhang et al., 2018), Generative Adversarial Network (GAN) (Yang et al., 2018), wavelet-based network (Kang et al., 20182018) and 3D U-Net (Kim et al., 2020) were proved to realize noise immunity and edge enhancement in medical reconstruction problems.

The superiority of artificial intelligence-based algorithm in medical CT problem has attracted the attention of scholars related to FCT field, which make it becomes a promising tactic to deal with the time consuming limitation of prevailing iteration method. Artificial intelligence-based reconstruction method can be considered as a "black-box". Taking one of the popular deep neural networks as example, the architecture of convolutional neural network (CNN) usually contains an input layer, multiple hidden layers as well as an output layer. As illustrated in **Figure 10** the hidden layer generally includes the convolutional layer, batch normalization (BN) layer, activation layer, pooling layer and fully connected layer. The FCT reconstruction procedures *via* artificial intelligence-based tactic are composed of training stage and testing stage. In training stage,

the projections as well as the distributions of reconstruction field which refer to the corresponding ground-truth constitute the data pairs and are fed into CNN model together. The training stage contains forward propagation process and back propagation process. During the forward propagation process, the salient features of input projections are extracted by convolution operations as well as down sampled via pooling operations to generate the feature column vector, which is multiplied by the coefficient and added with the biases to obtain the output results. The error between the output and ground-truth are calculated by loss function during back propagation process. Based on the gradient descent method, the parameters of neural network are adjusted gradually. Once the training stage is completed, the projections of test data are feeding into the system and the reconstruction results can be predicted rapidly.

As depicted in **Figure 11A**, the extreme learning machine (ELM) is adopted by T. Yu et al. to extract useful information from the previous reconstructions of 3,600 training samples. 50 samples were generated as the test data to validate the feasibility and high computing speed of ELM-based reconstruction algorithm via phantom study (Yu et al., 2018c). For the sake of investigating the performance of deep learning method in practical flame measurement, a rapid FCT reconstruction system based on convolutional neural networks (CNN) model was established in Y. Jin et al. shown in **Figure 11B**. The reconstruction capability of the proposed model was qualitatively and quantitatively verified by numerical simulation as well as experimental measurement with various field distributions. Additionally, the determination of the architecture of CNN framework was analyzed in detail. Compared with ART, MART, and TV method, their CNN model provides prominent advantage in term of computational efficiency (Jin et al., 2019). It is worth mentioning that the output data as well as input data are the horizontal slice of the 3D field and the corresponding projections, which mean the 3D reconstruction result were derived from the overlay method. Afterward, as illustrated in **Figure 11C**, J. Huang et al. investigated the capability of two kinds of CNN framework with distinct connections between layers for volumetric tomography of turbulent flames. The proof-of-concept and a series of comparative experiments were conducted to prove the noise immunity of proposed method with different classes of noise (Huang et al., 2020). Compared to the reconstruction network in (Jin et al., 2019), the CNN framework of Huang's research achieve the 3D reconstruction of FCT directly, which further decrease the time consuming of recovering.

Furthermore, in order to handle sparse view tomography problem, a 4D tomographic reconstruction framework, called TomoFluid, was presented by G. Zhang. A morphing-based view interpolation method of projection was considered as a novel regularization to equalize the missing projections neighboring perspectives. Meanwhile, the re-projection consistency constraint was employed as the optimization term to improve reconstruction quality (Zang et al., 2020). Although the practicability of TomoFluid was validated in their study, a thorough physical interpretation of the proposed view interpolation method still needs to investigate in further. Deep learning strategy has been proved to improve reconstruction spatial resolution in FCT. In general, it is a contradictory demand of the size of the reconstruction domain and spatial resolution. W. Xu reported a data-driven 3D super-resolution approach in light of the GAN framework and the architecture of 3D-SR-GAN, which is composed of a generator and a discriminator network to figure out the topographic information. Based on the given low-resolution counterpart, the high-resolution 3D structure of turbulent flame can be recovered by two times via proposed method (Xu et al., 2020b). Deep learning-based algorithm can be adopted not only to handle 3D reconstruction, but also to enable monitoring and prediction the combustion states. A combination of convolutional auto-encoder, principal component analysis, and the hidden Markov model was developed to generate an unsupervised classification framework by T. Qiu. By means of the projections collected from the furnace flame, the identification of combustion condition changing as the coal feed rate falls was achieved via their model (Qiu et al., 2019). J. Huang developed a hybrid CNN–long short-term memory (LSTM) network, which combined the FCT technique with DL algorithms, to predict the evolution of 3D flame structures on the basis of its history 2D projections via the data-driven approach. The CNN part was trained to extract flame features from projections, while the LSTM part was trained to model the temporal sequence in view of features (Huang et al., 2019b). The successful application of CNN-LSTM model is in light of the similarity of the training dataset and the testing dataset. As a consequence, the enhancement of generalization of the proposed model will be a tough challenge.

Artificial intelligence-based reconstruction algorithm has become another kind of critical algorithms of FCT. Although it shows significant superiority in terms of computational efficiency, the physical explanation of how deep learning methods work is still being explored. For the commonly used a data-driven approach of deep learning methods, a large number of pre-acquired data pairs are not only directly related to the quality of the reconstruction results, but also affects the generalization ability of reconstruction algorithm. As a result, it is not an appropriate tactic for practical reconstruction situation without sufficient ground-truth (e.g., real distribution of practical flame). Furthermore, the increase in reconstruction scene complexity as well as the number of data samples acquired makes deep learning methods suffer from the bottleneck of computing power.

SUMMARY AND OUTLOOK

To summarize, this study has reviewed the application demonstrations of FCT for practical 3D tomography experiments, and the definition, imaging acquirement and calibration, projection models, and reconstruction algorithms. The tomographic chemiluminescence spectroscopy method is complementary to point or planer detection tactics and has been successfully illustrated in laboratory as well as industrial

scenarios. Recent progress is going to extend the applicability of FCT to more complicated combustion environment, such as deflagration phenomenon monitoring, and, consequently, there still remain several issues to be addressed. One of the toughest challenge is that due to the presence of large amounts of combustion particle (e.g., soot), the frequently employed linear imaging models that ignore the effects of scattering and absorption of particle would be not appropriate to indicate the imaging process of FCT. As a consequence, a non-linear imaging model considers the scattering, and absorption is required for accurate 3D reconstruction in practical combustion diagnostics. Meanwhile, the severe vibration of combustion phenomenon becomes a risk to the stability of the system and the accuracy of the camera calibration. Additionally, although artificial intelligence-based reconstruction algorithm shows significant superiority in terms of computational efficiency, its data-driven method cannot be ideally adopted to practical situation without sufficient ground-truth (e.g. real distribution of practical flame), further resulting in limited generalization ability. A more systematic and theoretical analysis is required for designing a new paradigm by combining the physical imaging model of FCT and the neural model to overcome the limitations of the sample number and generalization issue. Transfer learning would enable a potential way for combining physical priors with sample data. Furthermore, with the increasing complexity of reconstruction scene and the bottleneck of computing power, the lightweight of the reconstruction algorithm framework (e.g., the decrease of neural model parameter number) is also imminent for in-line combustion monitoring and measurements. Finally, combined with other optical detection tactics, for instance, PIV and moiré deflection, FCT can potentially achieve simultaneous multidimensional information reconstruction of physical fields, such as spatiality, temporality, and hyper spectrum and provide the temperature, components, and velocity distribution of the combustion field. In brief, FCT technology faces challenges in building accurate imaging models, developing fast as well as lightweight reconstruction algorithms and accommodating multidimensional parameter experimental measurements. The FCT technique holds a significant promise for future; we hope that this review will serve as a reference for the development directions of FCT in the field. Last but not least, the theory of FCT is a kind of mathematical approach for 3D imaging, which can potentially be applied to other tomographic areas, such as electrical capacitance tomography, interferometric tomography, and medical tomography.

AUTHOR CONTRIBUTIONS

All authors listed have made a substantial, direct, and intellectual contribution to the work and approved it for publication.

FUNDING

The authors gratefully acknowledge financial support from the National Natural Science Foundation of China (61991452); Key Research Program of Frontier Sciences of the Chinese Academy of Sciences (QYZDB-SSW-JSC002); and Chinesisch-Deutsche Zentrum für Wissenschaftsförderung (GZ1391).

REFERENCES

Agrawal, A., Jain, A., and Kumar, B. S. (2019). *Deep Learning Based Classification for Assessment of Emotion Recognition in Speech* [Conference Presentation]. Jaipur-India: SUSCOM, Amity University Rajasthan. February https://papers.ssrn.com/sol3/papers.cfm?abstract_id=3356238.

Alviso, D., Mendieta, M., Molina, J., and Rolón, J. C. (2017). Flame Imaging Reconstruction Method Using High Resolution Spectral Data of OH *, CH * and C 2 * Radicals. *Int. J. Therm. Sci.* 121, 228–236. doi:10.1016/j.ijthermalsci.2017.07.019

Andersen, A. H., and Kak, A. C. (1984). Simultaneous Algebraic Reconstruction Technique (SART): a Superior Implementation of the ART Algorithm. *Ultrason. Imaging* 6 (1), 81–94. doi:10.1016/0161-7346(84)90008-710.1177/016173468400600107

Anikin, N., Suntz, R., and Bockhorn, H. (2010). Tomographic Reconstruction of the OH*-chemiluminescence Distribution in Premixed and Diffusion Flames. *Appl. Phys. B* 100 (3), 675–694. doi:10.1007/s00340-010-4051-5

Ax, H., and Meier, W. (2016). Experimental Investigation of the Response of Laminar Premixed Flames to Equivalence Ratio Oscillations. *Combustion and Flame* 167, 172–183. doi:10.1016/j.combustflame.2016.02.014

Beister, M., Kolditz, D., and Kalender, W. A. (2012). Iterative Reconstruction Methods in X-ray CT. *Physica Med.* 28 (2), 94–108. doi:10.1016/j.ejmp.2012.01.003

Bheemul, H. C., Lu, G., and Yan, Y. (2002). Three-Dimensional Visualization and Quantitative Characterization of Gaseous Flames. *Meas. Sci. Technol.* 13 (10), 1643–1650. doi:10.1088/0957-0233/13/10/318

Bracewell, R. N., and Riddle, A. C. (1967). Inversion of Fan-Beam Scans in Radio Astronomy. *ApJ* 150, 427. doi:10.1086/149346

Brisley, P. M., Lu, G., Yan, Y., and Cornwell, S. (2004). *Three Dimensional Temperature Measurement of Combustion Flames Using a Single Monochromatic CCD Camera*. [Conference presentation].I2MTC 2004, Como, Italy. https://ieeexplore.ieee.org/xpl/conhome/9320/proceeding.

Brisley, P. M., Lu, G., Yan, Y., and Cornwell, S. (2005). Three-Dimensional Temperature Measurement of Combustion Flames Using a Single Monochromatic CCD Camera. *IEEE Trans. Instrum. Meas.* 54 (4), 1417–1421. doi:10.1109/TIM.2005.851074

Busa, K. M., McDaniel, J. C., Brown, M. S., and Diskin, G. S. (2014). "Implementation of Maximum-Likelihood Expectation-Maximization Algorithm for Tomographic Reconstruction of TDLAT Measurements," in [Conference Presentation]. 52nd Aerospace Sciences Meeting. Maryland: National Harbor. https://arc.aiaa.org/doi/book/10.2514/masm14.

Cai, H., Song, Y., Shi, Y., Cao, Z., Guo, Z., Li, Z., et al. (2020). Flexible Multicamera Calibration Method with a Rotating Calibration Plate. *Opt. Express* 28 (21), 31397–31413. doi:10.1364/OE.402761

Cai, W., Li, X., Li, F., and Ma, L. (2013). Numerical and Experimental Validation of a Three-Dimensional Combustion Diagnostic Based on Tomographic Chemiluminescence. *Opt. Express* 21 (6), 7050–7064. doi:10.1364/OE.21.007050

Cai, W., Li, X., and Ma, L. (2013). Practical Aspects of Implementing Three-Dimensional Tomography Inversion for Volumetric Flame Imaging. *Appl. Opt.* 52 (33), 8106–8116. doi:10.1364/AO.52.008106

Cha, S., and Vest, C. M. (1979). Interferometry and Reconstruction of Strongly Refracting Asymmetric-Refractive-Index Fields. *Opt. Lett.* 4 (10), 311–313. doi:10.1364/OL.4.000311

Chen, H., Zhang, Y., Kalra, M. K., Lin, F., Chen, Y., Liao, P., et al. (2017). Low-Dose CT with a Residual Encoder-Decoder Convolutional Neural Network. *IEEE Trans. Med. Imaging* 36 (12), 2524–2535. doi:10.1109/TMI.2017.2715284

Chi, Y., Lei, Q., Song, E., Fan, W., and Sha, Y. (2021). Development and Validation of Evaluation Methods for 3D Flame Propagation Speed of Turbulent Non-premixed Edge Flames via Tomographic Chemiluminescence. *Flow Turbulence Combust* 108, 539–557. doi:10.1007/s10494-021-00285-8

Colburn, S., Chu, Y., Shilzerman, E., and Majumdar, A. (2019). Optical Frontend for a Convolutional Neural Network. *Appl. Opt.* 58 (12), 3179–3186. doi:10.1364/AO.58.003179

Dai, J., Yu, T., Xu, L., and Cai, W. (2018). On the Regularization for Nonlinear Tomographic Absorption Spectroscopy. *J. Quantitative Spectrosc. Radiative Transfer* 206, 233–241. doi:10.1016/j.jqsrt.2017.11.016

Daniele, S., Mantzaras, J., Jansohn, P., Denisov, A., and Boulouchos, K. (2013). Flame Front/Turbulence Interaction for Syngas Fuels in the Thin Reaction Zones Regime: Turbulent and Stretched Laminar Flame Speeds at Elevated Pressures and Temperatures. *J. Fluid Mech.* 724, 36–68. doi:10.1017/jfm.2013.141

Daun, K. J., Thomson, K. A., Liu, F., and Smallwood, G. J. (2006). Deconvolution of Axisymmetric Flame Properties Using Tikhonov Regularization. *Appl. Opt.* 45 (19), 4638–4646. doi:10.1364/AO.45.004638

Denisova, N. (2004). A Maximuma Posteriorireconstruction Method for Plasma Tomography. *Plasma Sourc. Sci. Technol.* 13 (3), 531–536. doi:10.1088/0963-0252/13/3/020

Denisova, N., Tretyakov, P., and Tupikin, A. (2013). Emission Tomography in Flame Diagnostics. *Combustion and Flame* 160 (3), 577–588. doi:10.1016/j.combustflame.2012.11.005

Deutsch, C. (1990). A FORTRAN 77 Subroutine for Determining the Fractional Area of Rectangular Grid Blocks within a Polygon. *Comput. Geosciences* 16 (3), 379–384. doi:10.1016/0098-3004(90)90071-Z

Dey, J., and King, M. A. (2009). "Theoretical and Numerical Study of MLEM and OSEM Reconstruction Algorithms for Motion Correction in Emission Tomography [Conference Presentation]," in IEEE Nuclear Science Symposium Conference Record, Dresden, Germany. https://ieeexplore.ieee.org/xpl/tocresult.jsp?isnumber=5280479.

Dong, R., Lei, Q., Chi, Y., Song, E., and Fan, W. (2021). Analysis of Global and Local Hydrodynamic Instabilities on a High-Speed Jet Diffusion Flame via Time-Resolved 3D Measurements. *Flow Turbulence Combust* 107, 759–780. doi:10.1007/s10494-021-00251-4

Dong, R., Lei, Q., Zhang, Q., and Fan, W. (2021). Dynamics of Ignition Kernel in a Liquid-Fueled Gas Turbine Model Combustor Studied via Time-Resolved 3D Measurements. *Combustion and Flame* 232, 111566. doi:10.1016/j.combustflame.2021.111566

Falkhytten, T. (2018). *Computed Tomography of Chemiluminescence in Interacting Reacting Flows*. [Master's thesis]. [Trondheim]: NTNU.

Faris, G. W., and Byer, R. L. (1988). Three-Dimensional Beam-Deflection Optical Tomography of a Supersonic Jet. *Appl. Opt.* 27 (24), 5202–5212. doi:10.1364/AO.27.005202

Floyd, J. (2009). *Computed Tomography of Chemiluminescence: A 3D Time Resolved Sensor for Turbulent Combustion*. [London]: Imperial College London. [PHD dissertation].

Floyd, J., Geipel, P., and Kempf, A. M. (20112011). Computed Tomography of Chemiluminescence (CTC): Instantaneous 3D Measurements and Phantom Studies of a Turbulent Opposed Jet Flame. *Combustion and Flame* 158 (8), 376–391. doi:10.1016/j.combustflame.2010.09.006

Floyd, J., Heyes, A. L., and Kempf, A. M. (2009). *Computed Tomography of Chemiluminescence (CTC): Instantaneous Measurements of a Matrix Burner* [Conference Presentation]. Vienna, Austria. ECM 2009. https://www.communicationmonitor.eu/2009/06/01/ecm-european-communication-monitor-2009-measurement-evaluation-strategy-trends-social-media-social-networks/.

Floyd, J., and Kempf, A. M. (2011). Computed Tomography of Chemiluminescence (CTC): High Resolution and Instantaneous 3-D Measurements of a Matrix Burner. *Proc. Combustion Inst.* 33 (1), 751–758. doi:10.1016/j.proci.2010.06.015

Gao, Y., Yu, Q., Jiang, W., and Wan, X. (2010). Reconstruction of Three-Dimensional Arc-Plasma Temperature Fields by Orthographic and Double-Wave Spectral Tomography. *Opt. Laser Tech.* 42 (1), 61–69. doi:10.1016/j.optlastec.2009.04.020

Gaydon, A. G., and Wolfhard, H. G. (1953). *Flames. Their Structure, Radiation, and Temperature*. London: Chapman & Hall.

GilabertLuYan, G. G. Y., Lu, G., and Yan, Y. (2007). Three-Dimensional Tomographic Reconstruction of the Luminosity Distribution of a Combustion Flame. *IEEE Trans. Instrum. Meas.* 56 (4), 1300–1306. doi:10.1109/TIM.2007.900161

Gordon, R., and Herman, G. T. (1971). Reconstruction of Pictures from Their Projections. *Commun. ACM* 14 (12), 759–768. doi:10.1145/362919.362925

Grauer, S. J., Unterberger, A., Rittler, A., Daun, K. J., Kempf, A. M., and Mohri, K. (2018). Instantaneous 3D Flame Imaging by Background-Oriented Schlieren Tomography. *Combustion and Flame* 196, 284–299. doi:10.1016/j.combustflame.2018.06.022

Griffiths, J. F. J., and Barnard, A. (1995). *Flame and Combustion*. Glasgow: CRC.

Guenther, R. B., Kerber, C. W., Killian, E. K., Smith, K. T., and Wagner, S. L. (1974). Reconstruction of Objects from Radiographs and the Location of Brain Tumors. *Proc. Natl. Acad. Sci.* 71 (12), 4884–4886. doi:10.1073/pnas.71.12.4884

Gupta, A. K., Bolz, S., and Hasegawa, T. (1999). Effect of Air Preheat Temperature and Oxygen Concentration on Flame Structure and Emission. *J. Energ. Resour-asme.* 121, 209–216. doi:10.1115/1.2795984

Häber, T., Bockhorn, H., and Suntz, R. (2020). Two-Dimensional Tomographic Simultaneous Multi-Species Visualization-Part I: Experimental Methodology and Application to Laminar and Turbulent Flames. *Energies* 13 (9), 2335. doi:10.3390/en13092335

Häber, T., Suntz, R., and Bockhorn, H. (2020). Two-Dimensional Tomographic Simultaneous Multispecies Visualization-Part II: Reconstruction Accuracy. *Energies* 13 (9), 2368. doi:10.3390/en13092368

Hartley, R. I. (1994). *An Algorithm for Self Calibration from Several Views* [Conference Presentation]. Seattle, WA, United States: CVPR. https://dblp.org/db/conf/cvpr/cvpr1994.html.

Herman, G. T., Lent, A., and Lutz, P. H. (1978). Relaxation Methods for Image Reconstruction. *Commun. ACM* 21 (2), 152–158. doi:10.1145/359340.359351

Hertz, H. M., and Faris, G. W. (1988). Emission Tomography of Flame Radicals. *Opt. Lett.* 13 (5), 351–353. doi:10.1364/OL.13.000351

Hossain, A., and Nakamura, Y. (2014). A Numerical Study on the Ability to Predict the Heat Release Rate Using CH* Chemiluminescence in Non-sooting Counterflow Diffusion Flames. *Combustion and Flame* 161 (1), 162–172. doi:10.1016/j.combustflame.2013.08.021

Hossain, M. M., Lu, G., Sun, D., and Yan, Y. (2013). Three-Dimensional Reconstruction of Flame Temperature and Emissivity Distribution Using Optical Tomographic and Two-Colour Pyrometric Techniques. *Meas. Sci. Technol.* 24 (7), 074010. doi:10.1088/0957-0233/24/7/074010

Hossain, M. M., Lu, G., and Yan, Y. (2011). *Three-Dimensional Reconstruction of Combustion Flame through Optical Fibre Sensing and CCD Imaging* [Conference Presentation]. I2MTC 2011. Hangzhou, China. http://imtc2011.ieee-ims.org/.

Huang, J., Liu, H., and Cai, W. (2019). Online *In Situ* Prediction of 3-D Flame Evolution from its History 2-D Projections via Deep Learning. *J. Fluid Mech.* 875. doi:10.1017/jfm.2019.545

Huang, J., Liu, H., Wang, Q., and Cai, W. (2020). Limited-Projection Volumetric Tomography for Time-Resolved Turbulent Combustion Diagnostics via Deep Learning. *Aerospace Sci. Tech.* 106, 106123. doi:10.1016/j.ast.2020.106123

Huang, L., Da, F., and Gai, S. (2019). Research on Multi-Camera Calibration and Point Cloud Correction Method Based on Three-Dimensional Calibration Object. *Opt. Lasers Eng.* 115, 32–41. doi:10.1016/j.optlaseng.2018.11.005

Hwang, C. H., Wang, W. C., and Chen, Y. H. (2013). *Camera Calibration and 3D Surface Reconstruction for Multi-Camera Semi-circular DIC System [Conference Presentation]. icOPEN2013, Singapore, Singapore*. http://www.icopen.com.sg/.

Iborra, A., Rodriguez-Alvarez, M. J., Soriano, A., Sanchez, F., Bellido, P., Conde, P., et al. (2015). Noise Analysis in Computed Tomography (CT) Image Reconstruction Using QR-Decomposition Algorithm. *IEEE Trans. Nucl. Sci.* 62 (3), 869–875. doi:10.1109/TNS.2015.2422213

Ishino, Y., Hirano, T., Hirano, M., and Ohiwa, N. (2007). *Non-scanning 3D-CT Visualizations of Premixed Flames with a 40-Lens Camera*. [Conference presentation]. PSFVIP6, Hawaii, United States https://www.researchgate.net/publication/313707915_Non-scanning_3d-ct_visualizations_of_premixed_flames_with_a_40-lens_camera.

Ishino, Y., Inagawa, O., and Nakamura, T. (2005). *Instantaneous Volume Imaging of Fuel Combustion Rate Distribution of a Turbulent Propane-Air Fuel-Rich Premixed Flame by Three-Dimensional Scanless Computerized Tomographic Reconstruction Method with a Multi-Lens-Camera*. Conference

presentation].TSFP4, Williamsburg, United States. http://www.tsfp-conference.org/proceedings/26-proceedings-of-tsfp-4-2005-williamsburg.html.

Ishino, Y., and Ohiwa, N. (2005). Three-Dimensional Computerized Tomographic Reconstruction of Instantaneous Distribution of Chemiluminescence of a Turbulent Premixed Flame. *JSME International Journal. Ser. B, Fluids Thermal Engineering* 48 (1), 34–40. doi:10.1299/jsmeb.48.34

Ishino, Y., Saiki, Y., Tomida, Y., and Okita, Y. (2011). 3D Visualization of Unsteady Flames by the Combined Technique of Multi-Directional Simultaneous Photography and 3D-Computed Tomography. *Kashika Joho Gakkaishi* 31 (120), 9. doi:10.3154/jvs.31.9

Ishino, Y., Takeuchi, K., Shiga, S., and Ohiwa, N. (2009). *Measurement of Instantaneous 3D-Distribution of Local Burning Velocity on a Turbulent Premixed Flame by Non-scanning 3D-CT Reconstruction* [Conference Presentation]. Birmingham, UK. ECM 2009. https://www.sciencedirect.com/journal/applied-thermal-engineering/vol/25/issue/16.

Iwama, N., Yoshida, H., Takimoto, H., Shen, Y., Takamura, S., and Tsukishima, T. (1989). Phillips-tikhonov Regularization of Plasma Image Reconstruction with the Generalized Cross Validation. *Appl. Phys. Lett.* 54 (6), 502–504. doi:10.1063/1.100912

Jeong, Y. K., Jeon, C. H., and Chang, Y. J. (2006). Evaluation of the Equivalence Ratio of the Reacting Mixture Using Intensity Ratio of Chemiluminescence in Laminar Partially Premixed CH4-Air Flames. *Exp. Therm. Fluid Sci.* 30 (7), 663–673. doi:10.1016/j.expthermflusci.2006.01.005

Jin, Y., Guo, Z., Song, Y., Li, Z., He, A., and Situ, G. (2021). Sparse Regularization-Based Reconstruction for 3D Flame Chemiluminescence Tomography. *Appl. Opt.* 60 (3), 513–525. doi:10.1364/AO.412637

Jin, Y., Song, Y., Qu, X., Li, Z., Ji, Y., and He, A. (2016). Hybrid Algorithm for Three-Dimensional Flame Chemiluminescence Tomography Based on Imaging Overexposure Compensation. *Appl. Opt.* 55 (22), 5917–5923. doi:10.1364/AO.55.005917

Jin, Y., Song, Y., Qu, X., Li, Z., Ji, Y., and He, A. (2017). Three-Dimensional Dynamic Measurements of CH* and C2* Concentrations in Flame Using Simultaneous Chemiluminescence Tomography. *Opt. Express* 25 (5), 4640–4654. doi:10.1364/OE.25.004640

Jin, Y., Song, Y., Wang, W., Ji, Y., Li, Z., and He, A. (2016). *An Improved Calculation Model of Weight Coefficient for Three-Dimensional Flame Chemiluminescence Tomography Based on Lens Imaging Theory* [Conference Presentation]. Beijing, China. OTA 2016. https://www.spiedigitallibrary.org/conference-proceedings-of-spie/10155.toc.

Jin, Y., Zhang, W., Song, Y., Qu, X., Li, Z., Ji, Y., et al. (2019). Three-Dimensional Rapid Flame Chemiluminescence Tomography via Deep Learning. *Opt. Express* 27 (19), 27308–27334. doi:10.1364/OE.27.027308

Kaminski, C. F., and Kaminski, C. F. (2014). A Tomographic Technique for the Simultaneous Imaging of Temperature, Chemical Species, and Pressure in Reactive Flows Using Absorption Spectroscopy with Frequency-Agile Lasers. *Appl. Phys. Lett.* 104 (3), 034101. doi:10.1063/1.4862754

Kang, E., Chang, W., Yoo, J., and Ye, J. C. (2018). Deep Convolutional Framelet Denosing for Low-Dose CT via Wavelet Residual Network. *IEEE Trans. Med. Imaging* 37 (6), 1358–1369. doi:10.1109/TMI.2018.2823756

Kang, M., Wu, Y., and Ma, L. (2014). Fiber-Based Endoscopes for 3D Combustion Measurements: View Registration and Spatial Resolution. *Combustion and Flame* 161 (12), 3063–3072. doi:10.1016/j.combustflame.2014.06.002

Kathrotia, T., Riedel, U., Seipel, A., Moshammer, K., and Brockhinke, A. (2012). Experimental and Numerical Study of Chemiluminescent Species in Low-Pressure Flames. *Appl. Phys. B* 107 (3), 571–584. doi:10.1007/s00340-012-5002-0

Kim, T., Lee, K., Ham, S., Park, B., Lee, S., Hong, D., et al. (2020). Active Learning for Accuracy Enhancement of Semantic Segmentation with CNN-Corrected Label Curations: Evaluation on Kidney Segmentation in Abdominal CT. *Sci. Rep.* 10 (1), 1–7. doi:10.1038/s41598-019-57242-9

Kojima, J., Ikeda, Y., and Nakajima, T. (2005). Basic Aspects of OH(A), CH(A), and C2(d) Chemiluminescence in the Reaction Zone of Laminar Methane-Air Premixed Flames. *Combustion and Flame* 140 (1-2), 34–45. doi:10.1016/j.combustflame.2004.10.002

Krizhevsky, A., Sutskever, I., and Hinton, G. E. (2017). ImageNet Classification with Deep Convolutional Neural Networks. *Commun. ACM* 60 (6), 84–90. doi:10.1145/3065386

LeCun, Y., Bottou, L., Bengio, Y., and Haffner, P. (1998). Gradient-Based Learning Applied to Document Recognition. *Proc. IEEE* 86 (11), 2278–2324. doi:10.1109/5.726791

Lee, M. C., Yoon, J., Joo, S., Kim, J., Hwang, J., and Yoon, Y. (2015). Investigation into the Cause of High Multi-Mode Combustion Instability of H2/CO/CH4 Syngas in a Partially Premixed Gas Turbine Model Combustor. *Proc. Combustion Inst.* 35 (3), 3263–3271. doi:10.1016/j.proci.2014.07.013

Lei, Q. (2016). *Development and Validation of Reconstruction Algorithms for 3D Tomography Diagnostics*. Virginia Polytechnic Institute and State University. [Doctoral dissertation]. [Virginia (Blacksburg)].

Li, X., and Ma, L. (2015). Capabilities and Limitations of 3D Flame Measurements Based on Computed Tomography of Chemiluminescence. *Combustion and Flame* 162 (3), 642–651. doi:10.1016/j.combustflame.2014.08.020

Li, X., and Ma, L. (2014). Volumetric Imaging of Turbulent Reactive Flows at kHz Based on Computed Tomography. *Opt. Express* 22 (4), 4768–4778. doi:10.1364/OE.22.004768

Ling, C., Chen, H., and Wu, Y. (2020). Development and Validation of a Reconstruction Approach for Three-Dimensional Confined-Space Tomography Problems. *Appl. Opt.* 59 (34), 10786–10800. doi:10.1364/AO.404458

Liu, H., Paolillo, G., Astarita, T., Shui, C., and Cai, W. (2019). Computed Tomography of Chemiluminescence for the Measurements of Flames Confined within a Cylindrical Glass. *Opt. Lett.* 44 (19), 4793–4796. doi:10.1364/OL.44.004793

Liu, H., Sun, B., and Cai, W. (2019). kHz-Rate Volumetric Flame Imaging Using a Single Camera. *Opt. Commun.* 437, 33–43. doi:10.1016/j.optcom.2018.12.036

Liu, H., Wang, Q., Peng, F., Qin, Z., and Cai, W. (2021). Flame Emission Tomography Based on Finite Element Basis and Adjustable Mask. *Opt. Express* 29 (25), 40841–40853. doi:10.1364/OE.443643

Liu, H., Yang, Z., and Cai, W. (2021). Application of Three-Dimensional Diagnostics on the Direct-Current Electric-Field Assisted Combustion. *Aerospace Sci. Tech.* 112, 106657. doi:10.1007/s10494-021-00294-710.1016/j.ast.2021.106657

Liu, H., Yu, T., Zhang, M., and Cai, W. (2017). Demonstration of 3D Computed Tomography of Chemiluminescence with a Restricted Field of View. *Appl. Opt.* 56 (25), 7107–7115. doi:10.1364/AO.56.007107

Liu, H., Zhao, J., Shui, C., and Cai, W. (2019). Reconstruction and Analysis of Non-premixed Turbulent Swirl Flames Based on kHz-Rate Multi-Angular Endoscopic Volumetric Tomography. *Aerospace Sci. Tech.* 91, 422–433. doi:10.1016/j.ast.2019.05.025

Liu, N., and Ma, L. (2020). Regularized Tomographic PIV for Incompressible Flows Based on Conservation of Mass. *Appl. Opt.* 59 (6), 1667–1677. doi:10.1364/AO.380720

Liu, N., Wu, Y., and Ma, L. (2018). Quantification of Tomographic PIV Uncertainty Using Controlled Experimental Measurements. *Appl. Opt.* 57 (3), 420–427. doi:10.1364/AO.57.000420

Liu, Y., Hossain, M., Sun, J., Xu, C., Zhang, B., and Wang, S. (2017). *Design a Cage-Typed Light Field Camera System for Flame MeasurementIEEE SENSORS 2017*. Glasgow, Scotland, United Kingdom. [Conference Presentation]. https://ieee-sensors.org/event/ieee-sensors-2017/.

Liu, Y., Tan, J., Wan, M., and Yao, X. (2020). OH* and CH* Chemiluminescence Characteristics in Low Swirl Methane-Air Flames. *AIP Adv.* 10 (5), 055318. doi:10.1063/5.0002660

Liu, Y., Zhu, M., Wang, T., Lei, G., Hossain, M. M., Zhang, B., et al. (2021). Spatial Resolution of Light Field Sectioning Pyrometry for Flame Temperature Measurement. *Opt. Lasers Eng.* 140, 106545. doi:10.1016/j.optlaseng.2021.106545

Lyu, M., Wang, W., Wang, H., Wang, H., Li, G., Chen, N., et al. (2017). Deep-Learning-Based Ghost Imaging. *Sci. Rep.* 7 (1), 1–6. doi:10.1038/s41598-017-18171-7

Ma, L., and Cai, W. (2008). Determination of the Optimal Regularization Parameters in Hyperspectral Tomography. *Appl. Opt.* 47 (23), 4186–4192. doi:10.1364/AO.47.004186

Ma, L., Wu, Y., Lei, Q., Xu, W., and Carter, C. D. (2016). 3D Flame Topography and Curvature Measurements at 5 kHz on a Premixed Turbulent Bunsen Flame. *Combustion and Flame* 166, 66–75. doi:10.1016/j.combustflame.2015.12.031

Melnikova, T. S., and Pickalov, V. V. (1984). Tomographic Measurements of Temperature Fields in Non-stationary Arc Plasma. *Beitr. Plasmaphys.* 24 (5), 431–445. doi:10.1002/ctpp.19840240502

Mohri, K., Görs, S., Schöler, J., Rittler, A., Dreier, T., Schulz, C., et al. (2017). Instantaneous 3D Imaging of Highly Turbulent Flames Using Computed Tomography of Chemiluminescence. *Appl. Opt.* 56 (26), 7385–7395. doi:10.1364/AO.56.007385

Moinul Hossain, M. M., Lu, G., and Yan, Y. (2012). Optical Fiber Imaging Based Tomographic Reconstruction of Burner Flames. *IEEE Trans. Instrum. Meas.* 61 (5), 1417–1425. doi:10.1109/TIM.2012.2186477

Navakas, R., Saliamonas, A., Striūgas, N., Džiugys, A., Paulauskas, R., and Zakarauskas, K. (2018). Effect of Producer Gas Addition and Air Excess Ratio on Natural Gas Flame Luminescence. *Fuel* 217, 478–489. doi:10.1016/j.fuel.2017.12.094

Niu, Z., Qi, H., Shi, J., Zhang, J., and Ren, Y. (2021). Temperature Field Reconstruction of 3D Luminous Flames Based on Light Field Tomography Theory. *Sci. China Technol. Sci.* 64, 223–236. doi:10.1007/s11431-019-1573-y

Nori, V., and Seitzman, J. (2008). "Evaluation of Chemiluminescence as A Combustion Diagnostic under Varying Operating Conditions [Conference Presentation]," in *46th AIAA Aerospace Sciences Meeting and Exhibit* (Reno, Nevada, United States. https://arc.aiaa.org/doi/book/10.2514/MASM08#paned5521a22-9898-435a-9faa-de90b3bee0b01.

Okawa, S., Hirasawa, T., Kushibiki, T., Fujita, M., and Ishihara, M. (2020). *Photoacoustic Tomography Reconstructing Absorption Coefficient and Effect of Regularization Minimizing P-Norm [Conference Presentation]. Photons Plus Ultrasound: Imaging and Sensing 2020*. San Francisco, California, USA. https://spie.org/Publications/Proceedings/Volume/11240?SSO=1.

Orain, M., and Hardalupas, Y. (2010). Effect of Fuel Type on Equivalence Ratio Measurements Using Chemiluminescence in Premixed Flames. *Comptes Rendus Mécanique* 338 (5), 241–254. doi:10.1016/j.crme.2010.05.002

Paolillo, G., and Astarita, T. (2019). *A Novel Camera Model for Calibrating Optical Systems Including Cylindrical Windows [Conference Presentation]AIAA Scitech 2019 Forum*. San Diego, California, United States. https://arc.aiaa.org/doi/pdf/10.2514/6.2019-0273.

Qi, H., Shi, J.-W., Su, Y.-X., Gao, B.-H., and Ren, Y.-T. (2021). Soot Temperature Measurement within 3D Flame by Light-Field Imaging Based on Wave Optics Theory. *Opt. Lasers Eng.* 138, 106419. doi:10.1016/j.optlaseng.2020.106419

Qi, Q., Hossain, M. M., Li, J.-J., Zhang, B., Li, J., and Xu, C.-L. (2021). Approach to Reduce Light Field Sampling Redundancy for Flame Temperature Reconstruction. *Opt. Express* 29 (9), 13094–13114. doi:10.1364/OE.424112

Qiu, T., Liu, M., Zhou, G., Wang, L., and Gao, K. (2019). An Unsupervised Classification Method for Flame Image of Pulverized Coal Combustion Based on Convolutional Auto-Encoder and Hidden Markov Model. *Energies* 12 (13), 2585. doi:10.3390/en12132585

Ramachandran, G. N., and Lakshminarayanan, A. V. (1971). Three-Dimensional Reconstruction from Radiographs and Electron Micrographs: Application of Convolutions Instead of Fourier Transforms. *Pnas* 68 (9), 2236–2240. doi:10.1073/pnas.68.9.2236

Remondino, F., and Fraser, C. (2006). "Digital Camera Calibration Methods: Considerations and Comparisons," in International Archives of the Photogrammetry [Conference presentation], Dresden, Germany (ISRPS). https://www.isprs.org/proceedings/XXXVI/part5/.

Ren, S., He, K., Girshick, R., and Sun, J. (2017). Faster R-Cnn: Towards Real-Time Object Detection with Region Proposal Networks. *IEEE Trans. Pattern Anal. Mach. Intell.* 39 (6), 1137–1149. doi:10.1109/TPAMI.2016.2577031

Ren, Z., Xu, Z., and Lam, E. Y. (2018). Learning-Based Nonparametric Autofocusing for Digital Holography. *Optica* 5 (4), 337–344. doi:10.1364/OPTICA.5.000337

Rising, C., Reyes, J., Knaus, D., Micka, D., Davis, B., Belovich, V., et al. (2021). Single-Sensor Filter-Intensified Fiber Optic 4D Tomographic CH* Chemiluminesence Flame Measurements. *Appl. Opt.* 60 (22), 6337–6341. doi:10.1364/AO.425887

Rossberg, A., and Funke, H. (2010). Determining the Radial Pair Distribution Function from X-ray Absorption Spectra by Use of the Landweber Iteration Method. *J. Synchrotron Radiat.* 17 (2), 280–288. doi:10.1107/S0909049509052200

Ruan, C., Yu, T., Chen, F., Wang, S., Cai, W., and Lu, X. (2019). Experimental Characterization of the Spatiotemporal Dynamics of a Turbulent Flame in a Gas Turbine Model Combustor Using Computed Tomography of Chemiluminescence. *Energy* 170, 744–751. doi:10.1016/j.energy.2018.12.215

Rudin, L. I., Osher, S., and Fatemi, E. (1992). Nonlinear Total Variation Based Noise Removal Algorithms. *Physica. D.* 60 (1-4), 259–268. doi:10.1016/0167-2789(92)90242-F

Sebald, N. (1980). Measurement of the Temperature and Flow Fields of the Magnetically Stabilized Cross-Flow N2 Arc. *Appl. Phys.* 21 (3), 221–236. doi:10.1007/BF00886172

Selivanov, V. V., and Lecomte, R. (2001). Fast PET Image Reconstruction Based on SVD Decomposition of the System Matrix. *IEEE Trans. Nucl. Sci.* 48 (3), 761–767. doi:10.1109/23.940160

Sellan, D., and Balusamy, S. (2021). Experimental Study of Swirl-Stabilized Turbulent Premixed and Stratified LPG/air Flames Using Optical Diagnostics. *Exp. Therm. Fluid Sci.* 121, 110281. doi:10.1016/j.expthermflusci.2020.110281

Shepp, L. A., and Logan, B. F. (1974). The Fourier Reconstruction of a Head Section. *IEEE Trans. Nucl. Sci.* 21 (3), 21–43. doi:10.1109/TNS.1974.6499235

Shi, J., Qi, H., Yu, Z., An, X., Ren, Y., and Tan, H. (2022). Three-Dimensional Temperature Reconstruction of Diffusion Flame from the Light-Field Convolution Imaging by the Focused Plenoptic Camera. *Sci. China Technol. Sci.* 65, 302–323. doi:10.1007/s11431-020-1761-2

Shui, C., Liu, H., and Cai, W. (2021). Benchmark Evaluation of Tomographic Algorithms for Simultaneous Reconstruction of Temperature and Volume Fraction Fields of Soot and Metal-Oxide Nanoparticles in Non-uniform Flames. *Sci. China Technol. Sci.* 64 (2), 237–250. doi:10.1007/s11431-019-1507-6

Simonyan, K., and Zisserman, A. (2014). *Very Deep Convolutional Networks for Large-Scale Image Recognition*. arXiv preprint arXiv:1409.1556.

Song, Y., Wang, J., Jin, Y., Guo, Z., Ji, Y., He, A., et al. (2016). Implementation of Multidirectional Moiré Computerized Tomography: Multidirectional Affine Calibration. *J. Opt. Soc. Am. A.* 33 (12), 2385–2395. doi:10.1364/JOSAA.33.002385

Strong, D., and Chan, T. (2003). Edge-Preserving and Scale-dependent Properties of Total Variation Regularization. *Inverse Probl.* 19 (6), S165–S187. doi:10.1088/0266-5611/19/6/059

Sun, D., Lu, G., Zhou, H., Yan, Y., and Liu, S. (2015). Quantitative Assessment of Flame Stability through Image Processing and Spectral Analysis. *IEEE Trans. Instrum. Meas.* 64 (12), 3323–3333. doi:10.1109/TIM.2015.2444262

Szegedy, C., Wei Liu, W., Yangqing Jia, Y., Sermanet, P., Reed, S., Anguelov, D., et al. (2015). Going Deeper with Convolutions. *IEEE. C. S.*. doi:10.1109/CVPR.2015.7298594

Unterberger, A., Kempf, A., and Mohri, K. (2019). 3D Evolutionary Reconstruction of Scalar Fields in the Gas-phase. *Energies* 12 (11), 2075. doi:10.3390/en12112075

Upton, T. D., Verhoeven, D. D., and Hudgins, D. E. (2011). High-Resolution Computed Tomography of a Turbulent Reacting Flow. *Exp. Fluids* 50 (1), 125–134. doi:10.1007/s00348-010-0900-6

Verhoeven, D. (1993). Limited-Data Computed Tomography Algorithms for the Physical Sciences. *Appl. Opt.* 32 (20), 3736–3754. doi:10.1364/AO.32.003736

Vest, C. M. (1974). Formation of Images from Projections: Radon and Abel Transforms*. *J. Opt. Soc. Am.* 64 (9), 1215–1218. doi:10.1364/JOSA.64.001215

Walsh, K. T., Fielding, J., and Long, M. B. (2000). Effect of Light-Collection Geometry on Reconstruction Errors in Abel Inversions. *Opt. Lett.* 25 (7), 457–459. doi:10.1364/OL.25.000457

Wan, M., Xie, H., Zhuang, J., and Xu, K. (2015). Three-Dimensional Reconstruction Method for Flame Chemiluminescence Distribution with Complicated Structure. *Appl. Opt.* 54 (31), 9071–9081. doi:10.1364/AO.54.009071

Wan, M., and Zhuang, J. (2018). Projection Model for Flame Chemiluminescence Tomography Based on Lens Imaging. *Opt. Eng.* 57 (4), 1. doi:10.1117/1.OE.57.4.043106

Wan, X., Xiong, W., Zhang, Z., and Chang, F. (2009). An Online Emission Spectral Tomography System with Digital Signal Processor. *Opt. Express* 17 (7), 5279–5286. doi:10.1364/OE.17.005279

Wan, X., Zhang, Z., and Chen, Q. (2013). Three-Dimensional Radiation Thermometer Combining Near-Infrared Passband Thermometry with Optical Fiber Bundle Tomography. *Epl* 103 (7), 50005. doi:10.1209/0295-5075/103/50005

Wang, G. (2016). A Perspective on Deep Imaging. *IEEE. Access.* 4, 8914–8924. doi:10.1109/ACCESS.2016.2624938

Wang, H., Lyu, M., and Situ, G. (2018). eHoloNet: a Learning-Based End-To-End Approach for In-Line Digital Holographic Reconstruction. *Opt. Express* 26 (18), 22603–22614. doi:10.1364/OE.26.022603

Wang, J., Song, Y., Li, Z.-h., Kempf, A., and He, A.-z. (2015). Multi-Directional 3D Flame Chemiluminescence Tomography Based on Lens Imaging. *Opt. Lett.* 40 (7), 1231–1234. doi:10.1364/OL.40.001231

Wang, J., Zhang, W., Zhang, Y., and Yu, X. (2016). Camera Calibration for Multidirectional Flame Chemiluminescence Tomography. *Opt. Eng.* 56 (4), 041307. doi:10.1117/1.OE.56.4.041307

Wang, K., Li, F., Zeng, H., and Yu, X. (2017). Three-Dimensional Flame Measurements with Large Field Angle. *Opt. Express* 25 (18), 21008–21018. doi:10.1364/OE.25.021008

Wang, K., Li, F., Zeng, H., Zhang, S., and Yu, X. (2016). *Computed Tomography Measurement of 3D Combustion Chemiluminescence Using Single Camera* [Conference Presentation]. Beijing, China. OTA 2016. https://www.spiedigitallibrary.org/conference-proceedings-of-spie/10155.toc.

Weinkauff, J., Michaelis, D., Dreizler, A., and Böhm, B. (2013). Tomographic PIV Measurements in a Turbulent Lifted Jet Flame. *Exp. Fluids* 54 (12), 1624–1628. doi:10.1007/s00348-013-1624-1

Wellander, R., Richter, M., and Aldén, M. (2014). Time-resolved (kHz) 3D Imaging of OH PLIF in a Flame. *Exp. Fluids* 55 (6), 1764. doi:10.1007/s00348-014-1764-y

Windle, C. I., Anderson, J., Boyd, J., Homan, B., Korivi, V., and Ma, L. (2021). *In Situ* Imaging of 4D Fire Events in a Ground Vehicle Testbed Using Customized Fiber-Based Endoscopes. *Combustion and Flame* 224, 225–232. doi:10.1016/j.combustflame.2020.11.022

Wiseman, S. M., Brear, M. J., Gordon, R. L., and Marusic, I. (2017). Measurements from Flame Chemiluminescence Tomography of Forced Laminar Premixed Propane Flames. *Combustion and Flame* 183, 1–14. doi:10.1016/j.combustflame.2017.05.003

Worth, N. A., and Dawson, J. R. (2012). Tomographic Reconstruction of OH* Chemiluminescence in Two Interacting Turbulent Flames. *Meas. Sci. Technol.* 24 (2), 024013. doi:10.1088/0957-0233/24/2/024013

Wu, Y., Rivenson, Y., Zhang, Y., Wei, Z., Günaydin, H., Lin, X., et al. (2018). Extended Depth-Of-Field in Holographic Imaging Using Deep-Learning-Based Autofocusing and Phase Recovery. *Optica* 5 (6), 704–710. doi:10.1364/OPTICA.5.000704

Xu, C., Yang, B., Guo, F., Zheng, W., and Poignet, P. (2020). Sparse-View CBCT Reconstruction via Weighted Schatten P-Norm Minimization. *Opt. Express* 28 (24), 35469–35482. doi:10.1364/OE.404471

Xu, W., Luo, W., Wang, Y., and You, Y. (2020). Data-Driven Three-Dimensional Super-resolution Imaging of a Turbulent Jet Flame Using a Generative Adversarial Network. *Appl. Opt.* 59 (19), 5729–5736. doi:10.1364/AO.392803

Yang, Q., Yan, P., Zhang, Y., Yu, H., Shi, Y., Mou, X., et al. (2018). Low-dose CT Image Denoising Using a Generative Adversarial Network with Wasserstein Distance and Perceptual Loss. *IEEE Trans. Med. Imaging* 37 (6), 1348–1357. doi:10.1109/TMI.2018.2827462

Yoon, G.-J., Cho, H., Won, Y.-Y., and Yoon, S. M. (2019). Three-Dimensional Density Estimation of Flame Captured from Multiple Cameras. *IEEE. Access* 7, 8876–8884. doi:10.1109/ACCESS.2018.2890717

Yu, B., and Tao, D. (2019). Anchor Cascade for Efficient Face Detection. *IEEE Trans. Image Process.* 28 (5), 2490–2501. doi:10.1109/TIP.2018.2886790

Yu, T., Bauer, F. J., Huber, F. J., Will, S., and Cai, W. (2021). 4D Temperature Measurements Using Tomographic Two-Color Pyrometry. *Opt. Express* 29 (4), 5304–5315. doi:10.1364/OE.412821

Yu, T., and Cai, W. (2017). Benchmark Evaluation of Inversion Algorithms for Tomographic Absorption Spectroscopy. *Appl. Opt.* 56 (8), 2183–2194. doi:10.1364/AO.56.002183

Yu, T., Cai, W., and Liu, Y. (2018). Rapid Tomographic Reconstruction Based on Machine Learning for Time-Resolved Combustion Diagnostics. *Rev. Scientific Instr.* 89 (4), 043101. doi:10.1063/1.5016403

Yu, T., Li, Z., Ruan, C., Chen, F., Lu, X., and Cai, W. (2019). Development of an Absorption-Corrected Method for 3D Computed Tomography of Chemiluminescence. *Meas. Sci. Technol.* 30 (4), 045403. doi:10.1088/1361-6501/ab01c1

Yu, T., Liu, H., and Cai, W. (2017). On the Quantification of Spatial Resolution for Three-Dimensional Computed Tomography of Chemiluminescence. *Opt. Express* 25 (20), 24093–24108. doi:10.1364/OE.25.024093

Yu, T., Liu, H., Zhang, J., Cai, W., and Qi, F. (2018). Toward Real-Time Volumetric Tomography for Combustion Diagnostics via Dimension Reduction. *Opt. Lett.* 43 (5), 1107–1110. doi:10.1364/OL.43.001107

Yu, T., Ruan, C., Chen, F., Wang, Q., Cai, W., and Lu, X. (2019). Measurement of the 3D Rayleigh Index Field via Time-Resolved CH* Computed Tomography. *Aerospace Sci. Tech.* 95, 105487. doi:10.1016/j.ast.2019.105487

Yu, T., Ruan, C., Liu, H., Cai, W., and Lu, X. (2018). Time-resolved Measurements of a Swirl Flame at 4 kHz via Computed Tomography of Chemiluminescence. *Appl. Opt.* 57 (21), 5962–5969. doi:10.1364/AO.57.005962

Zang, G., Idoughi, R., Wang, C., Bennett, A., Du, J., Skeen, S., et al. (2020). *TomoFluid: Reconstructing Dynamic Fluid from Sparse View Videos*. Seattle, WA, USA: CVPR 2020. https://cvpr2020.thecvf.com/.

Zhang, J., Wang, Q., Dai, J., and Cai, W. (2019). Demonstration of a Cost-Effective Single-Pixel UV Camera for Flame Chemiluminescence Imaging. *Appl. Opt.* 58 (19), 5248–5256. doi:10.1364/AO.58.005248

Zhang, Z. (2000). A Flexible New Technique for Camera Calibration. *IEEE Trans. Pattern Anal. Machine Intell.* 22 (11), 1330–1334. doi:10.1109/34.888718

Zhang, Z. (1999). *Flexible Camera Calibration by Viewing a Plane from Unknown Orientations* [Conference Presentation]. Fort Collins, CO, United States: IEEE CS 1999. https://ieeexplore.ieee.org/xpl/conhome/6370/proceeding.

Zhang, Z., Liang, X., Dong, X., Xie, Y., and Cao, G. (2018). A Sparse-View CT Reconstruction Method Based on Combination of DenseNet and Deconvolution. *IEEE Trans. Med. Imaging* 37 (6), 1407–1417. doi:10.1109/TMI.2018.2823338

Zhao, W., Zhang, B., Xu, C., Duan, L., and Wang, S. (2018). Optical Sectioning Tomographic Reconstruction of Three-Dimensional Flame Temperature Distribution Using Single Light Field Camera. *IEEE Sensors J.* 18 (2), 528–539. doi:10.1109/JSEN.2017.2772899

Zhou, H.-C., Lou, C., Cheng, Q., Jiang, Z., He, J., Huang, B., et al. (2005). Experimental Investigations on Visualization of Three-Dimensional Temperature Distributions in a Large-Scale Pulverized-Coal-Fired Boiler Furnace. *Proc. Combustion Inst.* 30 (1), 1699–1706. doi:10.1016/j.proci.2004.08.090

Conflict of Interest: The authors declare that the research was conducted in the absence of any commercial or financial relationships that could be construed as a potential conflict of interest.

Publisher's Note: All claims expressed in this article are solely those of the authors and do not necessarily represent those of their affiliated organizations, or those of the publisher, the editors, and the reviewers. Any product that may be evaluated in this article, or claim that may be made by its manufacturer, is not guaranteed or endorsed by the publisher.

frontiers | Frontiers in Photonics

BRIEF RESEARCH REPORT
published: 09 June 2022
doi: 10.3389/fphot.2022.907847

Coherent Noise Suppression of Single-Shot Digital Holographic Phase *Via* an Untrained Self-Supervised Network

Ju Tang[1], *Jiawei Zhang*[1], *Ji Wu*[1], *Jianglei Di*[2,1]* *and Jianlin Zhao*[1]*

[1]Key Laboratory of Light Field Manipulation and Information Acquisition, Ministry of Industry and Information Technology, Shaanxi Key Laboratory of Optical Information Technology, School of Physical Science and Technology, Northwestern Polytechnical University, Xi'an, China, [2]Advanced Institute of Photonics Technology, School of Information Engineering, and Guangdong Provincial Key Laboratory of Information Photonics Technology, Guangdong University of Technology, Guangzhou, China

In digital holography, the coherent noise affects the measurement accuracy and reliability greatly due to the high spatial and temporal coherence of the laser. Especially, compared with the speckle noise of intensity in digital holography, the coherent noise of phase contains more medium- and low-frequency characteristics, which hinders the effectiveness of noise suppression algorithms. Here, we propose a single-shot untrained self-supervised network (SUSNet) for the coherent noise suppression of phase, requiring only one noisy phase map to complete the optimization and learning. The SUSNet can smoothen and suppress the background fluctuations, parasitic fringes, and diffraction loops in a noisy phase and shows good generalization performance for samples with different shapes, sizes, and phase ranges. Compared with the traditional algorithms and the ground truth-supervised neural network (DnCNN), the SUSNet has the best noise suppression performance and background smoothing effect. As a result, the SUSNet can suppress the fluctuation range to ~20% of the original range.

Keywords: digital holography, coherent noise suppression, single-shot untrained self-supervised network, neural network, background smoothing

OPEN ACCESS

Edited by:
Pietro Ferraro,
National Research Council (CNR), Italy

Reviewed by:
Silvio Montresor,
Le Mans Université, France
Guoan Zheng,
University of Connecticut, United States

***Correspondence:**
Jianglei Di
jiangleidi@gdut.edu.cn
Jianlin Zhao
jlzhao@nwpu.edu.cn

Specialty section:
This article was submitted to Optical Information Processing and Holography, a section of the journal Frontiers in Photonics

Received: *30 March 2022*
Accepted: *28 April 2022*
Published: *09 June 2022*

Citation:
Tang J, Zhang J, Wu J, Di J and Zhao J (2022) Coherent Noise Suppression of Single-Shot Digital Holographic Phase Via an Untrained Self-Supervised Network. Front. Photonics 3:907847. doi: 10.3389/fphot.2022.907847

INTRODUCTION

Coherent noise is a vexing problem and has attracted many researchers in solving it. However, there is still no perfect solution for the coherent noise problem nowadays due to the high spatial and temporal coherence of the laser. In digital holography, coherent noise will lead to haphazardly distributed granular noise in the reproduced intensity, named as speckle noise, and the background fluctuations, parasitic fringes, and diffraction loops in the reconstructed phase, which we simply refer to as the coherent noise of phase. If the random fluctuation in intensity or phase is generated due to the object itself, it does not change over time. At this point, the fluctuation actually contains detailed object information. However, if the fluctuation is generated due to other factors within the system, it needs to be suppressed as much as possible to reduce the effect on observation and measurement. For speckle noise suppression, there are some methods, such as the averaging ideas with multiwavelength (Nomura et al., 2008), multi-polarization (Xiao et al., 2011), multi-angle illumination (Kang et al., 2007; Feng et al., 2009), slight displacements (Pan et al., 2011), and numerical multi-look (Bianco et al., 2013), and the decoherence idea with the replaced laser source (Kemper et al., 2008; Remmersmann et al., 2009; Langehanenberg et al., 2010). Nevertheless, the averaging method

always requires capturing a large number of holograms for suppression, while the decoherence method requires replacing the light emitting diode (LED) as the laser source which will limit the interference range of measurement, although those methods may be useful in suppressing the coherent noise of phase relatively.

In addition to optical methods, digital image processing approaches are also helpful in solving the coherent noise problem. The image processing methods mainly adopt the filtering idea, according to the theory of information optics, considering the differences between the distribution and characteristics of object and noise in the signal domain. At present, they are divided into the space-domain filtering-based (Darakis and Soraghan, 2006; Shortt et al., 2006; Uzan et al., 2013), transform-domain filtering-based (Maycock et al., 2007; Sharma et al., 2008; Choi et al., 2010), and deep learning–based methods (Zhang et al., 2017; Jeon et al., 2018; Wang et al., 2019; Montresor et al., 2020; Yin et al., 2020). Especially, the deep learning–based methods have achieved excellent performance over the traditional algorithms as soon as they appeared (Di et al., 2021). For example, Wang et al. discussed the suppression and resistance of deep neural networks to additional Gaussian and salt-and-pepper noises in phase unwrapping (Wang et al., 2019); Montresor et al. applied a residual network (DnCNN) (Zhang et al., 2017) to compare the generalization capability among three models, which were trained by the natural images with Gaussian noise, the noise-free fringe patterns with added Gaussian noise, and the phase data with realistic speckle noise, (Montresor et al., 2020); Yin et al. used the Noise2Noise strategy (Lehtinen et al., 2018) to reduce the speckle noises in computer-generated holography and digital holography without noise-free data as the ground truth (Yin et al., 2020).

Nevertheless, the low-level speckle noise has some statistical similarity with the regular additional noises, such as Gaussian noise, uniform noise, and salt-and-pepper noise, which have many high-frequency and low-correlation characteristics. Compared with these noises, the additional coherent phase noise may contain more medium- and low-frequency characteristics and some non-stationary features, such as background fluctuations, parasitic fringes, and diffraction loops. Facing these problems, it is difficult to play a good generalization with the network model only trained under high-frequency noise. Moreover, most of the existing deep learning methods are ground truth–supervised training with a large amount of data, but it is difficult and time-consuming to get the noise-free data or other noisy data additionally in practice.

Is it possible to train the network with one single image? We have tried to train a network to predict the diffraction distance from a pair of images for autofocusing (Tang et al., 2022), inspired by the deep image prior (Ulyanov et al., 2017). Facing the noise suppression requirements of the single-shot phase of digital holography, here, we propose a single-shot untrained self-supervised network (SUSNet). The SUSNet only needs a noisy phase for learning and optimization and can generalize to various samples with different noise disturbances. We describe the physical generation of coherent noise and our denoising model in **Section 2**. Subsequently, we measure some objects through a common-path off-axis digital holographic microscope system and compare and analyze the denoising results of various samples, including different shapes, sizes, and phase ranges, by traditional algorithms, DnCNN and SUSNet in **Section 3**.

PRINCIPLE AND METHOD

Physical Generation of Coherent Noise

In the recording stage of a digital hologram, the object wavefront $O(x, y)$ and the reference wavefront $R(x, y)$ interfere on the target plane of the camera, and the intensity distribution $I(x, y)$ of the obtained hologram can be expressed as

$$I(x,y) = |O(x,y)|^2 + |R(x,y)|^2 + O(x,y)R^*(x,y) + O^*(x,y)R(x,y), \quad (1)$$

where (x, y) is the coordinates of the recording plane and the symbol * describes the complex conjugation. In the reconstruction stage, the reconstructed object wavefront $U_d(\xi, \eta)$ can be expressed as follows:

$$U_d(\xi,\eta) = \frac{\exp(jkd)}{j\lambda d}\exp\left[j\frac{k}{2d}\left(\xi^2+\eta^2\right)\right] \cdot \mathrm{FT}\left\{R(x,y)I(x,y)\exp\left[j\frac{k}{2d}\left(x^2+y^2\right)\right]\right\}, \quad (2)$$

where (ξ, η) is the coordinates of the object plane, d is the distance from the recording plane to the object plane, $k = 2\pi/\lambda$ is the wave number, λ is the wavelength, and FT $\{\cdot\}$ is the Fourier transform operation. Ideally, the reconstructed wavefront $U_d(\xi, \eta)$ is equivalent to the initial object wavefront $U_o(\xi, \eta)$. However, a series of sub-waves occur when the laser beam passes through (or reflects from) some uneven or non-smooth objects and will be scattered by dust particles in the air. These sub-waves have subtle optical path differences, and coherent superposition occurs between sub-waves due to the high coherence of the laser, which is eventually recorded in the hologram. The additional components result in random fluctuations in reconstructed intensity and phase, called the coherent noise. In fact, the reconstructed wavefront $U_d(\xi, \eta)$ is the product of the ideal object wavefront $U_o(\xi, \eta)$ and the random complex amplitude $U_n(\xi, \eta)$ of noise

$$U_d(\xi,\eta) = U_o(\xi,\eta)\cdot U_n(\xi,\eta) = A_o\exp(j\varphi_o)\cdot A_n\exp(j\varphi_n) = A_oA_n\exp[j(\varphi_o+\varphi_n)], \quad (3)$$

where A_o and φ_o are the amplitude and phase of the object wavefront, while A_n and φ_n are those of the noisy complex amplitude, respectively. The phase distribution of the reconstructed wavefront is obtained as

$$\varphi(\xi,\eta) = \arctan\left\{\frac{\mathrm{Im}[U_d(\xi,\eta)]}{\mathrm{Re}[U_d(\xi,\eta)]}\right\}[\mathrm{mod}(2\pi)] = \varphi_o(\xi,\eta) + \varphi_n(\xi,\eta), \quad (4)$$

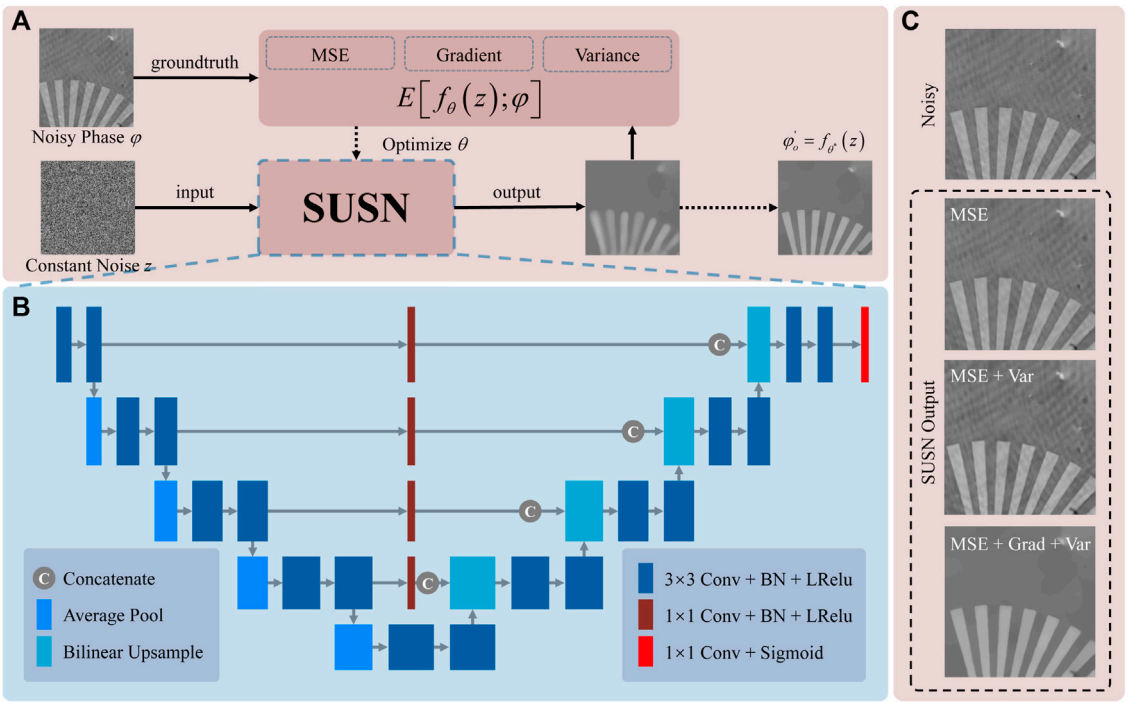

FIGURE 1 | Schematic diagram of the single-shot untrained self-supervised network (SUSNet). **(A)** Implementation procedure for learning and optimization. **(B)** Details for the U-shaped network structure. **(C)** Different outputs by the SUSNet with the same learning parameters except loss function.

where Im (·) and Re (·) take the real and imaginary parts of the complex amplitude, respectively, and mod (·) is the remainder function. It is obvious that the measured noisy phase $\varphi(\xi, \eta)$ obtained by digital holography is the sum of the true object phase $\varphi_o(\xi, \eta)$ and coherent noise term $\varphi_n(\xi, \eta)$. The presence of a coherent noise term will introduce additional phenomena, such as random fluctuations in the phase background, parasitic interference fringes, and dust diffraction loops, and decrease the signal-to-noise ratio of the whole phase map. In particular, the confidence of measurement is reduced for those objects with a small spatial scale or phase changes due to the noise drowning.

Single-Shot Untrained Self-Supervised Network

The traditional deep neural network is almost trained under the supervision of ground truth, based on a large amount of standard data. The learning process of the network can be formulized as

$$\theta^* = \arg\min_\theta E[f_\theta(\varphi); \bar{\varphi}], \quad \varphi_o' = f_{\theta^*}(\varphi), \tag{5}$$

where φ and $\bar{\theta}$ are the input and ground truth of the network, respectively; θ is the learnable parameter for optimization; θ^* is the suitable parameter after learning; $E[\cdot]$ is the denoising task term; and φ'_o is the final noise-free phase by the network $f_{\theta^*}(\cdot)$. In general, the ground truth can be the true object phase φ_o or another measured noisy phase φ' which consists of the same true phase φ_o and another noise term φ'_n, named as the Noise2Noise strategy (Lehtinen et al., 2018; Yin et al., 2020). However, either the true phase or another noisy phase is extremely difficult to obtain consistently with the large demand of datasets. Moreover, the diversity of the datasets limits the generalization capability of the trained network model. Although the neural network can greatly outperform the traditional algorithms on specific problems, its application is still resistant in practice.

Here, we focus on the problems of dataset requirement, ground truth, and generalization capability and propose the single-shot untrained self-supervised network (SUSNet). The learning process is changed as

$$\theta^* = \arg\min_\theta E[f_\theta(z); \varphi], \quad \varphi_o' = f_{\theta^*}(z), \tag{6}$$

where the noisy phase φ is set as the ground truth to supervise the optimization and z is a constant matrix with the same size as the ground truth, which is set as a random uniform noise during each training. The implementation procedure for learning and optimization is shown in **Figure 1A**, and the details of the U-shaped SUSNet structure are clearly shown in **Figure 1B**. The constant noise z and the noisy phase φ are regarded as the input and ground truth, respectively. During each step of learning, low-level random Gaussian noise is added in the input and ground truth to make the optimization more robust. It is regarded as a self-supervised way because no additional data acquisition is required except one noisy phase. Moreover, unlike the traditional network which needs to be trained first for a long time before implementing, SUSNet can directly optimize and achieve the denoising task using only one single-shot noisy phase with a little time. Moreover, it can generalize to arbitrary objects with targeting and adaptation for better results.

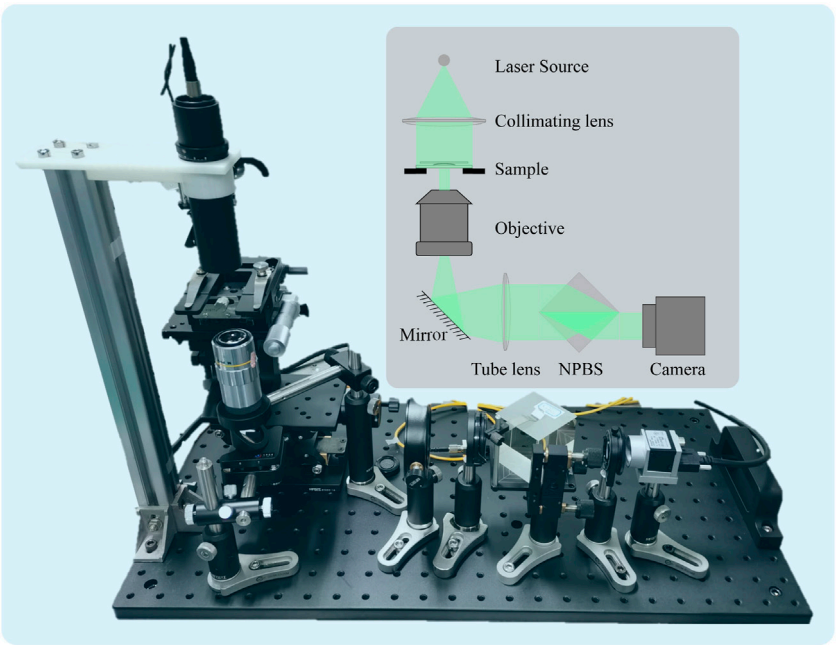

FIGURE 2 | Common-path off-axis digital holographic microscope system for hologram capture and noisy phase acquisition. NPBS: non-polarized beam splitter.

The denoising task term $E[\cdot]$ can be quantitatively represented by the sum of loss functions as

$$E[f_\theta(z);\varphi] = \mathrm{MSE}[f_\theta(z),\varphi] + \beta_1 \cdot \mathrm{Grad}[f_\theta(z)] + \beta_2 \cdot \mathrm{Var}[f_\theta(z)], \tag{7}$$

$$\mathrm{MSE}[f_\theta(z),\varphi] = \frac{\left\| f_\theta(z) - \varphi \right\|_2^2}{M \cdot N}, \tag{8}$$

$$\mathrm{Grad}[f_\theta(z)] = \frac{\sum_1^M \sum_1^N \sqrt{G_\xi^2 + G_\eta^2}}{M \cdot N}, \begin{cases} G_\xi = g_\xi * f_\theta(z) \\ G_\eta = g_\eta * f_\theta(z) \end{cases}, \tag{9}$$

$$\mathrm{Var}[f_\theta(z)] = \frac{\sum_1^M \sum_1^N [f_\theta(z) - \mu]^2}{M \cdot N}, \mu = \frac{\sum_1^M \sum_1^N f_\theta(z)}{M \cdot N}. \tag{10}$$

Where MSE $(\cdot)$, Grad $(\cdot)$, and Var $(\cdot)$ are the mean squared error function, tenengrad gradient function, and variance function, respectively; μ is the mean value; M and N are the numbers of pixels; and β_1 and β_2 are the hyperparameters to balance the influence of different loss functions. In **Eq. 9**, G_ξ and G_η are the gradients in the horizontal and vertical directions, respectively, which are obtained by the convolution * with Sobel operators g_ξ and g_η. The effect of SUSNet with different loss functions is shown in **Figure 1C**. It is clear that SUSNet with MSE or MSE + Var just generates the noisy phase without noise suppression, while SUSNet with MSE + Grad + Var suppresses and smoothens the background fluctuations, parasitic fringes, and other coherent noise phenomena effectively. In brief, the MSE term allows SUSNet to learn quickly from the noise z to the object phase information, and the edge gradient of the output is computed and minimized to abandon overfitting the coherent noise by the Grad term. The Var term plays a role in balancing the smoothing effect caused by the Grad term in the late training period. The initial learning rate is 0.002 and subsequently reduces by one-tenth every 100 steps with the Adam optimizer. $\beta_1 = 0.02$ and $\beta_2 = -0.15$ are used with possible fine-tuning. The optimization process takes ~35 s for 400 steps with the Intel Core i7-10700K CPU and NVIDIA GeForce RTX 1080Ti GPU.

Experimental Setup

Here, we implement the common-path off-axis digital holographic microscope system for the hologram capture and noisy phase acquisition, as shown in **Figure 2B**. A green light beam from a diode-pumped solid-state laser (Cobolt Samba ™ 50 532 nm, Linewidth <1 MHz) is collimated by a lens and is incident to the sample. Then, the laser is magnified and collimated again with the microscope objective (Mitutoyo M Plan Apo ×50) and the tube lens, and a non-polarized beam splitter (NPBS) is used to form the common-path structure. The wave is refracted and reflected by the NPBS placed at an angle of 45° and finally divided into two parts. The camera (Basler acA 2040-90 μm) is placed on a suitable plane to capture the in-focus image of the sample. This common-path setup benefits the object-free region of the other half spot as the reference wavefront, so the propagation path of the object and reference wavefronts is the same. The common-path design can improve the stability of the system simply and greatly but requires the sample to be sparse and sacrifices half of the field of view (FOV) (Zhang et al., 2021). After hologram acquisition, the double-exposure method is implemented to compensate the system aberration, and the measured noisy phases of different samples are obtained by numerical reconstruction according to **Eqs 1–4**.

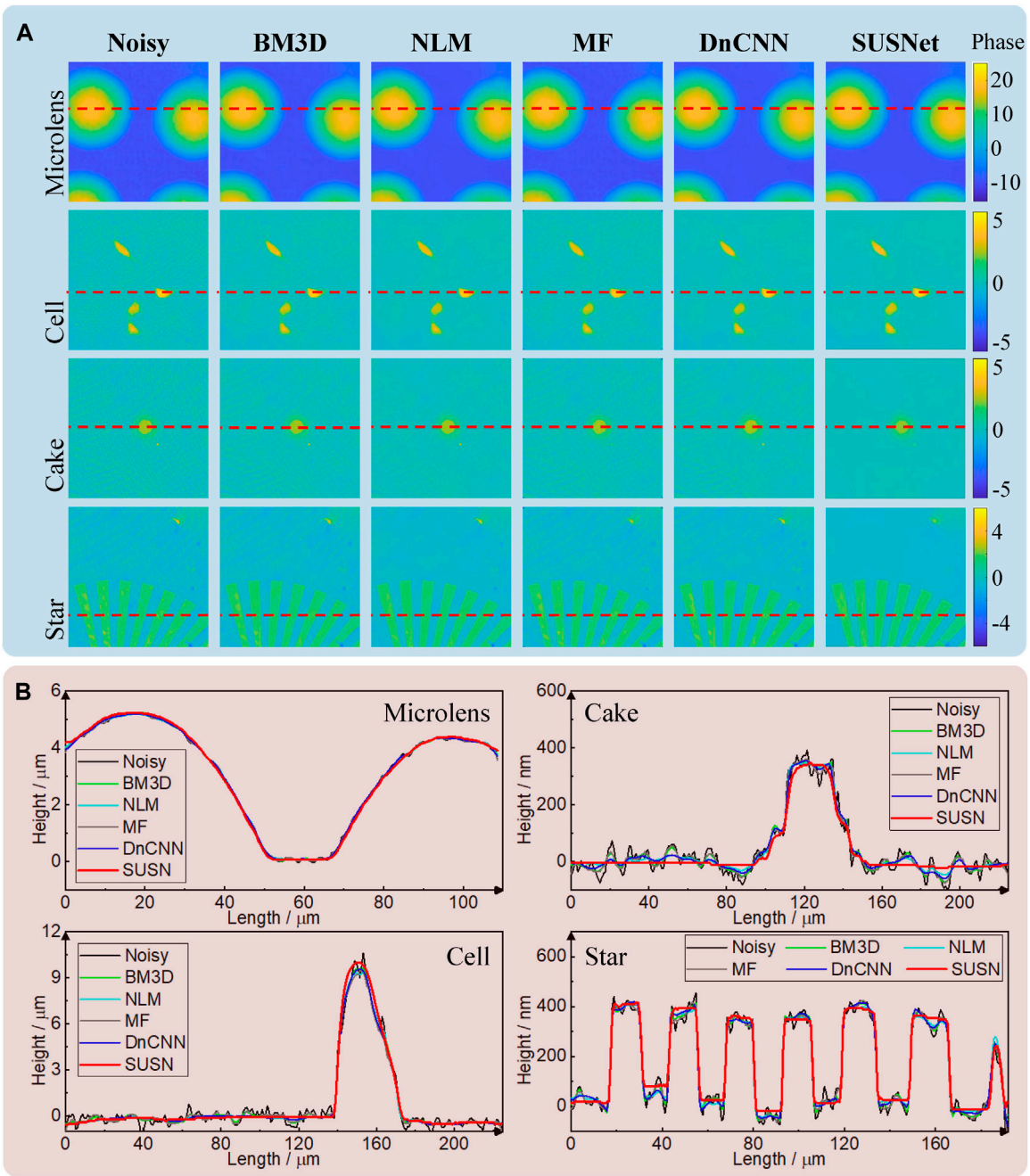

FIGURE 3 | Comparison of different noise suppression algorithms on experimental holographic phases with 532-nm green laser illumination. **(A)** Noisy phase maps of microlens, cell, cake, and star samples and their denoise results with BM3D, NLM, MF, DnCNN, and SUSNet. **(B)** Comparison of the height distribution along the truncated lines in **(A)**.

EXPERIMENTAL RESULTS

Noise Suppression With Various Samples

Here, we measure four samples, including microlens, cell, cake structure, and star structure, to obtain the noisy phases of various samples. The microlens array has a maximum height of 5 μm and a refractive index of 1.458, while the cake and star structures are both on the benchmark quantitative phase target with the refractive index of 1.52. The HT22 cells after overnight culturing have a uniform refractive index of 1.375, while the cell culture has a refractive index of 1.3377 (Lue et al., 2012). To observe the actual denoising effect of SUSNet, we take several traditional noise suppression algorithms for comparison, including BM3D (Dabov et al., 2007), non-local means filtering (NLM) (Uzan et al., 2013), median filtering (MF) (Darakis and Soraghan, 2006), and DnCNN (Zhang et al., 2017).

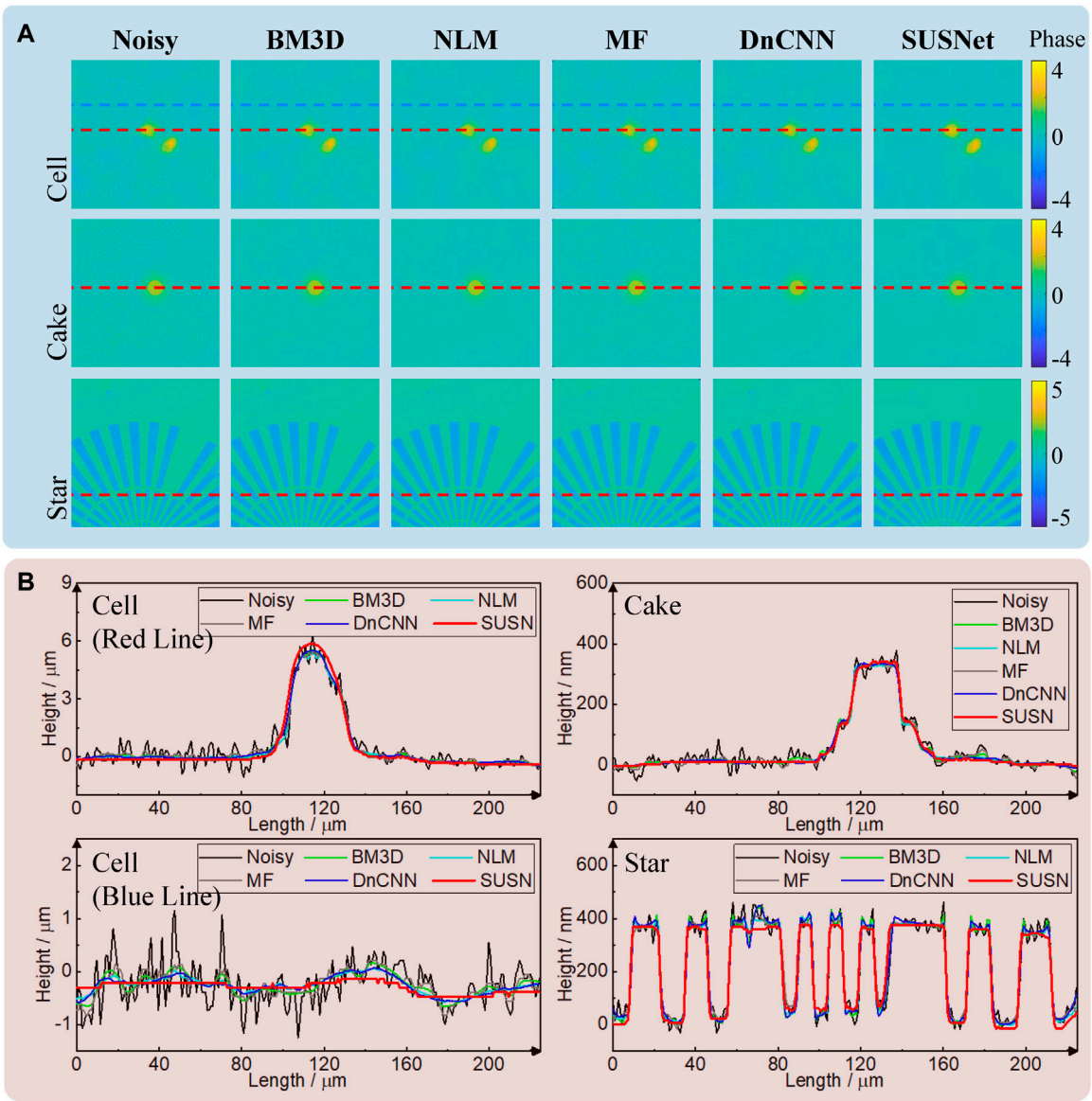

FIGURE 4 | Comparison of different noise suppression algorithms on experimental holographic phases with 640-nm red laser illumination. **(A)** Noisy phase maps of cell, cake, and star samples, and their denoise results with BM3D, NLM, MF, DnCNN, and SUSNet. **(B)** Comparison of height distribution along the truncated lines in **(A)**.

From **Figure 3A**, it is obvious that all noisy phases have background fluctuations, parasitic fringes, and even some damage defects. Intuitively, the BM3D, MF, and DnCNN can relatively suppress the fluctuations and fringes and improve the overall signal-to-noise ratio, but their actual effect is limited with insufficient smoothing and fringe residue. In comparison, the NLM is the most effective one among these noise suppression algorithms, but there are still some gaps compared with the SUSNet. We set several truncated lines on these phases and converted them to the height distribution along the lines in **Figure 3B**. From the truncated lines of microlens, the coherent noise is not drastic because the phase change of microlens is much larger than the fluctuation caused by the noise. However, these fluctuations on the truncated lines of cell, cake, and star structures are more pronounced and intense. In contrast, the red curves of the SUSNet ensure a flatter curve than other algorithms with the same fundamental shape. We select the truncated lines of the cell to calculate the ranges ($R = \mathrm{Max}(\cdot) - \mathrm{Min}(\cdot)$) as the reference values of background fluctuation. The noisy phase of the cell has 0.980 rad fluctuation, and the denoising results of BM3D, NLM, MF, and DnCNN have 0.292, 0.342, 0.588, and 0.265 rad fluctuations, respectively, while the noise-free phase of the SUSNet has 0.235 rad fluctuation, which is only 23.9% of the original range.

It is clear that SUSNet can effectively generalize and suppress noise for various samples of different shapes, sizes, and phase variations, which has reached the generalization capability of traditional algorithms, such as BM3D, MF, and NLM, and the neural network model, such as DnCNN, trained by a large amount of data. Another advantage of SUSNet is that it does not require a prior evaluation of the noise level, while the traditional algorithms need this prior as one hyperparameter for adjustment. For example, the results in **Figure 3A** are calculated using the standard deviation of 10 as a prior. The DnCNN is more necessary to load the corresponding model trained by the dataset with a similar noise level because the traditional neural networks limited by the dataset have difficulty generalizing to other noise levels and types beyond the training set. In contrast, the SUSNet prioritizes the extraction of object information while ignoring the noises during learning, even if the noises are not all high frequencies. As for the calculation cost, the SUSNet needs ~35 s for 400 steps of optimization, while BM3D, NLM, MF, and DnCNN spend 0.3, 30, 0.02, 8.35 s in calculating by CPU, respectively.

Noise Suppression at Another Level of Noise

Here, we change a red diode laser with a wavelength of 640 nm (Changchun New Industries, MRL-III-640-100 mW, Linewidth <4.4 GHz) as the source of the common-path off-axis digital holographic microscope system and re-measure the previous samples as shown in **Section 3.1**. The actual coherence length of the green laser is thousands of times longer than that of the red laser in the experiment, so the noisy phase obtained under the red laser will have different noise levels and distributions. The noisy phases and their denoising results of all algorithms, including SUSNet, are shown in **Figure 4A**. Compared with those under the green laser, the noises under the red laser have less parasitic fringes and damage defects, and the background fluctuations have lower amplitudes and higher frequencies. Intuitively, the performance of the SUSNet is still comparable to, or even better than that of these traditional algorithms. From **Figure 4B**, the effect of background fluctuations is evident in truncated lines, even affecting the fundamental shape. However, the red curves of the SUSNet are the flattest and smoothest compared with other color curves, especially in the blue truncated lines of the cell. We also calculate the range of curves in the blue truncated lines of the cell as the reference values of background fluctuations. The noisy phase has 0.878 rad fluctuation, and the denoising results of BM3D, NLM, MF, and DnCNN have 0.228, 0.300, 0.376, and 0.242 rad fluctuations, respectively, while the noise-free phase of the SUSNet has 0.125 rad fluctuation, which is only 14.2% of the original range. It is obvious that the SUSNet has a very powerful smoothing ability for fluctuations by ensuring accurate object information. However, SUSNet still has some shortcomings to be researched and overcome. It may not apply to the detailed structures (e.g., scratch and damage) as objects, and its smooth effect will bring some impact for some small-sized objects. In general, in the case of a single-shot noisy phase, it is surprising enough that an untrained network can learn a noise-free phase directly from a noisy image with the self-supervised method, not to mention that its noise suppression performance is relatively excellent.

CONCLUSION

In summary, we propose an untrained self-supervised network SUSNet for the coherent noise suppression of the phase map in digital holography. The proposed SUSNet can smooth and suppress background fluctuations, parasitic fringes, and diffraction loops and has good generalization performance for the samples with different shapes, sizes, and phase ranges. Compared with the conventional algorithms, such as BM3D, NLM, and MF, and the ground truth–supervised neural network DnCNN, the SUSNet has the best noise suppression performance and background smoothing effect. As a result, the SUSNet can reduce the fluctuation range to ~20% of the original range. The most important point is that SUSNet requires only one noisy phase to complete the optimization and learning without the ground truth and a large amount of data, which is the main challenge of traditional neural networks in applications.

DATA AVAILABILITY STATEMENT

The original contributions presented in the study are included in the article/Supplementary Material; further inquiries can be directed to the corresponding authors.

AUTHOR CONTRIBUTIONS

JT wrote the draft of the manuscript. JT and JW contributed to data analysis. JT and JZhang performed the experiments. JD and JZhao conceived and supervised the project. All the authors edited the manuscript.

FUNDING

This work was supported by the National Natural Science Foundation of China (NSFC) (Grant No. 61927810, Grant No. 62075183).

REFERENCES

Bianco, V., Paturzo, M., Memmolo, P., Finizio, A., Ferraro, P., and Javidi, B. (2013). Random Resampling Masks: a Non-bayesian One-Shot Strategy for Noise Reduction in Digital Holography. *Opt. Lett.* 38, 619–621. doi:10.1364/OL.38.000619

Choi, H. J., Seo, Y. H., and Kim, D. W. (2010). Noise Reduction for Digital Holograms in a Discrete Cosine Transform (DCT) Domain. *Opt. Appl.* 40, 991–1005. doi:10.1117/12.850803

Dabov, K., Foi, A., Katkovnik, V., and Egiazarian, K. (2007). Image Denoising by Sparse 3-D Transform-Domain Collaborative Filtering. *IEEE Trans. Image Process.* 16, 2080–2095. doi:10.1109/tip.2007.901238

Darakis, E., and Soraghan, J. J. (2006). Compression of Interference Patterns with Application to Phase-Shifting Digital Holography. *Appl. Opt.* 45, 2437–2443. doi:10.1364/AO.45.002437

Di, J., Tang, J., Wu, J., Wang, K., Ren, Z., Zhang, M., et al. (2021). Research Progress in the Applications of Convolutional Neural Networks in Optional Information Processing. *Laser optoelectron.* 58, 1600001. doi:10.3788/LOP202158.1600001

Feng, P., Wen, X., and Lu, R. (2009). Long-working-distance Synthetic Aperture Fresnel off-axis Digital Holography. *Opt. Express* 17, 5473–5480. doi:10.1364/OE.17.005473

Jeon, W., Jeong, W., Son, K., and Yang, H. (2018). Speckle Noise Reduction for Digital Holographic Images Using Multi-Scale Convolutional Neural Networks. *Opt. Lett.* 43, 4240–4243. doi:10.1364/OL.43.004240

Kang, X., Kang, X., and Tay, C. J. (2007). Speckle Noise Reduction in Digital Holography by Multiple Holograms. *Opt. Eng.* 46, 115801. doi:10.1117/1.2802060

Kemper, B., Stürwald, S., Remmersmann, C., Langehanenberg, P., and von Bally, G. (2008). Characterisation of Light Emitting Diodes (LEDs) for Application in Digital Holographic Microscopy for Inspection of Micro and Nanostructured Surfaces. *Opt. Lasers Eng.* 46, 499–507. doi:10.1016/j.optlaseng.2008.03.007

Langehanenberg, P., Bally, G. v., and Kemper, B. (2010). Application of Partially Coherent Light in Live Cell Imaging with Digital Holographic Microscopy. *J. Mod. Opt.* 57, 709–717. doi:10.1080/09500341003605411

Lehtinen, J., Munkberg, J., Hasselgren, J., Laine, S., Karras, T., Aittala, M., et al. (2018). "Noise2Noise: Learning Image Restoration without Clean Data," in Proceedings of the 35th International Conference on Machine Learning, Stockholmsmässan, Stockholm Sweden, 10-15 July 2018, 4620–4631. doi:10.48550/arXiv.1803.041897

Lue, N., Kang, J. W., Hillman, T. R., Dasari, R. R., and Yaqoob, Z. (2012). Single-shot Quantitative Dispersion Phase Microscopy. *Appl. Phys. Lett.* 101, 084101. doi:10.1063/1.4745785

Maycock, J., Hennelly, B. M., McDonald, J. B., Frauel, Y., Castro, A., Javidi, B., et al. (2007). Reduction of Speckle in Digital Holography by Discrete Fourier Filtering. *J. Opt. Soc. Am. A* 24, 1617–1622. doi:10.1364/JOSAA.24.001617

Montresor, S., Tahon, M., Laurent, A., and Picart, P. (2020). Computational De-noising Based on Deep Learning for Phase Data in Digital Holographic Interferometry. *Apl. Photonics* 5, 030802. doi:10.1063/1.5140645

Nomura, T., Okamura, M., Nitanai, E., and Numata, T. (2008). Image Quality Improvement of Digital Holography by Superposition of Reconstructed Images Obtained by Multiple Wavelengths. *Appl. Opt.* 47, D38–D43. doi:10.1364/AO.47.000D38

Pan, F., Xiao, W., Liu, S., Wang, F., Rong, L., and Li, R. (2011). Coherent Noise Reduction in Digital Holographic Phase Contrast Microscopy by Slightly Shifting Object. *Opt. Express.* 19, 3862–3869. doi:10.1364/OE.19.003862

Remmersmann, C., Stürwald, S., Kemper, B., Langehanenberg, P., and von Bally, G. (2009). Phase Noise Optimization in Temporal Phase-Shifting Digital Holography with Partial Coherence Light Sources and its Application in Quantitative Cell Imaging. *Appl. Opt.* 48, 1463–1472. doi:10.1364/AO.48.001463

Sharma, A., Sheoran, G., Jaffery, Z. A., and Moinuddin (2008). Improvement of Signal-To-Noise Ratio in Digital Holography Using Wavelet Transform. *Opt. Lasers Eng.* 46, 42–47. doi:10.1016/j.optlaseng.2007.07.004

Shortt, A. E., Naughton, T. J., and Javidi, B. (2006). A Companding Approach for Nonuniform Quantization of Digital Holograms of Three-Dimensional Objects. *Opt. Express* 14, 5129–5134. doi:10.1364/OE.14.005129

Tang, J., Wu, J., Zhang, J., Ren, Z., Di, J., and Zhao, J. (2022). Single-shot Diffraction Autofocusing: Distance Prediction via an Untrained Physics-Enhanced Network. *IEEE Photonics J.* 14, 1–6. doi:10.1109/JPHOT.2021.3138548

Ulyanov, D., Vedaldi, A., and Lempitsky, V. (2017). "Improved Texture Networks: Maximizing Quality and Diversity in Feed-Forward Stylization and Texture Synthesis," in Proceedings of the IEEE conference on computer vision and pattern recognition, San Francisco, CA, USA, 18-20 June 1996, 9446–9454. doi:10.1109/CVPR.2017.437

Uzan, A., Rivenson, Y., and Stern, A. (2013). Speckle Denoising in Digital Holography by Nonlocal Means Filtering. *Appl. Opt.* 52, A195–A200. doi:10.1364/AO.52.00A195

Wang, K., Li, Y., Kemao, Q., Di, J., and Zhao, J. (2019). One-step Robust Deep Learning Phase Unwrapping. *Opt. Express* 27, 15100–15115. doi:10.1364/OE.27.015100

Xiao, W., Zhang, J., Rong, L., Pan, F., Shuo Liu, S., Wang, F., et al. (2011). Improvement of Speckle Noise Suppression in Digital Holography by Rotating Linear Polarization State. *Chin. Opt. Lett.* 9, 60903–060901. doi:10.3788/COL201109.060901

Yin, D., Gu, Z., Zhang, Y., Gu, F., Nie, S., Feng, S., et al. (2020). Speckle Noise Reduction in Coherent Imaging Based on Deep Learning without Clean Data. *Opt. Lasers Eng.* 133, 106151. doi:10.1016/j.optlaseng.2020.106151

Zhang, J., Dai, S., Ma, C., XI, T., Di, J., and Zhao, J. (2021). A Review of Common-Path off-axis Digital Holography: Towards High Stable Optical Instrument Manufacturing. *Light. Adv. Manu.* 2, 333–349. doi:10.37188/lam.2021.023

Zhang, K., Zuo, W., Chen, Y., Meng, D., and Zhang, L. (2017). Beyond a Gaussian Denoiser: Residual Learning of Deep Cnn for Image Denoising. *IEEE Trans. Image Process.* 26, 3142–3155. doi:10.1109/TIP.2017.2662206

Conflict of Interest: The authors declare that the research was conducted in the absence of any commercial or financial relationships that could be construed as a potential conflict of interest.

Publisher's Note: All claims expressed in this article are solely those of the authors and do not necessarily represent those of their affiliated organizations, or those of the publisher, the editors, and the reviewers. Any product that may be evaluated in this article, or claim that may be made by its manufacturer, is not guaranteed or endorsed by the publisher.

frontiers | Frontiers in Photonics

ORIGINAL RESEARCH
published: 20 June 2022
doi: 10.3389/fphot.2022.929936

Augmentation of 3D Holographic Image Graticule With Conventional Microscopy

*Mehdi Askari and Jae-Hyeung Park**

Department of Information and Communication Engineering, Inha University, Incheon, Korea

In this paper, we report an implementation of a computer-generated holographic projection technique to display a holographic scene like a measuring graticule around the magnified sample image in a reflected bright-field microscopy. The implemented system acts as a gauging tool for lateral and longitudinal measurements of a sample that is being observed under a microscope through the assistance of a holographic measuring graticule. Numerical and experimental verifications have been performed, demonstrating the successful augmentation of a holographic projection system as a measuring tool with a conventional bright-field microscopic system.

Keywords: hologram, microscopy, augmentation, 3D, graticule

OPEN ACCESS

Edited by:
Ting-Chung Poon,
Virginia Tech, United States

Reviewed by:
Tomoyoshi Shimobaba,
Chiba University, Japan
Shuming Jiao,
Peng Cheng Laboratory, China

****Correspondence:***
Jae-Hyeung Park
jh.park@inha.ac.kr

Specialty section:
This article was submitted to Optical Information Processing and Holography, a section of the journal Frontiers in Photonics

Received: *27 April 2022*
Accepted: *26 May 2022*
Published: *20 June 2022*

Citation:
Askari M and Park J-H (2022) Augmentation of 3D Holographic Image Graticule With Conventional Microscopy. Front. Photonics 3:929936. doi: 10.3389/fphot.2022.929936

INTRODUCTION

Conventional optical microscopes have been around for many years and are extensively used in biological and medical science applications as well as in the electronics industry. An optical microscope has a simple optical geometry comprising an infinite-corrected objective lens and a tube lens to form a real, inverted, and magnified image of the sample at the back focal plane. This image is further magnified by an ocular lens or eyepiece responsible for presenting an upright magnified virtual image to the user's eye. Bright-field microscopy is one of the simplest optical microscopy in which a sample is illuminated, and the contrast is generated from the reflected light (McArthur, 1945; McArthur, 1958). For the measurement purpose of the sample on the microscopic stage, the optical microscopes are usually equipped with a reticle or graticule. A graticule is a two-dimensional (2D) disk that is present in an ocular lens to measure the lateral distances of samples on the microscope stage at the focal plane. Due to its 2D structure, it is not suitable for the depth estimation of a magnified sample on a longitudinal axis. Moreover, the 2D graticule needs to be calibrated whenever there is a need to change an objective lens. Usually, calibration can be done by adjusting the 2D graticule to lie side by side with a microscopic scale on the sample stage. From that, a conversion factor is calculated and used in the measurement of lateral distances of a magnified sample. In this paper, we propose implementing an augmentation of a three-dimensional (3D) holographic projection display with a conventional bright-field microscopic system for the lateral and longitudinal measurement of a magnified sample. With a conventional 2D graticule, only latitude measurements in a 2D plane are possible. Also, calibration has to be done with the micrometer scale on the stage sample. This needs to be done every time an objective lens has changed. A 2D graticule needs to be replaced with the appropriate one for different measurement purposes. With the proposed configuration, only complex field information needs to be synthesized without an actual replacement of a physical disk-shaped graticule. Also, longitudinal measurements are possible with the proposed method, which helps in the depth estimation or thickness measurement of an object sample. The proposed augmentation

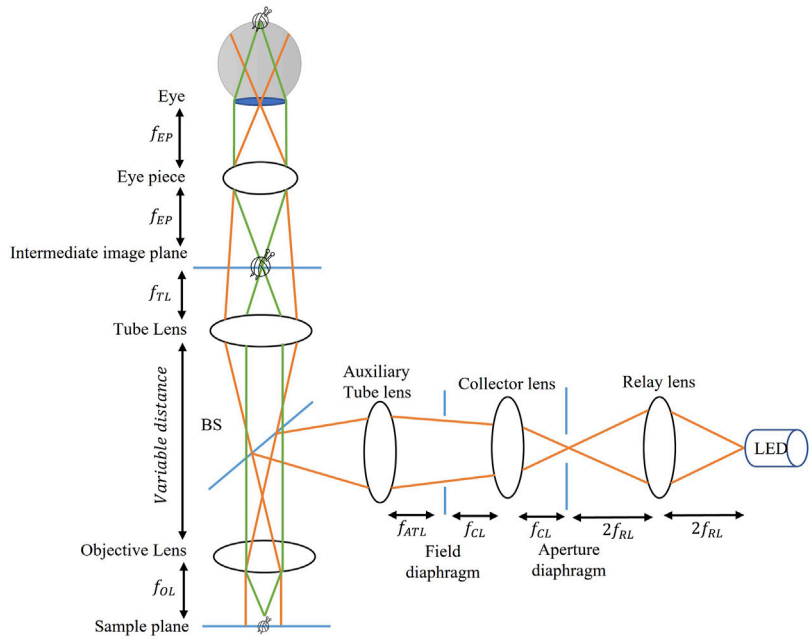

FIGURE 1 | Schematic of a reflected bright-field microscope.

of the 3D holographic projection graticule can be applied to other types of microscopy, e.g., reflected/transmitted brightfield or darkfield microscopic techniques.

For the generation of holographic contents in 3D displays and holographic projectors, computer generated hologram (CGH) plays a vital role. The 3D data of objects in CGH generation can be represented in various forms, such as point cloud (Lucente, 1933), light rays (Wakunami and Yamaguchi, 2011), depth layers (Zhao et al., 2015), and triangular meshes (Kim et al., 2008; Ji et al., 2016). The synthesized complex field is then encoded to either amplitude-only or phase-only CGH before being uploaded to the spatial light modulator (SLM) in the reconstruction process. A peculiar advantage of the CGH over 2D images is the conservation of depth information. Among various CGH techniques, the lensless holographic projection technique is attractive for its robustness and compact geometry, eliminating lens aberration and producing high contrast images (Buckley et al., 2011; Makowski et al., 2016a).

In this paper, we augment a 3D holographic graticule for the microscopic measurement of a magnified sample image around the intermediate image plane, i.e., the back focal plane of the tube lens. For the calculation of the complex field at the SLM plane, we consider a lensless holographic projection geometry that is capable of generating zoomable images with the use of the scaled and shifted Fresnel diffraction (Muffoletto et al., 2007; Shimobaba et al., 2012; Shimobaba et al., 2013; Zhang et al., 2019) algorithm. The scaled and shifted Fresnel diffraction is a fast Fourier transform (FFT) based diffraction calculation considering different sampling rates in the SLM and target image plane. We calculate a 2D holographic image graticule with a large depth of focus (DOF) for the lateral measurement by applying a slowly varying spherical phase distribution to the target image plane (Makowski et al., 2016b). We compute a 3D holographic layer-based graticule around an intermediate image plane for the longitudinal measurement, with each layer having a shallow DOF. Taking advantage of the capacity of superposition of the hologram, we can combine the two complex amplitude distributions before final encoding to a phase-only CGH at the reconstruction step. In the following sections, the principle and configuration of the proposed system is explained. The numerical simulation and optical experiment results are also presented for verification.

BRIEF INTRODUCTION TO REFLECTED BRIGHT-FIELD MICROSCOPY

Reflected bright-field microscopy is frequently used in industrial applications, especially in the semiconductor area with a metallic sample, integrated circuits, or surface of ceramics. Bright-field or dark-field illumination technique represents dark and bright images against bright and dark backgrounds, respectively (McArthur, 1945; McArthur, 1958). Each illumination technique has its merits and demerits depending on the observed sample. Our experiment considered the bright-field reflected-light microscopy with Kohler's illumination to eliminate incoherent light-emitting-diode (LED) source image in the intermediate image plane. **Figure 1** shows the schematic of a bright-field reflected-light microscope with light ray representation. Orange rays show

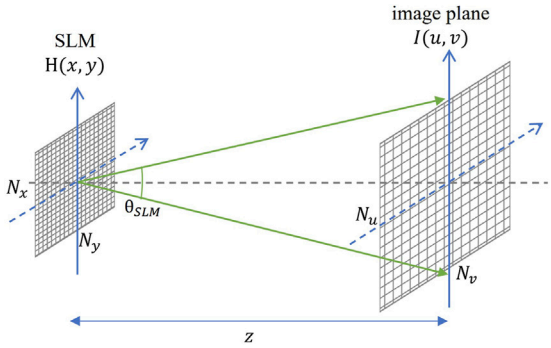

FIGURE 2 | Lensless holographic projection geometry.

the focus plane of the light source image, and green rays show the focus plane of the magnified sample image. The magnified sample image is focused in the intermediate image plane or user's retina, and the source image is highly defocused for better visual acuity. The sample object is placed in the front focal plane of an infinity-corrected objective lens to sharply focus the magnified image in the intermediate image plane with a designed tube lens. The objective lens has two functions: it acts as a condenser lens to focus light on the object sample and to form an image by collecting the reflected light. The parallel green rays from the objective lens to the tube lens constitute a variable distance and can be used to add optical components to the system, such as optical filters and beam splitters. The aperture diaphragm changes the illumination cone to project into the objective lens, which controls the contrast of the sample image. The field diaphragm controls the width of the bundle of light rays reaching the condenser or the objective lens in this reflected microscope case. The overall magnification of the system is calculated by multiplying the objective magnification with the ocular or eyepiece magnification. If a CCD sensor is used to capture the real magnified, inverted sample image in the intermediate image plane, the only magnification to be considered is that of the objective lens. The objective lens has different lateral and longitudinal magnifications like other optical imaging systems. Lateral magnification is defined as the ratio of image height to the object height and is given by the lens manufacturer as "×5", "×10" means the lens magnifies the object to look five or ten times larger than the actual size. The longitudinal magnification is defined as the square of lateral magnification along an optical axis. So, with a ×10 objective lens, the longitudinal magnification for an object sample would be ×100.

CALCULATION OF A COMPLEX HOLOGRAM

For the generation of complex amplitude distribution at the SLM plane, we consider the lensless holographic projection technique, as shown in **Figure 2**. It has a compact geometry with a single SLM and a projection screen at a propagation distance z. Note that the intermediate image plane in **Figure 1** and the image plane in **Figure 2** are overlapping image planes for a magnified sample image and a holographic image, respectively. They are given different names to avoid misunderstanding while discussing their optical geometries individually. At the reconstruction image plane, $I(u, v)$, the optical field is given by the 2D Fresnel diffraction (Goodman, 2005) formula as

$$I(u,v) = \frac{exp(jkz)}{j\lambda z}\iint_{-\infty}^{\infty} H(x,y)\, exp\left[j\frac{k}{\lambda z}\left\{(u-x)^2 + (v-y)^2\right\}\right] dxdy \quad (1)$$

which can be expressed in terms of 2D Fourier transform upon simplification as

$$I(u,v) = \frac{exp(jkz)}{j\lambda z} exp\left[j\frac{k}{2z}(u^2+v^2)\right]\iint_{-\infty}^{\infty} H(x,y)\, exp\left[j\frac{k}{\lambda z}(x^2+y^2)\right] exp\left[-j\frac{k}{z}(ux+vy)\right] dxdy \quad (2)$$

$$I(u,v) = \frac{exp(jkz)}{j\lambda z} exp\left[j\frac{k}{2z}(u^2+v^2)\right] F\left\{H(x,y)\, exp\left[j\frac{k}{\lambda z}(x^2+y^2)\right]\right\} \quad (3)$$

where $H(x, y)$ represents the hologram at the SLM plane. λ is the wavelength, k is the wave number, $k = 2\pi/\lambda$. F denotes the Fourier transform with spatial frequencies given as $f_x = u/\lambda z$ and $f_y = v/\lambda z$. According to the sampling rule of discrete Fourier transform, there is a relation between sampling intervals of source and reconstruction plane given as

$$\Delta_u = \frac{\lambda z}{N_x \Delta_x}\ ,\ \Delta_v = \frac{\lambda z}{N_y \Delta_y} \quad (4)$$

where we can see that the sampling intervals Δ_u and Δ_v at an image plane is inversely proportional to the sampling intervals Δ_x and Δ_y at the SLM plane. N_x and N_y are the sampling numbers in the source plane. For $\Delta_x = \Delta_y = \Delta_{SLM}$, $\Delta_u = \Delta_v = \Delta_I$, and N_h and N_I as total number of pixels in a hologram and the reconstructed image plane, the size of a hologram, L_h and the reconstructed image, L_I can be expressed as $L_h = N_h \times \Delta_{SLM}$ and $L_I = N_I \times \Delta_I$ respectively.

We focus on complex field information that produces graticule images at the image plane of different shapes and sizes for different measurement requirements like sample alignment, size or shape comparison, or area counting of a specimen. However, the sampling intervals here are constrained by Nyquist theory. To counter this limitation, we have two most common approaches. The first method increases the number of pixels while keeping the sampling pitch as defined in **Eq. 4**. However, the computation cost will increase in terms of time and memory. Nevertheless, we can use **Eq. 1** for sampling limitation, but again it is not computationally efficient as it does not use FFT. Second, we can consider variable sampling intervals at the SLM and the reconstructed image plane by keeping the number of pixels, N same in both planes. For this purpose, we use the scaled and shifted Fresnel diffraction algorithm, which computes the scaled Fourier transform by imposing a convolution theorem to

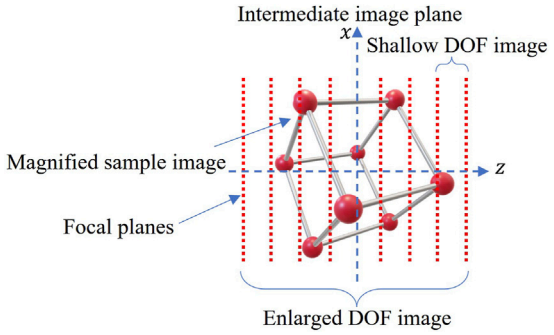

FIGURE 3 | Illustration of enlarged and shallow DOF around intermediate image plane.

the discrete 2D Fresnel diffraction algorithm as well as the off-axis image reproduction scheme by offsetting the target image plane from the optical axis to separate it from the DC term. The complex field is expressed as

$$\boldsymbol{I}(\boldsymbol{u}', \boldsymbol{v}') = \boldsymbol{C}_z \,.*\, \boldsymbol{F}^{-1}\{\boldsymbol{F}[\boldsymbol{a}(\boldsymbol{x}', \boldsymbol{y}')]\boldsymbol{F}[\boldsymbol{b}(\boldsymbol{x}', \boldsymbol{y}')]\} \tag{5}$$

where the details for $\boldsymbol{C}_z$, $\boldsymbol{a}$, and $\boldsymbol{b}$ are given in (Zhang et al., 2019). Here, $\boldsymbol{x}' = \boldsymbol{x}_0 + \boldsymbol{x}\boldsymbol{\Delta}_{SLM}$, $\boldsymbol{y}' = \boldsymbol{y}_0 + \boldsymbol{y}\boldsymbol{\Delta}_{SLM}$, $\boldsymbol{u}' = \boldsymbol{u}_0 + \boldsymbol{u}\boldsymbol{\Delta}_I$, and $\boldsymbol{v}' = \boldsymbol{v}_0 + \boldsymbol{v}\boldsymbol{\Delta}_I$ to represent the offset parameters $\boldsymbol{x}_0$, $\boldsymbol{y}_0$, $\boldsymbol{u}_0$, and $\boldsymbol{v}_0$ in offsetting the holographic image from the optical axis to separate the DC and conjugate terms from the target image. The algorithm is fast, keeping the same number of pixels, and involves three FFTs. Unfortunately, aliasing error may occur when propagating to a short distance. This is due to the diffraction angle, θ_{SLM} limited by the pixel pitch of the SLM expressed as

$$\boldsymbol{\theta}_{SLM} = \boldsymbol{sin}^{-1}\left(\frac{\boldsymbol{\lambda}}{\boldsymbol{\Delta}_{SLM}}\right) \approx \frac{\boldsymbol{\lambda}}{\boldsymbol{\Delta}_{SLM}} \tag{6}$$

The projected image size is limited by

$$\boldsymbol{L}_{I\_max} = \boldsymbol{N}_I\boldsymbol{\Delta}_I \leq \frac{\boldsymbol{\lambda z}}{\boldsymbol{\Delta}_{SLM}} \tag{7}$$

where the relation shows the image size is proportional to propagation distance and inversely proportional to the pixel pitch of SLM. To avoid an aliasing error by keeping the projected image size unchanged, the shorter propagation distance requires a much smaller sampling pitch, which is usually constrained by the pixel pitch of the physical SLM used in the experiment.

3D Layer-Based Hologram With Varying DOF

We need to reconstruct a holographic graticule to measure the sample on the microscope stage in a lateral and longitudinal direction. Lateral measurement is done in any planar dimension for the sample at the microscopic stage. It requires an enlarged DOF due to the sweeping of focal planes across the magnified sample image. On the other hand, longitudinal measurement requires a shallow DOF to axially evaluate the thickness and depth estimation of the magnified sample image.

The minimum angular spectrum range can be used to have enlarged or extended DOF. This can be done by multiplying the target image with a slowly varying spherical converging phase as in the random-phase-free method (Makowski et al., 2016a). In this way, the low-frequency information of a larger image can be spread to the hologram of a smaller size. The DOF is extended as each point in the image is formed by the limited circular effective aperture of the calculated hologram. The holographic image remains in focus in all focal planes, as illustrated in **Figure 3**.

To have a shallow DOF, we can generate a hologram at a maximum angular spectrum range limited by the pixel pitch of the SLM. This can be done by multiplying a target image with the random phase distribution. We calculate the 3D hologram in a layer-based manner with 2D images reconstructed at different focal planes across the intermediate image plane with shallow DOF. The distance between layers is fixed to evaluate sample thickness while sweeping through different focal planes. Each layer has its sampling intervals defined based on the distance from the hologram plane in the scaled and shifted Fresnel diffraction algorithm. Finally, we follow the algorithm discussed in the previous section to obtain corresponding holograms for the extended and shallow DOF. The obtained two holograms are added together to form the final hologram which is then encoded to the phase hologram before being uploaded to the SLM. Other methods such as Gerchberg-Saxton (GS) algorithm (Chang et al., 2015) or error diffusion method (Jiao et al., 2020) can be applied to the accumulated complex field for the optimization of phase-only hologram.

Aliasing Condition

To avoid aliasing error in the lensless optical configuration under consideration, the convergent angle of the spherical phase in calculating an enlarged DOF should not exceed the diffraction angle limit of the SLM. The focal length, $\boldsymbol{f}$ of the spherical phase can be set for the propagation distance, $\boldsymbol{z}$ considering the hologram size and image size as

$$\boldsymbol{f} = \frac{\boldsymbol{z}}{1 - \frac{\boldsymbol{L}_h}{\boldsymbol{L}_I}} \tag{8}$$

where $\boldsymbol{f}$ is proportional to the propagation distance, z, and inversely proportional to the hologram size at the SLM plane.

In **Figure 4**, the blue line shows the maximum diffraction angle limited by the given SLM, and the red line shows the angle of a convergent spherical phase. **Figure 4A** shows the geometry model where the hologram fits perfectly inside the converging spherical phase with $\phi = \boldsymbol{\theta}_{SLM}$. **Figure 4B** shows the geometry model in which $\phi < \boldsymbol{\theta}_{SLM}$. Although some part of the SLM area is used, the image can be reconstructed without aliasing. **Figure 4C** shows the case for aliasing where $\phi > \boldsymbol{\theta}_{SLM}$, the information from the image reaching the SLM exceeds its total area. However, the image will still be reconstructed with aliasing noise due to the feature of the Fresnel diffraction algorithm. The bottom row of

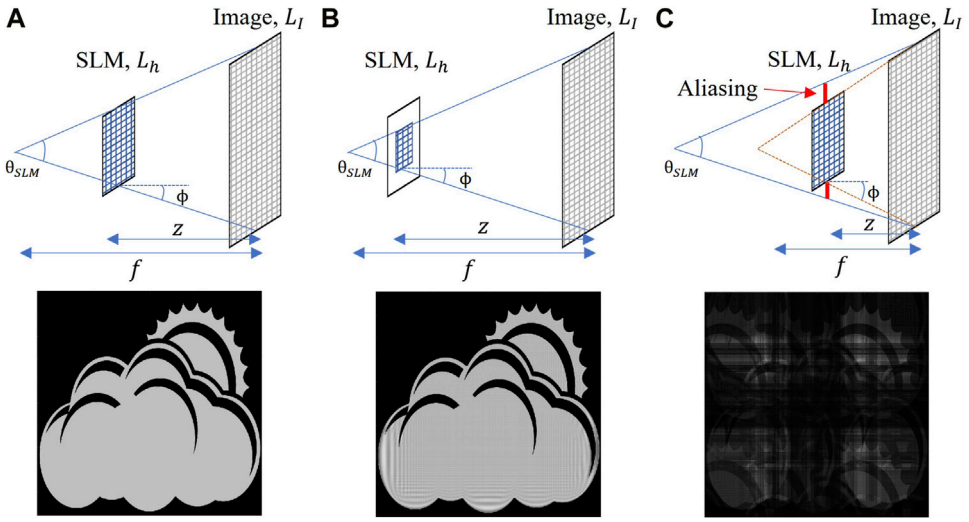

FIGURE 4 | Aliasing condition for implemented holographic projection geometry. **(A)** Geometric projection model when $\phi = \theta_{SLM}$ (no aliasing). **(B)** Geometric projection model when $\phi < \theta_{SLM}$ (no aliasing). **(C)** Geometric projection model when $\phi > \theta_{SLM}$ (aliasing occurs).

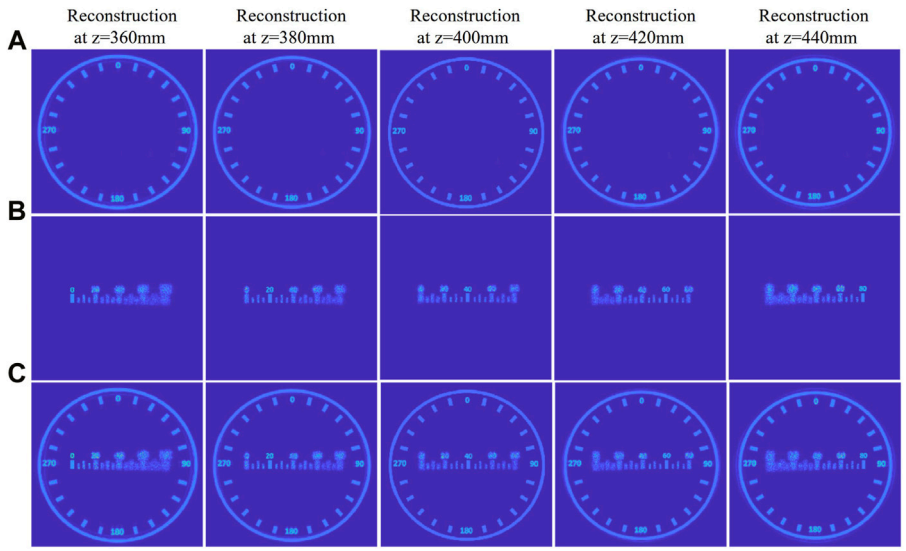

FIGURE 5 | Numerical simulated results. **(A)** Reconstruction results at different planes show enlarged DOF. **(B)** Reconstruction results at different planes show shallow DOF. **(C)** The reconstruction results of the combined hologram at different planes simultaneously showed enlarged and shallow DOF.

Figure 4 shows the numerically reconstructed result to demonstrate the aliasing effect.

NUMERICAL SIMULATION

In the numerical simulation, a holographic content is generated and centered around an intermediate image plane at the desired propagation distance, z. Two holograms are calculated for the extended and shallow DOF, respectively. The hologram with the extended DOF remains in focus over a large depth range with a slowly varying spherical phase distribution. On the other hand, the hologram with the shallow DOF is calculated in a layer-based fashion with layers having a random phase distribution and are separated by a particular distance. These two holograms are then accumulated in a single hologram for the numerical simulation results in **Figure 5**.

The pixel resolution of the computation window used in the simulation is identical for the hologram and the target image plane, which is $N \times N = 2160 \times 2160$ pixels. The sampling rate on the hologram plane is 3.6 um (which gives the size of the hologram, L_h to be about 7.7 mm × 7.7 mm). The propagation

TABLE 1 | Image quality measurement using PSNR and SSIM.

Quality metric	T_1	T_2	T_3	T_4	T_5
PSNR (dB)	28.29	31.59	35.38	31.01	28.05
SSIM	0.966	0.988	0.990	0.980	0.962

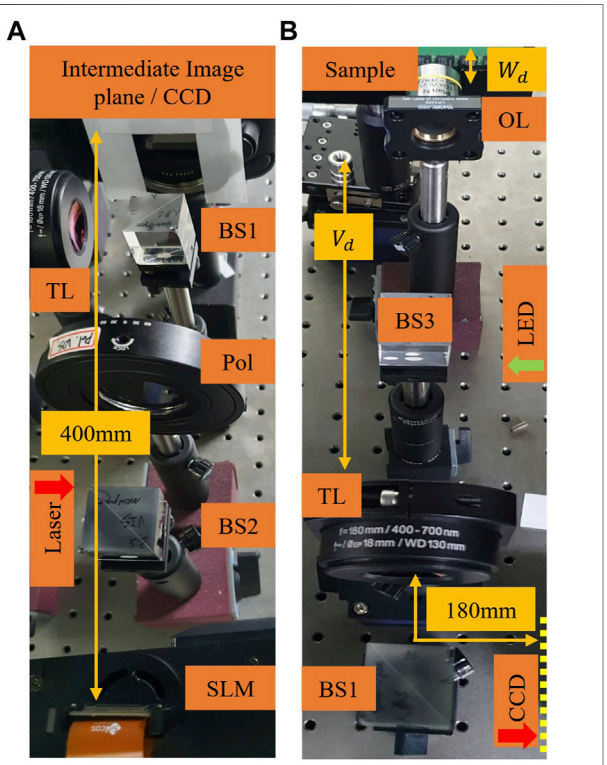

FIGURE 6 | Optical experimental setup. **(A)** Lensless holographic configuration. **(B)** Reflected bright-field optical microscopic configuration.

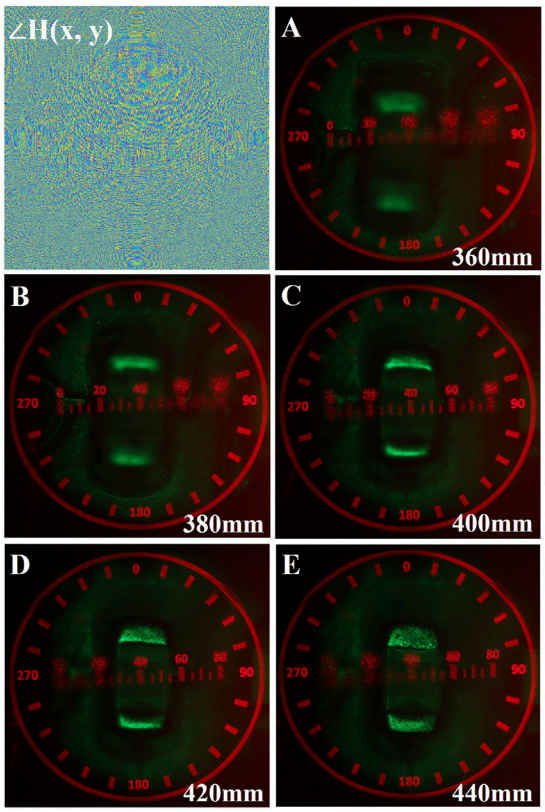

FIGURE 7 | Optical experimental results. Top-left image shows the phase part of the accumulated hologram synthesized using the proposed method. **(A–E)** Different parts of the magnified sample image focus on the holographic image content at 360 mm, 380 mm, 400 mm, 420 mm, and 440 mm, respectively.

distance, z is 400 mm. The sampling rate of the reconstructed image at an intermediate image plane is about 32um. The wavelength of light is 633 nm.

Figure 5A shows the reconstructed results for a hologram synthesized with enlarged DOF at different focal planes. The image can be seen as a sample alignment graticule, each division with an angular separation of 15 degrees. We can see that the image is reconstructed with enlarged DOF. **Figure 5B** shows the results for a layer-based hologram synthesized for having a shallow DOF. Here, we have five 2D layers with numbers showing 0, 20, 40, 60, and 80 centered around an intermediate image plane spanning 80 mm longitudinal depth with the separation of 20 mm between each layer. Depending on the maximum angular range defined by the SLM, the separation between each layer can be increased or decreased, making the final reconstructed image show reasonable blur among different layers. The reconstructed scene here can be used for the depth estimation of a magnified sample image at the microscopic stage. As the reconstruction depth increases from left to right, different numbers in layers come into focus at a particular distance. **Figure 5C** shows the reconstructed results for an accumulated hologram at different reconstruction planes.

For the quantitative evaluation of the reconstructed holographic images at different planes for the enlarged DOF, we used two metrics: peak-signal-to-noise ratio (PSNR) and structural similarity index (SSIM). **Table 1** shows the results. T_1, T_2, T_3, T_4 and T_5 represents the reconstructed image results in **Figure 5A** (top row) respectively. It can be seen from **Table 1** that the highest quality is at the intermediate image plane (z = 400 mm), and the quality degrades slowly while sweeping across the intermediate image plane.

EXPERIMENTAL RESULTS

Figure 6 shows the experimental optical setup for the lensless holographic and reflected bright-field microscopic configurations. In **Figure 6A**, the hologram is loaded to a spatial light modulator (SLM) after the phase encoding. We shifted the target image to separate it from the DC and conjugate term at the reconstruction plane. The reconstructions are captured around the intermediate image plane or CCD at a

distance of 400 mm from the SLM plane. The wavelength of the laser light source used in the experiment is 633 nm. The reflection-type phase modulating SLM (model name: IRIS-U62) from MAY DISPLAY is used in the experiment that has the specifications of 3.6 um pixel pitch and 3840 × 2160 resolution. A hologram with enlarged DOF is synthesized with a slowly varying converging spherical phase, and a layer-based hologram with a shallow DOF is synthesized with a random phase distribution in each layer. Holograms are synthesized for the same pixel resolution of 2160 × 2160 as used in the numerical simulation. Finally, the two holograms are accumulated. In the encoding process, for the phase modulating SLM, the phase part of the final hologram was extracted and loaded to the SLM.

In **Figure 6B**, we used an infinity-corrected plan achromatic objective lens (OL) of design magnification of ×10 at the working distance, W_d of 1.2 mm from a sample stage. A tube lens (TL) of the effective focal length of 180 mm is used, designed for the infinity-corrected objective lens used in the experiment. The tube lens focuses the magnified sample image on the intermediate image plane. With such an arrangement of using an infinity-corrected objective lens and the tube lens, we obtain the variable distance, V_d that is useful in positioning additional optical components. We used a M530L3 LED from Thorlabs as an incoherent light source with a wavelength centered around 530 nm. We used Kohler's illumination technique to eliminate the source image at the CCD plane.

Figure 7 shows the optical experimental results. The phase part of the accumulated hologram, $H(x, y)$, used in the reconstruction process is shown in the top-left image. **Figures 7A–E** shows the reconstructed image results at various distances, i.e., 360–440 mm, with 20 mm separation from the SLM plane.

In **Figure 7A**, no part of the magnified sample image comes in focus with the holographic image number "0" (at 360 mm). At the distance of 380 mm in **Figure 7B**, the bottom part of the magnified sample focuses on the holographic image number "20". By moving the CCD plane on the longitudinal axis further away from the SLM plane, different parts of the magnified sample image come into focus with the contents of holographic images. At the distance of 440 mm in **Figure 7E**, the top part of the sample focuses on the holographic image showing the number "80". From this, we can analyze that the approximate thickness of the magnified sample is around 60 mm, from when the bottom part comes in focus at 380 mm up to the top part at 440 mm. As the longitudinal magnification of the magnified sample image is square of the lateral's magnification, which is ×10 in our case, the magnified sample image has a longitudinal magnification of 100 times. From this, the total thickness of the sample approximates about 60 mm/100 (0.60 mm). The object sample we used is the multilayer ceramic capacitor from Samsung Electro-Mechanics (SEMCO) with the product code (CL05) having a thickness of 0.60 ± 0.10 mm, which is in good agreement with the experimental result. The error in the longitudinal measurement from the holographic graticule comes from the total number of 2D layers used in the hologram synthesis. As the layers are separated by 20 mm each, the maximum error in the longitudinal measurement of the object sample could be around ± 20 mm. By increasing the number of layers used in the layer-based hologram synthesis, we can minimize the error but at the cost of higher computation. The outer circular part of the holographic image shows the 360-degree alignment graticule with a 15-degree angular separation between each bar. We can see that it remains in focus at all reconstruction depths showing enlarged DOF.

CONCLUDING REMARKS

We proposed an augmentation of a 3D holographic content with the microscopic image to have an application of measurement graticule for a microscopic sample in lateral and longitudinal directions. This is done by combining two holograms synthesized for having an enlarged and shallow DOF. The optical geometry we used is the lensless holographic projection for its compactness and production of high contrast images. It is also easy to augment such a system with the conventional optical microscope as it requires no additional lenses between SLM and the projection screen to avoid lens aberrations. We have discussed aliasing conditions for considered projection geometry to avoid discrepancies with high-order diffracted results. Finally, we combined the two holograms and presented the numerical and experimental results to verify the proposed augmentation of the two systems.

DATA AVAILABILITY STATEMENT

The raw data supporting the conclusions of this article will be made available by the authors, without undue reservation.

AUTHOR CONTRIBUTIONS

MA conceived the idea, conducted the experiments, and wrote the manuscript. J-HP reviewed the experimental results and supervised this project. The manuscript has been revised and corrected by all authors.

FUNDING

This research was supported by the National Research Foundation of Korea (NRF) grant funded by the Korea Government (MSIT) (2022R1A2C2013455).

REFERENCES

Buckley, E. (2011). Holographic Laser Projection. *J. Disp. Technol.* 7 (3), 135–140. doi:10.1109/jdt.2010.2048302

Chang, C., Xia, J., Yang, L., Lei, W., Yang, Z., and Chen, J. (2015). Speckle-Suppressed Phase-Only Holographic Three-Dimensional Display Based on Double-Constraint Gerchberg-Saxton Algorithm. *Appl. Opt.* 54 (23), 6994–7001. doi:10.1364/ao.54.006994

Goodman, J. W. (2005). *Introduction to Fourier Optics*. Englewood, Colorado: Roberts and Co. Publishers.

Ji, Y.-M., Yeom, H., and Park, J.-H. (2016). Efficient Texture Mapping by Adaptive Mesh Division in Mesh-Based Computer Generated Hologram. *Opt. Express* 24 (24), 28154–28169. doi:10.1364/oe.24.028154

Jiao, S., Zhang, D., Zhang, C., Gao, Y., Lei, T., and Yuan, X. (2020). Complex-amplitude Holographic Projection with a Digital Micromirror Device (DMD) and Error Diffusion Algorithm. *IEEE J. Sel. Top. Quantum Electron.* 26 (5), 2800108. doi:10.1109/jstqe.2020.2996657

Kim, H., Hahn, J., and Lee, B. (2008). Mathematical Modeling of Triangle-Mesh-Modeled Three-Dimensional Surface Objects for Digital Holography. *Appl. Opt.* 47 (19), D117–D127. doi:10.1364/ao.47.00d117

Lucente, M. E. (1993). Interactive Computation of Holograms Using a Look-Up Table. *J. Electron. Imaging* 2 (1), 28–34. doi:10.1117/12.133376

Makowski, M., Ducin, I., Kakarenko, K., Suszek, J., and Kowalczyk, A. (2016a). Performance of the 4k Phase-Only Spatial Light Modulator in Image Projection by Computer-Generated Holography. *Photonics Lett. Pol.* 8 (1), 26–28. doi:10.4302/plp.2016.1.10

Makowski, M., Shimobaba, T, and Tomoyoshi, I. (2016b). Increased Depth of Focus in Random-phase-free Holographic Projection. *Chinese Optics Letters* 14 (12), 120901–120905. doi:10.3788/col201614.120901

McArthur, J. (1945). Advances in the Design of the Inverted Prismatic Microscope. *J. R. Microsc. Soc.* 65 (1-4), 8–16. doi:10.1111/j.1365-2818.1945.tb00927.x

McArthur, J. (1958). A New Concept in Microscope Design for Tropical Medicine. *Am. J. Trop. Med. Hyg.* 7 (4), 382–385. doi:10.4269/ajtmh.1958.7.382

Muffoletto, R. P., Tyler, J. M., and Tohline, J. E. (2007). Shifted Fresnel Diffraction for Computational Holography. *Opt. Express* 15 (9), 5631–5640. doi:10.1364/oe.15.005631

Shimobaba, T., Kakue, T., Masuda, N., and Ito, T. (2012). Numerical Investigation of Zoomable Holographic Projection without a Zoom Lens. *Jnl Soc. Info Disp.* 20 (9), 533–538. doi:10.1002/jsid.116

Shimobaba, T., Makowski, M., Kakue, T., Oikawa, M., Okada, N., Endo, Y., et al. (2013). Lensless Zoomable Holographic Projection Using Scaled Fresnel Diffraction. *Opt. Express* 21 (21), 25285–25290. doi:10.1364/oe.21.025285

Wakunami, K., and Yamaguchi, M. (2011). Calculation for Computer Generated Hologram Using Ray-Sampling Plane. *Opt. Express* 19 (10), 9086–9101. doi:10.1364/oe.19.009086

Zhang, H., Cao, L., and Jin, G. (2019). Scaling of Three-Dimensional Computer-Generated Holograms with Layer-Based Shifted Fresnel Diffraction. *Appl. Sci.* 9 (10), 2118. doi:10.3390/app9102118

Zhao, Y., Cao, L., Zhang, H., Kong, D., and Jin, G. (2015). Accurate Calculation of Computer-Generated Holograms Using Angular-Spectrum Layer-Oriented Method. *Opt. Express* 23 (20), 25440–25449. doi:10.1364/oe.23.025440

Conflict of Interest: The authors declare that the research was conducted in the absence of any commercial or financial relationships that could be construed as a potential conflict of interest.

frontiers | Frontiers in Photonics

ORIGINAL RESEARCH
published: 21 June 2022
doi: 10.3389/fphot.2022.929031

Multi-View Acoustic Field Imaging With Digital Color Holography

Saoucene Hassad[1,2,3], *Kouider Ferria*[2], *Larbi Bouamama*[2] *and Pascal Picart*[1,3]*

[1]*Laboratoire d'Acoustique de l'Université du Mans (LAUM), UMR 6613, Institut d'Acoustique-Graduate School (IA-GS), CNRS, Le Mans Université, Le Mans, France,* [2]*Laboratoire d'Optique Appliquée, IOMP, Université Ferhat Abbas, Setif, Algeria,* [3]*ENSIM, École Nationale Supérieure d'Ingénieurs du Mans, Le Mans, France*

This paper proposes an approach for acoustic field imaging using simultaneous multi-view digital holography based on three-color digital off-axis holography. Considering spatio-chromatic multiplexing and the recording with a monochrome sensor, the numerical processing of time-sequences of holograms yields both the amplitude and phase of the acoustic field along three different directions of observation. Distortion analysis is presented and the acousto-optic interaction along the optical beam is discussed using a theoretical modelling. Experimental results with an emitter at 40 kHz establish the proof-of-concept of the proposed multi-view imaging for acoustic fields.

Keywords: holography, digital holography, color holography, spatial multiplexing, acoustic field imaging, multi-view imaging

Edited by:
Pietro Ferraro,
National Research Council (CNR), Italy

Reviewed by:
Lei Liu,
Harbin Engineering University, China
Hongyi Bai,
Heilongjiang University, China

***Correspondence:**
Pascal Picart
pascal.picart@univ-lemans.fr

Specialty section:
This article was submitted to Optical Information Processing and Holography, a section of the journal Frontiers in Photonics

Received: *26 April 2022*
Accepted: *12 May 2022*
Published: *21 June 2022*

Citation:
Hassad S, Ferria K, Bouamama L and Picart P (2022) Multi-View Acoustic Field Imaging With Digital Color Holography. Front. Photonics 3:929031. doi: 10.3389/fphot.2022.929031

1 INTRODUCTION

The characterization and control of waves in acoustics, and more generally in wave physics, is of great interest because resulting technological innovations may impact several domains: environmental and energy transition (frugal engineering, lightening of structures, energy recovery, bio-sourced materials), health sector (medical imaging, remote consultation, diagnostic assistance), and industrial sector in the broadest sense (transportation, audio, musical instrument making, agriculture, electronics, and telecommunications). The characterization requires to develop new approaches to provide qualitative and quantitative insight of the acoustic fields of interest. Generally, imaging acoustic fields is performed by using microphone arrays (Flanagan et al., 1985; Hafizovic et al., 2012; Groschup and Grosse, 2015). Unfortunately, these methods intrinsically have several problems. Especially, microphone arrays have a low spatial resolution because the pitch of the microphones of the array is several millimeters (or more), and the presence of microphones may affect the acoustic field to be investigated.

In order to overcomes these limitations, optical techniques for measuring the acoustic field have been reported, for example, imaging with schlieren (Hargather et al., 2010), laser Doppler velocimetry (LDV) (Frank and Schell, 2005; Malkin et al., 2014), acousto-optic tomography (AOT) (Torras-Rosell et al., 2012), or laser feedback interferometry (LFI) (Bertling et al., 2014; Ortiz et al., 2018). Although schlieren simultaneously yields a collection of data points, its sensitivity to the air fluctuation due to acoustic wave is overall reduced because the approach is not directly sensitive to the refraction index of the medium. LDV, AOT and LFI are intrinsically sensitive to the refractive index of the medium in which the acoustic waves do propagate, but they require scanning to get a collection of data points. That makes these approaches less attractive than alternatives able to directly provide full-field data. Indeed, data acquisition and processing may be a critical issue for high-speed applications. Digital holography is a potential approach that can quantitatively measure the three-dimensional distribution of the refractive index of any transparent specimen or medium. This method takes a particular place because it records and retrieves the phase of the optical waves

interacting with the medium (Schnars and Jüptner, 1994; Picart, 2015). Since the optical phase is closely related to the optical path difference, it includes the variation in the refractive index experienced by the light beam having crossed the acoustic field. Recent works reported the use of phase shifting digital holography (Yamaguchi and Zhang, 1997; Yamaguchi et al., 2002) to investigate acoustic waves (Matoba et al., 2014; Ishikawa et al., 2016; Ishikawa et al., 2018; Rajput et al., 2018; Ruiz et al., 2019; Takase et al., 2021; Hashimoto et al., 2022). Using off-axis digital holography (Picart, 2015), other authors reported the quantitative investigation of the acoustic field in acoustic wave guides (Penelet et al., 2016; Gong et al., 2018). However, acoustic wave guides are a particular case and the case of free space acoustic fields has to be investigated.

In this paper, we aim at demonstrating the proof-of-concept of simultaneous full-field and multi-view imaging of acoustic field in the free space using digital color holography and a single monochromatic high-speed sensor. The simultaneous acquisition of the necessary set of data is thus realized "single shot" and then numerical process yields images of both the amplitude and phase of the acoustic field along three different directions of observation. This has for advantage of permitting consistent and rapid data acquisition. The paper is organized as follows. **Section 2** presents the theoretical basics of digital holography and spatio-chromatic multiplexing of holograms, **Section 3** presents the amplitude and phase retrieval of the acoustic field along each view and discusses on the distortion in the measurement and **Section 5** discusses on the experimental results obtained with the proposed method. Finally, **Section 6** draws conclusions about the study.

2 THEORETICAL BASICS

2.1 Off-Axis Hologram Recording and Reconstruction

In this paper, one considers off-axis digital holograms. This approach is the most adapted to dynamic events, especially to the investigation of acoustic fields which are time-varying. Recording a single hologram per time instant is powerful for carrying out high-speed data acquisition. At the sensor plane, the reference wave $\mathcal{R}$ is mixed with the wave $\mathcal{O}$ from the probed area to produce the digital hologram, expressed as,

$$\mathcal{H} = |\mathcal{R}|^2 + |\mathcal{O}|^2 + \mathcal{R}^*\mathcal{O} + \mathcal{R}\mathcal{O}^*. \tag{1}$$

Note that term $\mathcal{R}^*\mathcal{O}$ refers to the +1 order of the hologram, and is considered in this paper. In the off-axis arrangement, the reference wave impacts the image sensor with an angle. Thus, the reference wave can be written as follows (a_λ is considered as constant and (u_λ, v_λ) denotes spatial frequencies, at wavelength λ):

$$\mathcal{R}(x, y) = a_\lambda \exp\left(2i\pi\left(u_\lambda x + v_\lambda y\right)\right). \tag{2}$$

The recovery of the complex-valued amplitude of the image of the object is obtained by filtering the +1 order in the Fourier spectrum of the hologram. Filtering can be written as follows to yield the recovered complex image (*FT* means Fourier transform):

$$A_r = a_r \exp\left(i\varphi_r\right) = \mathcal{R}^*\mathcal{O} \simeq \mathrm{FT}^{-1}\left[\mathrm{FT}\left[\mathcal{H}\right] \times G\right]. \tag{3}$$

Equation 3 is a convolution formula, and the transfer function G is given by the bandwidth-limited angular-spectrum transfer function in the Fresnel approximation:

$$G(u, v) = \begin{cases} \exp\left(-i\pi d_r \lambda\left((u - u_\lambda)^2 + (v - v_\lambda)^2\right)\right) \\ \text{if } |u - u_\lambda| \le \Delta u_\lambda/2 \text{ and } |v - v_\lambda| \le \Delta v_\lambda/2 \\ 0 \quad \text{if not.} \end{cases} \tag{4}$$

In **Equation 4**, (Δu_λ, Δv_λ) are the cut-off spatial frequencies for wavelength λ, and d_r is the refocus distance between the sensor and the area of interest. The spatial bandwidth of the filtering must be adapted to the extension of the +1 order to be filtered, and not too large in order to avoid over-sensitivity to noise. In (Gong et al., 2021), the noise standard deviation of the phase φ_r was demonstrated to be depending on the spatial bandwidths according to **Eq. 5** (with the hypothesis of white noise),

$$\sigma_\varphi = \frac{2\sqrt{p_x p_y \Delta u_\lambda \Delta v_\lambda}}{m\alpha N_{sat}} \sqrt{\alpha N_{sat} + \sigma_{ro}^2 + \frac{N_{sat}^2}{12\left(2^{nb} - 1\right)^2}}, \tag{5}$$

where (p_x, p_y) are the pixel pitches of the sensor, m the modulation of the hologram, α the saturation rate of the hologram, N_{sat} is the maximum number of photo-electrons in the pixels, σ_{ro} is the read out noise and nb is the number of bits of the sensor. So, in order to minimize the noise in phase data, one has to increase m, α and to minimize (Δu_λ, Δv_λ). It follows that (Δu_λ, Δv_λ) have to be carefully chosen.

2.2 Multiplexed Three-Wavelength Digital Holography

Multi-view digital holography was discussed in literature and several architectures were proposed and demonstrated to be quite efficient for information encoding (Seo et al., 2007; Shaked et al., 2009; Shimobaba et al., 2010; Takaki, 2015; Ren et al., 2019). In this paper, we aim at considering multi-color digital holography. The use of three-wavelength digital holography has advantages compared to single-wavelength holography because it makes it possible to multiplex data from different sight views of the volume under interest. Having three laser beams at three different wavelengths generating three probe beams and three reference beams enable simultaneously recording the complex-valued data from three different sight-views in a single three-color hologram. The basic principle is depicted in **Figure 1A** with three laser beams propagating in the measurement volume along three different directions, and the probe beams being then combined with the three reference beams at the sensor plane. The reference waves have different incident angles in order to provide different spatial frequencies (u_λ, v_λ). **Figure 1B** illustrates the power spectrum density of the spatially-multiplexed three color hologram. Note that the simultaneous recording of three holograms at three different wavelengths has for consequence

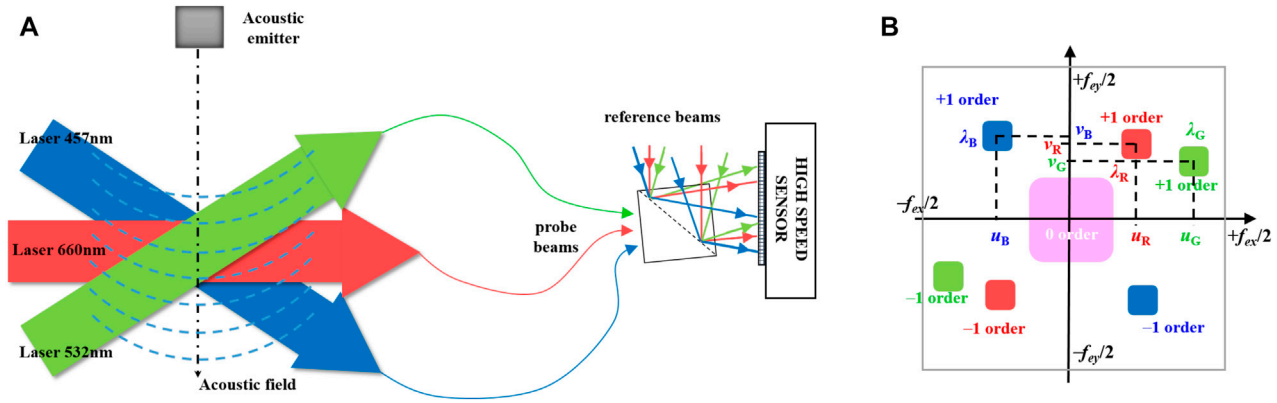

FIGURE 1 | (A) Basic scheme for probing the acoustic field along three different directions with off-axis three color holography, **(B)** spectral distribution of the multiplexed off-axis digital holograms in the Fourier domain with three wavelengths (f_{ex} and f_{ey} refer to the spatial sampling frequencies of the sensor, i.e., $f_{ex} = 1/p_x$ and $f_{ey} = 1/p_y$).

to increase the sensitivity to noise. Indeed, the total number of photo-electrons available for one single hologram is now divided by three, to be equal to $N_{sat}/3$. Considering **Eq. 5**, σ_φ is thus increased.

2.3 From Optical Phase to Acoustic Pressure

The laser beam crossing the acoustic field generated by any emitter (refer to **Figure 1B**) is perturbed by the acoustic pressure at any point in the propagation medium. The phase φ_r is related to the refractive index $n_O(s, t)$ along the light path s according to the integral relationship **Eq. 6**.

$$\varphi_r = \frac{2\pi}{\lambda}\int_L (n_O(s,t) - n_R)ds, \tag{6}$$

with n_R the reference refractive index along the reference optical path. So, the holographic measurement provides an average value of the refractive index along the interaction distance L. With help of the Gladstone-Dale relationship, the phase is related to the fluid density (Merzkirch, 2012). The density of the fluid at the pixels (x, y) of the image of the probed area is given by **Equation 7** according to:

$$\langle\rho\rangle(x,y,t) = \frac{2}{3\hat{r}}(\langle n_O\rangle(x,y,t) - n_R). \tag{7}$$

In **Equation 7**, $\hat{r} = 0.1505 \times 10^{-3}\text{kg}^{-1}.\text{m}^3$ is the specific refractivity of air measured at temperature 288 K and wavelength 660 nm (Merzkirch, 2012), which does not exhibits significant variation over the visible range of wavelengths. When air is submitted to the acoustic field, the air pressure fluctuates so that, holography measures, through the phase φ_r, the mean density $\langle\rho\rangle$ and the fluctuating component due to the propagation of the sound wave, $\langle\rho'\rangle$, included in the fluctuating part of phase, φ_r'. With the assumption of adiabatic process, the fluctuating part of the density is related to the pressure fluctuation, p', according to (c_0 is the sound velocity in air) (Pierce and Beyer, 1990):

$$p' = \langle\rho'\rangle c_0^2 = \frac{2}{3\hat{r}}\frac{\lambda c_0^2}{2\pi L}\varphi_r'. \tag{8}$$

Note that in **Equations 6**, **8**, L is the length of the line of sight. So, the value of L must be known in order to convert holographic phase data to acoustic pressure. In addition, in case where the acoustic field is not organized as plane waves, the effect of the interaction length with the laser beam is not straightforward to evaluate and requires minimum knowledge about the acoustic field.

3 ACOUSTIC AMPLITUDE AND PHASE RETRIEVAL

3.1 Digital Synchronous Estimation

The optical phase extracted from the reconstructed object field, at any instant t, is given by,

$$\psi(t) = \varphi_r + \varphi_r'(t) = \varphi_r + \varphi_{ac}\sin(\omega_{ac}t + \phi_{ac}), \tag{9}$$

where φ_{ac} is the phase due to the acoustic fluctuation, and according to **Eq. 8**, is equal to:

$$\varphi_{ac} = \frac{3\hat{r}}{2}\frac{2\pi L}{\lambda}\frac{p_{ac}}{c_0^2}, \tag{10}$$

with p_{ac} is the maximum acoustic pressure at pulsation ω_{ac} (period is $T_{ac} = 1/f_{ac}$, and f_{ac} the acoustic frequency) and ϕ_{ac} is the acoustic phase. Considering a time-sequence at sampling rate $f_s = 1/T_s$, including n_h digital holograms, the phase difference between two consecutive instants $t_{n+1} = (n + 1)T_s$ and $t_n = nT_s$ is thus,

$$\begin{aligned}\Delta\psi_n &= \psi(t_{n+1}) - \psi(t_n)\\ &= 2\varphi_{ac}\sin(\beta\pi)\cos(\phi_{ac})\cos((2n+1)\beta\pi)\\ &\quad - 2\varphi_{ac}\sin(\beta\pi)\sin(\phi_{ac})\sin((2n+1)\beta\pi).\end{aligned} \tag{11}$$

In **Equation 11**, $\beta = T_s/T_{ac}$. From **Equation 11**, both φ_{ac} and ϕ_{ac} can be retrieved by $L2$ norm minimization. **Equation 11** can be

approached with matrices. So, matrix $\boldsymbol{X}$ corresponds to known theoretical coefficients, vector $\boldsymbol{\Delta\psi}$ includes the measured phase differences and vector $\boldsymbol{y}$ includes the two unknown $(\varphi_{ac}, \phi_{ac})$ to be retrieved. We have $\boldsymbol{y} = [\, y_1 \;\; y_2 \,]^T$ (upper script T meaning transpose matrix), with $y_1 = 2\varphi_{ac}\sin(\beta\pi)\cos(\phi_{ac})$ and $y_2 = 2\varphi_{\mathrm{ac}}\sin(\beta\pi)\sin(\phi_{ac})$. From **Equation 11**, matrix $\boldsymbol{X}$ is explicated according to:

$$\boldsymbol{X} = \begin{pmatrix} \cos(\beta\pi) & -\sin(\beta\pi) \\ \cos(3\beta\pi) & -\sin(3\beta\pi) \\ \cos(5\beta\pi) & -\sin(5\beta\pi) \\ \cdots & \cdots \\ \cdots & \cdots \\ \cdots & \cdots \\ \cos((2n_h+1)\beta\pi) & -\sin((2n_h+1)\beta\pi) \end{pmatrix}. \tag{12}$$

The minimization of the $L2$ norm leads to the estimation of $\boldsymbol{y}$ using the cost function $\boldsymbol{J} = (\boldsymbol{\Delta\psi} - \boldsymbol{Xy})^T\boldsymbol{I}(\boldsymbol{\Delta\psi} - \boldsymbol{Xy})$. Minimizing according to the calculation of $\partial\boldsymbol{J}/\partial\boldsymbol{y}$ yields the optimal solution $\boldsymbol{y_{opt}} = (\boldsymbol{X}^T\boldsymbol{IX})^{-1}\boldsymbol{X}^T\boldsymbol{I\Delta\psi}$, with $\boldsymbol{I}$ being the identity matrix. Finally, one gets $\phi_{ac} = \tan^{-1}(y_2/y_1)$ and $\varphi_{ac} = \sqrt{(y_1^2 + y_2^2)}/2\sin(\beta\pi)$. So, from the optical phase extracted from the hologram sequence can be retrieved the amplitude-phase (φ_{ac}) due to the acoustic fluctuation and its oscillating phase (ϕ_{ac}). In the next sections, the method for acoustic amplitude and phase retrieval refers to *SoundRetrieval*.

3.2 Distortion in the Measurement

When recording the hologram sequence, the exposure time of the sensor has a major role in the accuracy of the retrieved amplitude and phase of the acoustic field. Indeed, the instantaneous hologram is time-integrated by the image sensor. Consider ΔT the exposure time, then the effectively recorded hologram is given by:

$$\mathcal{H}_{eff} = |\mathcal{R}|^2 + \int_{t_1}^{t_1+\Delta T} \left(|\mathcal{O}(t)|^2 + \mathcal{R}^*\mathcal{O}(t) + \mathcal{R}\mathcal{O}^*(t)\right)dt. \tag{13}$$

The temporal integration in **Equation 13** can be derived considering the acoustic fluctuation in **Equation 9**, so that we have:

$$\int_{t_1}^{t_1+\Delta T} \exp\left(i\varphi_{ac}\sin(\omega_{ac}t + \phi_{ac})\right)dt = \Delta T\sum_k J_k(\varphi_{ac})\mathrm{sinc}\left(k\omega_{ac}\frac{\Delta T}{2}\right)\exp\left(ik\left(\omega_{ac}t_1 + \phi_{ac} + \frac{\omega_{ac}\Delta T}{2}\right)\right). \tag{14}$$

Since the sinc function can be expanded as:

$$\mathrm{sinc}\left(k\pi\frac{\Delta T}{T_{ac}}\right) = 1 + P\left(k\pi\frac{\Delta T}{T_{ac}}\right) \quad \text{with} \quad P(x) = \sum_{n=1}^{n=\infty}(-1)^n\frac{x^{2n}}{(2n+1)!}, \tag{15}$$

it follows that the time-averaging of the acoustic amplitude can be rewritten,

$$\int_{t_1}^{t_1+\Delta T} \exp\left(i\varphi_{ac}\sin(\omega_{ac}t + \phi_{ac})\right)dt = \Delta T\exp\left(i\varphi_{ac}\sin\left(\omega_{ac}t_1 + \phi_{ac} + \frac{\omega_{ac}\Delta T}{2}\right)\right) + \Delta T q\exp(i\gamma), \tag{16}$$

where q and γ both depend on the expansion of the sinc function according to:

$$\gamma = \arg\sum_k J_k(\varphi_{ac})P\left(k\pi\frac{\Delta T}{T_{ac}}\right)\exp\left(ik\left(\omega_{ac}t_1 + \phi_{ac} + \frac{\omega_{ac}\Delta T}{2}\right)\right), \tag{17}$$

and

$$q = \left|\sum_k J_k(\varphi_{ac})P\left(k\pi\frac{\Delta T}{T_{ac}}\right)\exp\left(ik\left(\omega_{ac}t_1 + \phi_{ac} + \frac{\omega_{ac}\Delta T}{2}\right)\right)\right|. \tag{18}$$

From **Equations 3**, **17**, **18**, the phase extracted from the hologram and due to the time average of the acoustic pressure from the temporal integration of the sensor is given by:

$$\psi = \arg(A_r) = \varphi_r + \psi_{ac} - \tan^{-1}\left(\frac{q\sin(\psi_{ac} - \gamma)}{1 + q\cos(\psi_{ac} - \gamma)}\right), \tag{19}$$

with

$$\psi_{ac} = \varphi_{ac}\sin\left(\omega_{ac}t + \phi_{ac} + \frac{\omega_{ac}\Delta T}{2}\right). \tag{20}$$

Equation 20 shows that the phase from the hologram includes the expected phase fluctuation from acoustics and a phase error which depends on both the acoustic phase fluctuation and the ratio between ΔT and T_{ac}. The phase error is given by:

$$\psi_{err} = \tan^{-1}\left(\frac{q\sin(\psi_{ac} - \gamma)}{1 + q\cos(\psi_{ac} - \gamma)}\right). \tag{21}$$

The phase error can be high and may strongly distort the measured phase fluctuation. In order to illustrate the error generated by the temporal integration due to the exposure time, one considers those physical parameters: $f_{ac} = 40$ kHz, $p_{ac} = 20$ Pa, $\phi_{ac} = \pi/4$, $\Delta T = 10$ µs, $\lambda = 660$ nm, $L = 50$ mm, and $c_0 = 340$ m/s. Then, the optical phase fluctuation amplitude due to acoustics is $\varphi_{ac} = 0.0185$ rad $\simeq 2\pi/340$. The error is calculated using **Eq. 21** and the distortion ratio of the amplitude φ_{ac} is estimated at $\tau_{err} = 100 \times \psi_{err}/\varphi_{ac} = 24.3\%$.

Figure 2A shows the temporal acoustic oscillation with comparison with the exposure time and the acoustic period for the chosen parameters. In **Figure 2B** is displayed the comparisons between the acoustic oscillations in the ideal case (red curve, no distortion), the ideal case with phase shift $\omega_{ac}\Delta T/2$ (black curve, no distortion), and the acoustic oscillation distorted by the time-average of the exposure time (blue curve). The comparison between the simulated phase error by considering numerical integration of the ideal signal in **Figure 2A** and the theoretical expression (**Eq. 21**) is provided in **Figure 2C**. It can be observed that the theoretical expression very well fits the numerical estimation, thus validating the proposed theoretical

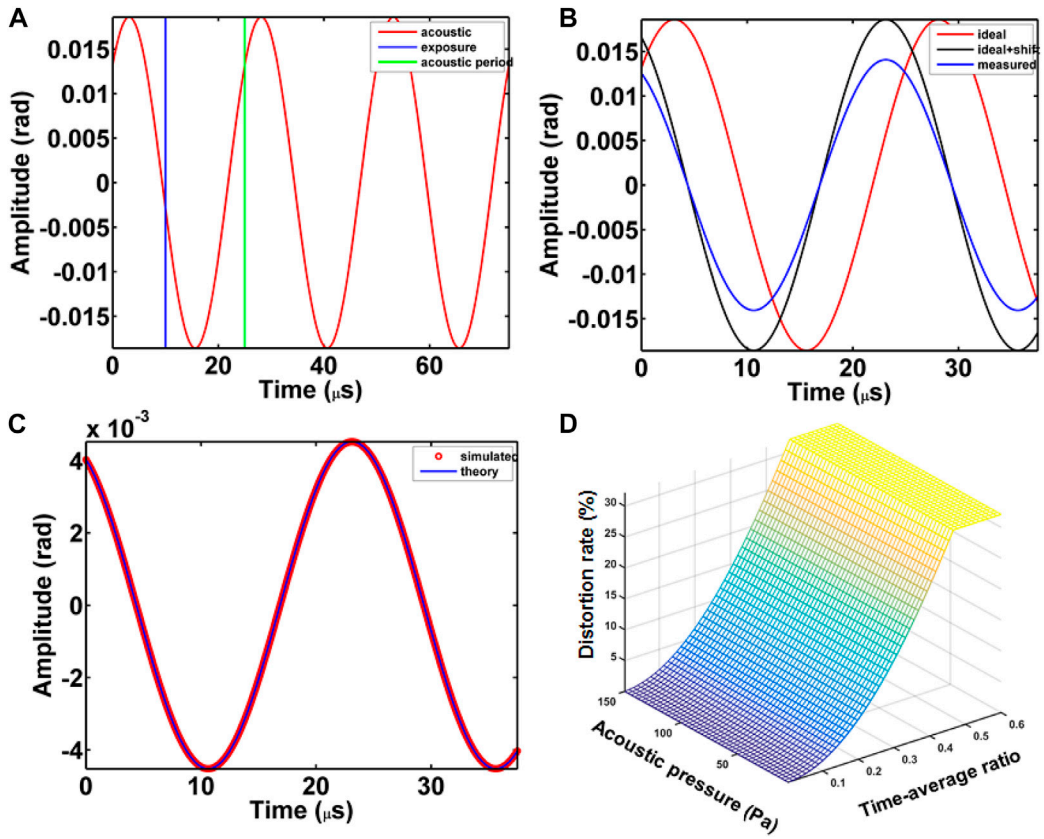

FIGURE 2 | (A) Temporal acoustic oscillation with comparison with the exposure time and the acoustic period for f_{ac} = 40 kHz, $\phi_{ac} = \pi/4$, and ΔT = 10 μs, **(B)** comparisons of acoustic oscillations, red: ideal as in **(A)**, black: ideal with phase shift of $\omega_{ac}\Delta T/2$, blue: distorted by the time-average of the exposure time, **(C)** comparison between the simulated phase error and the theoretical expression from Eq. 20, **(D)** evolution of the distortion rate (%) versus the acoustic pressure from 5 to 150 Pa and the time-average ratio $\Delta T/T_{ac}$ for exposure time varying from 1 to 10 μs.

approach. When considering the variation of the acoustic pressure from 5 to 150 Pa and exposure time varying from 1 to 10 μs, the distortion rate plotted versus the time-average ratio $\alpha = \Delta T/T_{ac}$ is given in **Figure 2D**. It can be seen that the distortion rate mainly depends on the acoustic amplitude and that it may be larger than 30% for ratio $\Delta T/T_{ac} \simeq 0.6$ and P_{ac} = 150 Pa. Note also that the measured acoustic oscillation includes a phase shift $\omega_{ac}\Delta T/2 = \alpha\pi$ compared to the emitted signal. This phase shift is irrelevant if α tends to 0, that is $\Delta T \ll T_{ac}$.

4 EXPERIMENTAL SET-UP

4.1 Three Color Digital Holographic Set-Up

The optical set-up is described in (**Figure 3**) Three continuous lasers at λ_R = 660 nm (300 mW), λ_B = 457 nm (150 mW) and λ_G = 532 nm (300 mW) are split into three reference beams and three illumination beams. Half wave plates for the three laser beams are used, namely, $\lambda_R/2$ the half wave plate for the red laser, $\lambda_G/2$ the half wave plate for the green laser, and $\lambda_B/2$ that for the blue laser. These are used to adjust, on one hand, the amount of power in the reference and probe beams, and on the other hand, to turn the polarisation in the R-G-B reference beam so that interference may occur. The three reference beams are then combined into a single R-G-B beam using dichroic plates. The object volume is illuminated simultaneously along the different propagation directions by the red beam along the direct direction, "direct view", along the orthogonal direction by the green beam, "orthogonal view", and in one direction inclined from almost 21° for the blue beam, "tilted view". Thus, three simultaneous illumination angles (0°, 21.31°, 90°) are produced. The measurement volume corresponds to the zone of space in which the three color laser probes are mixed. The volume is almost a sphere 20 mm in diameter localized at $d_r \simeq -1{,}310$ mm from the sensor area. Each measurement and reference beam is spatially filtered and expanded to produce plane and smooth waves. Using beam splitter cubes, the six beams are recombined onto a high-speed camera (Photron SA-X2; nb = 12 bits) with a spatial resolution of 1,024 × 1,024 pixels at 12,500 fps. The pixel pitches of the sensor are $p_x = p_y$ = 20 μm and the exposure time is set at ΔT = 1 μs, in order to avoid distortion from the time-averaging. The off-axis recording is adjusted by tilting cubes in order to produce the three different carrier frequencies along each viewing direction. This has for consequence that the monochrome recorded hologram

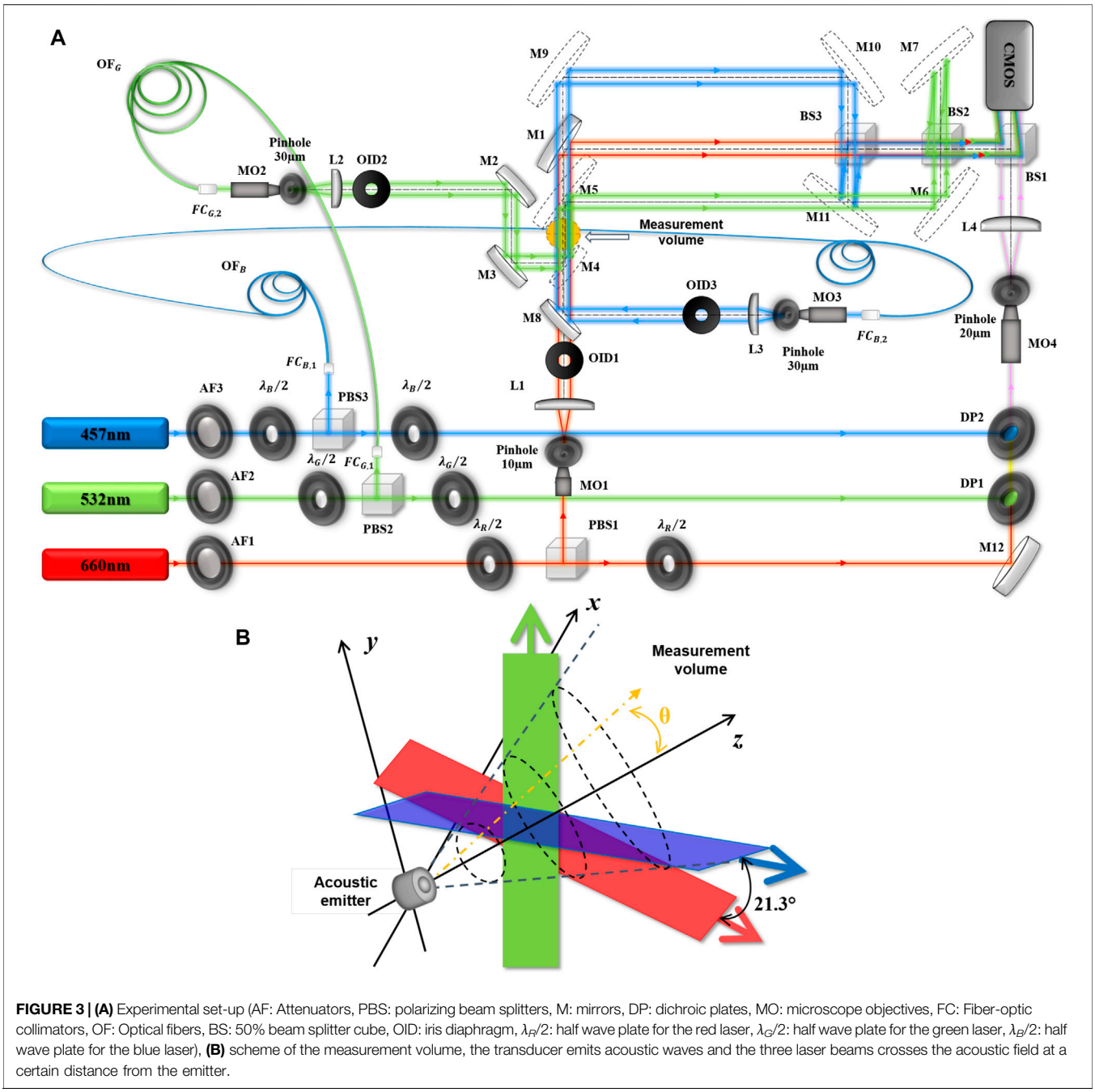

FIGURE 3 | (A) Experimental set-up (AF: Attenuators, PBS: polarizing beam splitters, M: mirrors, DP: dichroic plates, MO: microscope objectives, FC: Fiber-optic collimators, OF: Optical fibers, BS: 50% beam splitter cube, OID: iris diaphragm, $\lambda_R/2$: half wave plate for the red laser, $\lambda_G/2$: half wave plate for the green laser, $\lambda_B/2$: half wave plate for the blue laser), **(B)** scheme of the measurement volume, the transducer emits acoustic waves and the three laser beams crosses the acoustic field at a certain distance from the emitter.

includes three spatially multiplexed color holograms at each wavelength. It follows that the three color holograms can be separated in the Fourier spectrum of the digital hologram. The localized filtering with adapted spatial bandwidth (Δu, Δv) for each wavelength, permits to extract the complex images A_r along each view. Then, the temporal phase differences are calculated for each color and processed with the *SoundRetrieval* algorithm to get the amplitude and phase of the acoustic oscillation for each sight view. It follows that the set-up permits to simultaneously measure the amplitude and phase of the acoustic field along three different lines of views.

4.2 Acoustic Emitter Characterization

The acoustic field is generated using an acoustic emitter as an ultrasonic piezoelectric transducer (MA40S4S; diameter 9.9 mm). The transducer is localized at a few centimeter from the measurement volume and emits acoustic waves at frequency f_{ac} = 40 kHz and is driven by sinusoidal voltage (typ. 10V peak-to-valley). The acoustic wavelength is then $\lambda_{ac} = c_0/f_{ac}$ = 8.5 mm. From the provider, the sound pressure may reach 120 dB in the far field (so almost 120 Pa). The characterization of the acoustic emitter is carried out using a microphone (GRAS 40BP 1/4" Ext. Polarized Pressure Microphone) which has a sensitivity

TABLE 1 | Sensitivities of the acoustic emitter MA40S4S at different distances.

Distance (mm)	4	90	100	300
Sagital (dB)	1,050	136	126	43.2
Parallel (dB)	1,050	136	128	55.9

of 1.6 mV/Pa over a frequency range 4–70 kHz and a dynamic range of 34–169 dB. The microphone is powered by a NEXUS conditioning amplifier type 2692-C linked to an oscilloscope to measure the amplitude of the sound pressure oscillations. In order to measure the sound pressure, or the sensitivity S delivered by the ultrasonic transducer, as a function of the angle θ of emission, the transducer is mounted on one rotating header. The microphone is also mounted on a static support in front of the center of the acoustic emitter. The transducer header is adjusted so that angle $\theta = 0$ coincides with the maximum emission (acoustic signal is maximum). The sensitivity of the receiver is set at 1.651 mV/Pa. This value is considered as a reference acoustic pressure S_o. **Table 1** gives the sensitivities calculated at different distances between the transmitter and the receiver in the sagital and parallel planes. The sensitivity is estimated by calculating $S(dB) = 20\log\frac{S_v}{S_o}$, with S_v the measured microphone voltage at each emission angle. The sensitivities in **Table 1** reach almost the 1,050 dB, which is measured at a reference sound pressure equal to 10 V/Pa. Note that for measuring such high sound pressure close to the emitter, the excitation signal was lowered so as to avoid saturation from the microphone and then the pressure was estimated by assuming linear behavior of the microphone. The experimental radiation patterns of the acoustic wave from the transducer are shown in **Figures 4A,B**, both at 40 kHz. The measurements of the voltages are carried out in the sagital and parallel planes. As expected, the piezoelectric emitter produces an almost Lambertian radiation, with a strong directivity in the central axis for both distances $d = 90$ mm and $d = 100$ mm. By comparing the measurements presented in the technical sheet carried out in an anechoic chamber and those presented in **Figures 4A,B**, we observe a relative error of 13.3% for the sensitivity measured at a distance $d = 90$ mm at both sagital and parallel planes. That is almost acceptable considering that our measurements were not realized in a perfectly controlled acoustic environment.

5 EXPERIMENTAL RESULTS

5.1 Spatio-Chromatic Multiplexed Hologram and Related Power Spectrum Densities

Figure 5A shows the recorded three-color digital hologram with exposure time set at 1 µs. In **Figure 5B**, a zoom of the digital hologram exhibits the fine structure of the hologram where the micro fringes related to each of the individual R, G and B colors are mixed to produce a kind of mosaic. The color bar in **Figure 5A** relates to gray levels of the digital hologram. The sensor has $nb = 12$ bits quantization, so the maximum value of the gray levels is 4095. In **Figure 5A**, the maximum value of the color bar is around 1000. It follows that digital holograms occupy almost 1/4 of the full sensor dynamics. In **Figure 5C**, the spatial frequency power spectrum density is displayed. The different orders along each color can be observed and they are marker with squares and related R-G-B letter. As can be seen, the +1 orders can be easily filtered since they are well separated in the power spectrum. The spatial frequencies of the centers of each order are $(u_R, v_R) = (-17.76, -12.55)\ \text{mm}^{-1}$ for the red laser, $(u_G, v_G) = (+20.74, -18.66)\ \text{mm}^{-1}$ for the green one and $(u_B, v_B) = (+5.32, -15.52)\ \text{mm}^{-1}$ for the blue laser. The filtering bandwidth according to **Eq. 4** depends on the laser beam it follows that for the set-up, they were chosen to be $\Delta u_R = \Delta v_R = 1.11\ \text{mm}^{-1}$, $\Delta u_G = \Delta v_G = 2.17\ \text{mm}^{-1}$ and $\Delta u_B = \Delta v_B = 0.83\ \text{mm}^{-1}$ respectively for the R-G-B beams. From the average amplitude of the +1 and 0 orders extracted from the numerical processing, along each color, the average modulation and saturation rate of the holograms can be estimated. For the red beam, $(m, \alpha) = (66, 7.6)\%$, for the green beam, $(m, \alpha) = (4.1, 6.1)\%$ and for the blue one, $(m, \alpha) = (21, 3)\%$. As can be seen, the G hologram has the weakest modulation and this increases its sensitivity to noise, whereas the two others have reasonable modulation although the optimal modulation would be close to 1. The reason for average modulations is not clear in the set-up, although the beam polarisation and optical path difference are well managed. The B beam is saturated at only 3% and this is due to lack of laser power. Overall, the saturation rate of the three beams does not exceed 10%. Ideally, that would be better to be close to $\alpha \simeq 1/6$, that is almost 16%. But considering the exposure time at 1 µs and the available average power per

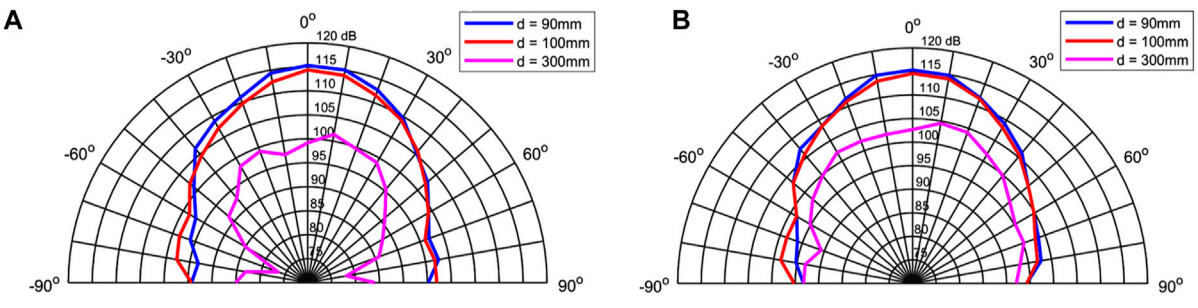

FIGURE 4 | Directivity of the acoustic radiation of the ultrasonic transmitter (MA40S4S), **(A)** sagittal plane, **(B)** vertical plane.

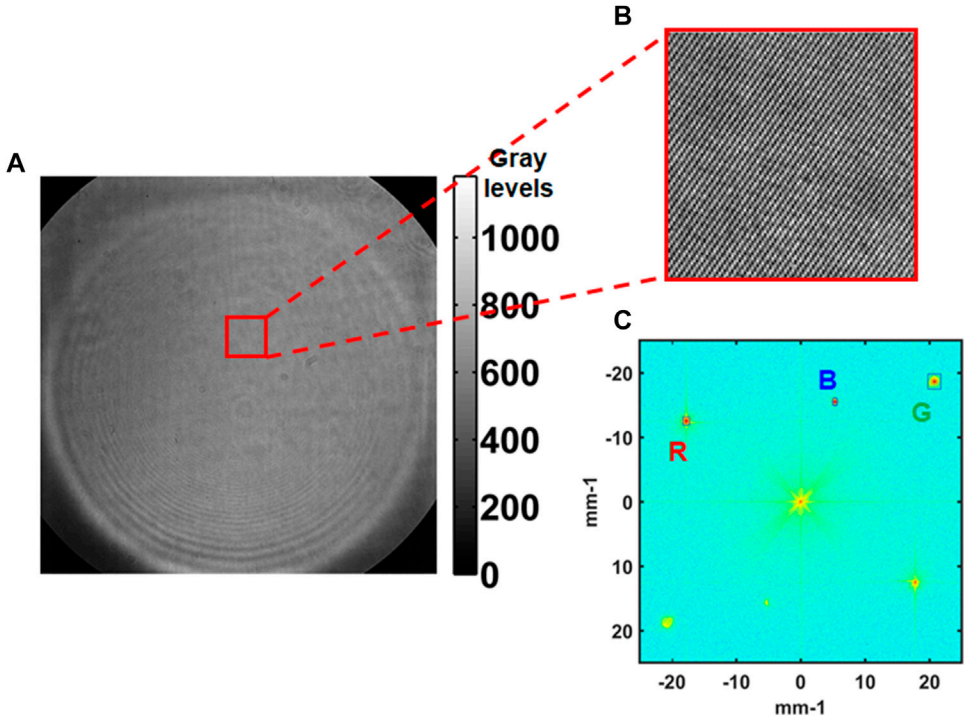

FIGURE 5 | (A) Recorded three color hologram, **(B)** zoom of the hologram exhibiting the fine structure due to the spatio-chromatic multiplexing of the three R, G and B holograms, **(C)** power spectrum density of the three color hologram with the diffraction orders and the spatial bandwidth of the filtering; the useful +1 orders are framed by squares which correspond to the spatial filtering bandwidth.

channel (< 300 mW), such ratio is not reachable. Using the values of (m, α) and **Eq. 5**, the estimation of the standard deviation of noise can be given and correlated with the experimental estimation. This point is discussed in the next section.

5.2 Phase Noise Characterisation

The phase noise is characterized by recording a time sequence of digital color holograms without any acoustic wave in the measurement volume. Separately, in order to check the noise amount for each wavelength, a sequence of monochromatic holograms with duration 160 ms was recorded at frame rate 12,500 Hz (exposure time at 1 μs) to yield almost 2000 digital holograms. Then, for each R-G-B sequence, the phase differences $\psi(t)$ are calculated and the standard deviations of noise are estimated. A region of 15 × 15 pixels at the center of the fields of view was selected to yield 225 temporal signals. The probability density function of the 225 signals is estimated. The power spectrum density $[S_\lambda(\nu)]$ of each signal was calculated using fast Fourier transforms (Oppenheim, 1999), and then averaged to yield $(\hat{S}_\lambda(\nu))$. The standard deviation of noise over a spectral bandwidth was calculated according to:

$$\sigma_n = \int_{f_1}^{f_2} \hat{S}_\lambda(\nu) d\nu. \tag{22}$$

Figure 6 summarizes the results obtained for the three beams. In **Figures 6A–C**, the plots of the 225 temporal signals respectively along the R, G and B wavelength are displayed. The plots clearly shows that the phase fluctuation is the smallest in the R beam, whereas it is larger for the G, and more than π rad for the B beam. The R and B signals show that the noise fluctuations include deterministic parts whereas the G beam seems to be more randomly distributed. This is confirmed when considering **Figures 6D–F** which exhibit the probability density functions estimated from 225 signals for the R-G-B beams respectively. The G probability density function exhibits Gaussian shape, and none of the two others. The strong parasitic oscillation observed in the B channel is unexplained. In **Figures 6G–I** are plotted the average power spectrum densities of the set of signals for R-G-B respectively. As intuited by the temporal signals, the G spectrum is more related to white noise than the two others. According to these observations, the amount of pure noise can be estimated from both **Eq. 5** and the averaged power spectrum densities. For the estimated values of (m, α) and (Δu_λ, Δv_λ) for the R-G-B holograms, with N_{sat} = 16,000 electrons, σ_{ro} = 27 electrons, nb = 12 bits, the theoretical standard deviation of noise was calculated to $\sigma_{\varphi,R}$ = 0.0027 rad, $\sigma_{\varphi,G}$ = 0.088 rad and $\sigma_{\varphi,B}$ = 0.011 rad. The experimental standard deviation of noise was estimated with **Eq. 22** for the bandwidth almost corresponding to white noise, between f_1 = 4,500 Hz and f_2 = 6,000 Hz, leading

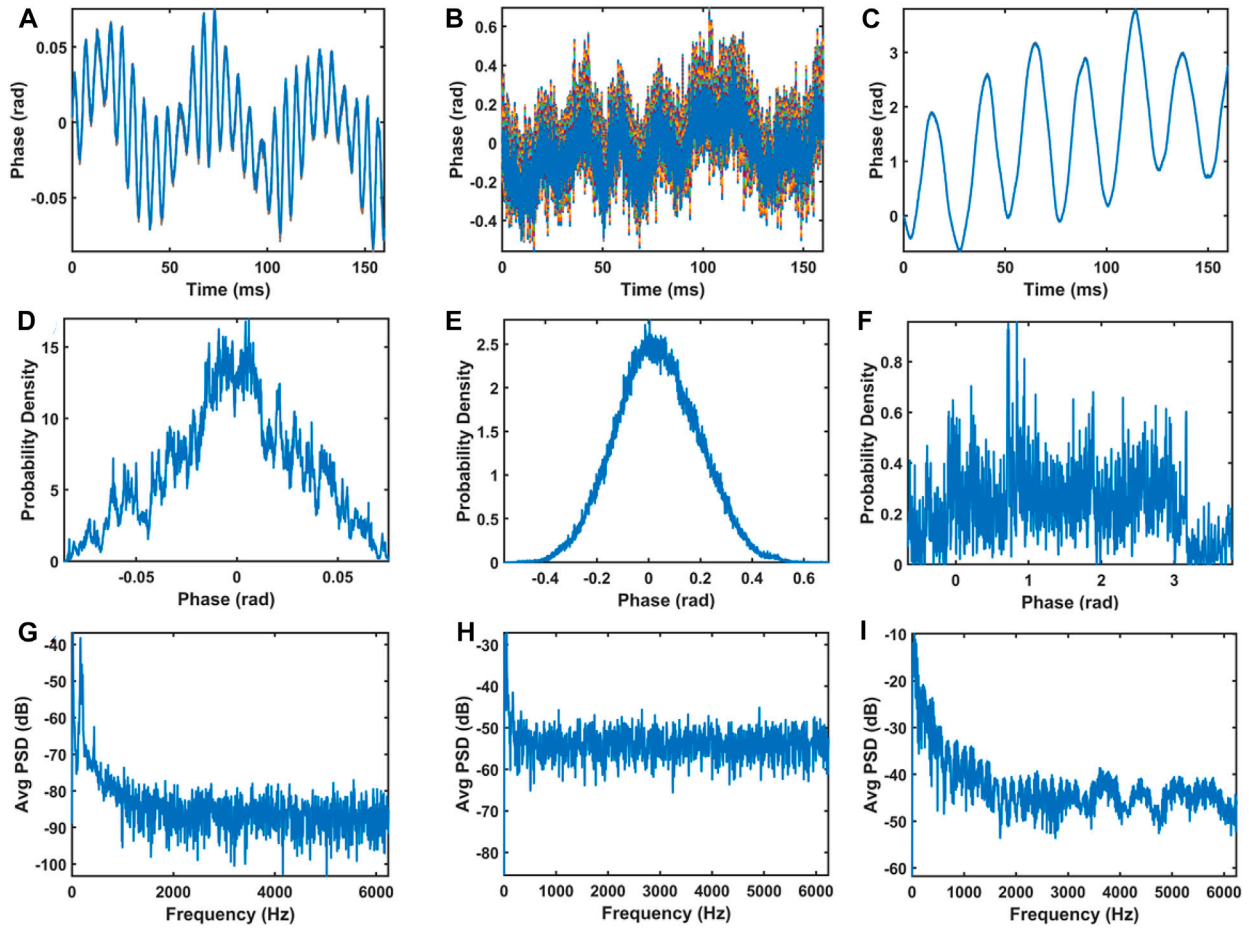

FIGURE 6 | (A–C) Plots of a set of 225 temporal signals respectively along the red, green and blue beams, **(D–F)** probability density functions estimated from the set of signals for R-G-B respectively, **(G–I)** average power spectrum densities of the set of signals for R-G-B respectively.

to $\sigma_{\varphi,R-\exp} = 0.0024$ rad, $\sigma_{\varphi,G-\exp} = 0.094$ rad and $\sigma_{\varphi,B-\exp} = 0.24$ rad. So, it follows that for the R and G beams, the theoretical estimations are almost close to the experimental values in the white noise hypothesis. However, for the B beam, the difference is high because the hypothesis is broken since the bandwidth in the range (4,500, 6,000) Hz is not as flat as expected.

5.3 Multi-Views of the Acoustic Field

The acoustic transducer was excited at 40 kHz and placed at different distances from the measurement volume, that are d = 0 mm, d = 90 mm, d = 100 mm and d = 200 mm. For distance d = 0 mm, that is the transducer is close to the measurement volume, the acoustic pressure was measured with the microphone at almost 1,050 Pa. Temporal sequences of digital color holograms were recorded with frame rate at 12.5 kHz and exposure time at 1 µs. At this frame rate, matrices of 1024 × 1024 pixels are recorded and $\alpha = 0.04$. With f_{ac} = 40 kHz, the Shannon conditions for temporal sampling are not fulfilled, since the basic requirement would lead to sampling rate larger than 80 kHz. However, at 80 kHz, the spatial resolution would be drastically reduced. In order to keep a good spatial resolution at 1024 × 1024 pixels, the frame rate was voluntarily chosen less than the acoustic frequency. This requires to make adjustments of the parameters of the *SoundRetrieval* algorithm. Especially, since aliasing occurs, the acoustic frequency is observed at $f'_{ac} = 2500$ Hz in the power spectrum density. Considering **Figure 6**, the noise bandwidth becomes to be almost flat in this frequency band thus enabling the measurement of the acoustic frequency. Practically, one has to consider a virtual sampling period that depends on the ratio between the acoustic frequency and the actual sampling frequency, according to $T'_s = T_s - k_s \times T_{ac}$, with $k_s = floor\ (f_{ac}/f_s)$ (*floor* (. . .) meaning lower rounding). So, this yields the new virtual sampling frequency $f'_s = 1/T'_s$ that is required for the *SoundRetrieval*. With the experimental parameters, we have $k_s = 3$, $T'_s = 5 \times 10^{-6}$ s, $f'_s = 200$ kHz to be injected in the sound retrieval method.

It follows from the previous section that the distortion rate is estimated 0.26% for $\alpha = 0.04$ and phase amplitude ranging from 0.01 to 0.04 rad. So, it appears that for this range of α value and measured phase amplitude, there is no specific requirement for

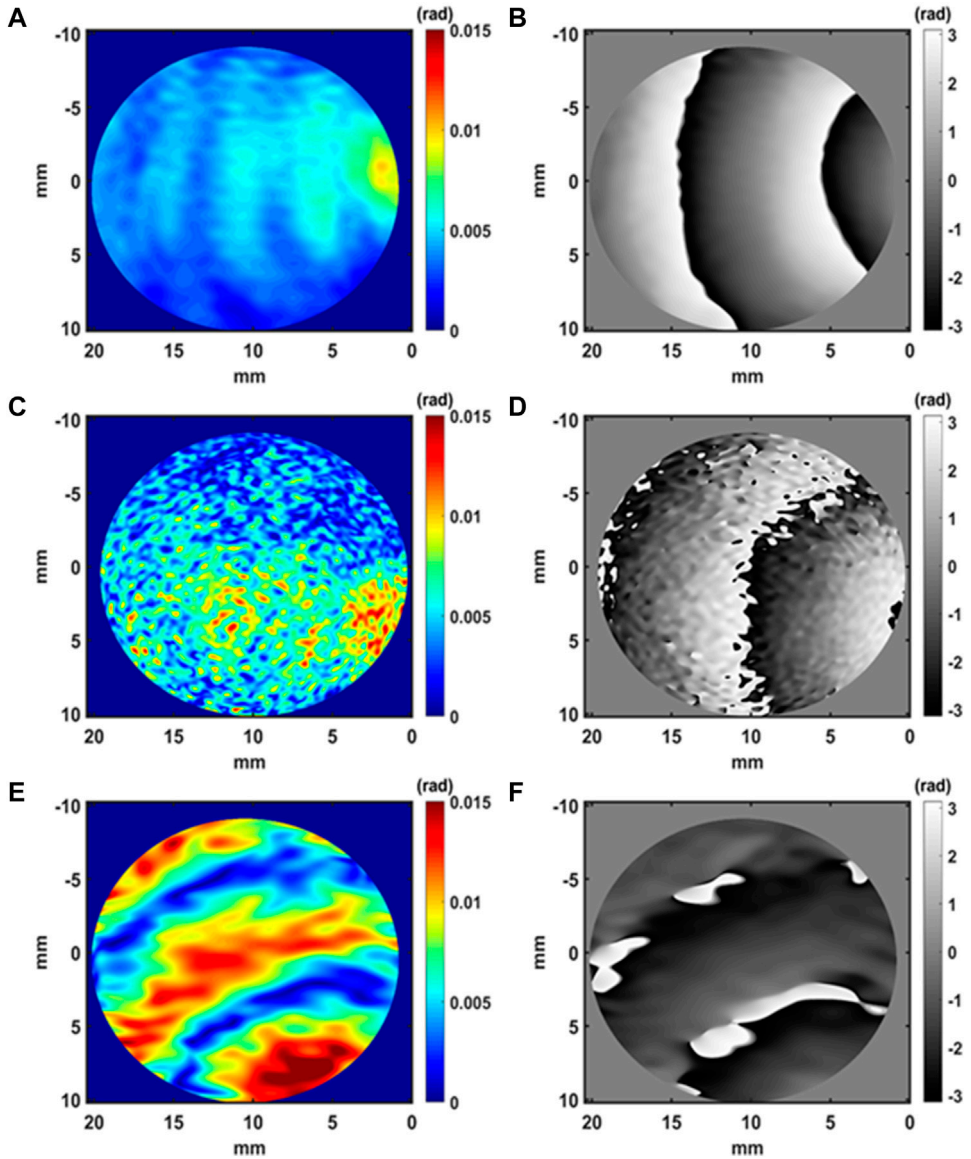

FIGURE 7 | Amplitude and phase of the acoustic field at 0 mm, **(A,B)** along the R view, **(C,D)** along the G view, **(E,F)** along the B view.

compensating for the distortion due to the time-average of the exposure time.

Figures 7A,C,E, **8A,C,E**, **9A,C,E**, **10A,C,E** show the measured acoustic amplitude for respectively the red, green and blue channels for the excitation at $f_{ac} = 40$ kHz. The acoustic amplitude is expressed in radians rather than in pressure units. This point will be discussed in the next section. **Figure 7B,D,F**, **8B,D,F**, **9B,D,F**, **10B,D,F** show the measured acoustic phase for respectively the red, green and blue channels. In **Figures 7**, **8**, **9**, **10**, one clearly observes dark and bright fringes that demonstrate the existence of the acoustic wave in the free field. The acoustic wave is spherical when the transducer is close to the measurement volume (**Figure 7**). Then, it becomes to be plane wave far from the emitter as in **Figure 8**, **9**, **10**. Note that, the image quality along the G and B channels are lower than for the R channel and this in close correlation with **Figure 6**.

If one considers **Equation 10**, then we can estimate the interaction length of the laser beam in the acoustic field as,

$$L = \frac{2\lambda}{3\hat{r}} \frac{c_0^2}{p_{ac}} \frac{\varphi_{ac}}{2\pi}. \tag{23}$$

With the R channel at distance $d = 0$ mm, we can consider the measured value at $\varphi_{ac} \simeq 0.010$ rad (**Figure 7A**). With the physical parameters, the estimated value of the interaction length is $L \simeq 0.5$ mm. From **Figure 7A** we can estimate that the acoustic field

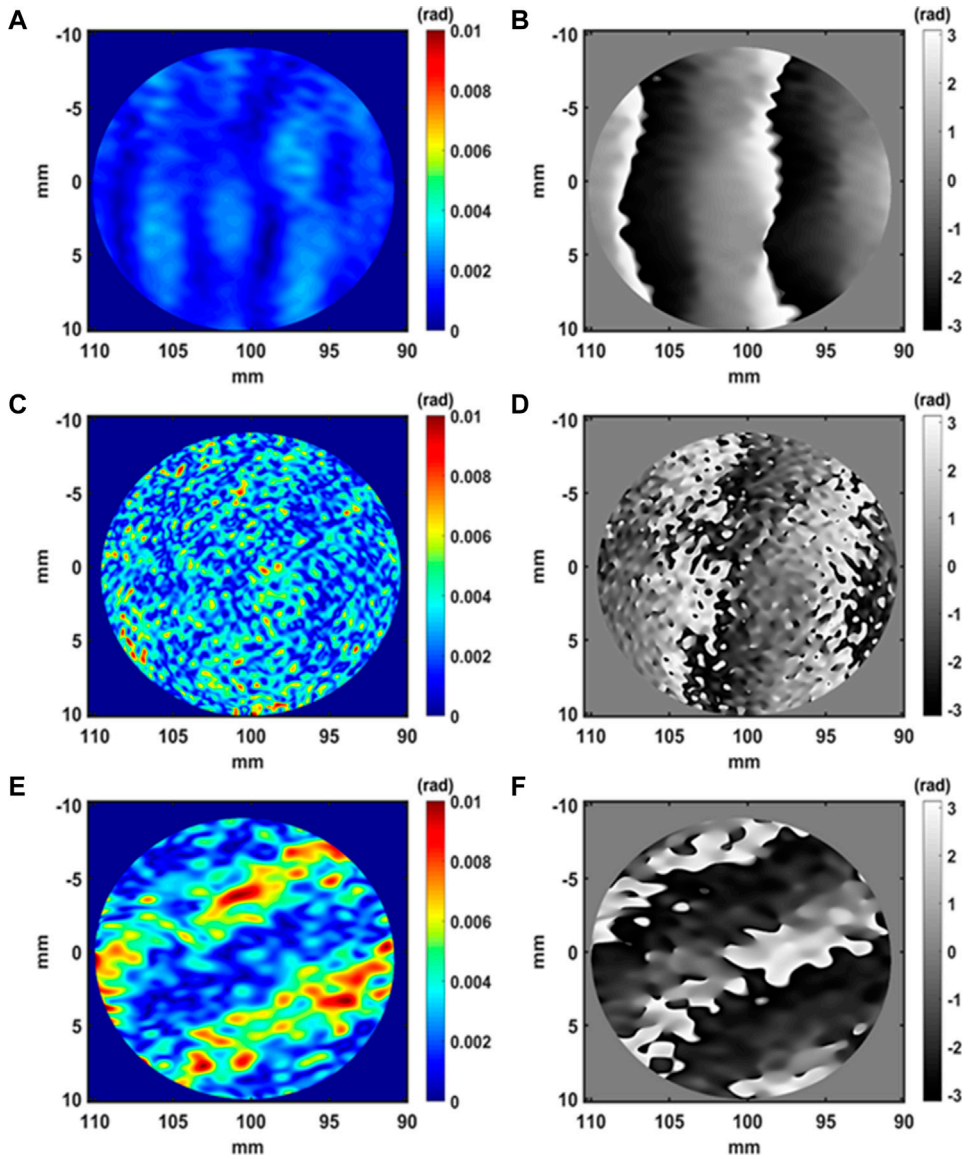

FIGURE 8 | Amplitude and phase of the acoustic field at 90 mm, **(A,B)** along the R view, **(C,D)** along the G view, **(E,F)** along the B view.

seems to be extended on a width quite larger that L, at almost ≃ 4–5 mm. Thus, this result obtained by the holographic method seems to be not in agreement with the microphone measurement in the sound field. With **Figure 9A**, one can estimate that $\varphi_{ac} \simeq$ 0.0040 rad. With the microphone at the center of the field at distance d = 100 mm, P_{ac} = 126 Pa, and one can then estimate $L \simeq$ 1.07 mm. We see that the estimated interaction distance increases, which is expected since the transducer produces a divergent wave. However, considering the strong divergence of the acoustic beam, this value is probably not correct, as for distance d = 0 mm.

The maximum values of the acoustic amplitudes measured for the R, G and B at the different distances from the measurement volume (0, 90 mm, 100 mm, 200 mm) are presented in **Table 2**. This table requires a few comments. The amplitudes measured along the R-G-B channels follow a similar trend, except for channel B at distance 200 mm. Indeed, the measured amplitudes decrease with distance, which is expected for a spherical wave. For channel B at 200 mm, it is likely that the measurement is strongly influenced by noise because it should be lower than measurements at other distances, which is not the case. The measurements along G follow a consistent pattern although the maps of **Figures 7 –10** appear to be the noisiest of all the measurements.

In order to investigate the noise contribution at f_{ac} = 40 kHz, the *SoundRetrieval* algorithm was applied to the noise sequence

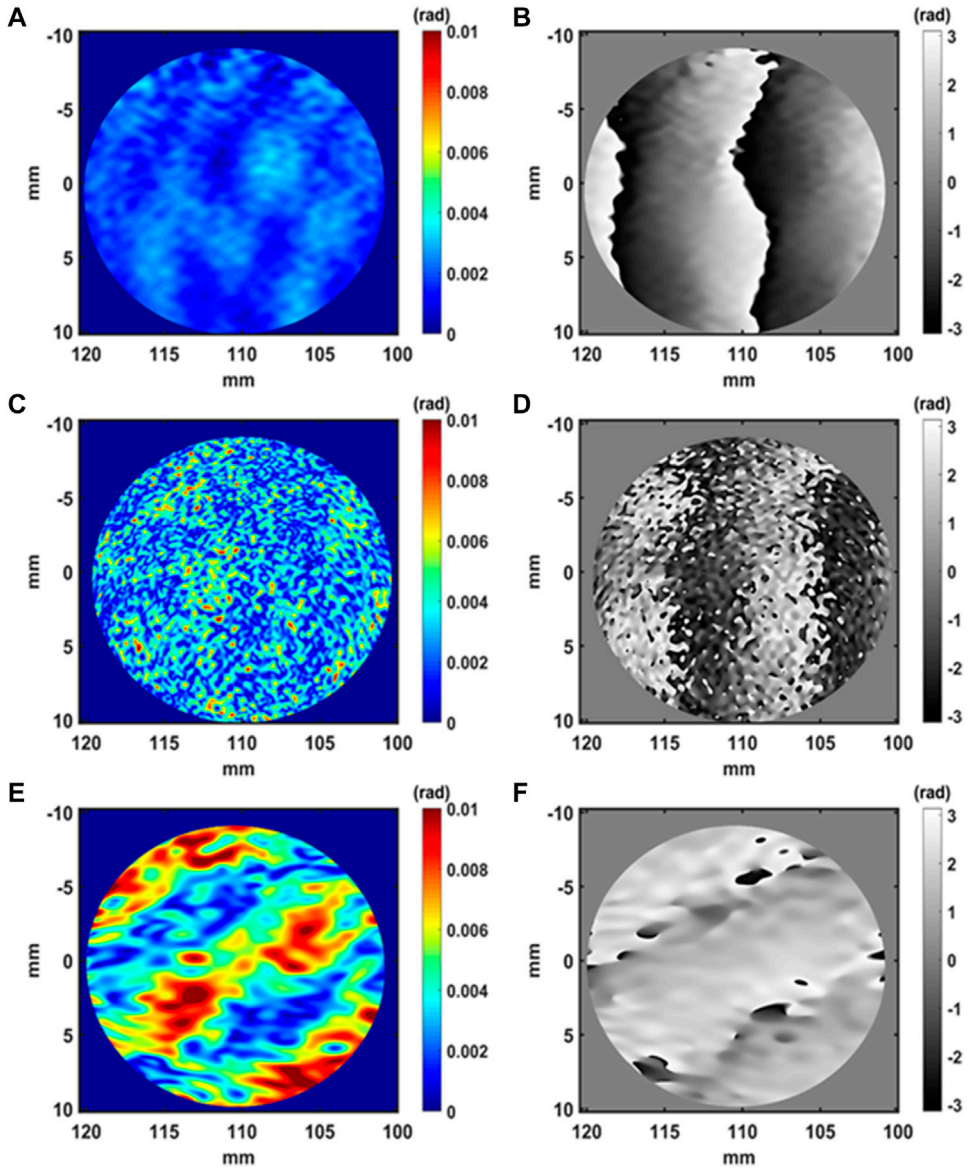

FIGURE 9 | Amplitude and phase of the acoustic field at 100 mm, **(A,B)** along the R view, **(C,D)** along the G view, **(E,F)** along the B view.

from the previous section. **Figure 11** shows the amplitude and phase of the noise contribution at 40 kHz for the three R-G-B channels. The standard deviations along each noise amplitude map were estimated to $\sigma_R = 8.23 \times 10^{-6}$ rad, $\sigma_G = 4.63 \times 10^{-4}$ rad, and $\sigma_B = 4.7 \times 10^{-5}$ rad. As mentioned before the red channel provides the lowest noise contribution to the acoustic measurement.

In **Figures 7–10**, phase jumps are observed in the phase map of the acoustic field. These indicate that each phase jump corresponds to change in the sign of the acoustic oscillation, in close relation with the acoustic wavelength as depicted in **Figure 12A**. **Figure 12B** plots the profile of the acoustic phase along the horizontal direction in the R measurement. From that, the acoustic wavelength is estimated to $\lambda_{ac-exp} \simeq 8.86$ mm and is close to the theoretical $\lambda_{ac} = 8.5$ mm. So the two wavelengths are in good agreement, confirming that the acoustic field is well measured by the holographic imaging system.

6 DISCUSSION

In this section, the acoustic field is recovered according to the theoretical basics described previously, that is integrated along the line of view of the laser beam. In order to qualitatively

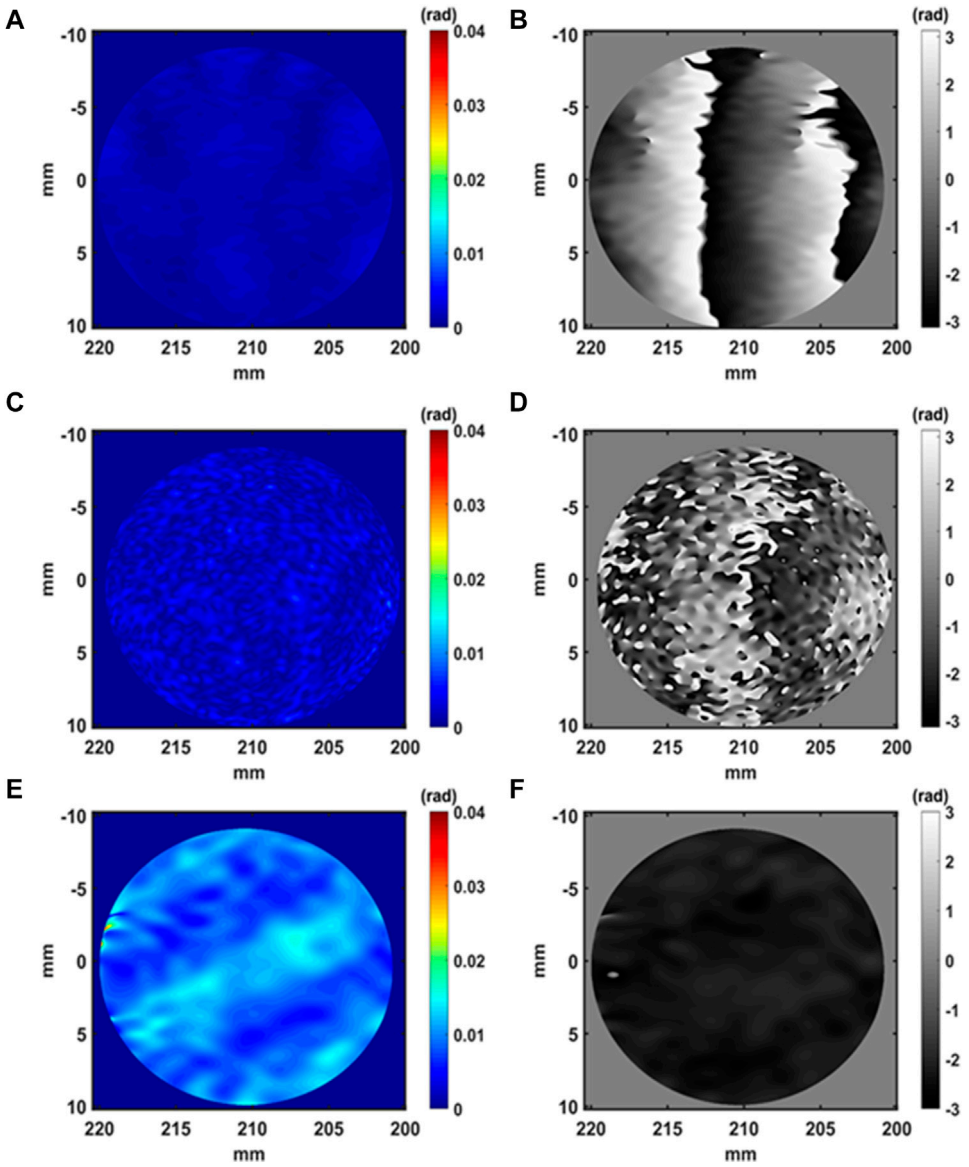

FIGURE 10 | Amplitude and phase of the acoustic field at 200 mm, **(A,B)** along the R view, **(C,D)** along the G view, **(E,F)** along the B view.

TABLE 2 | The maximum values of the acoustic amplitudes measured for the R,G and B views at different distances from the measurement volume.

Distance (mm)	0	90	100	200
Maximum amplitude R (rad)	0.010	0.003	0.0034	0.0031
Maximum amplitude G (rad)	0.0156	0.011	0.0106	0.0094
Maximum amplitude B (rad)	0.019	0.0127	0.0116	0.0334

appraise the effect of the integration along the optical path and to evaluate the relevance of the results obtained in the previous section, simulations were carried out. The aim is to investigate the amplitude and the phase of the acoustic field when considering realistic simulations as close as possible to the experiments of the paper. The case of interest is that of non-plane acoustic wave. In the case of plane waves in an acoustic wave guide, the correspondence between the actual phase and the measured one is straightforward (Penelet et al., 2016; Gong et al., 2018; Gong et al., 2021). The simulation of the acoustic field was carried out for transducer as a rigid piston in a baffle with radius a = 4.95 mm, and executing harmonic oscillations at frequency f_{ac} = 40 kHz. The theoretical relation describing the acoustic field is given in **Eq. 24** (Pierce and Beyer, 1990),

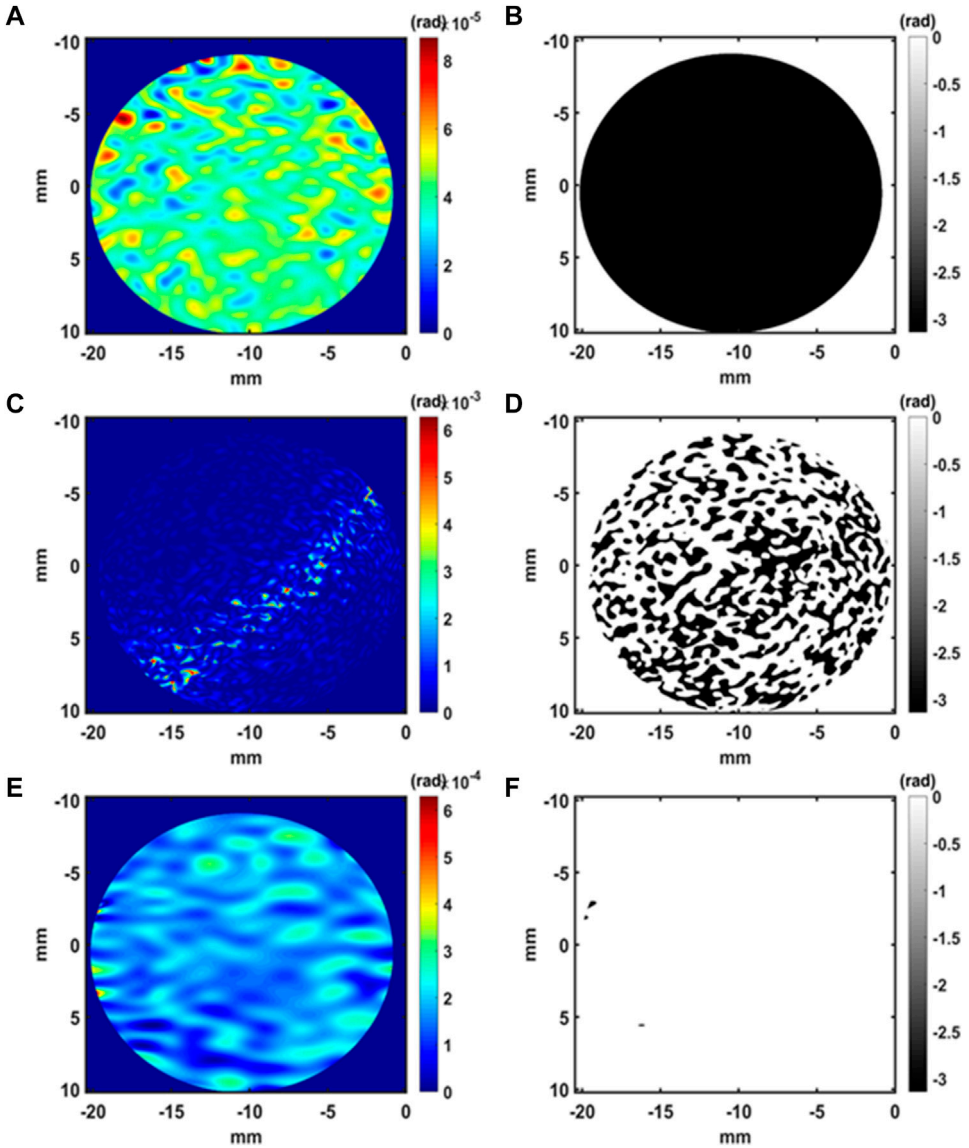

FIGURE 11 | Amplitude and phase of the at f_{ac} = 40 kHz, **(A,B)** along the R view, **(C,D)** along the G view, **(E,F)** along the B view.

$$p_{ac} \propto \frac{\exp(ik_{ac}r)}{r} \frac{J_1(k_{ac}a\sin(\theta))}{k_{ac}a\sin(\theta)}, \tag{24}$$

with $k_{ac} = 2\pi/\lambda_{ac}$ the acoustic wave vector, $r = \sqrt{(x-x_0)^2 + (y-y_0)^2 + (z-z_0)^2}$, (x_0, y_0, z_0) the coordinates of the center of the acoustic emitter and θ the angle of the propagation direction (refer to **Figures 13A,B**). Here, the main propagation direction of the acoustic wave is oriented along z. The simulation considers the length of integration at L = 61.4 mm and the measurement volume localized at d = 90 mm from the emitter. The width of the laser beam is 12.7 mm. **Figure 13** summarizes the simulation principle and results. In **Figure 13A** the scheme of the acoustic emitter and of the amplitude of the acoustic field is depicted. The laser beam represented as a red line crossing the acoustic field is also shown. The length of the optical path is considered to be the length of the picture, almost 61.4 mm. In **Figure 13B** is represented the same scheme with the acoustic phase displayed. Phase jumps can be observed and the distance separating the phase jumps corresponds to the acoustic wavelength (λ_{ac} = 8.5 mm). **Figure 13C** shows the profile of the amplitude along the z direction and **Figure 13D** that of the phase. In **Figure 13E** the profile of the amplitude of the integrated acoustic field along the laser beam is shown, whereas **Figure 13F**

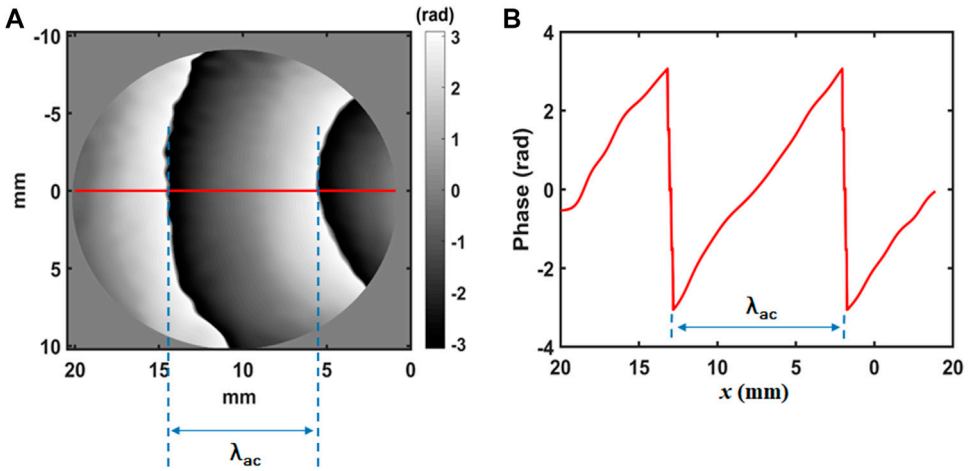

FIGURE 12 | Acoustic wavelength measured along the R view, **(A)** scheme of the phase of the acoustic field at distance 0 mm, **(B)** Phase profile of the acoustic field along the *x* direction for an excitation frequency of 40 kHz.

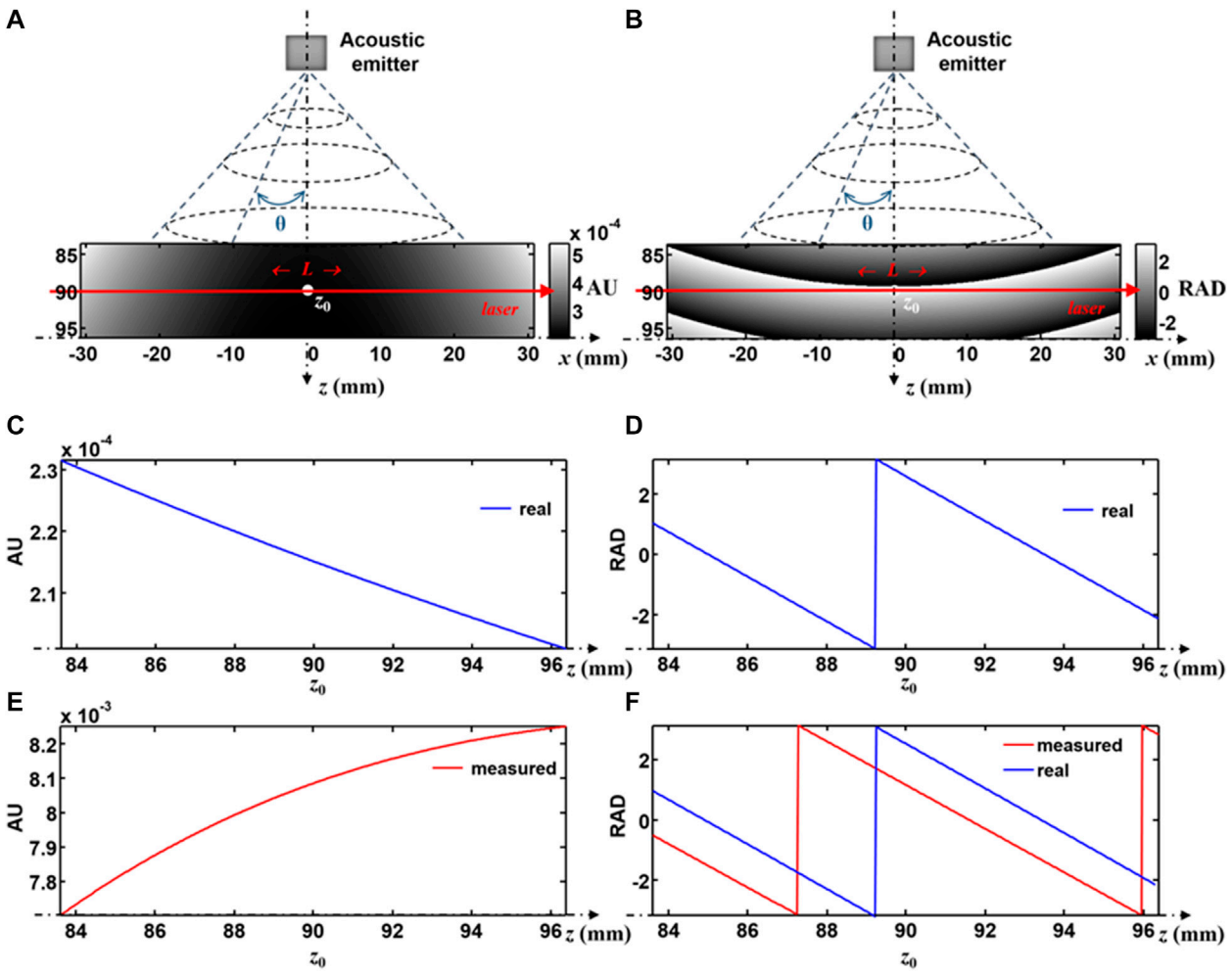

FIGURE 13 | Schemes of the acoustic emitter, **(A)** scheme of the amplitude of the acoustic field, **(B)** scheme of the phase of the acoustic field, **(C)** amplitude profile along the *z* direction, **(D)** phase profile along the *z* direction, **(E)** amplitude profile of the integrated acoustic field along the laser beam, **(F)** phase profile of the integrated acoustic field along the laser beam (red line), comparison with the real phase profile (blue line).

shows the profile of the measured phase with integration. Comparison with the phase profiles is provided (ideal: red line, integrated: blue line).

So, **Equations 10**, **23** result from a "plane wave" consideration for the acoustic field. However, the transducer does not emit a plane wave because it is strongly divergent. The simulation shows that the further away from the acoustic source, the more the integrated amplitude deviates from the true amplitude. Thus, this probably explains the disagreement between interaction length estimation from holography and microphone measurements. It follows that the question of the conversion of the phase measurement into acoustic pressure remains open in the case of a non-plane acoustic field. The problem of quantitative measurement of the acoustic field by holography then remains to be investigated.

7 CONCLUSION

This paper presents the proof-of-concept for a simultaneous recording of multiple views for acoustic fields imaging. The principle is based on off-axis holography and spatial multiplexing of multi-wavelength holograms. Three wavelengths from three different laser lines are used to illuminate, at different incidence angles, the volume in which an acoustic wave propagates. The reference beams from the lasers are combined into a single three color beam and the spatial frequencies of the reference waves are adjusted so as to allow for the spatial multiplexing of digital holograms with the monochromatic sensor. After de-multiplexing and processing of the temporal sequence of digital color holograms, the amplitude and phase of the acoustic field along the views are obtained. The distortion of the acoustic amplitude is investigated with a theoretical modelling. Simulations permit to validate the modelling and the distortion rate can be estimated according to the experimental conditions. It follows that the distortion can be a posteriori compensated in order to get a correct amplitude measurement. The way to get quantitative acoustic pressure measurement is discussed according to realistic acoustic simulations and opens the way for future investigations. The first experimental results are presented for the case of the acoustic field emitted by an ultrasound transducer exited at the frequency of 40 kHz. Since the transducer does emit a spherical wave, the integrated amplitude along the laser beam deviates from the true amplitude. Thus, the question of the conversion of the holographic data into acoustic pressure is still open for free-field acoustic waves. This would open the way to quantitative holographic tomography of acoustic fields.

DATA AVAILABILITY STATEMENT

Data underlying the results presented in this paper are not publicly available at this time but maybe obtained from Data underlying the results presented in this paper are not publicly available at this time but maybe obtained from the authors upon reasonable request.

AUTHOR CONTRIBUTIONS

PP and KF directed the project. SH and PP prepared the theory and simulations. SH and PP performed the experiments. SH, KF, LB, and PP analyzed the experimental results. All authors contributed to the discussions and the preparation of the paper.

ACKNOWLEDGMENTS

The authors gratefully thank Guillaume Penelet from LAUM for very help-full discussions and recommendations. The authors thank the PROFAS B+ program for the scholarship provided to support the research program of Saoucene Hassad.

REFERENCES

Bertling, K., Perchoux, J., Taimre, T., Malkin, R., Robert, D., Rakić, A. D., et al. (2014). Imaging of Acoustic Fields Using Optical Feedback Interferometry. *Opt. Express* 22, 30346–30356. doi:10.1364/oe.22.030346

Flanagan, J. L., Johnston, J. D., Zahn, R., and Elko, G. W. (1985). Computer-steered Microphone Arrays for Sound Transduction in Large Rooms. *J. Acoust. Soc. Am.* 78, 1508–1518. doi:10.1121/1.392786

Frank, S., and Schell, J. (2005). "Sound Field Simulation and Visualisation Based on Laser Doppler Vibrometer Measurements," in *Forum Acousticum*. Budapest: EAA Events Proceedings, 91–97.

Gong, L., Penelet, G., and Picart, P. (2018). Experimental and Theoretical Study of Density Fluctuations Near the Stack Ends of a Thermoacoustic Prime Mover. *Int. J. Heat Mass Transf.* 126, 580–590. doi:10.1016/j.ijheatmasstransfer.2018.05.027

Gong, L., Penelet, G., and Picart, P. (2021). Noise and Bias in off-axis Digital Holography for Measurements in Acoustic Waveguides. *Appl. Opt.* 60, A93–A103. doi:10.1364/AO.404301

Groschup, R., and Grosse, C. (2015). Mems Microphone Array Sensor for Air-Coupled Impact-Echo. *Sensors* 15, 14932–14945. doi:10.3390/s150714932

Hafizovic, I., Nilsen, C.-I. C., Kjølerbakken, M., and Jahr, V. (2012). Design and Implementation of a Mems Microphone Array System for Real-Time Speech Acquisition. *Appl. Acoust.* 73, 132–143. doi:10.1016/j.apacoust.2011.07.009

Hargather, M. J., Settles, G. S., and Madalis, M. J. (2010). Schlieren Imaging of Loud Sounds and Weak Shock Waves in Air Near the Limit of Visibility. *Shock Waves* 20, 9–17. doi:10.1007/s00193-009-0226-6

Hashimoto, S., Takase, Y., Inoue, T., Nishio, K., Xia, P., Rajput, S. K., et al. (2022). Simultaneous Imaging of Sound Propagations and Spatial Distribution of Acoustic Frequencies. *Appl. Opt.* 61, B246–B254. doi:10.1364/ao.444760

Ishikawa, K., Tanigawa, R., Yatabe, K., Oikawa, Y., Onuma, T., and Niwa, H. (2018). Simultaneous Imaging of Flow and Sound Using High-Speed Parallel Phase-Shifting Interferometry. *Opt. Lett.* 43, 991–994. doi:10.1364/ol.43.000991

Ishikawa, K., Yatabe, K., Chitanont, N., Ikeda, Y., Oikawa, Y., Onuma, T., et al. (2016). High-speed Imaging of Sound Using Parallel Phase-Shifting Interferometry. *Opt. Express* 24, 12922–12932. doi:10.1364/oe.24.012922

Malkin, R., Todd, T., and Robert, D. (2014). A Simple Method for Quantitative Imaging of 2d Acoustic Fields Using Refracto-Vibrometry. *J. Sound Vib.* 333, 4473–4482. doi:10.1016/j.jsv.2014.04.049

Matoba, O., Inokuchi, H., Nitta, K., and Awatsuji, Y. (2014). Optical Voice Recorder by off-axis Digital Holography. *Opt. Lett.* 39, 6549–6552. doi:10.1364/ol.39.006549

Merzkirch, W. (2012). *Flow Visualization*. New York: Academic Press.

Oppenheim, A. V. (1999). *Discrete-time Signal Processing*. Pearson Education India.

Ortiz, P. F. U., Perchoux, J., Arriaga, A. L., Jayat, F., and Bosch, T. (2018). Visualization of an Acoustic Stationary Wave by Optical Feedback Interferometry. *Opt. Eng.* 57, 051502. doi:10.1117/1.oe.57.5.051502

Penelet, G., Leclercq, M., Wassereau, T., and Picart, P. (2016). Measurement of Density Fluctuations Using Digital Holographic Interferometry in a Standing Wave Thermoacoustic Oscillator. *Exp. Therm. Fluid Sci.* 70, 176–184. doi:10.1016/j.expthermflusci.2015.09.012

P. Picart (Editor) (2015). *New Techniques in Digital Holography* (London : Hoboken, NJ: ISTE Ltd ; John Wiley & Sons, Inc). Instrumentation and measurement series.

[Dataset] Pierce, A. D., and Beyer, R. T. (1990). *Acoustics: An Introduction to its Physical Principles and Applications*. 1989 edition. Acoustical Society of America.

Rajput, S. K., Matoba, O., and Awatsuji, Y. (2018). Characteristics of Vibration Frequency Measurement Based on Sound Field Imaging by Digital Holography. *OSA Contin.* 1, 200–212. doi:10.1364/osac.1.000200

Ramos Ruiz, A. E., Gürtler, J., Kuschmierz, R., and Czarske, J. W. (2019). Measurement of the Local Sound Pressure on a Bias-Flow Liner Using High-Speed Holography and Tomographic Reconstruction. *IEEE Access* 7, 153466–153474. doi:10.1109/access.2019.2948084

Ren, F., Wang, Z., Qian, J., Liang, Y., Dang, S., Cai, Y., et al. (2019). Multi-view Object Topography Measurement with Optical Sectioning Structured Illumination Microscopy. *Appl. Opt.* 58, 6288–6294. doi:10.1364/ao.58.006288

Schnars, U., and Jüptner, W. (1994). Direct Recording of Holograms by a CCD Target and Numerical Reconstruction. *Appl. Opt.* 33, 179–181. doi:10.1364/AO.33.000179

Seo, Y.-H., Choi, H.-J., Bae, J.-W., Kang, H.-J., Lee, S.-H., Yoo, J.-S., et al. (2007). A New Coding Technique for Digital Holographic Video Using Multi-View Prediction. *IEICE Trans. Inf. Syst.* E90-D, 118–125. doi:10.1093/ietisy/e90-1.1.118

Shaked, N. T., Rinehart, M. T., and Wax, A. (2009). Dual-interference-channel Quantitative-phase Microscopy of Live Cell Dynamics. *Opt. Lett.* 34, 767–769. doi:10.1364/OL.34.000767

Shimobaba, T., Masuda, N., Ichihashi, Y., and Ito, T. (2010). Real-time Digital Holographic Microscopy Observable in Multi-View and Multi-Resolution. *J. Opt.* 12, 065402. doi:10.1088/2040-8978/12/6/065402

Takaki, Y. (2015). Super Multi-View and Holographic Displays Using Mems Devices. *Displays* 37, 19–24. doi:10.1016/j.displa.2014.09.002

Takase, Y., Shimizu, K., Mochida, S., Inoue, T., Nishio, K., Rajput, S. K., et al. (2021). High-speed Imaging of the Sound Field by Parallel Phase-Shifting Digital Holography. *Appl. Opt.* 60, A179–A187. doi:10.1364/ao.404140

Torras-Rosell, A., Barrera-Figueroa, S., and Jacobsen, F. (2012). Sound Field Reconstruction Using Acousto-Optic Tomography. *J. Acoust. Soc. Am.* 131, 3786–3793. doi:10.1121/1.3695394

Yamaguchi, I., Matsumura, T., and Kato, J.-i. (2002). Phase-shifting Color Digital Holography. *Opt. Lett.* 27, 1108–1110. doi:10.1364/OL.27.001108

Yamaguchi, I., and Zhang, T. (1997). Phase-shifting Digital Holography. *Opt. Lett.* 22, 1268. doi:10.1364/OL.22.001268

Conflict of Interest: The authors declare that the research was conducted in the absence of any commercial or financial relationships that could be construed as a potential conflict of interest.

Publisher's Note: All claims expressed in this article are solely those of the authors and do not necessarily represent those of their affiliated organizations, or those of the publisher, the editors and the reviewers. Any product that may be evaluated in this article, or claim that may be made by its manufacturer, is not guaranteed or endorsed by the publisher.

frontiers | Frontiers in Photonics

TYPE Original Research
PUBLISHED 26 July 2022
DOI 10.3389/fphot.2022.936561

OPEN ACCESS

EDITED BY
Ting-Chung Poon,
Virginia Tech, United States

REVIEWED BY
Pascal Picart,
Le Mans Université, France
Jae-Hyeung Park,
Inha University, South Korea

*CORRESPONDENCE
Peng Gao,
peng.gao@xidian.edu.cn
Chao Zuo,
zuochao@njust.edu.cn

SPECIALTY SECTION
This article was submitted to Optical Information Processing and Holography,
a section of the journal
Frontiers in Photonics

RECEIVED 05 May 2022
ACCEPTED 30 June 2022
PUBLISHED 26 July 2022

CITATION
Shen Q, Sun J, Fan Y, Li Z, Gao P, Chen Q and Zuo C (2022), High-throughput artifact-free slightly off-axis holographic imaging based on Fourier ptychographic reconstruction.
Front. Photonics 3:936561.
doi: 10.3389/fphot.2022.936561

High-throughput artifact-free slightly off-axis holographic imaging based on Fourier ptychographic reconstruction

Qian Shen[1,2,3], Jiasong Sun[1,2,3], Yao Fan[1,2,3], Zhuoshi Li[1,2,3], Peng Gao[4]*, Qian Chen[3] and Chao Zuo[1,2,3]*

[1]Smart Computational Imaging Laboratory (SCILab), School of Electronic and Optical Engineering, Nanjing University of Science and Technology, Nanjing, JS, China, [2]Smart Computational Imaging Research Institute (SCIRI) of Nanjing University of Science and Technology, Nanjing, JS, China, [3]Jiangsu Key Laboratory of Spectral Imaging and Intelligent Sense, Nanjing, JS, China, [4]School of Physics, Xidian University, Xi'an, China

Slightly off-axis digital holographic microscopy (DHM) has recently gained considerable attention due to its unique ability to improve the space-bandwidth product (SBP) of the imaging system while separating the object information from the background intensity to a certain extent. In order to obtain a decent image reconstruction, the spectral aliasing problem still needs to be addressed, which, however, is difficult to be achieved by the conventional linear Fourier domain filtering. To this end, in this paper, we propose a high-throughput artifact-free slightly off-axis holographic reconstruction method based on Fourier ptychographic microscopy (FPM). Inspired by the nonlinear optimized phase reconstruction algorithm of FPM, we perform constrained updates between the real and Fourier domains in an iterative manner to reconstruct the complex amplitude by the hologram intensity. Experimental results on live HeLa cell samples show that the proposed method can provide higher reconstruction accuracy and better image quality compared with the conventional Fourier method and the Kramers–Kronig (KK) relation-based method.

KEYWORDS

digital holographic microscopy, quantitative phase imaging, space-bandwidth product, fourier ptychography, nonlinear optimization

Introduction

In the field of optical microscopy, quantitative phase imaging (QPI) is an essential tool for biomedical research, possessing the distinctive ability of optical thickness measurement of live cells without exogenous contrast agents (Lee et al., 2013; Zuo et al., 2015; Sun et al., 2017; Zuo et al., 2017; Fan et al., 2019; Zuo et al., 2020). As a classical QPI technique, digital holographic microscopy (DHM) (Cuche et al., 1999; Mann et al., 2005; Chen et al., 2011) combines the principle of interferometry and holography, allowing for single-shot digital recording and numerical reconstruction

of the object wavefront to quantitatively recover amplitude and phase with high accuracy in real time. Based on the off-axis architecture, DHM introduces an additional coherent reference beam that is tilted superimposed with the object beam, which encodes the invisible phase information into an interferogram. Capture the intensity signal of the hologram by imaging devices such as a CCD and then perform phase demodulation with fringe analysis algorithms.

During the hologram acquisition process, the intensity of the two coherent beams (often referred to as the zero-order term) and the object complex amplitude information are superimposed on the recorded signal simultaneously (Gao et al., 2013). Conventional off-axis holography completely separates the real image from its twin image and zero-order term in the spatial frequency domain by adjusting the tilt angle. Combining band-pass filtering and deconvolution to realize high-speed single-shot measurement, i.e. Fourier method (Takeda et al., 1982). However, the linear solution involves solely Fourier domain filtering , sacrificing the utilization of spatial bandwidth. The imaging throughput is quantitatively described by the space-bandwidth product (SBP), which varies with the recovery method and the modulation direction of the reference beam. Since the zero-order has a bandwidth of twice the one of the imaging term (the twin images), the maximum spatial bandwidth achieved by this linear solution is $\frac{N}{2+3\sqrt{2}}$ (Pavillon et al., 2009) for a region of $N \times N$ pixels with uniform sampling in the absence of spectral overlap. The limited bandwidth of the off-axis system is inefficient regarding the SBP of the complex amplitude image. It is negative for enhancing the imaging resolution, while the realization of real-time high-throughput imaging is the fundamental target constantly pursued in the development of microscopic imaging technology (Trusiak, 2021).

To improve the SBP of off-axis holography, spectral aliasing of zero-order with diffraction terms in the spatial frequency domain is unavoidable, which leads to a loss of imaging quality, such as reduced resolution or produced artifacts. So how to make full use of the spatial bandwidth and achieve artifact-free imaging while maintaining the diffraction limit resolution is a crucial issue. Various zero-order suppression methods have been proposed (Trusiak et al., 2020). The nonlinear filtering (Pavillon et al., 2009) in the cepstral domain can confine the object wave modulation to one quadrant of the spectrum and enhance the utilization of spatial bandwidth to $\frac{N}{4}$. Alternatively, the zero-order can be suppressed by subtracting the object intensity from the hologram with the reconstructed object wavefront in an iterative manner, loosening the constraints on bandwidth (Pavillon et al., 2010). Furthermore, on the basis of the nonlinear filtering method, high SBP off-axis holographic imaging can be achieved by exploiting the Kramers–Kronig (KK) relations (Baek et al., 2019). With the zero-padding operation in the frequency domain, the spectral aliasing is substantially reduced without an iterative process or imposing any restriction on objects, which theoretically increases the spatial bandwidth to $\frac{N}{2+\sqrt{2}}$. However, these methods are not applicable when the intensity of the reference beam is smaller than that of the object beam since the power series of the object-reference ratio is divergent in the Fourier domain.

With the proposal of phase retrieval (Fienup, 1982; Bauschke et al., 2002; Shechtman et al., 2015), nonlinear optimization algorithms provide a new demodulation perspective on optical phase microscopy. A particularly classic method in this field to recover phase from a single intensity measurement is the Gechberg-Saxton (GS) algorithm (Gerchberg, 1972, 1971), and related improved algorithms have also been proposed (Gonsalves, 1976; Fienup, 1978). These methods are based on nonlinear optimal iterations, which usually define a cost function similar to the intensity difference, and reconstruct the phase by constrained updates back and forth between the intensity in the spatial domain and aperture in the frequency domain. Nonlinear optimal iterative reconstruction methods have been widely applied in the field of QPI, such as lens-free microscopic imaging (Ozcan and Demirci, 2008; Seo et al., 2009) and Fourier ptychographic microscopy (FPM) (Zheng et al., 2013), etc. The original solutions to FPM are based on the gradient descent method, which retrieves the phase information of the samples by alternating iterations in the real and Fourier spaces, and is a highly representative integration of nonlinear optimization algorithms and QPI techniques.

Nevertheless, nonlinear optimization algorithms are rarely reported in holographic phase recovery since conventional DHM already has convenient demodulation methods (Fourier method for off-axis holography (Takeda et al., 1982) and phase-shift method for on-axis holography (Hariharan et al., 1987)), which can recover the phase in a single step without complicated iterative processes (Latychevskaia, 2019). However, when breaking the SBP limitation of conventional off-axis holography, the Fourier method cannot reconstruct the phase correctly due to the aliasing of spectral information. Therefore, nonlinear optimization algorithms are considered to solve the above problem. We present and experimentally demonstrate a QPI technique for high-throughput artifact-free slightly off-axis holographic imaging based on a nonlinear optimization algorithm similar to Fourier ptychographic reconstruction. Inspired by the phase retrieval process of FPM, the complex amplitude recovery is viewed as a nonlinear optimization problem to be solved by a method like the GS algorithm. In the premise that the linear method cannot correctly solve for the object wavefront, the proposed optimal iterative solution algorithm is more universal with no restrictions on the intensity of two coherent beams and unconstrained spectral configuration, which is distinct from all previous off-axis holography phase recovery methods.

Principle

Based on the nonlinear iterative solution of FPM, first built the forward mathematical modeling of the off-axis digital holographic imaging process. The spectrum of the object beam that reaches the camera target surface is $O(u, v)P(u, v)$, where $O(u, v)$ is the spectrum of the complex amplitude distribution of the measured object, $P(u, v)$ represents the pupil function defined by the NA of the microscope objective and the illumination wavelength, and (u, v) denotes the frequency domain coordinates. The corresponding complex amplitude of the object beam is $O(x, y) = \mathcal{F}^{-1}[O(u, v)P(u, v)]$, where $\mathcal{F}^{-1}$ denotes inverse Fourier transform. The reference beam is considered as a quasi-plane wave with a tilt angle θ to the object beam, which is expressed as $R(x, y) = |R| \exp(-ik \sin\theta x)$. According to the interference principle of coherent superposition, the complex amplitude distribution of the hologram is

$$U(x, y) = O(x, y) + R(x, y) \tag{1}$$

where the complex amplitude of the reference beam is reconstructed by the amplitude information obtained from the captured intensity image of the reference beam and the offset of ±1-order in the hologram spectrum. So $R(x, y)$ is regarded as a known quantity for the subsequent calculations.

Since only the intensity distribution of the optical wavefield can be converted to a digital signal while the phase information is completely lost during the camera recording process, the complex wavefront requires some phase recovery methods for reconstruction. We learn from the nonlinear optimization idea of FPM and use the alternating projection method similar to the GS iterative algorithm, which recognize the complex amplitude reconstruction of the hologram as a nonlinear optimization problem. Essentially, the proposed phase recovery method for the slightly off-axis holography is to define a cost function that will converge to a minimum by updating functions back and forth between the real and Fourier spaces.

Next, we specify the objective cost function and the optimal solution algorithm used in the proposed iterative method. Define the cost function with the purpose of minimizing the amplitude error

$$\varepsilon(O) = \sum_{x,y} \left| \sqrt{I(x, y)} - \left| F^{-1}[O(u, v)P(u, v)] + R(x, y) \right| \right|^2. \tag{2}$$

where $I(x, y) = |U(x, y)|^2$ is the intensity of the hologram. As the iterations proceed, the amplitude of the hologram reconstructed from the object complex wavefront to be recovered will gradually approach that of the captured hologram. Theoretically, the cost function, i.e., the amplitude error function, can eventually converge to zero, at which point the hologram complex amplitude update also converges to the real distribution.

Then we derive the update equation for the nonlinear optimization solution algorithm mentioned above. According to Parseval's theorem, the cost function ε can be simplified as

$$\varepsilon(O) = \sum_{u,v} \|U^u(u, v) - U^e(u, v)\|^2 \tag{3}$$

where $U^e(u, v) = O(u, v)P(u, v) + R(u, v)$ represents the subspectrum before the update and $U^u(u, v)$ represents the subspectrum after the update exploiting the captured hologram intensity $I(x, y)$. The update process is expressed by the equation $U^u(x, y) = \sqrt{I(x, y)} \frac{U^e(x,y)}{|U^e(x,y)|}$.

The first-order derivative of the cost function is thus a component of Eq 11 and can be expressed as

$$\nabla_O \varepsilon(O) = -\left[P^*(u, v)\left(U^u(u, v) - U^e(u, v)\right)\right]. \tag{4}$$

The derivation process is explained in Appendix A. By minimizing the derivative with the gradient descent method to make it infinitely close to zero, thus the cost function Eq 2 can be reduced to the minimum value.

Finally, we achieve the update equation for the hologram complex amplitude distribution

$$U(u, v) = U(u, v) + \alpha \frac{|P(u, v)|^2}{|P(u, v)|^2_{\max}} \frac{P^*(u, v)}{|P(u, v)|^2 + \delta} [U^u(u, v) - U^e(u, v)]. \tag{5}$$

α is the update step length and usually ranges from 0.5 to 1. Values of α around 1 (not greater than 1) works well in our simulations and experiments. δ is a regularization parameter (a minimal value near 0) to prevent the denominator from going to zero. It should be noted that the $P(u, v)$ in Eqs 3–5 is a mask function for spectrum selection of the numerical reconstruction in the actual phase recovery process (the ideal state is the above-mentioned pupil function determined by NA).

The iterative procedures derived from Eq 5 are shown in algorithm 1 and Figure 1 as an example for the case where the value of update step α is 1. During the iterative process, the square root of the intensity of the recorded digital hologram is always employed to update the reconstructed complex amplitude. Based on the gradient descent method, the cost function gradually converges to zero by updating functions back and forth between the real and Fourier spaces. Then the complex amplitude distribution of the hologram is reconstructed to recover the phase information of the sample.

Exploiting the nonlinear optimization algorithm, we can construct an slightly off-axis holographic system with extreme resolution that makes full use of the space bandwidth, in which the spectral configuration of the twin images is exactly tangent at the origin without overlapping by diagonal modulation of the reference beam and selection of suitable system parameters. In

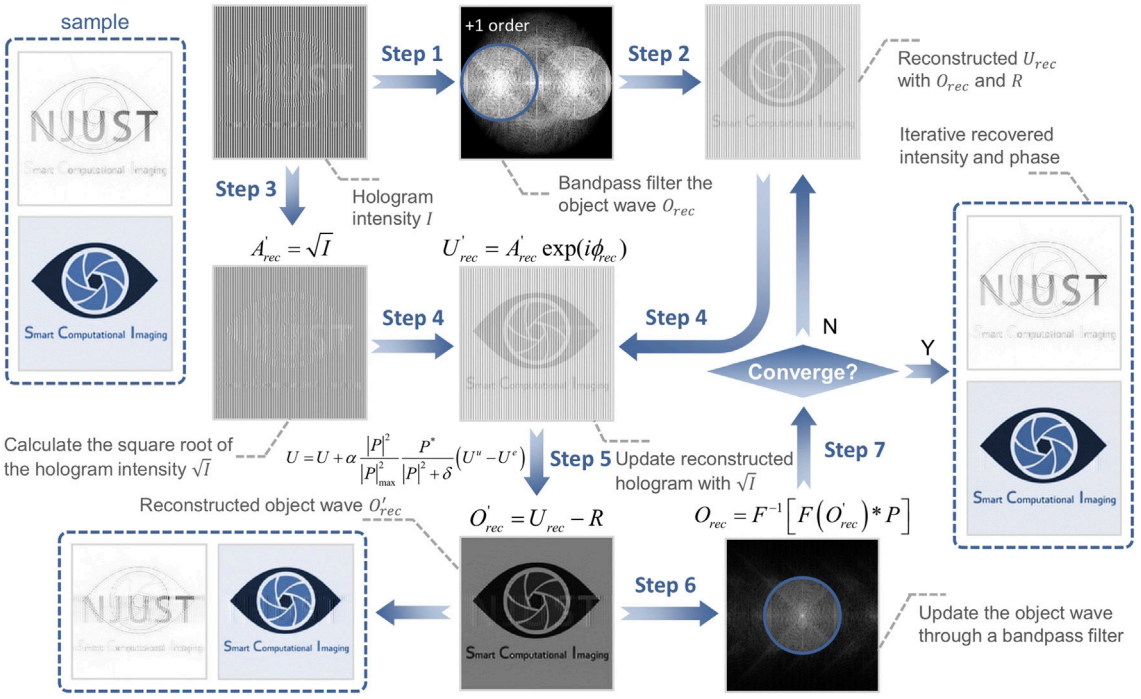

FIGURE 1
Flow chart of the nonlinear optimization iterative algorithm for phase recovery.

other words, it is able to iteratively reconstruct the object complex amplitude while guaranteeing a maximum spatial bandwidth of $\frac{N}{2+\sqrt{2}}$, and there is no additional requirement for the intensity of the object and reference beam in the iterative process.

Algorithm 1. Nonlinear optimization iterative algorithm based on FPM for slightly off-axis DHM phase recovery

Require: the hologram intensity distribution I; the reference wave complex amplitude R; the pupil function $P(u, v)$.

$I = |O + R|^2 = |O|^2 + |R|^2 + RO^* + R^*O$
$A'_{rec} = \sqrt{I}$
$O_i = \mathscr{F}^{-1}[P(u,v) \cdot \mathscr{F}(I)]/R^*$
$O_{rec} = O_i$
repeat
  $U_{rec} = O_{rec} + R = A_{rec}\exp(i\phi_{rec})$
  $U'_{rec} = A'_{rec}\exp(i\phi_{rec})$
  $U_{rec} = U_{rec} + \alpha\frac{|P|^2}{|P|^2_{max}}\frac{P^*}{|P|^2+\delta}(U'_{rec} - U_{rec})$
  $O'_{rec} = U_{rec} - R$
  $O_{rec} = \mathscr{F}^{-1}[P(u,v) \cdot \mathscr{F}(O'_{rec})]$
until converge
return O_{rec}

Simulation

Simulations are carried out to verify the validity and effectiveness of the proposed algorithm. To investigate the performance of the proposed method for phase demodulation at $R < O$, we choose the case of $R/O = 0.7$ for simulation and compare the reconstruction results with that of the conventional off-axis method and KK method. The simulation results are shown in Figure 2. Figure 2A1, A2 are used as amplitude image and phase image respectively to generate the hologram [Figue 2A3]. Here we used a vertical reference beam modulation in these simulations and the spectrum of the hologram is shown in Figure 2A4. To compare the QPI results of the above methods more intuitively, we also calculated the root mean square error (RMSE) images of the reconstructed amplitude and phase. It is obvious that the proposed algorithm can reconstruct the complex amplitude image of the object wave with high accuracy and its errors are almost indistinguishable to the naked eye, as shown in Figures 2B1–B4. In contrast, the conventional off-axis method has many artifacts in the reconstructed amplitude and phase due to the inability to suppress the 0-order term [Figures 2C1–C4], and the results of the KK method not only have artifacts, but also a constant term error on the background of the amplitude image [Figures 2D1–D4].

In order to further verify the stability, convergence, and robustness properties of the proposed nonlinear optimization algorithm, and further compare the effectiveness of the above methods at an arbitrary reference-object ratio (R/O), we simulate all cases with R/O from 0 to 1.2 and plotted the correlation curves demonstrated in Figure 3. It can be seen that the blue curve always lies above the curves of the other colors and tends to be

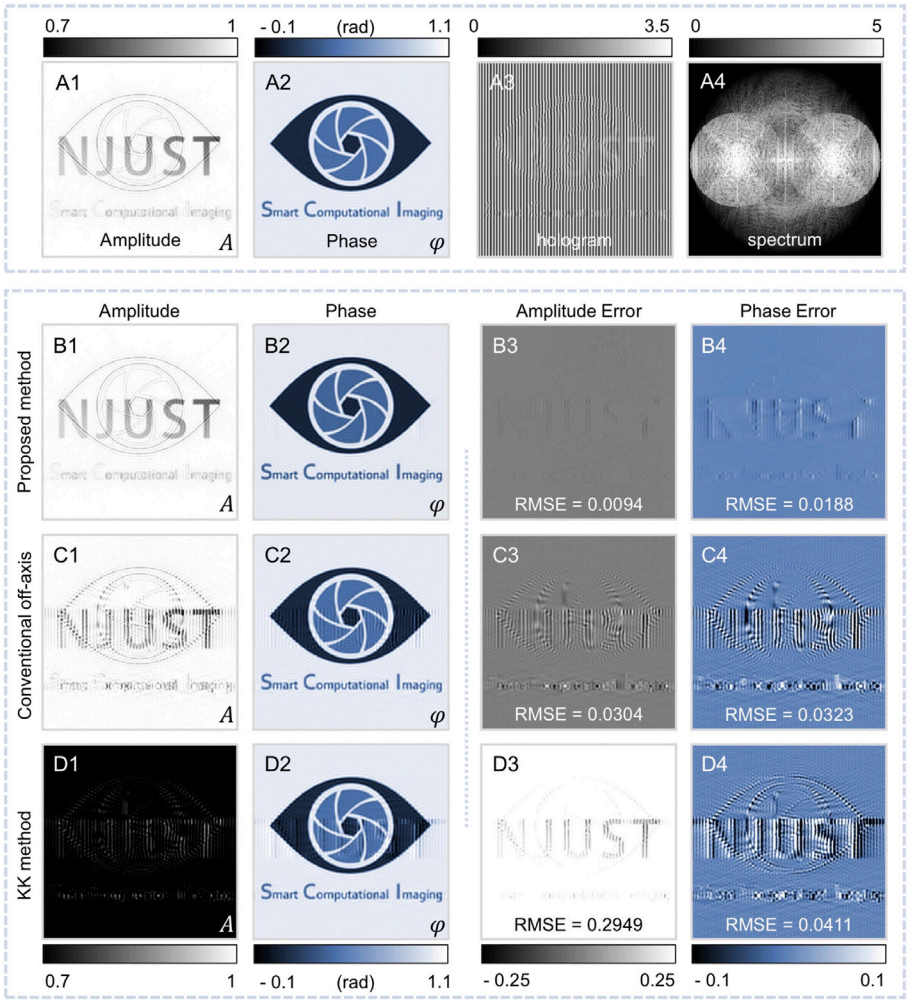

FIGURE 2
Comparison of the simulation results of the proposed method, conventional off-axis method and KK method in case of R/O = 0.7. **(A1,A2)** Simulated amplitude and phase. **(A3)** Hologram simulated with **(A1,A2)**. **(A4)** Spectrum of the hologram. **(B1–B4)** Reconstructed amplitude, phase and the corresponding errors with the proposed method. **(C1–C4)** Reconstructed amplitude, phase and the corresponding errors with conventional off-axis method. **(D1–D4)** Reconstructed amplitude, phase and the corresponding errors with KK method.

close to one even when the intensity of the reference beam is as small as almost one-tenth of the object beam, much higher than the other curves. This shows that the proposed method is applicable to all reference-object ratios and has better performance than the linear methods even when $R > O$. We also compare the convergence of the RMSE between the proposed iterative method and Pavillon method for the case of $R/O = 0.7$ and $R/O = 0.9$ of the hologram in Figure 4 and display the best reconstruction result during the iteration ($R/O = 0.7$). It is obvious that the RMSE of the Pavillon method is divergent when $R/O = 0.7$ and its best result still has serious artifacts. In comparison, our method has a stable declining RMSE trend and maintains a very small error, which means that the RMSE converges in only 10 iterations, ensuring the efficiency of phase recovery. (RMSE 0.0188 rad, total computation time 0.035s with a 2.60 GHz laptop).

Let's specifically analyze why the Pavillon method and KK method are not applicable in the case of object-reference ratios (O/R) greater than or equal to 1. The parasitic terms of the error between the estimator and the object 0-order of the Pavillon method are powers of O/R that must meet the conditions of $O < R$ to not diverge. The nonlinear filtering and KK methods convert the extraction of +1-order to the solution of $\log(1 + O/R)$, which is a power series of O/R through Taylor expansion. When $O/R < 1$, $(O/R)^n$ decreases rapidly with increasing order n and decays outward in the spectrum along the modulation direction, with the overflow superimposed on its conjugate image on the other side of the spectrum. The KK method ensures the continuity and

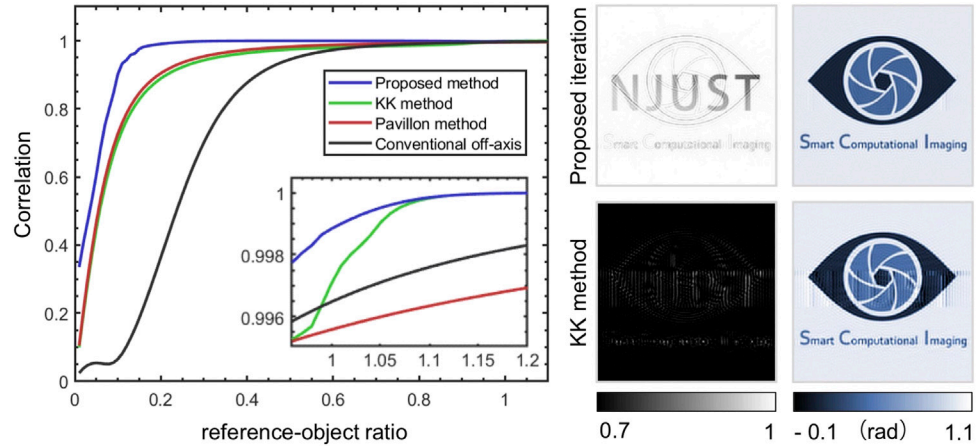

FIGURE 3
Correlation curves of the proposed method, KK method, Pavillon method and conventional Fourier method.

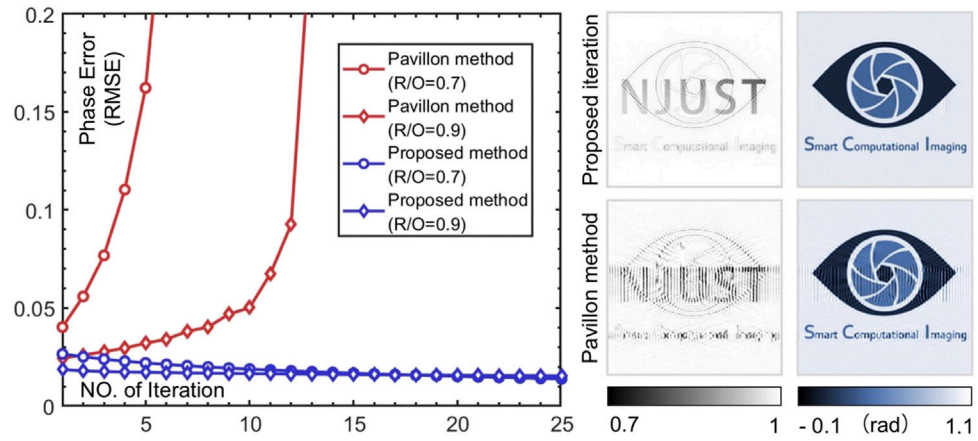

FIGURE 4
Comparison between two iterative methods. Left: RMSE curves versus the iteration number for the case of R/O = 0.7 and R/O = 0.9 of the hologram. Right: the best reconstruction results for the case of R/O = 0.7.

integrity of higher-order terms in the frequency domain by zero-padding. Nevertheless, if $O/R \geq 1$, the higher-order terms tend to diverge and overlap severely with the conjugate term. As a result, the Hilbert transform (HT) cannot separate $\log(1 + O/R)$ and thus the residual intensity information will damage the accuracy of phase recovery. Therefore, only when the reference-object ratio is greater than 1, the convergence of the Pavillon method can be guaranteed and high precision recovery of the KK method can be ensured. In addition, the KK method should change the direction of the zero-padding operation and HT for different spectral configurations, so the parameters have to be adjusted according to the imaging system in practice.

Experiment

To demonstrate the capability of the nonlinear optimization algorithm, various samples are imaged, under the condition where the zero-order and diffraction terms severely overlap in the frequency space. Digital holographic smart computational light microscope (DH-SCLM) (Fan et al., 2021) developed by SCILab is used to acquire the hologram. The beam is transmitted by the objective lens (UPLanSAPO ×10/0.4NA, Olympus, Japan) and recorded by the camera (The Imaging Source DMK 23U274, 1600 × 1200, 4.4 μm). The central wavelength of the illumination is 532 nm. With these system parameters, adjust the tilt angle of the reference beam until the imaging term is diagonally tangent

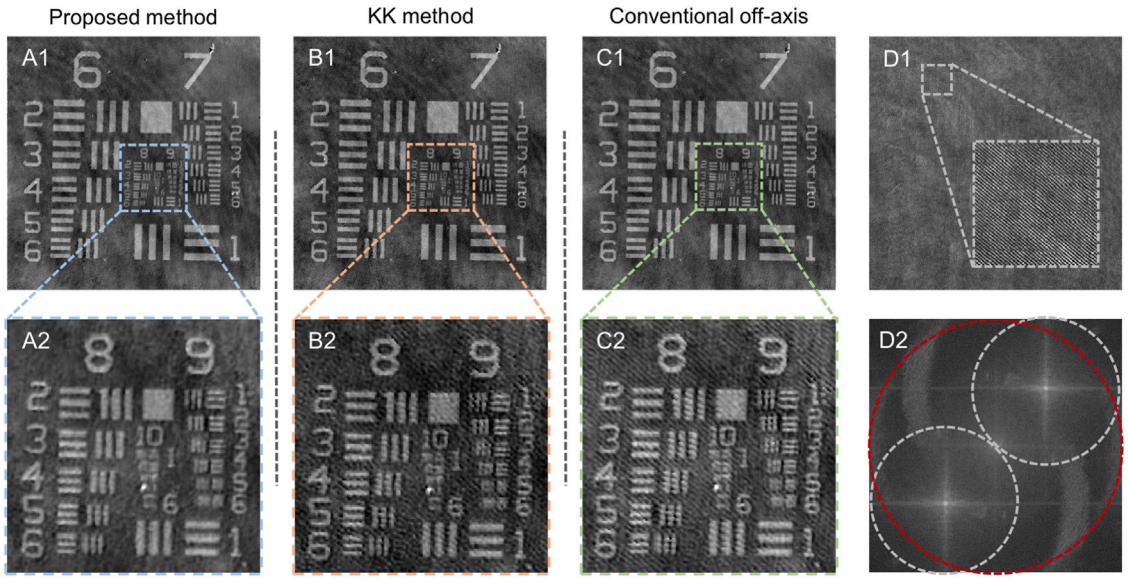

FIGURE 5
Comparison of the experimental results of the proposed method, KK method and conventional Fourier method. **(A1)** Reconstructed phase with the proposed method. **(A2)** The enlarged sub-region of interest of the reconstructed phase in **(A1)**. **(B1)** Reconstructed phase with KK method. **(B2)** The enlarged sub-region of interest of the reconstructed phase in **(B1)**. **(C1)** Reconstructed phase with conventional off-axis method. **(C2)** The enlarged sub-region of interest of the reconstructed phase in **(C1)**. **(D1)** Hologram in the experimental condition. **(D2)** Fourier transform of **(D1)** (red circle indicates 0-order, white circles indicate ±1-order).

in the frequency space to achieve maximum utilization of the spatial bandwidth. The biggest advantage of the proposed method is the relaxed restriction on the reference-object ratio, so we conduct the experiments under the same conditions as the simulation ($R/O = 0.7$). Complex amplitudes are recovered by the proposed method, the KK method, and the conventional off-axis method, respectively. For comparison, an identical interferogram per sample is used for the three methods. In addition, the intensity of the reference beam is recorded for the subsequent phase reconstruction algorithm, which needs to be measured only once.

Interferogram of a standard phase resolution target (QPT^{TM}, Benchmark Technologies Corporation, United States , RIn = 1.52) is imaged as shown in Figure 5. The proposed iterative method recovers the quantitative phase with high accuracy in the case of reaching the theoretical resolution of the holographic imaging system and without excess background [Figures 5A1, A2]. However, since the reference-object ratio of the system is less than 1, the KK method cannot suppress all the 0-order so that the reconstructed phase image still carries some artifacts formed by the intensity information of the hologram [Figures 5B1, B2]. And in the conventional method, the recovered phase image has severe artifacts [Figures 5C1, C2] due to the lack of ability to remove the part of the 0-order term that overlaps with the +1-order in the frequency domain by bandpass filtering. In this case, the slightly off-axis hologram has a fringe pattern with high spatial frequency [Figure 5D1] and a spectral configuration with the maximum SBP [Figure 5D2].

Then the nonlinear optimization algorithm is applied to the QPI of live HeLa cells as shown in Figure 6. The phase images reconstructed by the proposed iterative method are shown in Figures 6A1–A3, which obtain the internal structure of the cells without any artifacts since the unwanted zero-order term is completely suppressed. The field of view (FoV) of Figure 6A1 is 0.33 × 0.44 mm with a diffraction-limited size of 0.81 μm. The SBP of the complex amplitude image is 257000 pixels [the area of the FoV, 0.1452 mm^2, multiplied by the area of the spatial frequency band, $\pi(\mathrm{NA}/\lambda)^2$]. For comparison, the KK method can suppress the zero-order term to some extent, but it cannot converge and result in blurring or even loss of cell details and obvious artifacts in the background [Figures 6B1–B3]. When the phase is recovered by the conventional method, simple filtering retains some of the intensity information of the object beam and reference beam, thus drastically reducing the correctness of the phase reconstruction [Figures 6C1–C3].

Finally, we perform an experiment to verify the enhancement in the SBP of the proposed method. For imaging, an Olympus 20× (0.4 NA) objective lens is adopted. The total magnification of the setup is kept at 20, identical to the magnification of the objective lens. Adjust the tilt angle of the reference beam to generate an absolute diagonal off-axis hologram with the ±1-order completely separated from the 0-order. Image the same

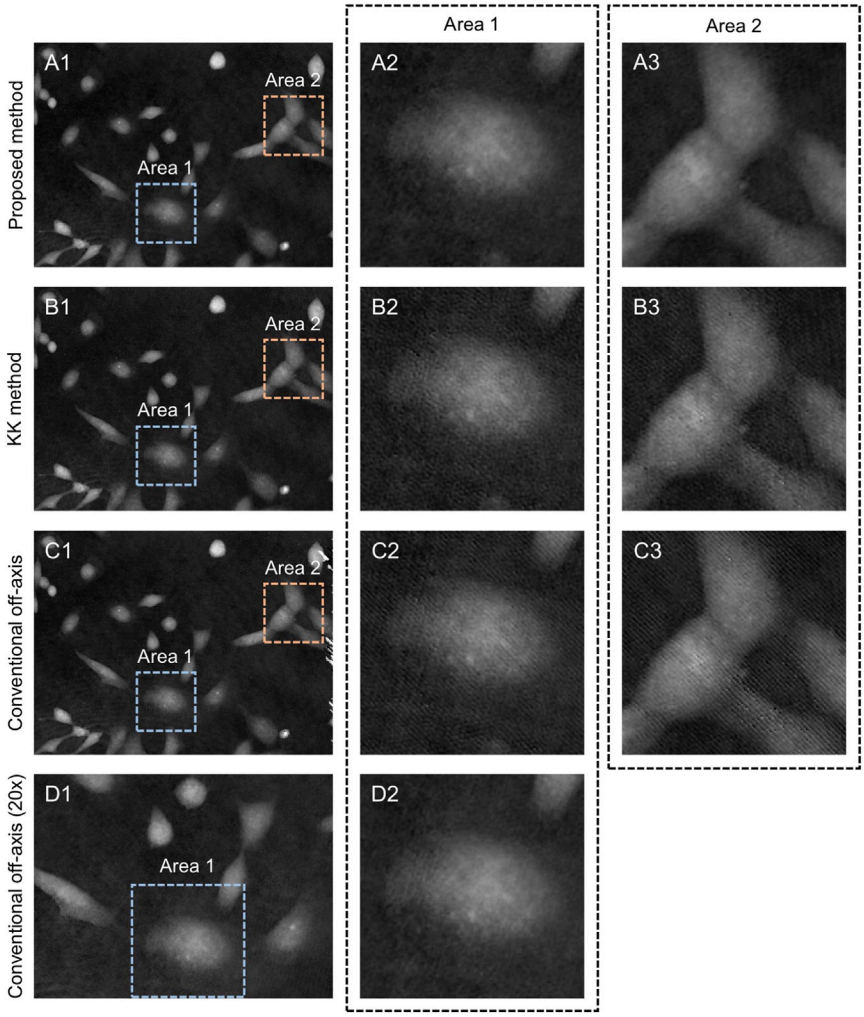

FIGURE 6
Comparison of the experimental results of the proposed method, KK method and conventional off-axis method. **(A1)** Reconstructed phase with the proposed method. **(A2,A3)** The sub-regions of interest of phase in **(A1)**. **(B1)** Reconstructed phase with KK method. **(B2)**, **(B3)** The sub-regions of interest of phase in **(B1)**. **(C1)** Reconstructed phase with conventional off-axis method (magnification = 10). **(C2,C3)** The sub-regions of interest of phase in **(C1)**. **(D1)** Reconstructed phase with conventional off-axis method (magnification = 20). **(D2)** The sub-regions of interest of phase in **(D1)**.

HeLa sample with the system and conduct phase recovery by the conventional off-axis method. The measured quantitative phase image is shown in Figures 6D1, D2, which is almost the same as that reconstructed by our proposed nonlinear optimization method in a diagonal tangent spectral configuration. The ×10 and ×20 objectives have the same numerical aperture, which means both achieve the same lateral resolution. However, the difference in objective magnification results in the FoV and SBP at ×20 objective reduced to 1/4 of that at ×10 objective, where SBP is only 64200 pixels. In contrast, the proposed method provide a 4-fold increase in the SBP compared to the conventional method while performing the phase recovery correctly.

Discussion and conclusion

We have demonstrated a QPI technique for high-SBP slightly off-axis DHM based on Fourier ptychographic reconstruction. Exploiting the reconstruction principle of FPM, the optimal iterative solution algorithm reconstructs an exact complex amplitude of the object wavefront without imposing any constraint on the reference-object ratio. It effectively utilizes the spatial bandwidth to provide a 4-fold increase in the SBP compared to the linear solution and achieve the ultimate maximum bandwidth in all off-axis holography since there is no requirement for spectral configuration. The nonlinear optimization algorithm is experimentally demonstrated to have

high accuracy at an arbitrary reference-object ratio and can realize high-throughput artifact-free imaging with spectral aliasing.

The optimal iterative solution algorithm is fundamentally different from previous methods for zero-order suppression under the spectral overlap in slightly off-axis holography. The suppression principle of the nonlinear filtering and KK method involves constructing an intermediate function whose Taylor expansion is a power series of the object-reference ratio. Nonlinear filtering first proposes the idea of taking the logarithm of the intensity ratio of the hologram to the reference beam, which transforms the product into a sum, allowing for the subsequent separation of the interference terms from the zero-order term. The KK method brilliantly proves the analyticity of the intermediate function, i. e., a variant of the object-reference ratio, in the upper half-plane, thus guaranteeing the KK relationship between the real and imaginary parts of the intermediate function. However, these must be based on the condition that the object-reference ratio is less than 1. Otherwise, the higher-order terms will diverge in the frequency domain and severely overlap with other terms as the order increases. Similarly, the error between the estimator and the object zero-order in the Pavillon method contains a power series of the object-reference ratio, which also converges only under this condition.

In contrast, the proposed method uses the nonlinear optimization algorithm to derive the update equation by forward modeling the process of holographic imaging. As long as the spectrum of the +1-order and -1-order do not overlap (which is sufficiently fulfilled by all off-axis holographic systems), the optimal iterative solution algorithm can be applied. During the phase recovery process, the reconstructed hologram amplitude gradually approximates the recorded true value by iteration until the error converges to zero, i.e., the measured complex amplitude is exact. The nonlinear optimization iteration is unconstrained for object-reference ratio and spectral configuration, which greatly relaxes the requirements on the system parameters and exhibits enhanced robustness to system errors.

The proposed method can be combined with other techniques for further improvement. Referring to the adaptive step-size strategy introduced by Zuo (Zuo et al., 2016) et al., the stability and robustness of the phase reconstruction towards noise can be enhanced by altering the fixed step-size to an adaptive step-size. OU (Ou et al., 2014) et al. propose the embedded pupil function recovery (EPRY), which is expected to be combined with the proposed method to reconstruct the aberration of the objective lens while recovering the quantitative phase of the object. In addition, the integration of nonlinear optimization with synthetic aperture digital holography can also be considered to improve the spatial resolution (Gao and Yuan, 2022). We envision that the proposed method will benefit off-axis holographic imaging with an enhanced SBP and contribute to the combination of nonlinear optimal phase reconstruction algorithm with more QPI techniques for application in large-scale studies of cells and other fields.

Data availability statement

The original contributions presented in the study are included in the article further inquiries can be directed to the corresponding authors.

Author contributions

CZ conceived the idea. QS did the experiments. CZ, JS, and QC supervised the project. All the authors contributed to discussion on the results for this manuscript.

Funding

This work was supported by the National Natural Science Foundation of China (61905115, 62105151, 62175109, U21B2033), Leading Technology of Jiangsu Basic Research Plan (BK20192003), Youth Foundation of Jiangsu Province (BK20190445, BK20210338), Fundamental Research Funds for the Central Universities (30920032101), and Open Research Fund of Jiangsu Key Laboratory of Spectral Imaging and Intelligent Sense (JSGP202105, JSGP202201).

Conflict of interest

The authors declare that the research was conducted in the absence of any commercial or financial relationships that could be construed as a potential conflict of interest.

Publisher's note

References

Baek, Y., Lee, K., Shin, S., and Park, Y. (2019). Kramers–kronig holographic imaging for high-space-bandwidth product. *Optica* 6, 45. doi:10.1364/optica.6.000045

Bauschke, H. H., Combettes, P. L., and Luke, D. R. (2002). Phase retrieval, error reduction algorithm, and fienup variants: a view from convex optimization. *J. Opt. Soc. Am. A* 19, 1334–13345. doi:10.1364/josaa.19.001334

Chen, N., Yeom, J., Jung, J.-H., Park, J.-H., and Lee, B. (2011). Resolution comparison between integral-imaging-based hologram synthesis methods using rectangular and hexagonal lens arrays. *Opt. Express* 19, 26917–26927. doi:10.1364/oe.19.026917

Cuche, E., Bevilacqua, F., and Depeursinge, C. (1999). Digital holography for quantitative phase-contrast imaging. *Opt. Lett.* 24, 291. doi:10.1364/ol.24.000291

Fan, Y., Li, J., Lu, L., Sun, J., Hu, Y., Zhang, J., et al. (2021). Smart computational light microscopes (sclms) of smart computational imaging laboratory (scilab). *PhotoniX* 2, 19. doi:10.1186/s43074-021-00040-2

Fan, Y., Sun, J., Chen, Q., Pan, X., Tian, L., Zuo, C., et al. (2019). Optimal illumination scheme for isotropic quantitative differential phase contrast microscopy. *Photonics Res.* 7, 890–904. doi:10.1364/prj.7.000890

Fienup, J. R. (1982). Phase retrieval algorithms: a comparison. *Appl. Opt.* 21, 2758. doi:10.1364/ao.21.002758

Fienup, J. R. (1978). Reconstruction of an object from the modulus of its fourier transform. *Opt. Lett.* 3, 27–29. doi:10.1364/ol.3.000027

Gao, P., Pedrini, G., and Osten, W. (2013). Structured illumination for resolution enhancement and autofocusing in digital holographic microscopy. *Opt. Lett.* 38, 1328–1330. doi:10.1364/ol.38.001328

Gao, P., and Yuan, C. (2022). Resolution enhancement of digital holographic microscopy via synthetic aperture: a review. *gxjzz.* 3, 105. doi:10.37188/lam.2022.006

Gerchberg, R. W. (1972). A practical algorithm for the determination of phase from image and diffraction plane pictures. *Optik* 35, 237–246.

Gerchberg, R. W. (1971). Phase determination for image and diffraction plane pictures in the electron microscope. *Opt. Stuttg.* 34, 275.

Gonsalves, R. (1976). Phase retrieval from modulus data. *J. Opt. Soc. Am.* 66, 961. doi:10.1364/josa.66.000961

Hariharan, P., Oreb, B. F., and Eiju, T. (1987). Digital phase-shifting interferometry: a simple error-compensating phase calculation algorithm. *Appl. Opt.* 26, 2504. doi:10.1364/ao.26.002504

Latychevskaia, T. (2019). Iterative phase retrieval for digital holography: tutorial. *J. Opt. Soc. Am. A* 36, D31–D40. doi:10.1364/josaa.36.000d31

Lee, K., Kim, K., Jung, J., Heo, J., Cho, S., Lee, S., et al. (2013). Quantitative phase imaging techniques for the study of cell pathophysiology: from principles to applications. *Sensors* 13, 4170–4191. doi:10.3390/s130404170

Mann, C. J., Yu, L., Lo, C.-M., and Kim, M. K. (2005). High-resolution quantitative phase-contrast microscopy by digital holography. *Opt. Express* 13, 8693. doi:10.1364/opex.13.008693

Ou, X., Zheng, G., and Yang, C. (2014). Embedded pupil function recovery for fourier ptychographic microscopy. *Opt. Express* 22, 4960–4972. doi:10.1364/oe.22.004960

Ozcan, A., and Demirci, U. (2008). Ultra wide-field lens-free monitoring of cells on-chip. *Lab. Chip* 8, 98–106. doi:10.1039/b713695a

Pavillon, N., Arfire, C., Bergoënd, I., and Depeursinge, C. (2010). Iterative method for zero-order suppression in off-axis digital holography. *Opt. Express* 18, 15318–15331. doi:10.1364/oe.18.015318

Pavillon, N., Seelamantula, C. S., Kühn, J., Unser, M., and Depeursinge, C. (2009). Suppression of the zero-order term in off-axis digital holography through nonlinear filtering. *Appl. Opt.* 48, H186–H195. doi:10.1364/ao.48.00h186

Seo, S., Su, T.-W., Tseng, D. K., Erlinger, A., and Ozcan, A. (2009). Lensfree holographic imaging for on-chip cytometry and diagnostics. *Lab. Chip* 9, 777–787. doi:10.1039/b813943a

Shechtman, Y., Eldar, Y. C., Cohen, O., Chapman, H. N., Miao, J., Segev, M., et al. (2015). Phase retrieval with application to optical imaging: a contemporary overview. *IEEE Signal Process. Mag.* 32, 87–109. doi:10.1109/msp.2014.2352673

Sun, J., Zuo, C., Zhang, L., and Chen, Q. (2017). Resolution-enhanced fourier ptychographic microscopy based on high-numerical-aperture illuminations. *Sci. Rep.* 7, 1187. doi:10.1038/s41598-017-01346-7

Takeda, M., Ina, H., and Kobayashi, S. (1982). Fourier-transform method of fringe-pattern analysis for computer-based topography and interferometry. *J. Opt. Soc. Am.* 72, 156. doi:10.1364/josa.72.000156

Trusiak, M., Cywińska, M., Mico, V., Picazo-Bueno, J. Á., Zuo, C., Zdańkowski, P., et al. (2020). Variational hilbert quantitative phase imaging. *Sci. Rep.* 10, 13955. doi:10.1038/s41598-020-69717-1

Trusiak, M. (2021). Fringe analysis: single-shot or two-frames? quantitative phase imaging answers. *Opt. Express* 29, 18192–18211. doi:10.1364/oe.423336

Zheng, G., Horstmeyer, R., and Yang, C. (2013). Wide-field, high-resolution fourier ptychographic microscopy. *Nat. Photonics* 7, 739–745. doi:10.1038/nphoton.2013.187

Zuo, C., Li, J., Sun, J., Fan, Y., Zhang, J., Lu, L., et al. (2020). Transport of intensity equation: a tutorial. *Opt. Lasers Eng.* 135, 106187. doi:10.1016/j.optlaseng.2020.106187

Zuo, C., Sun, J., and Chen, Q. (2016). Adaptive step-size strategy for noise-robust fourier ptychographic microscopy. *Opt. Express* 24, 20724–20744. doi:10.1364/oe.24.020724

Zuo, C., Sun, J., Li, J., Zhang, J., Asundi, A., Chen, Q., et al. (2017). High-resolution transport-of-intensity quantitative phase microscopy with annular illumination. *Sci. Rep.* 7, 7654. doi:10.1038/s41598-017-06837-1

Zuo, C., Sun, J., Zhang, J., Hu, Y., and Chen, Q. (2015). Lensless phase microscopy and diffraction tomography with multi-angle and multi-wavelength illuminations using a led matrix. *Opt. Express* 23, 14314–14328. doi:10.1364/oe.23.014314

Appendix A: Gradient calculation

Eq 3 can be transformed as follows (coordinates are omitted for convenience):

$$\varepsilon(O) = \sum \|U^u - U^e\|^2 = \sum\left(|U^e|^2 - 2\sqrt{I}\,|U^e| + I\right). \tag{6}$$

Then calculate the derivative of ε with respect to O, and it can then be expressed as

$$\nabla_O \varepsilon(O) = \sum\left[\frac{\partial \varepsilon(O)}{\partial O}\right]^*. \tag{7}$$

The equation in parentheses in Eq. 7 can be decomposed into three parts combined with Eq. 6 as follows:

$$\frac{\partial |U^e|^2}{\partial O} = \frac{\partial |OP + R|^2}{\partial O} = O^*|P|^2 + PR^* \tag{8}$$

$$\frac{\partial\left(2\sqrt{I}\,|U^e|\right)}{\partial O} = 2\sqrt{I}\;\frac{\partial |OP + R|}{\partial O} = \sqrt{I}P\frac{O^*P^* + R^*}{|OP + R|} \tag{9}$$

$$\frac{\partial I}{\partial O} = 0 \tag{10}$$

By plugging these three terms into Eq. 6, the gradient of ε with respect to O becomes

$$\begin{aligned}\nabla_O \varepsilon(O) &= \sum\left(O|P|^2 + P^*R - \sqrt{I}\,P^*\frac{OP + R}{|OP + R|}\right)\\ &= \sum\left[P^*\left(U^e - U^u\right)\right].\end{aligned} \tag{11}$$

Frontiers in Photonics

Research which sheds light on the science of photonics

An exciting new journal in its field which explores the science and technology of light and its many applications in our lives, from farming to communications.

Discover the latest Research Topics

See more →

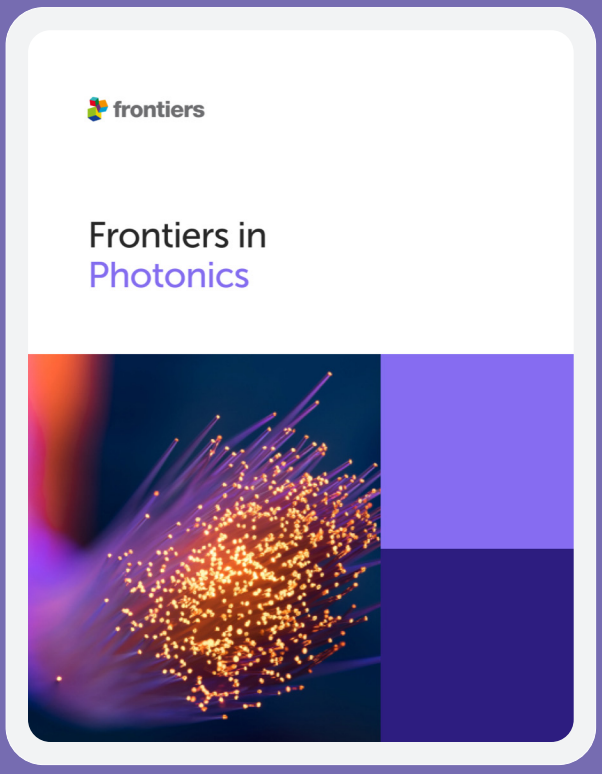

Frontiers

Avenue du Tribunal-Fédéral 34
1005 Lausanne, Swizerland
frontiersin.org

Contact us

+41 (0)21 510 17 00
frontiersin.org/about/contact